



D I S S E R T A T I O N

# Continuous-time Quantum Monte Carlo in the Hybridization Expansion: Implementations and Applications

ausgeführt zum Zwecke der Erlangung des akademischen Grades des  
Doktors der technischen Wissenschaften (Dr. techn.)

am Institut für Festkörperphysik der  
Technischen Universität Wien

unter Anleitung von  
Univ.-Prof. Dr. Karsten Held

durch  
Dipl.-Ing. Patrik Gunacker

Sambeckgasse 38, 1140 Wien  
Matrikelnummer 00826793



*Eidesstattliche Erklärung*

Ich erkläre an Eides statt, dass die vorliegende Arbeit nach den anerkannten Grundsätzen für wissenschaftliche Abhandlungen von mir selbstständig erstellt wurde. Alle verwendeten Hilfsmittel, insbesondere die zugrunde gelegte Literatur, sind in dieser Arbeit genannt und aufgelistet. Die aus den Quellen wörtlich entnommenen Stellen, sind als solche kenntlich gemacht.

Das Thema dieser Arbeit wurde von mir bisher weder im In- noch Ausland einer Beurteilerin/einem Beurteiler zur Begutachtung in irgendeiner Form als Prüfungsarbeit vorgelegt.

---

Datum, Ort

---

Unterschrift

*Affidavit*

I declare in lieu of oath, that I wrote this thesis and performed the associated research myself, using only literature cited in this volume. If text passages from sources are used literally, they are marked as such.

I confirm that this work is original and has not been submitted elsewhere for any examination, nor is it currently under consideration for a thesis elsewhere.

---

Date, Place

---

Signature



# Kurzfassung

Das Anderson-Störstellenmodell (AIM) ist von grundlegender Bedeutung für die Untersuchung von Materialien und Modellen mit starken elektronischen Korrelationen. Es steht außerdem im Zentrum Feynman-diagrammatischer Methoden wie der dynamischen Molekularfeldtheorie (DMFT) oder auch Erweiterungen zur DMFT, insbesondere was den numerischen Aufwand betrifft. Letztere quantifizieren sowohl lokale- als auch nicht-lokale elektronische Korrelationseffekte. Während lokale Korrelationseffekte in der DMFT durch Ein-Teilchen-Selbstenergien darstellbar sind, werden nicht-lokale Korrelationseffekte in diagrammatischen Erweiterungen zur DMFT aus Zwei-Teilchen-Vertexfunktionen berechnet. Diese beschreiben alle möglichen Streuungen zweier Teilchen im wechselwirkenden System. Allerdings besitzen sie auch eine wesentlich höhere Komplexität als die Ein-Teilchen-Selbstenergien.

Quantenmechanische Monte-Carlo Simulationen in kontinuierlicher Zeit (CT-QMC) erlauben es, die unendliche Störungsreihe der Zustandssumme stochastisch aufzusummieren, und liefern somit numerische Lösungen des AIM in einem großen Parameterbereich. Eine besonders erwähnenswerte Klasse dieser Störstellenlöser, sogenannte CT-HYB Algorithmen, entwickeln die Zustandssumme als Störungsreihe im Hybridisierungsanteil des AIM. Die Formulierung basiert auf einer Stark-Kopplungs-Entwicklung und erlaubt eine Erweiterung auf Mehrband-Systeme. Dadurch wird eine Analyse elektronischer und magnetischer Eigenschaften korrelierter Materialien möglich.

Die vorliegende Arbeit beschreibt die Messung der Zwei-Teilchen-Greenschen Funktion innerhalb des Mehrband-CT-HYB Algorithmus. Die zusätzliche Orbitalabhängigkeit der lokalen Wechselwirkung führt zu einer grundlegend unterschiedlichen Struktur der Zwei-Teilchen-Greenschen Funktion im Gegensatz zu der Ein-Teilchen-Greenschen Funktion: Für  $SU(2)$ -symmetrische Wechselwirkungen beinhaltet die Zwei-Teilchen-Greensche Funktion Komponenten, welche der Struktur von Spin-Umklapp- und Paar-Hüpf-Termen entsprechen. Auch wenn Störstellen-Greensche Funktionen lokal definiert sind, wird in der traditionellen Formulierung von CT-HYB die Greensche Funktion aus der Störungsreihe der Zustandssumme, bestehend aus Hybridisierungsereignissen, berechnet. Daraus folgt ein intrinsischer Mangel in dem ursprünglichen Algorithmus alle Zwei-Teilchen-Greensche Funktionen zu berechnen. In dieser Arbeit wird daher Wurm-Sampling entwickelt um dies zu ermöglichen. Im Zusammenhang mit CT-HYB, wird hier stattdessen die unendliche Störungsreihe der Observable stochastisch aufsummiert. Dadurch kann einerseits die vollständige Zwei-Teilchen-Greensche Funktion gemessen werden, aber auch verbesserte Schätzer für verwandte Größen wie z.B. die Vertex-Asymptotik. Neben der Diskussion diagrammatischer Grundlagen des Wurm-Samplings, werden in dieser Arbeit außerdem die technischen Aspekte des Algorithmus erläutert.

Der Zusammenhang zwischen den methodischen Überlegungen dieser Arbeit und der Physik wird in diversen Anwendungen hergestellt. Dabei werden Ein-Band- und Mehrband-Systeme im Bezug auf lokale und nicht-lokale Korrelationen diskutiert.



# Abstract

The Anderson impurity model (AIM) is crucial to material- and model considerations of strong electronic correlations in condensed matter physics. Numerically, the multi-orbital AIM is the center-piece of several Feynman diagrammatic methods such as the dynamical mean field theory (DMFT) or diagrammatic extensions to DMFT, which attempt to quantify local- and non-local electronic correlation effects. While local correlations in DMFT are best captured by one-particle self-energies, non-local correlations in diagrammatic extensions to DMFT originate from two-particle vertex functions. The latter describe all possible scattering events of two particles in an interacting system and greatly exceed the former in terms of complexity.

Continuous-time quantum Monte Carlo (CT-QMC) impurity solvers provide solutions to the AIM over a wide range of parameters. A noteworthy class of these solvers, CT-HYB algorithms, stochastically sample the infinite series expansion of the partition function in terms of the hybridization part of the AIM. This strong-coupling formulation allows for a straight-forward extension to multi-orbital systems, highly relevant for the analysis of electronic- and magnetic properties in correlated materials.

The following thesis attempts to incorporate the measurement of two-particle Green's function into the multi-orbital CT-HYB algorithm. An additional orbital-dependency in the local interaction significantly changes the structure of the two-particle Green's function as opposed to its one-particle counterpart. For  $SU(2)$ -symmetric interactions, the two-particle Green's function features components that resemble the amputated outer leg structure of pair-hopping and spin-flip terms. Although impurity Green's functions are defined locally, the traditional formulation of CT-HYB generates Green's function estimates directly from the stochastic series expansion of the partition function in terms of hybridization events. This leads to intrinsic shortcomings in the original formulation, which are remedied by a technique referred to as worm sampling. In the context of CT-HYB, one instead stochastically samples the infinite series expansion of the observable directly. This technique not only allows one to measure the full multi-orbital two-particle Green's function, but also leads to improved estimates of closely related quantities, such as the asymptotical structure of two-particle vertex functions. Alongside diagrammatic considerations of worm sampling, this thesis further discusses technical aspects of the algorithm itself.

In an attempt to create a link of methodological considerations featured in this work to physics, several applications to single- and multi-orbital systems are discussed with respect to local- and non-local correlation effects.





# Contents

<b>1</b>	<b>Introduction and Outline</b>	<b>1</b>
<b>2</b>	<b>Models and Methods</b>	<b>5</b>
2.1	Lattice Models . . . . .	5
2.1.1	Hubbard Lattice . . . . .	5
2.1.2	Tight-binding Lattice . . . . .	6
2.1.3	Atomic Limit . . . . .	12
2.1.4	Heisenberg Lattice . . . . .	13
2.1.5	Lattice Phase Diagram . . . . .	14
2.2	Impurity Models . . . . .	16
2.2.1	Anderson Impurity . . . . .	16
2.2.2	Kondo Model . . . . .	20
2.2.3	Falicov-Kimball Model and Resonant Level Model . . . . .	24
2.3	Multi-orbital Hubbard Model . . . . .	26
2.4	Dynamical Mean Field Theory . . . . .	27
2.5	Diagrammatic Extensions to DMFT . . . . .	31
2.5.1	Dynamical Vertex Approximation . . . . .	33
2.5.2	Dual Fermion Approach . . . . .	37
2.6	Analytic Continuation . . . . .	39
2.6.1	Padé . . . . .	42
2.6.2	Maximum Entropy Method . . . . .	42
2.6.3	Sparse Modeling . . . . .	44
<b>3</b>	<b>Continuous-time Quantum Monte Carlo</b>	<b>47</b>
3.1	Impurity Observables . . . . .	51
3.1.1	Green's Functions . . . . .	51
3.1.2	Occupation . . . . .	52
3.1.3	Self-energy . . . . .	53
3.1.4	Vertex Function . . . . .	54
3.2	Hybridization Expansion . . . . .	55
3.2.1	Partition Function . . . . .	55
3.2.2	Hybridization Estimators . . . . .	57
3.3	Worm Sampling . . . . .	64
3.3.1	Operator Sampling . . . . .	65
3.3.2	Worm Insertion and Removal Steps . . . . .	67

3.3.3	Pair Insertion and Removal Steps in Green's Function Space . . . . .	68
3.3.4	Worm Replacement Step in Green's Function Space . . . . .	69
3.3.5	$\delta$ -Estimators . . . . .	71
3.3.6	Full Estimators . . . . .	76
3.3.7	Normalization . . . . .	79
3.3.8	Component Sampling . . . . .	81
3.3.9	Autocorrelation . . . . .	85
3.4	Symmetric Improved Estimators . . . . .	90
3.4.1	One-Particle Symmetric Improved Estimator . . . . .	90
3.4.2	Two-Particle Symmetric Improved Estimator . . . . .	94
3.4.3	Generalizations and Feasibility . . . . .	99
<b>4</b>	<b>Single-Orbital Applications</b>	<b>101</b>
4.1	Mass-imbalanced Hubbard Model . . . . .	101
4.2	Vertex Divergences in the AIM . . . . .	105
4.3	Dual Fermion for the Hubbard Model . . . . .	110
4.3.1	Three-particle Corrections . . . . .	110
4.3.2	Dual Fermion Self-consistency . . . . .	115
<b>5</b>	<b>Multi-orbital Applications</b>	<b>123</b>
5.1	Spin-susceptibilities in the AIM . . . . .	123
5.2	Vertex Asymptotics . . . . .	125
5.3	AbinitoDFA . . . . .	129
<b>6</b>	<b>Conclusion</b>	<b>133</b>
	<b>Appendices</b>	<b>137</b>
<b>A</b>	<b>Limits of the Hubbard Model</b>	<b>139</b>
A.1	Non-interacting Limit . . . . .	139
A.2	Atomic Limit . . . . .	140
A.3	Heisenberg Limit . . . . .	142
A.4	Falicov-Kimball Limit . . . . .	143
<b>B</b>	<b>Two-particle Frequency Conventions</b>	<b>145</b>
<b>C</b>	<b>Functional Derivation of the Dual Fermion Approach</b>	<b>147</b>
<b>D</b>	<b>Multi-orbital Hubbard Model</b>	<b>151</b>
D.1	Half-filling Condition in DMFT . . . . .	151
D.2	Lowest-order Contributions to $F$ . . . . .	153
<b>E</b>	<b>Autocorrelation in CT-HYB</b>	<b>155</b>
E.1	Error Estimation for Correlated Samples . . . . .	155

*CONTENTS* xi

**F Symmetric Improved Estimators** **157**

    F.1 Two-particle Symmetric Improved Estimator . . . . . 157

**Bibliography** **161**

**Acknowledgements** **175**

**Curriculum Vitae** **177**

**Publication List** **179**



# Chapter 1

## Introduction and Outline

In 1918, exactly one century ago, the theoretical physicist Max Planck was awarded the Nobel prize in physics “in recognition of the services he rendered to the advancement of Physics by his discovery of energy quanta” [Nobel Media, 2014]. In order to explain the evident absence of the ultraviolet catastrophe of black body radiation, Planck introduced a quantized energy unit. Although seemingly unspectacular, this observation triggered the groundbreaking development of quantum mechanics, which not only fundamentally altered physical intuition, but further influenced the digital revolution beyond imagination.

While the diversity of quantum-mechanical particles was (and still is) systematically uncovered by high-energy physicists, solid-state physicists started to investigate the collective behavior of quantum-mechanical particles in periodic lattice structures. Electronic correlation effects are encoded in the quantum many-body problem and are believed to be responsible for some of the most interesting properties of condensed matter physics, including superconductivity, correlation-driven metal-to-insulator transitions and some of the recently much-discussed properties of topological insulators.

The quantum-mechanical solution of these deceptively simple lattice systems is, in general, exponentially difficult. The Hilbert space of the underlying Hamiltonian for spin-1/2 particles (i.e. fermions) scales with  $4^N$ , where  $N$  is the number of lattice sites or bands considered. Despite the advancements in modern computer technology, solutions to the quantum many-body problem for lattice systems remain out of reach.

Classical lattice systems, such as the Ising model, and lattice systems for particles with an integer spin (i.e. bosons) can be efficiently solved with Monte Carlo methods. However, a straight-forward application of Monte Carlo onto the fermionic lattice problem results in an exponentially hard sign problem, which is rooted in the sign flip when exchanging two fermions in the many-body wave function. The sign problem can be controlled for relatively small finite-sized clusters or single impurity sites. For that matter Feynman diagrammatic mappings may be formulated between the lattice problem and the impurity problem.

This work introduces the Hubbard model as the prototypical lattice model of solid state physics in Chapter 2.1. In the following the weak-coupling and strong-coupling limit of the Hubbard model are discussed in greater detail. The Anderson impurity model is introduced as the prototypical impurity model (i.e. an impurity embedded in a non-interacting bath) in Chapter 2.2. Different limiting cases of impurity models are discussed

similar to the lattice models. Additional derivations for lattice and impurity models are presented in Appendix A.

The lattice- and impurity models of this chapter are primarily formulated for the single-orbital case in order to avoid unnecessary complications by introducing additional degrees of freedom. However, the multi-orbital lattice- and impurity models generally possess a much richer phase diagram. The multi-orbital extension to the Hubbard model in terms of the  $SU(2)$ -symmetric Slater-Kanamori interaction is introduced in Chapter 2.3.

Having formulated the lattice and impurity models, the remaining chapter introduces various methods, which provide solutions for such model systems. For infinite lattice dimensions, the exact mapping of the Hubbard lattice onto the Anderson impurity, referred to as dynamical mean field theory (DMFT), is introduced in Chapter 2.4. When considering finite dimensional lattices, the exact mapping of DMFT is no longer fulfilled. Such low-dimensional lattice systems, however, are especially interesting due to non-local correlation effects. In order to approximate non-local properties of the lattice, the local two-particle diagrams of DMFT can be used to construct additional non-local Feynman diagrams. The two most prominent diagrammatic extensions to DMFT, the dynamical vertex approximation (D $\Gamma$ A) and the dual fermion (DF) approximation are introduced in Chapter 2.5.

Thermal quantum field theories are commonly represented in the Matsubara formalism, which establishes an a priori artificial link between the time- and temperature domain to simplify calculations. Diagrammatic methods and finite-temperature results obtained from impurity solvers are mostly expressed in this formalism. The transition between the Matsubara (imaginary) time/frequency domain and the real time/frequency domain is accomplished by analytic continuation. Chapter 2.6 introduces the concept of analytic continuation and further discusses different algorithms for its solution.

While DMFT formulates self-consistency equations for mapping the Hubbard model onto an (auxiliary) impurity model, a priori the method does not specify how to solve the impurity model itself. As of today, continuous-time quantum Monte Carlo (CT-QMC) impurity solvers are the most popular option for solving the impurity model because of their ability to treat continuous baths, their parameter robustness and (maybe most important) their superior scaling in terms of the number of orbitals/sites in comparison to methods based on exact diagonalizations of the Hamiltonian. Chapter 3 deals with the CT-QMC algorithm in the hybridization expansion (CT-HYB). The chapter begins with discussing CT-HYB in context of various other impurity solvers. In Chapters 3.1 and 3.2 the fundamentals of the conventional sampling- and estimator theory of CT-HYB are derived and some resulting shortcomings are discussed. These sections describe the CT-HYB method prior to this work. Chapter 3.3 discusses the theory and implications of worm sampling as an extension to the CT-HYB algorithm and may be considered the most important chapter of this work. Extending CT-HYB by worm sampling allows for the complete measurement of the impurity two-particle Green's functions in the multi-orbital case, being the main ingredient for multi-orbital diagrammatic extensions to DMFT. Several technical aspects including worm estimator theory, normalization and autocorrelation are discussed. Chapter 3.4 concludes the discussion of CT-HYB by contrasting the one- and two-particle Green's function estimators with their analogs in weak-coupling CT-QMC. This comparison ultimately motivates the derivation of symmetric improved estimators,

resulting in enhanced Green's function estimates over the entire frequency range.

The following two chapters summarize various applications of the CT-HYB algorithm for the single-orbital (Chapter 4) and the multi-orbital case (Chapter 5), which were worked out with several co-workers. Further, these two chapters attempt to create a link to the lattice- and impurity models introduced in Chapter 2.1. Besides exploring physical implications of the different applications, several technical aspects with respect to Chapter 3 are discussed.

Chapter 4.1 investigates the transition between the Hubbard model and the Falicov-Kimball model in the mass-imbalanced Hubbard model on the one-particle level. From a technical point of view, this may be considered the physical counterpart to the implications of the algorithmic extensions of CT-HYB by worm sampling. Chapter 4.2 investigates divergences in irreducible subsets of diagrams of the two-particle vertex function for the Anderson impurity model. These divergences generally indicate a break-down of perturbation theory in a parameter region of the phase diagram, which otherwise seems to be inconspicuous. Chapter 4.3 explores the phase diagram of the two-dimensional Hubbard model by employing the DF approach. Various assumptions of the DF approach are critically investigated.

Chapter 5.1 investigates the  $SU(2)$ -symmetry of the two-particle Green's function for the multi-orbital Anderson impurity model. The complete two-particle Green's functions includes renormalized vertices with an outer structure similar to the spin-flip and pair-hopping bare vertex functions of the  $SU(2)$ -symmetric interaction itself. A complete knowledge of the impurity two-particle Green's function is necessary when constructing non-local diagrams in the following. Chapter 5.2 derives the asymptotical frequency structure of the multi-orbital impurity two-particle vertex function. The asymptotical structure allows one to minimize box effects in frequency summations, which are important when determining susceptibilities or self-energies from the corresponding vertex functions. Furthermore, a two-particle vertex function including the spin-flip and pair-hopping contributions and the asymptotical structure is constructed for the testbed material  $SrVO_3$ . Chapter 5.3 concludes the multi-orbital applications by calculating non-local effects for  $SrVO_3$  within D $\Gamma$ A.

Chapter 6 summarizes the key findings of this work, especially with regard to extensions to the CT-HYB algorithm with worm sampling and applications to the Hubbard model. A concluding outlook is given, where open problems and future work is discussed.

On a final note, considerable efforts made in interfacing the CT-HYB algorithm with various diagrammatic methods are not thoroughly described in this work. Instead, for further information the reader is referenced to the following theses to be read in conjunction: Ref. [Wallerberger, 2016] for DMFT, Ref. [Galler, 2017] for D $\Gamma$ A and Ref. [Ribic, 2018] for DF.





# Chapter 2

## Models and Methods

### 2.1 Lattice Models

#### 2.1.1 Hubbard Lattice

The single-orbital Hubbard model [Hubbard, 1964] in second quantization is given by

$$\hat{H}_{\text{hubbard}} = \frac{1}{2} \sum_{ij,\sigma}^N t_{ij} (\hat{c}_{i\sigma}^\dagger \hat{c}_{j\sigma} + \hat{c}_{j\sigma}^\dagger \hat{c}_{i\sigma}) + \sum_i^N U \hat{n}_{i\uparrow} \hat{n}_{i\downarrow}, \quad (2.1)$$

where  $\hat{c}_{i\sigma}^{(\dagger)}$  is the annihilation (creation) operator at site  $i$  with spin  $\sigma = \{\uparrow, \downarrow\}$  and  $\hat{n}_{i\sigma} = \hat{c}_{i\sigma}^\dagger \hat{c}_{i\sigma}$  is the density operator. The kinetic energy of the system is determined by the hopping amplitude  $t_{ij}$  between sites  $i$  and  $j$  and the potential energy is determined by the on-site Coulomb repulsion  $U$ . The above form of the Hamiltonian does not specify the dimension or geometry of the lattice, although the site index in principle ranges over a countably infinite set (i.e.  $N \rightarrow \infty$ ). As  $\hat{H}_{\text{hubbard}}$  is Hermitian, the hopping amplitude satisfies  $t_{ij} = t_{ji}^*$ . The factor  $\frac{1}{2}$  in the kinetic energy term compensates double counting.

While the hopping amplitude  $t_{ij}$  further connects any two sites  $i$  and  $j$  on the infinite Hubbard lattice, in most cases it is useful to limit the hopping to neighboring sites only. For nearest neighbor hopping, the above Hamiltonian simplifies, such that the kinetic energy term reduces to

$$\frac{1}{2} \sum_{ij,\sigma}^N t_{ij} (\hat{c}_{i\sigma}^\dagger \hat{c}_{j\sigma} + \hat{c}_{j\sigma}^\dagger \hat{c}_{i\sigma}) \rightarrow -\mu \sum_{i,\sigma} \hat{c}_{i\sigma}^\dagger \hat{c}_{i\sigma} - \frac{t}{2} \sum_{\langle ij \rangle, \sigma}^N (\hat{c}_{i\sigma}^\dagger \hat{c}_{j\sigma} + \hat{c}_{j\sigma}^\dagger \hat{c}_{i\sigma}), \quad (2.2)$$

where  $\langle ij \rangle$  includes nearest-neighbors only, and  $-t$  is the respective hopping. The onsite-energy  $\mu$  usually encoded in  $t_{ii}$  is now explicit. An illustration of the Hubbard model on a square lattice with nearest-neighbor and next-nearest-neighbor hopping is given in Figure 2.1.

One can now observe that the kinetic energy term reduces the overall energy of the system if a particle hops from one site to another, while the potential energy term increases the energy if two electrons are located at the same site. Alternatively, one can interpret this behavior as the interplay between single-particle processes (hopping) and two-particle

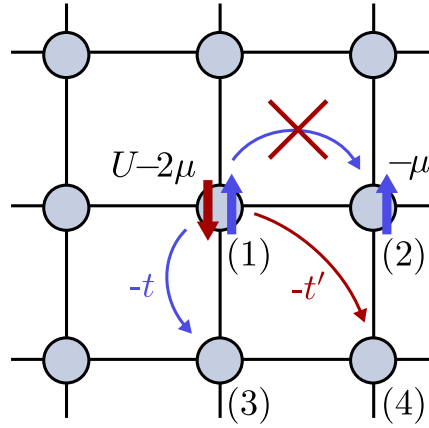


Figure 2.1: Hubbard model for the two-dimensional square lattice. Spin-up electrons are marked with blue arrows, spin-down electrons with red arrows. (1) double occupation with energy cost  $U - 2\mu$ . (2) single occupation with energy cost  $-\mu$ . (1)  $\rightarrow$  (2) hopping forbidden due to Pauli principle. (1)  $\rightarrow$  (3) nearest-neighbor hopping with amplitude  $-t$ . (1)  $\rightarrow$  (4) next-nearest-neighbor hopping with amplitude  $-t'$ .

processes (interaction). The intrinsic problem becomes more apparent, when transforming the kinetic energy term into momentum-space:

$$\hat{H}_{\text{hubbard}} = \sum_{\vec{k}, \sigma} \varepsilon_{\vec{k}} \hat{c}_{\vec{k}\sigma}^\dagger \hat{c}_{\vec{k}\sigma} + \sum_i^N U \hat{n}_{i\uparrow} \hat{n}_{i\downarrow}. \quad (2.3)$$

This shows that the kinetic energy term is now diagonal in momentum space, while the potential energy term is diagonal in real space. Intuitively, the kinetic energy term favors the non-localized band behavior of electrons, while the potential energy term favors the localized electron behavior. In the limiting case of a vanishing potential energy term ( $U \rightarrow 0$ ), the system becomes non-interacting and the Hamiltonian reduces to a tight-binding like Hamiltonian, without any implicit many-body effects. Sometimes this is referred to as the non-interacting limit. The case where the kinetic energy term is significantly larger than the potential energy term ( $t \gg U$ ) is referred to as weak-coupling limit. On the other hand, the case where the potential energy term is significantly larger than the kinetic energy term ( $U \gg t$ ) is referred to as the strong-coupling limit. If the kinetic energy term vanishes ( $t \rightarrow 0$ ), the Hamiltonian reduces to an atomic-limit like Hamiltonian, which can be solved analytically.

Nevertheless, the most interesting physics take place if the kinetic energy term is of a similar magnitude as the potential energy term. Without further simplifications, apart from the one-dimensional lattice chain no analytic expressions exist for the Hubbard model at this point and approximate solutions need to be considered.

### 2.1.2 Tight-binding Lattice

In the non-interacting limit, the potential energy term of the Hubbard model vanishes as  $U/t \rightarrow 0$ . The Hubbard Hamiltonian then reduces to the tight-binding model [Slater and

Koster, 1954] in real space:

$$\hat{H}_{\text{tb}} = \frac{1}{2} \sum_{ij,\sigma}^N t_{ij} (\hat{c}_{i\sigma}^\dagger \hat{c}_{j\sigma} + \hat{c}_{j\sigma}^\dagger \hat{c}_{i\sigma}). \quad (2.4)$$

The Fourier transform for the operators  $\hat{c}_{j\sigma}$  and  $\hat{c}_{i\sigma}^\dagger$  is defined as:

$$\hat{c}_{i\sigma} = \frac{1}{\sqrt{N}} \sum_{\vec{k}}^{\text{BZ}} e^{-i\vec{k}\vec{r}_i} \hat{c}_{\vec{k}\sigma} \quad (2.5)$$

$$\hat{c}_{i\sigma}^\dagger = \frac{1}{\sqrt{N}} \sum_{\vec{k}}^{\text{BZ}} e^{i\vec{k}\vec{r}_i} \hat{c}_{\vec{k}\sigma}^\dagger \quad (2.6)$$

This can be applied to the tight-binding Hamiltonian (2.4):

$$\hat{H}_{\text{tb}} = \frac{1}{2N} \sum_{\vec{k}\vec{k}'}^{\text{BZ}} \sum_{ij,\sigma}^N t_{ij} (e^{i\vec{k}\vec{r}_i} e^{-i\vec{k}'\vec{r}_j} \hat{c}_{\vec{k}\sigma}^\dagger \hat{c}_{\vec{k}'\sigma} + e^{i\vec{k}'\vec{r}_j} e^{-i\vec{k}\vec{r}_i} \hat{c}_{\vec{k}'\sigma}^\dagger \hat{c}_{\vec{k}\sigma}) \quad (2.7)$$

The non-interacting system is diagonal in momentum space, such that  $\vec{k} = \vec{k}'$ . This recovers (2.3) for  $U = 0$  and defines the relation between the hopping matrix  $t_{ij}$  and the dispersion relation  $\varepsilon_{\vec{k}}$ :

$$\varepsilon_{\vec{k}} = \frac{1}{2N} \sum_{ij}^N t_{ij} (e^{i\vec{k}(\vec{r}_i - \vec{r}_j)} + e^{i\vec{k}(\vec{r}_j - \vec{r}_i)}) \quad (2.8)$$

By specifying the dimension and geometry of the lattice, one can now calculate the dispersion relation  $\varepsilon_{\vec{k}}$  explicitly. In the following the lattice parameter is set to  $a = 1$ , so that  $|\vec{k}| \in [0, 2\pi)$  and  $\vec{r}_i = \vec{e}_i$ . For the two-dimensional tight-binding model on a square lattice with nearest neighbor hopping  $-t$  each lattice site contributes with eight hopping terms (only four being unique due to double counting reasons) and one on-site term  $t_{ii} = -\mu$ , such that:

$$\varepsilon_{\vec{k}} = -\mu - t(e^{ik_x} + e^{-ik_x} + e^{ik_y} + e^{-ik_y}) \quad (2.9)$$

$$= -\mu - 2t(\cos k_x + \cos k_y) \quad (2.10)$$

When also considering next-nearest neighbor hopping with  $-t'$  another four terms contribute:

$$\varepsilon_{\vec{k}} = -\mu - 2t(\cos k_x + \cos k_y) - 2t'(\cos(k_x + k_y) + \cos(k_x - k_y)) \quad (2.11)$$

$$= -\mu - 2t(\cos k_x + \cos k_y) - 4t'(\cos k_x \cos k_y) \quad (2.12)$$

From a pragmatic point of view, it is more common to extract the density of states (DOS) and Fermi surfaces from the dispersion relation. Both quantities follow from the non-interacting Green's function (in real frequencies  $\omega$ ):

$$\mathcal{G}(\vec{k}, \omega) = \frac{1}{\omega - \varepsilon_{\vec{k}} + i\delta}, \quad (2.13)$$

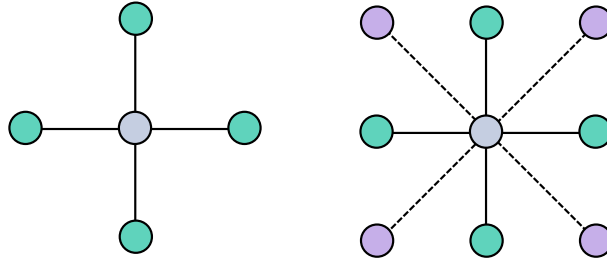


Figure 2.2: Nearest neighbors (green) along the x- and y-axis and next-nearest neighbors (purple) along the diagonals in the tight-binding model for the two-dimensional square lattice.

where  $i\delta$  is an imaginary-offset for the poles of the retarded-Green's function. Relation (2.13) can be interpreted as a direct analytic continuation, which is possible if the frequency dependence is known analytically. A more general form for interacting Green's functions is discussed later. The momentum dependent DOS is given as:

$$A_\sigma(\vec{k}, \omega) = -\frac{1}{\pi} \Im \mathcal{G}(\vec{k}, \omega) = -\frac{1}{\pi} \Im \frac{1}{\omega - \varepsilon_{\vec{k}} + i\delta}, \quad (2.14)$$

where the subscript  $\sigma$  is the spin-dependence, which is necessary to assure the integrated DOS evaluates to unity for each flavor. A direct evaluation of the above expression yields:

$$A_\sigma(\vec{k}, \omega) = \frac{1}{\pi} \frac{\delta}{(\omega - \varepsilon_{\vec{k}})^2 + \delta^2}, \quad (2.15)$$

which is nothing but the definition of the  $\delta$ -distribution following a Lorentzian with  $\delta \rightarrow 0$ . The momentum integrated spectral function follows as:

$$A_\sigma(\omega) = \frac{1}{N} \sum_{\vec{k}}^{\text{BZ}} \delta(\omega - \varepsilon_{\vec{k}}). \quad (2.16)$$

In case more orbitals are involved the dispersion relation needs to be diagonalized in the first place. Intuitively, relation (2.16) can be interpreted as counting the number of  $k$ -points whose eigen-energy  $\varepsilon_{\vec{k}}$  equals a given energy  $\omega$ .

The DOS for the two-dimensional tight-binding model of relation (2.11) is shown in Figure 2.3. The integral over all frequencies for a given spin yields unity, which accounts for the conservation of the particle number. Different types of critical points exist in the two-dimensional DOS, which relate back to extrema of the dispersion relation. The minimal and the maximal value of the dispersion relation form sharp edges of the spectra on either side. The saddle-point of the dispersion relation at  $\vec{k} = (\pi, 0)$  is responsible for the logarithmic divergence at  $\omega = 0$ , which is also known as the Van Hove singularity [Van Hove, 1953]. In general, these features are also present in density of states calculated from density functional theory for materials, although in practice they may be further smoothed by scattering with phonons or other quasi-particles. A more complete discussion about singularities in the DOS is found in literature (e.g. Bassani and Parravicini [Bassani and

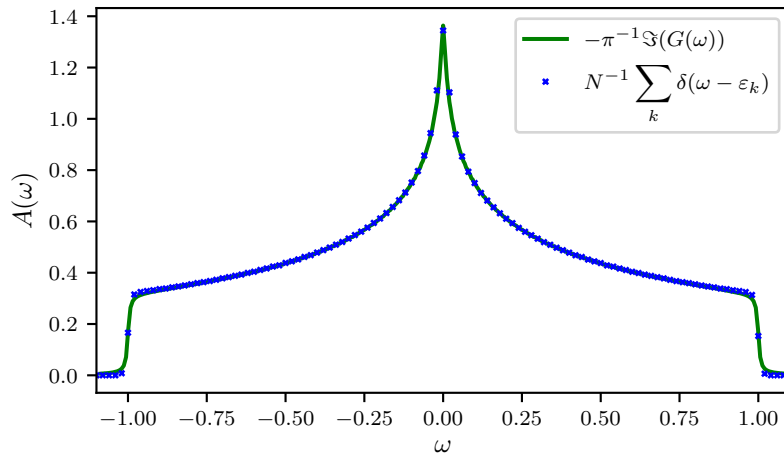


Figure 2.3: DOS of the two-dimensional tight-binding model for a given spin on a square lattice with nearest-neighbor hopping  $t = 0.25$  at half-filling  $\mu = 0$  and 400 k-points in both directions. The DOS is evaluated at the level of the Green's function (2.16) on a logarithmic  $\omega$ -grid around the origin with 400 points (green) and at the level of binning of eigen-energies (2.14) for a linear  $\omega$ -grid with 2000 points (blue). The latter was smoothed using a Gaussian filter to reduce the artifacts from the  $\delta$ -like bins. The filtering procedure is in direct analogy to the imaginary offset  $i\delta$  of the Green's function, which was set to  $\delta = 5 \cdot 10^{-3}$ . This smoothing also yields a cut-off for the Van Hove singularity at  $\omega = 0$ .

Parravicini, 1975]). The bandwidth of the DOS follows from the minimal and maximal possible value in the dispersion relation with  $W = 8t$  in two dimensions.

The Fermi surface can be extracted from the  $k$ -dependent density of states with  $A(\vec{k}, \omega = \mu)$ . For the non-interacting case very sharp one-dimensional boundaries define the Fermi surface. Wave vectors within the Fermi surface  $\varepsilon_{\vec{k}} < \varepsilon_F$  correspond to the occupied energy levels, while wave vectors above the Fermi wave vector are unoccupied. The Fermi surface for the two-dimensional tight-binding model is shown in Figure 2.4. At half-filling the Fermi surface resembles a diamond-shaped boundary, with perfect nesting at a nesting vector  $\vec{Q} = (\pm\pi, \pm\pi)$ . This exactly coincides with the Van Hove singularity discussed earlier. Below half-filling the Fermi surface is a closed structure and above half-filling it opens at wave vectors around  $\vec{k} = (\pm\pi, 0)$  and  $\vec{k} = (0, \pm\pi)$ . Also for the interacting case the analysis of the Fermi surface stays relevant. The Fermi surface gives first hints about instabilities along nesting vectors or the formation of gaps.

In order to determine the magnetic ordering of the Hubbard model in the non-interacting case it is necessary to investigate the static spin-susceptibility  $\chi_s(\vec{q}, \omega = 0)$  in more detail. In a first approximation one can express the spin- and charge susceptibility

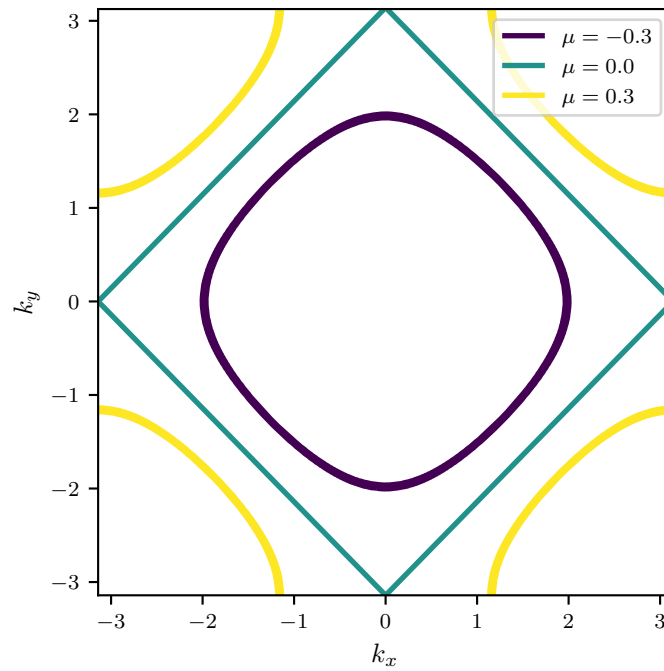


Figure 2.4: Fermi surface (i.e. constant energy contours) of the two-dimensional tight-binding model with the parameters defined in Figure 2.3 for the underdoped case (purple), half-filling (turquoise) and the overdoped case (yellow). The underdoped case relates to a closed Fermi surface centered around the origin. The half-filled case relates to a diamond shaped Fermi surface with a nesting vector  $\vec{Q} = (\pm\pi, \pm\pi)$ . The overdoped case relates to a Fermi surface where the four arcs form a closed Fermi surface if periodic boundary conditions are included.

as a diagrammatic ladder construction of (single-particle) Green's functions:

$$\chi_s(\vec{q}, \omega = 0) = \frac{\chi_0(\vec{q}, 0)}{1 - U\chi_0(\vec{q}, 0)} \quad (2.17)$$

$$\chi_c(\vec{q}, \omega = 0) = \frac{\chi_0(\vec{q}, 0)}{1 + U\chi_0(\vec{q}, 0)}, \quad (2.18)$$

where  $\chi_0(\vec{q}, \omega)$  is the bubble-term, which is constructed from non-interacting Green's functions only

$$\chi_0(\vec{q}, \omega) = \frac{1}{N} \sum_{\vec{k}}^{\text{BZ}} \frac{f(\varepsilon_{\vec{k}-\vec{q}}) - f(\varepsilon_{\vec{k}})}{\omega + i\delta - (\varepsilon_{\vec{k}-\vec{q}} - \varepsilon_{\vec{k}})} \quad (2.19)$$

where  $f(x) = 1/(1 + e^{\beta x})$  is the Fermi distribution function. The ladder construction is more commonly known as the random phase approximation (RPA), originally formulated by Bohm and Pines [Bohm and Pines, 1953]. A more detailed derivation of the bubble-term for the non-interacting Green's is given in Appendix A.1. The static (i.e.  $\omega = 0$ ) part of the bubble-term shows a logarithmic divergence for the nesting vector  $\vec{q} = \vec{Q}$  as the dispersion relation maps to itself (i.e.  $\varepsilon_{\vec{k}} = \varepsilon_{\vec{k}-\vec{Q}}$ ). This suggests that the system is magnetically ordering. As opposed to the Green's function itself, the susceptibility shows an explicit temperature dependence due to the Fermi distribution functions. The divergence of the bubble-term with the temperature follows as [Shimahara and Takada, 1988]

$$\chi_0(\vec{q} = \vec{0}, \omega = 0) \sim \frac{1}{t} \ln t\beta \quad (2.20)$$

$$\chi_0(\vec{q} = \vec{Q}, \omega = 0) \sim \frac{1}{t} \ln^2 t\beta, \quad (2.21)$$

which suggests that the temperature divergence occurs at  $\vec{q} = \vec{Q}$  first, before occurring at  $\vec{q} = \vec{0}$ . Thus, the non-interacting two-dimensional Hubbard model with nearest neighbor hopping has a tendency to order anti-ferromagnetically with  $\vec{Q} = (\pm\pi, \pm\pi)$ . The behavior of the bubble-term for different values of  $\vec{q}$  and inverse temperatures  $\beta$  is shown in Figure 2.5. In order to extract the anti-ferromagnetic transition temperature, the spin susceptibility in (2.17) needs to be analyzed. The expression diverges for  $U\chi_0(\vec{q} = \vec{Q}, 0) = 1$ , resulting in a transition temperature  $T_N \sim te^{-\sqrt{t/U}}$ .

In the non-interacting system, the Green's function itself has no explicit temperature dependence. In the next section the atomic limit is investigated. While the analytic solution of the Green's function in the Matsubara frequency formalism shows a temperature dependence for the Matsubara frequencies, the temperature can be considered as a parameter which determines the "resolution" of the analytic result on the Matsubara axis. A true energy scale due to temperature effects is only observed in interacting-systems, where both the potential energy and the kinetic energy term are present.

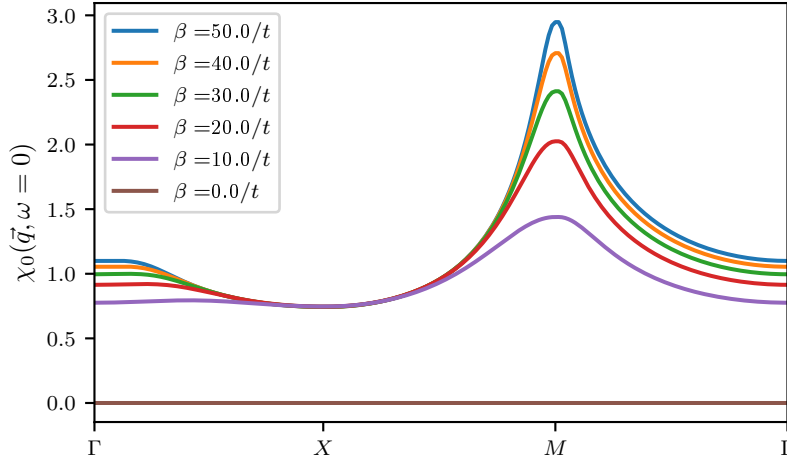


Figure 2.5: Non-interacting bubble-term  $\chi_0(\vec{q}, \omega = 0)$  for a  $q$ -path through the Brillouin zone, where the  $\Gamma$ -point is at  $\vec{q} = (0, 0)$ , the  $X$ -point is at  $\vec{q} = (\pi, 0)$  and the  $M$ -point at  $\vec{q} = (\pi, \pi)$  for different inverse temperatures  $\beta \in [0, 50/t]$ . The logarithmic divergence at the  $\Gamma$ -point and the quadratic logarithmic divergence at the  $M$ -point with inverse temperature can be observed. The system has a tendency to order anti-ferromagnetically.

### 2.1.3 Atomic Limit

In the atomic limit, the kinetic energy term of the Hubbard model vanishes as  $U/t \rightarrow \infty$ . The Hubbard Hamiltonian then reduces to a lattice of disconnected Hubbard atoms:

$$\hat{H}_{\text{at}} = \sum_i^N \left( -\mu(\hat{n}_{i\uparrow} + \hat{n}_{i\downarrow}) + U\hat{n}_{i\uparrow}\hat{n}_{i\downarrow} \right). \quad (2.22)$$

Contrary to the non-interacting case, the above Hamiltonian displays properties of many-body physics due to the non-vanishing two-particle interaction. More specifically, the strong correlation effects present in the interacting atomic lattice, as opposed to the non-interacting lattice, are captured in a non-vanishing self-energy. This can, nevertheless, be solved analytically by first calculating the imaginary time Green's function in the Lehmann representation.<sup>1</sup> A detailed derivation can be found in Appendix A.2. Here, only the results for the Green's function in Matsubara frequencies and the DOS are given:

$$G_\sigma(i\nu) = \int_0^\beta e^{i\nu\tau} G_\sigma(\tau) = \frac{1}{1 + 2e^{\beta\mu} + e^{-\beta(U-2\mu)}} \left( \frac{1 + e^{\beta\mu}}{i\nu + \mu} + \frac{e^{\beta\mu} + e^{\beta(2\mu-U)}}{i\nu + \mu - U} \right), \quad (2.23)$$

with the fermionic Matsubara frequency  $i\nu = i\frac{(2n+1)\pi}{\beta}$  and  $n \in \mathbb{Z}$ . For the half-filling case the above simplifies to:

$$G_\sigma(i\nu) = \frac{1}{2} \left( \frac{1}{i\nu - \frac{U}{2}} + \frac{1}{i\nu + \frac{U}{2}} \right). \quad (2.24)$$

<sup>1</sup>It is common to refer to the spectral representation of expectation values as the ‘‘Lehmann representation’’ explicitly. Historically, the spectral representation was independently formulated by Källén [Källén, 1952] and Lehmann [Lehmann, 1954] in order to derive a general expression of the two-point Green's function in interacting quantum field theories.



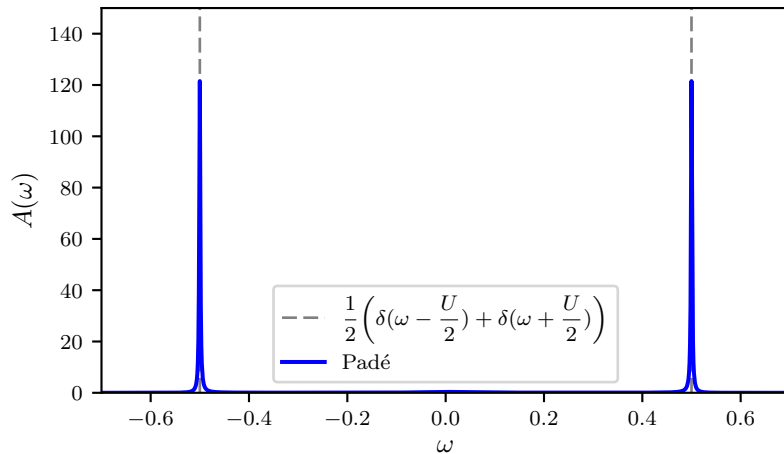


Figure 2.6: DOS of the atomic limit for  $U = 1$ . The DOS is extracted from the Green’s function and analytically continued using Padé approximants (blue). The analytic result of two  $\delta$ -peaks symmetrically offset from the origin by  $\pm \frac{U}{2}$  is shown in dashed-lines (gray).

From the poles of the Green’s function, one can immediately read off the DOS as:

$$A_{\sigma}(\omega) = \frac{1}{2} \left( \delta\left(\omega - \frac{U}{2}\right) + \delta\left(\omega + \frac{U}{2}\right) \right). \quad (2.25)$$

The  $\delta$ -peak at  $\omega = -\frac{U}{2}$  corresponds to the filled single-occupied states  $\langle \uparrow |$  and  $\langle \downarrow |$ , while the  $\delta$ -peak at  $\omega = +\frac{U}{2}$  corresponds to the empty state  $\langle |$  and double-occupied state  $\langle \uparrow \downarrow |$ . The two peaks are separated by an overall “distance” of  $U$ . The DOS of the atomic limit is presented in Figure 2.6. Besides the analytic formula, a Padé approximant was fit to the Matsubara data, to motivate the introduction of analytic continuation techniques. A more thorough discussion of the analytic continuation procedure is given in Section 2.6.

The atomic limit fully suppresses any motion on the lattice. At half-filling, the lowest lying energy states are occupied, i.e  $\langle \uparrow |$  and  $\langle \downarrow |$ . The double-occupied state  $\langle \uparrow \downarrow |$  is not filled, according to the intuition that the potential energy cost becomes infinitely large with respect to the kinetic energy. As there is no coupling between neighboring sites, there exists no magnetic ordering at any given temperature. One may argue that this limit is rather fabricated. If one instead allows for a finite, but non-vanishing hopping and a much higher Coulomb repulsion  $U \gg t$ , the system is close to the atomic limit and the double-occupied state can be ignored. In this scenario, the system can then be mapped onto a Heisenberg model discussed in the next section.

### 2.1.4 Heisenberg Lattice

The spin-1/2 anti-ferromagnetic Heisenberg model [Heisenberg, 1928] is the limit of the Hubbard model for  $U \gg t$ , i.e. a model which is close to the atomic limit, but not the atomic limit itself. This immediately suggests formulating a perturbation theory around the atomic limit to derive the Heisenberg model. Starting from the Hubbard model

in (2.1), one sets the potential energy term as the unperturbed Hamiltonian  $\hat{H}_0$  and the kinetic energy term as the perturbation  $\hat{H}_1$ . With second-order perturbation theory and nearest-neighbor hopping the Hubbard model reduces to the  $tJ$ -model:

$$\hat{H}_{tJ} = \frac{1}{2} \sum_{\langle ij \rangle, \sigma} t_{ij} (\hat{c}_{i\sigma}^\dagger \hat{c}_{j\sigma} + \hat{c}_{j\sigma}^\dagger \hat{c}_{i\sigma}) + \frac{1}{2} \sum_{\langle ij \rangle} J_{ij} \left( \hat{S}_i \cdot \hat{S}_j - \frac{1}{4} \hat{n}_i \hat{n}_j \right), \quad (2.26)$$

where  $J_{ij} = 4t_{ij}^2/U$  is the spin-spin interaction due to second-order virtual processes for electrons with opposite spin on neighboring sites and  $\hat{n}_i = (\hat{n}_{i\uparrow} + \hat{n}_{i\downarrow})$  is the density for site  $i$ . Further,  $\hat{S}_i$  is the spin-operator at site  $i$  with:

$$\hat{S}_i = \frac{1}{2} \begin{pmatrix} \hat{c}_{i\uparrow}^\dagger & \hat{c}_{i\downarrow}^\dagger \end{pmatrix} \vec{\sigma} \begin{pmatrix} \hat{c}_{i\uparrow} \\ \hat{c}_{i\downarrow} \end{pmatrix}, \quad (2.27)$$

with  $\vec{\sigma} = (\sigma_x, \sigma_y, \sigma_z)^T$  being the vector of Pauli-matrices. At half-filling the  $tJ$ -model further reduces to the Heisenberg model:

$$\hat{H}_{\text{heisenberg}} = \frac{1}{2} \sum_{\langle ij \rangle} J_{ij} \hat{S}_i \cdot \hat{S}_j, \quad (2.28)$$

The Heisenberg model assumes that the double-occupied state  $\langle \uparrow\downarrow |$  itself is never realized for any prolonged period of time due to the high potential energy costs. Instead, the double-occupied state is only temporarily realized during a second-order virtual process, where an electron hops onto a site already occupied by another electron and either of the electrons hops off the site immediately afterwards. Due to the Pauli principle, such a process is only possible if the two electrons have opposite spin, such that the Heisenberg model favors anti-ferromagnetic ordering. Intuitively the information about the second-order virtual process is already encoded in  $J_{ij} = 4t_{ij}^2/U$ . A detailed derivation is given in Appendix A.3. The first-order and second-order processes of the  $tJ$ - and the Heisenberg model are illustrated in Figure 2.7.

While the Heisenberg model itself allows for both ferromagnetic and anti-ferromagnetic coupling, only the latter is realized in the limit of the Hubbard model. The magnetic ordering of the Heisenberg model is further to be interpreted on top of the formation of a local magnetic moment, which is already described in the atomic limit, where each lattice site acts individually and is not connected to its neighboring sites. Ultimately, the Heisenberg model thus adds insight into the anti-ferromagnetic ordering in the phase diagram of the Hubbard model for large  $U/t$  with an ordering temperature  $T_N \sim t^2/U$ .

### 2.1.5 Lattice Phase Diagram

The previous sections analyze different lattice models. Starting from the Hubbard model, the weak-coupling and the strong-coupling limit are reviewed.

The non-interacting limit ( $U/t = 0$ , i.e. the weakest-coupling possible) of the Hubbard model is described by the tight-binding model (see Section 2.1.2). The two-dimensional square lattice at half-filling (or close to half-filling) shows distinct features in the DOS and

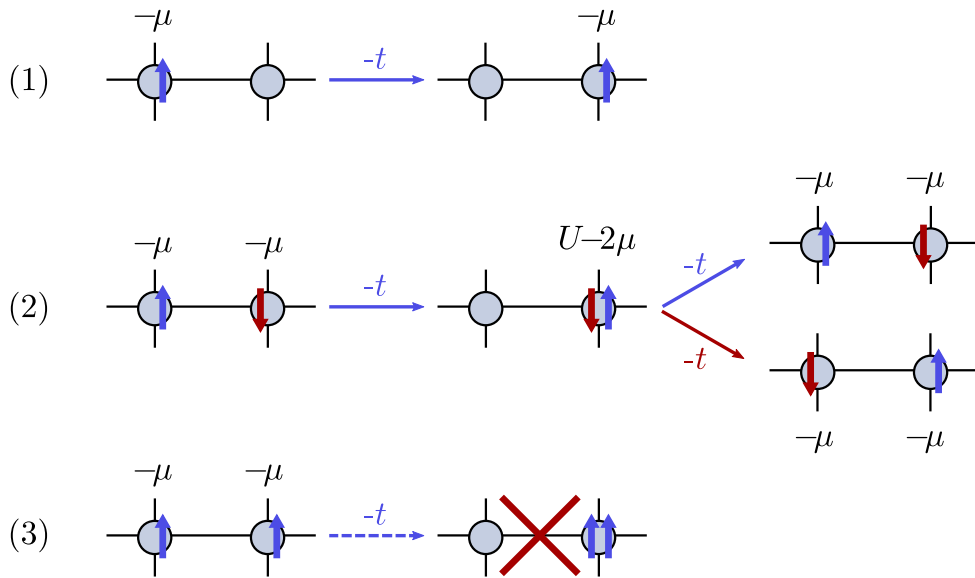


Figure 2.7: Dynamics in the  $tJ$ -model for two neighboring sites  $i$  and  $j$ . (1): First order hopping  $-t$  of a spin-up electron onto an empty site. (2): Second order virtual hopping from a spin-up electron onto a spin-down occupied site. As double-occupation is prohibited, an immediate hopping of either the spin-up or spin-down electron back to the empty site follows. The two neighboring sites are anti-ferromagnetically ordered. (3): Attempted hop of a spin-up electron on a spin-up occupied site. Due to the Pauli-principle this process is forbidden. The two neighboring sites are ferromagnetically ordered. All processes also exist when exchanging spin-up and spin-down. In the Heisenberg model only process (2) exists, while process (1) is not realized due to half-filling.

the Fermi surface, such as the Van Hove singularity or perfect nesting. The RPA-ladder construction of the spin-susceptibility can be considered a perturbative expansion around the non-interacting limit. Although a full weak-coupling perturbation theory gives more insight to the Hubbard model, the magnetic ordering for small  $U/t$  is determined to be anti-ferromagnetic.

The atomic limit, on the other hand, ( $U/t = \infty$ , i.e. the strongest-coupling possible) of the Hubbard model is described by the atomic lattice (see Section 2.1.3). The DOS reduces to  $\delta$ -peaks separated by the Coulomb repulsion  $U$ , which correspond to the single-occupied states below the Fermi energy and the empty and double-occupied state above. The atomic lattice itself is special, as neighboring sites do not interact because there is no hopping. Hence, any spatial- or momentum dependence is lost, and there is no magnetic ordering for any given temperature. A perturbative expansion around the atomic lattice is necessary to recover the strong-coupling case, which is given by the  $tJ$ -model or, at half-filling, by the spin-1/2 Heisenberg lattice. The Pauli principle for electrons on the same site is inherited from the Hubbard lattice, such that the Heisenberg model orders anti-ferromagnetic. An illustration of the phase diagram of the Hubbard model according to these limits is given in Figure 2.8.<sup>2</sup>

It is important to point out that other lattice models exist for limiting cases of the Hubbard model, namely the periodic Anderson model, the Kondo lattice model and the Falicov-Kimball lattice model. Alternatively, these models can be formulated as impurity models, where a (single) impurity in the lattice is treated explicitly, with the rest of the lattice being reformulated as a surrounding non-interacting bath. The mapping of such lattice models onto impurity models is usually justified in cases of high lattice dimension and becomes exact for infinite lattice dimensions, which is the principle of the dynamical mean field theory. These impurity models are hence discussed in greater detail in the next section.

## 2.2 Impurity Models

### 2.2.1 Anderson Impurity

The single-orbital Anderson impurity model (AIM) [Anderson, 1961] in second quantization is given by

$$\hat{H}_{\text{aim}} = \frac{1}{2} \sum_{ij,\sigma}^N t_{ij} (\hat{c}_{i\sigma}^\dagger \hat{c}_{j\sigma} + \hat{c}_{j\sigma}^\dagger \hat{c}_{i\sigma}) + \sum_{i\sigma}^N \left( \tilde{V}_{i\sigma} \hat{c}_{i\sigma}^\dagger \hat{d}_\sigma + \tilde{V}_{i\sigma}^* \hat{d}_\sigma^\dagger \hat{c}_{i\sigma} \right) - \sum_{\sigma} \mu_d \hat{d}_\sigma^\dagger \hat{d}_\sigma + U \hat{d}_\uparrow^\dagger \hat{d}_\uparrow \hat{d}_\downarrow^\dagger \hat{d}_\downarrow, \quad (2.29)$$

where  $\hat{c}_{i\sigma}^{(\dagger)}$  is now the annihilation (creation) operator at bath site  $i$  with spin  $\sigma = \{\uparrow, \downarrow\}$  and  $\hat{d}_\sigma^{(\dagger)}$  is the annihilation (creation) operator at the impurity site. As opposed to Hubbard

---

<sup>2</sup>While parts of the derivations for the ordering temperature  $T_N$  are here presented for the two-dimensional Hubbard model at half-filling for reasons of simplicity, the low dimension and symmetry actually suppress  $T_N$  completely. The absence of ferromagnetism or antiferromagnetism in the one- or two-dimensional isotropic Heisenberg model was shown in the work of Mermin and Wagner of the same title [Mermin and Wagner, 1966]. The same theorem holds for the two-dimensional Hubbard model. In one dimension the theorem is more commonly known as Lieb-Mattis theorem [Lieb et al., 1961].

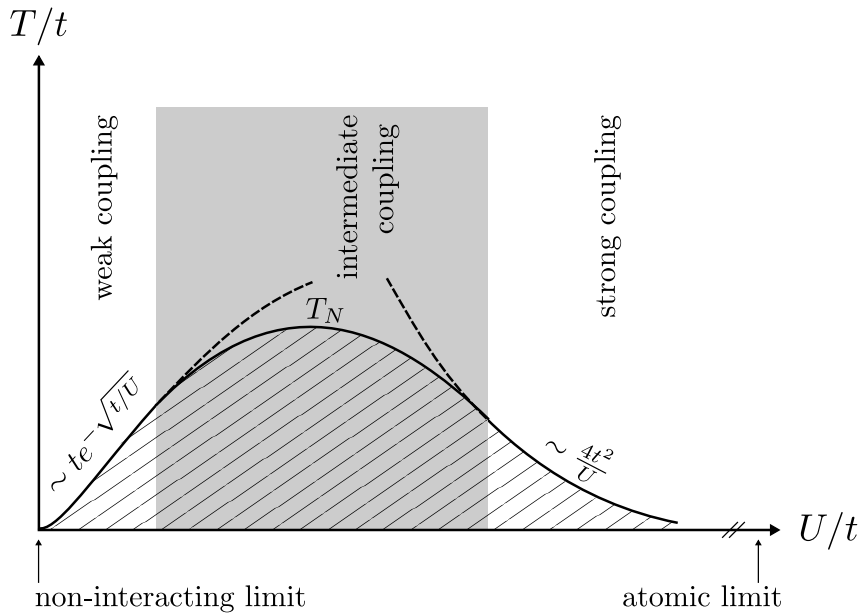


Figure 2.8: Illustration of the phase diagram for the Hubbard lattice with no magnetic ordering above the ordering temperature  $T_N$ , and anti-ferromagnetic ordering below (hatched region). In the weak coupling limit  $T_N$  is approximated from the RPA ladder. In the strong coupling limit  $T_N$  follows from the Heisenberg model. The gray region represents intermediate coupling, where neither of the two limits is valid. The non-interacting limit (tight-binding model) follows for  $U/t = 0$  and the atomic limit for  $U/t = \infty$ .

model, the kinetic energy of the AIM consists of two parts: the hopping  $t_{ij}$  between two bath sites  $i$  and  $j$  and the hopping/hybridization  $\tilde{V}_{i\sigma}^*$  from the bath onto the impurity and vice versa. The main difference to the Hubbard model is that the interaction energy term is now restricted to the impurity only.

Similar to the Hubbard model, it makes sense to reformulate the kinetic energy term (bath and hybridization) of (2.29) in momentum space, where it is diagonal. The potential energy term (impurity) of the Hamiltonian is kept in the real space formulation, such that

$$\hat{H}_{\text{aim}} = \sum_{\vec{k}\sigma} \varepsilon_{\vec{k}} \hat{c}_{\vec{k}\sigma}^\dagger \hat{c}_{\vec{k}\sigma} + \sum_{\vec{k}\sigma} \left( V_{\vec{k}\sigma} \hat{c}_{\vec{k}\sigma}^\dagger \hat{d}_\sigma + V_{\vec{k}\sigma}^* \hat{d}_\sigma^\dagger \hat{c}_{\vec{k}\sigma} \right) - \sum_{\sigma} \mu_d \hat{d}_\sigma^\dagger \hat{d}_\sigma + U \hat{d}_\uparrow^\dagger \hat{d}_\uparrow \hat{d}_\downarrow^\dagger \hat{d}_\downarrow, \quad (2.30)$$

where the hybridization amplitude transforms with

$$V_{\vec{k}\sigma} = \frac{1}{\sqrt{N}} \sum_{i\sigma} \tilde{V}_{i\sigma} e^{i\vec{k}\vec{r}_i}. \quad (2.31)$$

An illustration of the AIM is given in Figure 2.9.

Tackling the problem from the impurity perspective, one is not interested in the hoppings within the bath. In fact, the only relevant coupling is the hybridization of the impurity to the bath and the density of states of the bath electrons. Both are encoded in the hybridization function. The hybridization function can be extracted from the action formalism, where one exploits the fact that the bath is non-interacting. The path integral

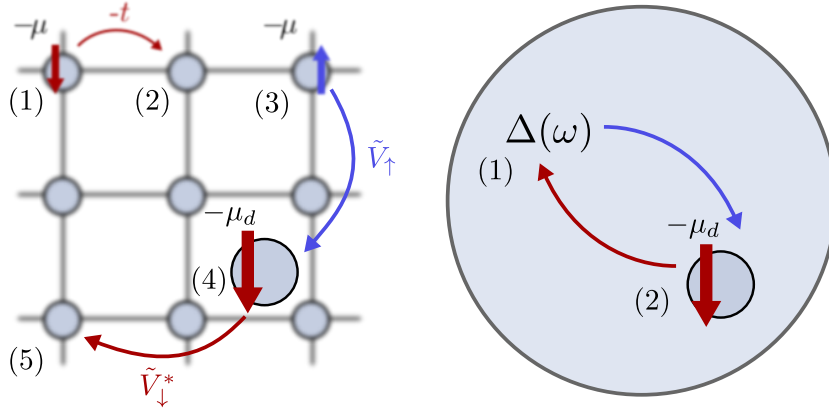


Figure 2.9: Illustration of the Anderson impurity model. Left: The non-interacting bath is assumed to be a two-dimensional square lattice. (1) and (3): bath site occupation with energy cost  $-\mu$ . (4): impurity occupation with energy cost  $-\mu_d$ . (1)  $\rightarrow$  (2): nearest-neighbor bath hopping with amplitude  $-t$ . (3)  $\rightarrow$  (4) hopping of a spin-up electron from the bath onto the interacting impurity with a hybridization amplitude  $\tilde{V}_\uparrow$  (resulting in an energy cost of  $U - 2\mu$  for the impurity). (4)  $\rightarrow$  (5): hopping of a spin-down electron from the impurity onto the bath with a hybridization amplitude  $\tilde{V}_\downarrow^*$ . Right: Non-interacting bath represented by hybridization function  $\Delta(\omega)$ , where the bath degrees of freedom have been integrated out. (1)  $\rightarrow$  (2): spin-up electron hybridizing onto interacting impurity. (2)  $\rightarrow$  (1): spin-down electron hybridizing off the impurity.

of the bath part is then of Gaussian form, so that an analytic integration is possible. This is usually referred to as integrating out the bath degrees of freedom. The hybridization function of the AIM in fermionic Matsubara frequencies  $i\nu$  is given by

$$\Delta_\sigma(i\nu) = \sum_{\vec{k}}^{\text{BZ}} \frac{|V_{\vec{k}\sigma}|^2}{i\nu - \varepsilon_{\vec{k}}}. \quad (2.32)$$

Identifying the denominator of the above expression as the non-interacting Green's function, one can reformulate the hybridization function in terms of the density of states in real frequencies  $\omega$  with

$$\Delta_\sigma(i\nu) = \int_{-\infty}^{\infty} d\omega \sum_{\vec{k}}^{\text{BZ}} |V_{\vec{k}\sigma}|^2 \frac{\delta(\omega - \varepsilon_{\vec{k}})}{i\nu - \omega} = -\frac{1}{\pi} \int_{-\infty}^{\infty} d\omega \frac{\Im(\Delta_\sigma(\omega))}{i\nu - \omega} \quad (2.33)$$

$$\Im(\Delta_\sigma(\omega)) = -\pi \sum_{\vec{k}}^{\text{BZ}} |V_{\vec{k}\sigma}|^2 \delta(\omega - \varepsilon_{\vec{k}}) = -\pi \sum_{\vec{k}}^{\text{BZ}} |V_{\vec{k}\sigma}|^2 \mathcal{A}_\sigma(\vec{k}, \omega), \quad (2.34)$$

where  $\mathcal{A}_\sigma(\vec{k}, \omega)$  is the non-interacting DOS of the bath. One can now observe that the hybridization function  $\Delta_\sigma(\omega)$  is directly proportional to  $\mathcal{A}_\sigma(\vec{k}, \omega)$ , where the real part of  $\Delta_\sigma(\omega)$  follows from the imaginary part using the Kramers-Kronig relations.<sup>3</sup> The impurity

<sup>3</sup>Mathematically the Kramers-Kronig relations are a special case of the Sokhotski-Plemelj theorem. Nevertheless, the practical use was popularized by the two theoretical physicists Kramers [Kramers, 1927] and Kronig [Kronig, 1926].

Green's function  $G_\sigma(\omega)$  can be expressed using the hybridization function as:

$$G_\sigma(\omega) = \frac{1}{\omega - \Delta_\sigma(\omega)}. \quad (2.35)$$

Directly related, the impurity DOS for the non-interacting impurity ( $U = 0$ ) follows as:

$$A_\sigma(\omega) = -\frac{1}{\pi} \Im \frac{1}{\omega - \Delta_\sigma(\omega)} = -\frac{1}{\pi} \frac{\Im \Delta_\sigma(\omega)}{(\omega - \Re \Delta_\sigma(\omega))^2 + \Im \Delta_\sigma(\omega)^2}. \quad (2.36)$$

Using relation (2.34), for a flat (i.e. featureless) non-interacting DOS  $\mathcal{A}_\sigma(\omega) = \theta(\frac{1}{2} - |\omega|)$  with bandwidth  $W = 1$  and a momentum-independent hybridization amplitude  $V_\sigma = V_{k\sigma}$ ,<sup>4</sup> the impurity DOS can be approximated by

$$A_\sigma(\omega) \approx \frac{V_\sigma^2 \mathcal{A}_\sigma(\omega)}{\omega^2 + (\pi V_\sigma^2 \mathcal{A}_\sigma(\omega))^2}, \quad (2.37)$$

where this result is valid for  $V_\sigma/W \ll 1$ , i.e. small hybridization amplitudes (sometimes referred to as the broad-band limit, which is commonly employed). The Lorentzian shape of the impurity DOS relates to a broadening due to the hybridization with the flat non-interacting DOS. This implies that the existence of impurities in the host lattice broadens energy levels and peak structures of the non-interacting DOS due to impurity scattering events, even in the absence of an impurity interaction  $U$ . The non-interacting flat DOS and the Lorentzian-shaped impurity DOS are illustrated in Figure 2.10. An extended discussion of the AIM in general [Hewson, 1993] and specifically for the non-interacting AIM [Mahmoud and Gebhard, 2015] can be found in literature.

In order to describe a non-interacting lattice with several impurities, the AIM may be redefined as an impurity lattice. Such a model system is usually referred to as the periodic Anderson model (PAM), which follows from (2.30) by introducing a sum over the impurity terms with

$$\hat{H}_{\text{pam}} = \sum_{\vec{k}\sigma} \varepsilon_{\vec{k}} \hat{c}_{\vec{k}\sigma}^\dagger \hat{c}_{\vec{k}\sigma} + \sum_{\vec{k}\sigma,i}^{\text{BZ}} \left( V_{\vec{k}\sigma} \hat{c}_{\vec{k}\sigma}^\dagger \hat{d}_{i\sigma} + V_{\vec{k}\sigma}^* \hat{d}_{i\sigma}^\dagger \hat{c}_{\vec{k}\sigma} \right) - \sum_{\sigma,i}^N \mu_d \hat{d}_{i\sigma}^\dagger \hat{d}_{i\sigma} + \sum_i^N U \hat{d}_{i\uparrow}^\dagger \hat{d}_{i\uparrow} \hat{d}_{i\downarrow}^\dagger \hat{d}_{i\downarrow} \quad (2.38)$$

Although being a lattice model, the PAM is quite different from the Hubbard model. More specifically, while the Hubbard model describes a lattice where interacting sites are coupled directly to one another, the PAM describes a lattice, where interacting sites are only coupled to one another indirectly over a non-interacting bath all of the impurity sites share. Nonetheless, the two models share many common features and can be mapped onto each other in certain limiting cases [Held et al., 2000, Held and Bulla, 2000].

In the following, different limits of the AIM are considered in a similar fashion as for the Hubbard (lattice) model. When completely decoupling bath and impurity by setting  $V_{\vec{k}\sigma} = 0$ , the two extreme limits, i.e. the non-interacting case and the atomic limit, are identical for the impurity and lattice sites respectively. The equivalence in the non-interacting limit is straight-forward, as the non-interacting bath of the AIM fully describes

<sup>4</sup>In the context of the dynamical mean field theory the hybridization amplitudes and the DOS are adapted self-consistently in the DMFT equations.

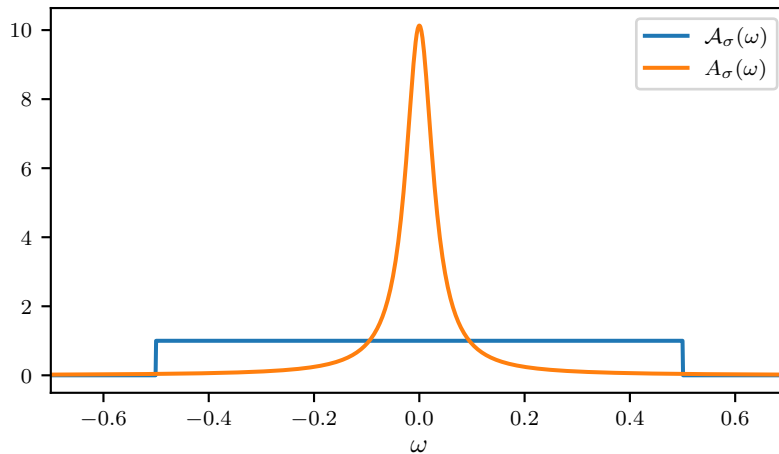


Figure 2.10: Impurity DOS  $A_\sigma(\omega)$  of the non-interacting Anderson impurity model with hybridization amplitude  $V_\sigma = 0.1W$  for a flat non-interacting DOS  $\mathcal{A}_\sigma(\omega)$  for the bath with bandwidth  $W = 1$ . The Lorentzian broadening of the impurity level can be observed.

tight-binding physics, where the impurity is entirely ignored (i.e. no hybridization  $V_{\vec{k}\sigma}$  of impurity and bath and no interaction  $U$  on the impurity).

The atomic limit of the AIM, on the other hand, is equivalent to the atomic limit of the Hubbard model. While for the Hubbard model, the hopping  $t$  vanishes in the atomic limit, in the AIM the hopping  $t$  and the hybridization amplitude  $V_{\vec{k}\sigma}$  vanish in the atomic limit (i.e. the total kinetic energy expression vanishes), which can be equivalently formulated by requiring  $\Delta_\sigma(\omega) = 0$ .

While the non-interacting limit and the atomic limit formally connect lattice and impurity models, the weak coupling and strong coupling limit differ. In the strong coupling limit the AIM is given by the Kondo impurity model.

## 2.2.2 Kondo Model

The Kondo model<sup>5</sup> was introduced by Zener [Zener, 1951] and describes scattering processes of non-interacting electrons with a local moment on a given impurity, where the coupling of impurity to the bath is given by the spin-spin interaction. The spin-1/2 Kondo Hamiltonian follows as

$$\hat{H}_{\text{kondo}} = \sum_{\vec{k}\sigma} \varepsilon_{\vec{k}} \hat{c}_{\vec{k}\sigma}^\dagger \hat{c}_{\vec{k}\sigma} - \frac{1}{2} \sum_{\vec{k}\vec{k}'} J_{\vec{k}\vec{k}'} \hat{S}_{\vec{k}\vec{k}'} \hat{S}, \quad (2.39)$$

<sup>5</sup>Historically, the Kondo model was introduced as the  $s-d$  model. This designation stems from the application to materials: the non-localized  $s$ -orbitals relate to the non-interacting bath, while the localized  $d$ -orbital relates to the impurities in the host lattice.



where the bath spin operator  $\hat{S}_{\vec{k}}$  and an impurity spin operator  $\hat{S}$  are defined as

$$\hat{S}_{\vec{k}} = \frac{1}{2} \begin{pmatrix} \hat{c}_{\vec{k}\uparrow}^\dagger & \hat{c}_{\vec{k}\downarrow}^\dagger \end{pmatrix} \vec{\sigma} \begin{pmatrix} \hat{c}_{\vec{k}'\uparrow} \\ \hat{c}_{\vec{k}'\downarrow} \end{pmatrix} \quad (2.40)$$

$$\hat{S} = \frac{1}{2} \begin{pmatrix} \hat{d}_\uparrow^\dagger & \hat{d}_\downarrow^\dagger \end{pmatrix} \vec{\sigma} \begin{pmatrix} \hat{d}_\uparrow \\ \hat{d}_\downarrow \end{pmatrix}. \quad (2.41)$$

Further,  $\vec{\sigma}$  denotes the Pauli matrices. The coupling constant in (2.39) is sometimes chosen to be momentum independent, i.e.  $J = J_{\vec{k}\vec{k}'}$ . The Kondo Hamiltonian favors anti-ferromagnetic coupling of the non-interacting bath to the impurity for  $J > 0$ .

The spin-1/2 Kondo model is obtained from the AIM in the strong coupling limit. Mathematically this is achieved by a Schrieffer-Wolff transformation [Schrieffer and Wolff, 1966]. The transformation is closely related to the approach presented in Section 2.1.4 and Appendix A.3. High-energy states are projected out and perturbation theory is considered up to second order in the low energy model. Spin-flips between the non-interacting bath and the impurity follow from second-order virtual processes, where an electron of a given spin jumps onto a singly-occupied impurity of opposite spin, shortly resulting in a doubly-occupied impurity, which then relaxes to its original occupation with opposite spin. The Schrieffer-Wolff transformation further sets the coupling to

$$J_{\vec{k}\vec{k}'} = V_{\vec{k}} V_{\vec{k}'}^* \left( \frac{1}{\mu_d} + \frac{1}{U - \mu_d} \right). \quad (2.42)$$

Assuming a momentum independent hybridization  $V = V_{\vec{k}}$  and half-filling  $\mu_d = U/2$  the above simplifies to  $J = 4V^2/U$ , which is identical to the anti-ferromagnetic Heisenberg coupling  $J$  if one replaces  $t^2 \rightarrow V^2$ .

The Kondo model in itself has been studied extensively, as it describes electronic scattering processes in host metals with magnetic impurities (local moments). The famous Kondo effect, which states that there is a (negative) logarithmic behavior of the resistivity due to electron-impurity scattering for low temperatures, follows from third-order perturbation theory. In combination with the polynomial scaling of electron-electron scatterings (quadratic) and electron-phonon scatterings (quintic), this results in a resistivity minimum at finite temperatures, which was observed experimentally. The Kondo scattering implies a logarithmic divergence of the resistivity with  $T \rightarrow 0$ , which, on the other hand, has not been observed and thus became known as the Kondo problem. The Kondo problem was, at last, solved by a renormalization group approach, proposing a finite resistivity at  $T = 0$  [Wilson, 1975]. Note that at low temperatures the perturbative approach of the Kondo effect is no longer valid.

In the context of this work, only two results of Kondo physics are considered in greater detail: the Kondo temperature, i.e. the temperature scale at which the perturbative approach breaks down, and the related Kondo peak - a central resonance of the DOS at the Fermi energy relating to spin fluctuations of the local moment.

The Kondo peak at the Fermi energy is a sharp resonance resulting from electrons scattering off the broadened impurity resonance introduced in (2.37) for the non-interacting AIM. Following the derivations of Langreth [Langreth, 1966], in the following the height

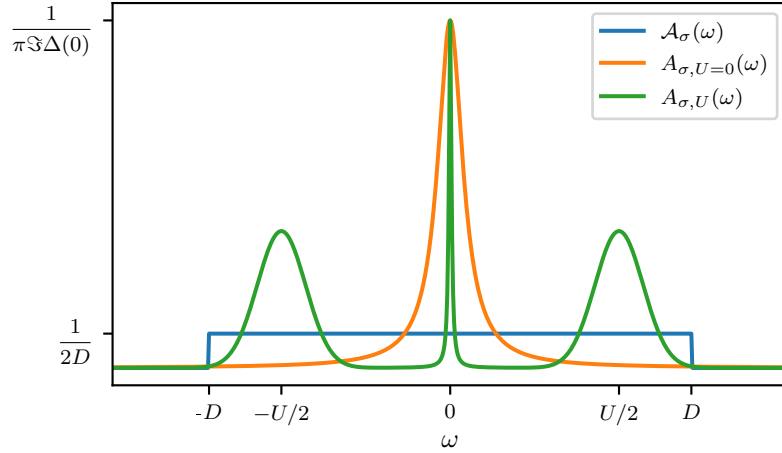


Figure 2.11: Illustration of the interacting DOS  $A_{\sigma,U}(\omega)$  of the AIM, with a central Kondo resonance for finite  $U$ . The resonance height of the non-interacting DOS  $A_{\sigma,U=0}(\omega)$  of the AIM with the broadening due to impurity scattering is identical to the interacting resonance. Additionally, the featureless non-interacting DOS in the absence of impurities  $\mathcal{A}_{U=0}(\omega)$  is given for reference.

of the central Kondo resonance is calculated. Diagrammatically, the propagation of an electron through the entire lattice  $G_{\text{lat}}$  is given by the non-interacting propagation  $\mathcal{G}$ , which is modified by hybridizations of the electron onto the impurity, a propagation  $G$  within the impurity and a (backwards) hybridization into the bath, such that

$$G_{\text{lat}}(\vec{k}, \vec{k}', \omega) = \mathcal{G}(\vec{k}, \omega) \delta_{\vec{k}\vec{k}'} + \mathcal{G}(\vec{k}, \omega) V_{\vec{k}}^* G(\omega) V_{\vec{k}'} \mathcal{G}(\vec{k}', \omega) \quad (2.43)$$

In the following the hybridization amplitudes are chosen momentum-independent, i.e.  $V = V_{\vec{k}}$ . The scattering amplitude in the above propagation directly relates to the impurity Green's function (2.35) with

$$T(\omega) = V^2 G(\omega) \approx V^2 \frac{1}{\omega - i\Im\Delta(\omega)}, \quad (2.44)$$

where the approximate result is valid for the wide-band limit  $V/W \ll 1$  as  $\Re\Delta(\omega) \ll \omega$ . More importantly, one is interested in the phase shift  $\delta(\omega)$  due to scattering,<sup>6</sup> which follows as

$$\delta(\omega) = \cot^{-1} \left( \frac{\omega}{\Im\Delta(\omega)} \right) \quad (2.45)$$

As  $\Im\Delta(\omega) < 0$ , far below the Fermi energy (i.e.  $\omega \rightarrow -\infty$ ), the phase-shift is equal to zero. Far above the Fermi energy (i.e.  $\omega \rightarrow \infty$ ), the phase-shift is equal to  $\pi$ . At the Fermi energy itself, the scattering becomes prominent with a phase shift of  $\delta_f = \delta(0) = \pi/2$ .<sup>7</sup>

<sup>6</sup>The relationship between the T-matrix and the S-matrix follows from the optical theorem  $S(\omega) = 1 - 2\pi i \mathcal{A}(\omega) T(\omega)$ . With  $S(\omega) = e^{2i\delta(\omega)}$  one can solve for  $T(\omega) = -1/(\pi \mathcal{A}(\omega) (\cot \delta(\omega) - 1))$ .

<sup>7</sup>The above is a simplified form of the Friedel sum rule, where the density at the Fermi energy is given by  $n = \delta(0)/\pi$ .

By adiabatically turning on the interaction  $U$ , the broadened DOS  $A_{\sigma,U=0}(\omega)$  transforms into a DOS with two Hubbard-bands separated by  $U$  and a central peak of the height following Fermi liquid theory

$$A(0) = -\frac{\sin^2 \delta_f}{\pi \Im \Delta(0)} = -\frac{1}{\pi} \frac{1}{\Im \Delta(0)}. \quad (2.46)$$

This is however also the height of the broadened DOS at the Fermi energy defined in (2.37), which is why sometimes one refers to the Kondo peak as being pinned [Coleman, 2015]. An illustration of the different DOS for the Kondo model is shown in Figure 2.11.

Fermi-liquid theory assumes the area under the Kondo resonance is given by the renormalization factor  $Z$ , such that the width of the Kondo resonance needs to be approximately renormalized by  $\sim Z\Delta$ . The width, however, further determines the life-time of the quasi-particles, resulting in a new energy-scale  $T_K \sim Z\Delta$ , which is nothing but the Kondo temperature. Thus, the Kondo temperature is to be interpreted with respect to the Kondo resonance itself: low energy excitations probe the metallic properties of the system, where the impurity is screened by the bath electrons resulting in a Fermi-liquid. High energy excitations probe the local moments, as the impurities are no longer fully screened. Analytically, the Kondo temperature for the half-filled AIM for a flat bath dispersion was determined to [Hewson, 1993]

$$T_K = \sqrt{\frac{JU^2 \mathcal{A}(0)}{2}} \exp\left(-\frac{1}{2J\mathcal{A}(0)}\right). \quad (2.47)$$

Kondo physics also becomes relevant for the behavior of the charge susceptibility as a function of interaction  $U$  and temperature  $T$ . As the (non-self-consistent) AIM, and for that matter the Kondo model, stays metallic for all  $U$ , the static local charge susceptibility does not display any discontinuities around the Fermi energy, as it would be the case for Mott metal-to-insulator transitions. Further, for temperatures  $T < T_K$ , the bath electrons screen the impurity, which retains Fermi-liquid-like behavior. For temperatures  $T > T_K$ , the local moments are only partially screened, and the impurities display an anti-ferromagnetic coupling to the bath [Janiš and Augustinský, 2008].

Similar to the periodic Anderson model, which is the lattice formulation of the AIM, the Kondo model may be redefined as a lattice model. The Kondo lattice model (KLM) [Doniach, 1977] follows from (2.39) by switching to the real-space representation and introducing a sum over the impurity sites

$$\hat{H}_{\text{klm}} = \sum_{\vec{k}\sigma}^{\text{BZ}} \varepsilon_{\vec{k}} \hat{c}_{\vec{k}\sigma}^\dagger \hat{c}_{\vec{k}\sigma} - J \sum_i^N \hat{\mathcal{S}}_i \hat{\mathcal{S}}_i, \quad (2.48)$$

where now  $\hat{\mathcal{S}}_i$  is the bath spin operator evaluated at the impurity  $i$  and  $\hat{S}_i$  is the impurity spin operator at site  $i$ . The Kondo lattice allows for the RKKY exchange mechanism, where two local moments interact over the non-interacting bath indirectly. While the Kondo effect attempts to screen local impurities, the RKKY exchange favors (anti-ferromagnetic) ordering in the KLM, which leads to a more complex lattice phase diagram.

### 2.2.3 Falicov-Kimball Model and Resonant Level Model

To this point, only SU(2)-symmetric models were considered. More specifically, the models discussed in the previous sections stay invariant under an exchange of spins  $\uparrow \leftrightarrow \downarrow$ . More insight to the physics of impurity models may be gained when considering the SU(2)-symmetry broken phase. The Falicov-Kimball model (FKM) assumes one spin (e.g.  $\downarrow$ ) to be localized, that is  $t_\downarrow = 0$ , while the other spin (i.e.  $\uparrow$ ) is considered to be itinerant, hence  $t_\uparrow = t \neq 0$ .<sup>8</sup> In the limit of  $U/t = \infty$ , the itinerant spin becomes just as localized as the fixed spin, such that the impurity inherits the properties of the atomic limit. On the other hand, in the limit of  $U/t = 0$ , the non-interacting bath of the itinerant spin behaves like a tight-binding lattice. The additional existence of non-interacting impurities broadens the DOS of the itinerant spin, as discussed in the context of the AIM. A finite Coulomb repulsion  $U$  controls the level of correlation between the two spins. The resonant level model, i.e. the impurity equivalent of the FKM [Falicov and Kimball, 1969], in second quantization is given by:

$$\hat{H}_{\text{fk}} = - \sum_{l>1}^N \left( t_{0l} \hat{c}_0^\dagger \hat{c}_l + t_{l0}^* \hat{c}_l^\dagger \hat{c}_0 + \mu_c \hat{c}_l^\dagger \hat{c}_l \right) + U \hat{f}^\dagger \hat{f} \hat{c}_0^\dagger \hat{c}_0 - \mu_f \hat{f}^\dagger \hat{f} - \mu_c \hat{c}_0^\dagger \hat{c}_0, \quad (2.49)$$

where  $\hat{c}_i^{(\uparrow)}$  is the annihilation (creation) operator of the itinerant electron at site  $i$  and  $\hat{f}^{(\uparrow)}$  is the annihilation (creation) operator of the fixed electron at the impurity site  $i = 0$ .

The specific properties of the FKM allow for an analytic solution in terms of Green's function. This is achieved by applying the equation of motion (EOM), i.e. the (imaginary) time derivative of either the itinerant creation or annihilation operator, on the impurity- and on the bath-level successively. The itinerant  $c$ -electron impurity Green's function of the resonant level model in fermionic Matsubara frequencies was calculated by Brandt and Mielsch [Brandt and Mielsch, 1989]

$$G^c(i\nu) = \frac{1}{i\nu + \mu_c - \Delta(i\nu) - UN_f}, \quad (2.50)$$

with the hybridization function defined as  $\Delta(i\nu) = \sum_{l>1}^N \frac{t_{0l} t_{l0}^*}{i\nu + \mu_c}$ . Further, the impurity is either unoccupied or occupied by a localized  $f$ -electron with  $N_f = \{0, 1\}$  (where a capital  $N_f$  was used to denote a classical (binary) occupation). A derivation of the above result is found in Appendix A.4.

More frequently than relation (2.50), usually the Green's function is interpolated between the two occupations  $N_f = \{0, 1\}$ . By defining  $p$  as the probability of the impurity being unoccupied, the  $c$ -electron Green's function is then formulated as

$$G^c(i\nu) = p \frac{1}{i\nu + \mu_c - \Delta(i\nu)} + (1 - p) \frac{1}{i\nu + \mu_c - \Delta(i\nu) - U}. \quad (2.51)$$

---

<sup>8</sup>More often, the FKM is referred to as a spinless model consisting of spinless itinerant electrons and localized ions. In this case, the Coulomb interaction  $U$  is either repulsive or attractive and the ordering mechanism of the itinerant electrons is classified by their charge/density on the lattice. In this work the FKM is considered as a limit of the mass-imbalanced Hubbard model, where the hopping of one species is set to zero.

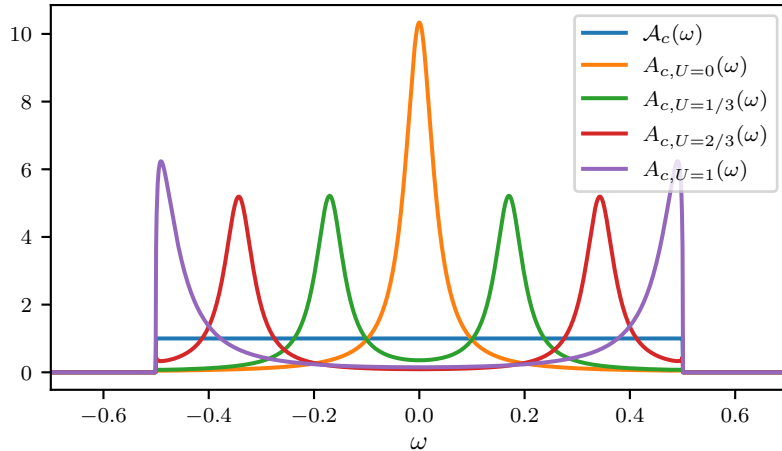


Figure 2.12: Impurity DOS of the  $c$ -electrons for the Falicov-Kimball impurity model following a flat non-interacting DOS  $\mathcal{A}_c(\omega)$  with bandwidth  $W = 1$ . Due to scattering with non-interacting impurities  $A_{c,U=0}(\omega)$  reproduces the Lorentzian broadening of the non-interacting AIM for  $U = 0$ . For finite interaction values, two Hubbard bands separated by  $U$  form symmetrically around the Fermi energy, until they are cut off by the band edges, where the interacting DOS starts to diverge.

For half-filling, the  $f$ -electron occupation is fixed to  $p = 1 - p = 0.5$  and further  $\mu_c = U/2$ . Figure 2.12 shows the  $c$ -electron DOS for the half-filled resonant level model following a flat non-interacting DOS (i.e. a flat hybridization). As opposed to the Kondo model, the resonant level model does not display a quasi-particle peak. The absence of the Kondo resonance follows from the localization of one electron spin, which forbids spin flips and, consequently, the Kondo effect as a whole. If the interaction strength is of the order of the bandwidth  $U \sim W$ , the two Hubbard peaks are cut off by the band edges, which results in a divergence at the band edge itself and a metal-to-insulator transition.<sup>9</sup>

In an attempt to determine the ordering of the FKM, first the resonant level model needs to be cast into its lattice version. Considering the FKM as a limit to the mass-imbalanced Hubbard model, with localized and itinerant electrons associated with different spins, the FKM orders magnetically [Kennedy and Lieb, 1986]. While the ordering is in general dependent on the electron filling, analytic solutions exist for rational number fillings [Kennedy, 1998]. At half-filling and low enough temperatures, the FKM on a lattice orders anti-ferromagnetically, while above the critical temperature the system is in a paramagnetic, i.e. disordered, state.<sup>10</sup>

<sup>9</sup>This feature is common for impurity models. In the context of the non-interacting AIM, the divergence at the band edges can be tuned as a function of the hybridization. The square-root divergence at the band edges for the semi-elliptical DOS can be derived analytically [Mahmoud and Gebhard, 2015].

<sup>10</sup>Sometimes the anti-ferromagnetic ordering is referred to as a charge-density wave, which is motivated by just considering itinerant spinless electrons, which order periodically.

## 2.3 Multi-orbital Hubbard Model

To this point only the limiting cases of single-orbital models were discussed. These included variations in the interaction strength  $U$  with respect to the hopping  $t$ , the lattice dimensionality  $d$  (and for that matter the number of nearest neighbors  $Z$ ) and breaking the  $SU(2)$ -symmetric hopping amplitudes. Nevertheless, up to this point the number of orbitals was fixed to one. Extending the Hubbard model to multiple orbitals allows for additional orbital-related physics, which are not present in the single-orbital model. Effects like inter-orbital couplings and Hund's exchange enrich the phase diagram of the multi-orbital Hubbard model with respect to the phase diagram of the single-orbital Hubbard model. New phases include orbital orderings [Tokura and Nagaosa, 2000], ferromagnetic orderings [Held and Vollhardt, 1998], orbital-selective Mott-Hubbard metal-to-insulator transitions [Anisimov, V. I. et al., 2002] and Jan-Teller metal phases [Hoshino and Werner, 2017]. The multi-orbital Hubbard with nearest neighbor hopping follows as

$$\begin{aligned} \hat{H}_{\text{hubbard}} = & -\frac{1}{2} \sum_{\alpha\beta}^{N_b} t_{\alpha\beta} \sum_{\langle ij \rangle, \sigma}^N (\hat{c}_{i\alpha\sigma}^\dagger \hat{c}_{j\beta\sigma} + \hat{c}_{j\beta\sigma}^\dagger \hat{c}_{i\alpha\sigma}) \\ & + \frac{1}{2} \sum_i^N \sum_{\alpha\beta\gamma\delta}^{N_b} \sum_{\sigma\sigma'} U_{\alpha\beta\gamma\delta} \hat{c}_{i\alpha\sigma}^\dagger \hat{c}_{i\beta\sigma'}^\dagger \hat{c}_{i\delta\sigma'} \hat{c}_{i\gamma\sigma}, \end{aligned} \quad (2.52)$$

where Greek indices denote orbital degrees of freedom, such that  $t_{\alpha\beta}$  is the orbital dependent nearest neighbor hopping and  $U_{\alpha\beta\gamma\delta}$  is the orbital dependent interaction matrix. Further  $N_b$  is the number of orbitals considered. It is common to parameterize the multi-orbital Hubbard model with the intra-orbital coupling  $U$ , the inter-orbital coupling  $V$  and the Hund's coupling  $J$ , such that the generalized density-density Hubbard model follows as

$$\begin{aligned} \hat{H}_{\text{hubbard,DD}} = & -\frac{1}{2} \sum_{\alpha\beta}^{N_b} t_{\alpha\beta} \sum_{\langle ij \rangle, \sigma}^N (\hat{c}_{i\alpha\sigma}^\dagger \hat{c}_{j\beta\sigma} + \hat{c}_{j\beta\sigma}^\dagger \hat{c}_{i\alpha\sigma}) \\ & + \sum_i^N \sum_{\alpha}^{N_b} U \hat{n}_{i\alpha\uparrow} \hat{n}_{i\alpha\downarrow} + \sum_i^N \sum_{\alpha \neq \beta, \sigma}^{N_b} (V \hat{n}_{i\alpha\sigma} \hat{n}_{i\beta-\sigma} + (V - J) \hat{n}_{i\alpha\sigma} \hat{n}_{i\beta\sigma}). \end{aligned} \quad (2.53)$$

However, only in the limit of a single-orbital, the above expression retains  $SU(2)$ -symmetry. In the multi-orbital case, the spin-flip term recovers the spin-symmetry and the pair hopping term the orbital-symmetry, such that the  $SU(2)$ -symmetric Slater-Kanamori [Kanamori, 1963] interaction follows as

$$\hat{H}_{\text{hubbard,SK}} = \hat{H}_{\text{hubbard,DD}} + \sum_i^N \sum_{\alpha \neq \beta, \sigma}^{N_b} J \left( \hat{c}_{i\alpha\sigma}^\dagger \hat{c}_{i\beta-\sigma}^\dagger \hat{c}_{i\alpha-\sigma} \hat{c}_{i\beta\sigma} + \hat{c}_{i\alpha\sigma}^\dagger \hat{c}_{i\alpha-\sigma}^\dagger \hat{c}_{i\beta-\sigma} \hat{c}_{i\beta\sigma} \right) \quad (2.54)$$

Further assuming  $V = U - 2J$ ,<sup>11</sup> the Slater-Kanamori Hamiltonian becomes  $SO(N_b) \times SU(2)$ -symmetric. In order to show the connection between the Hubbard model with

<sup>11</sup>The constraint  $V = U - 2J$  is imposed by spherical symmetry. More often the constraint is also applied for cubic symmetry, where the deviations are mostly negligible for three orbitals ( $\sim 1\%$  for  $\text{SrVO}_3$ ), while becoming significant for five orbitals (25% for  $\text{BaOsO}_3$ ) [Ribic et al., 2014]

Parameterization	Spin	Type
$U_{\alpha\sigma\alpha\sigma'} \rightarrow U$	$\sigma \neq \sigma'$	Intra-orbital
$U_{\alpha\sigma\beta\sigma'} \rightarrow V$	$\sigma = \sigma', \sigma \neq \sigma'$	Inter-orbital
$U_{\alpha\sigma\beta\sigma} \rightarrow J$	$\sigma = \sigma'$	Hund
$U_{\alpha\sigma\beta\sigma'} \rightarrow J$	$\sigma \neq \sigma'$	Spin-flip
$U_{\alpha\sigma\alpha\sigma'} \rightarrow J$	$\sigma \neq \sigma'$	Pair-hopping

Table 2.1: SU(2)-symmetric Slater-Kanamori parameterization of the interaction matrix with parameters  $U, V$  and  $J$  for  $\alpha \neq \beta$ .

Slater-Kanamori interaction and the general expression (2.52) it is helpful to additionally specify the implicit spin-indices<sup>12</sup>

$$U_{\alpha\sigma,\beta\sigma',\gamma\sigma,\delta\sigma'} := U_{\alpha\beta\gamma\delta}. \quad (2.55)$$

The parametrization of the Slater-Kanamori interaction is shown in Table 2.1. The half-filling condition for the multi-orbital case is derived in Appendix D.

## 2.4 Dynamical Mean Field Theory

In the previous sections different limits of the Hubbard (lattice) model and the Anderson impurity model were discussed in terms of the ratio of potential energy over kinetic energy  $U/t$ . A summary of the links between the various models is illustrated in Figure 2.13. Up to this point, the lattice dimension was assumed to be fixed (i.e. in most cases a two-dimensional lattice was considered). However, the lattice dimension in itself proves to be an important parameter to determine the limits of the Hubbard model. For the one-dimensional Hubbard lattice (chain) analytic expressions were first derived by Lieb and Wu [Lieb and Wu, 1968] employing the Bethe-Ansatz.<sup>13</sup>

For infinite lattice dimension, an exact mapping from lattice models onto impurity models was formulated by Metzner and Vollhardt [Metzner and Vollhardt, 1989] and Georges and Kotliar [Georges and Kotliar, 1992]. The latter work shows that the solution of the Hubbard model can be obtained by a self-consistent mapping onto an auxiliary AIM.

When naively considering the Hubbard Hamiltonian (2.1) for infinite lattice-dimensions, however, the kinetic energy will dominate, resulting in a trivial tight-binding lattice. While the potential energy term is not affected by the lattice dimension, the hopping of the kinetic energy results in a diverging contribution, as each lattice site has infinitely many neighboring sites.

Historically, this observation was first quantified by Wolff [Wolff, 1983] who calculated the DOS for the infinite-dimensional hyper-cubic lattice with nearest neighbor hopping,

<sup>12</sup>In principle, the orbital-dependent interaction matrix  $U_{\alpha\beta\gamma\delta}$  sufficiently describes all possible local interactions.

<sup>13</sup>The Bethe-Ansatz is an analytic method originally formulated for a one-dimensional Heisenberg chain [Bethe, 1931].

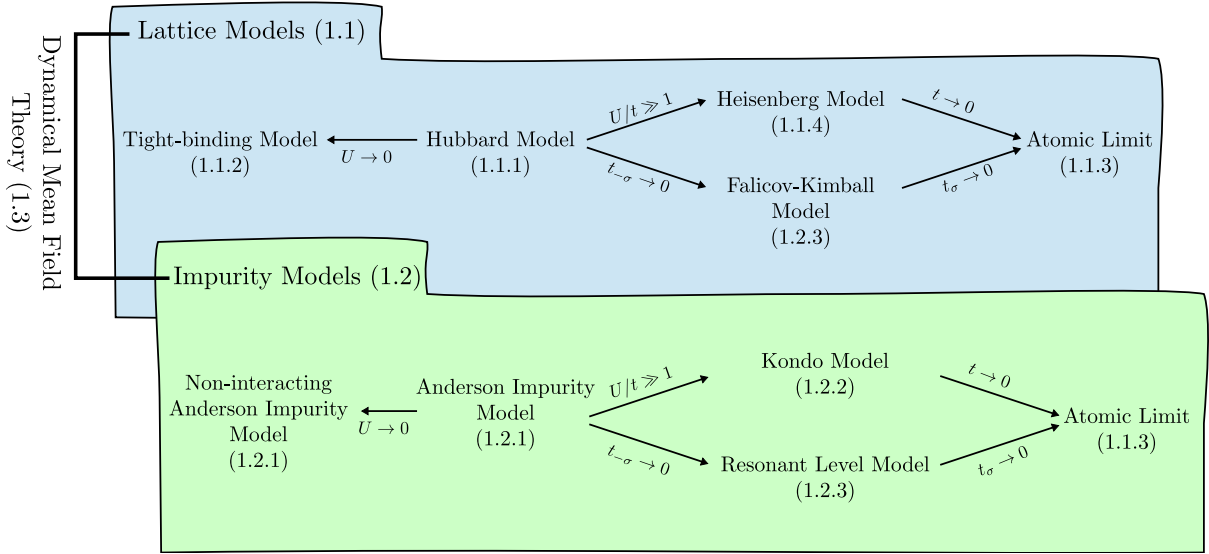


Figure 2.13: Sketch of the connection between different lattice models and impurity models for various interaction strengths (weak, intermediate and strong coupling). The corresponding sections are given in parentheses. All impurity models exist also in a lattice formulation, where the impurities on a lattice couple to each other via a non-interacting bath. At infinite lattice dimension, the lattice models can be mapped onto impurity models via the dynamical mean field theory.

where the dispersion relation is given by

$$\varepsilon_{\vec{k}} = -\mu - 2t \lim_{d \rightarrow \infty} \sum_{i=1}^d \cos(k_i). \quad (2.56)$$

The index  $i$  represents the dimension and  $k_i \in [0, 2\pi)$ . The DOS (see relation (2.16)) for a given frequency  $\omega$  can be evaluated by generating random vectors in the  $d$ -dimensional momentum space. For  $d \rightarrow \infty$  the central limit theorem applies, such that the DOS can be formulated as

$$A_\sigma(\omega) = \frac{1}{\sqrt{2\pi}\sqrt{2dt}} e^{-\frac{1}{2}\left(\frac{\omega}{\sqrt{2dt}}\right)^2}, \quad (2.57)$$

which is a Gaussian distribution with standard deviation  $\sqrt{2dt}$  (alternatively referred to as  $\mathcal{N}(0, 2d t^2)$ ). In Figure 2.14 the non-interacting DOS for the hyper-cubic lattice for different lattice dimensions is shown. At lattice dimension  $d = 50$ , the DOS calculated naively using relation (2.16) already agrees well with the Gaussian result obtained from the central limit theorem.<sup>14</sup>

<sup>14</sup>Looking at Figure 2.14, one observes that for higher dimensions  $d$ , the DOS develops a peak structure around the Fermi energy, where most of the weight is centered. When assuming finite-dimensional dispersion relations in DMFT, it is thus common to rescale the bandwidth  $W = 4td$  by a factor  $1/\sqrt{2d}$  to sustain a similar weight for a given frequency independent of the lattice dimension. For  $d = 2$  the bandwidth is then  $W = 4t$  and for  $d = 3$  the bandwidth is  $W = 2\sqrt{6}t$ .



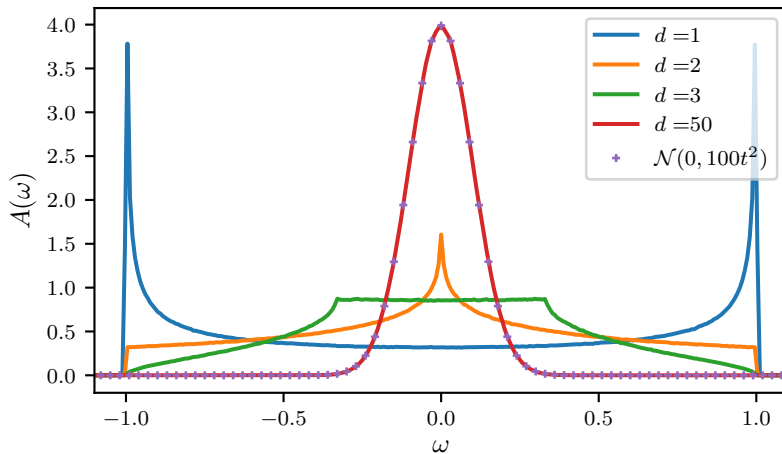


Figure 2.14: Non-interacting densities of states for the hyper-cubic lattice with nearest neighbor hopping for various dimensions  $d$ . The half-bandwidth for all dimensions was fixed to  $D = 1$ . At dimension  $d = 50$ , the DOS is already well approximated by a Gaussian with standard deviation  $\sigma = \sqrt{2dt}$  following the central limit theorem. Results were obtained by a straight-forward Monte Carlo integration of (2.16) for the hyper-cubic dispersion relation.

When taking the limit  $d \rightarrow \infty$ , relation (2.57) goes towards zero, unless rescaling  $t \rightarrow t^*/\sqrt{d}$ . The Hubbard Hamiltonian with a rescaled kinetic energy and nearest neighbor hopping follows as:

$$\hat{H}_{\text{hubbard}} = -\frac{1}{2} \frac{t^*}{\sqrt{d}} \sum_{ij,\sigma} (\hat{c}_{i\sigma}^\dagger \hat{c}_{j\sigma} + \hat{c}_{j\sigma}^\dagger \hat{c}_{i\sigma}) + \sum_i U \hat{n}_{i\uparrow} \hat{n}_{i\downarrow}. \quad (2.58)$$

Based on this reasoning, Metzner and Vollhardt were able to show that self-energy diagrams of the Hubbard model with infinite lattice dimension become purely local, i.e.  $\Sigma(\vec{k}, \omega) = \Sigma(\omega)$ . The momentum-independence (i.e. locality) of the self-energy already hints at the connection to impurity models. Indeed, Georges and Kotliar were then able to show the mapping of the Hubbard model to the Anderson impurity model and further provided the self-consistent solution. Mathematically, the diagrammatic connection between the lattice and impurity model is expressed with Green's functions. An illustration of the DMFT self consistency equations is shown in Figure 2.15.

The major successes of DMFT include its ability to predict the Mott-Hubbard metal-to-insulator transition (MIT) [Mott, 1968]. In the previous sections, it was shown that the atomic lattice at half filling has two peaks separated by the interaction strength  $U$ . The repulsion between electrons assures that each atomic lattice site is singly-occupied and the movement of electrons is effectively frozen due to the high energy costs of double occupation. Consequently, the atomic lattice at half-filling is insulating. On the other hand, the non-interacting (i.e. tight-binding) lattice at half-filling is metallic due to the non-vanishing weight of the DOS at the Fermi level. Electrons feel no Coulomb repulsion  $U$  and are allowed to move freely in the lattice. In order to remedy these two limits, a

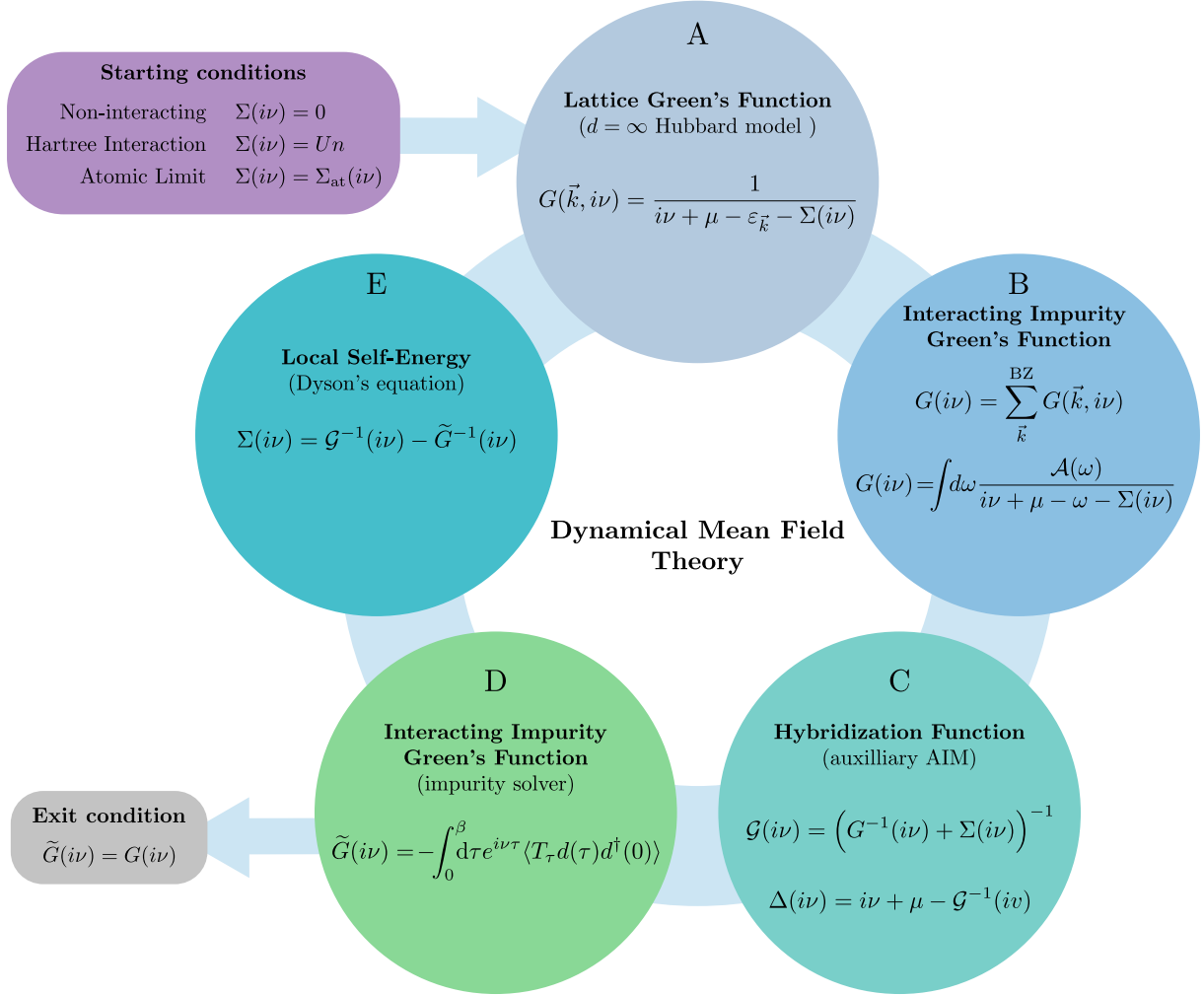


Figure 2.15: Illustration of the dynamical mean field theory self-consistency cycle. A: the lattice Green's function is typically initialized with a vanishing self-energy (non-interacting), with a Hartree-like self-energy or the atomic-limit self-energy. B: in general, the interacting impurity Green's function is generated by  $k$ -space integration. Alternatively, in the single-orbital case it can be generated from the non-interacting DOS due to a Hilbert-transform. C: the auxiliary AIM is defined by the non-interacting impurity Green's function or equivalently the hybridization function. D: a new impurity Green's function is generated by an impurity solver. if the new impurity Green's function is equal (equality is determined for a given norm) to the initial impurity Green's function, self-consistency has been achieved. E: The local self-energy is calculated as a new feedback for the lattice Green's function.

MIT is necessary for a given  $U_c/t$ .

In the previous sections it was also shown that the AIM has no MIT at half-filling and low temperatures. Instead, the transition is protected by the central Kondo resonance, which allows for a Fermi-liquid interpretation of the low-energy physics. Thus, the self-consistency feedback of the DMFT loop is required to adjust the bath- and hybridization parameters of the auxiliary AIM in order to allow for the MIT in the infinite-dimensional Hubbard model.

In Figure 2.16 the Mott-Hubbard MIT is shown for the three-dimensional Hubbard model at half-filling in DMFT.<sup>15</sup> The self-energy is approximated in second-order perturbation theory self-consistently, referred to as iterated perturbation theory (IPT) [Georges and Kotliar, 1992]. The DMFT equations were calculated in the Matsubara formalism and the DOS was extracted from Padé approximants.

The MIT is a first order phase transition, which results in a coexistence region, where DMFT converges to either metallic or insulating solutions depending on the starting conditions. Only by determining the minimum of the free-energy, the exact value of  $U_c$  can be determined. In two dimensions, DMFT yields a finite  $U_c$ , although it was shown that anti-ferromagnetic fluctuations fully suppress the MIT, such that  $U_c = 0$ . A full discussion of the MIT in the two-dimensional case (and the one- and three-dimensional case in context) is found elsewhere [Schäfer et al., 2015].

Extending DMFT to the multi-orbital Hubbard model is state-of-the art and is mostly done in the context of combining DMFT with ab-initio methods like density functional theory (DFT), first done by Anisimov *et al.* [Anisimov et al., 1997] and Lichtenstein *et al.* [Lichtenstein and Katsnelson, 1998]. DFT+DMFT approaches come with a whole set of challenges including determining correlated subspaces, screening the local interactions and double counting issues. A more detailed review of DFT+DMFT was given by Held [Held, 2007]. An alternative route to combining ab-initio methods with DMFT was followed by Aryasetiawan *et al.* [Aryasetiawan et al., 2004] starting with the GW method.<sup>16</sup> As the GW method is a diagrammatic approach, double counting corrections are quantifiable. However, due to the non-local interactions of GW, the impurity interaction becomes frequency dependent.

## 2.5 Diagrammatic Extensions to DMFT

DMFT allows for an exact mapping of the lattice model onto an impurity model at infinite lattice dimensions. At finite lattice dimension, it turns out that the number of neighboring sites is more relevant than the lattice dimension itself. Up to this point, only primitive cubic lattices were discussed, where there are six nearest neighbors in three-dimensions.

<sup>15</sup>For finite-dimensional lattice systems, DMFT is no more an exact mapping between lattice and impurity model. Instead, the physical correlation (self-energy) in the lattice is only approximated by its local contribution. The three-dimensional Hubbard model as opposed to the two-dimensional model was chosen in order to distinguish between the Kondo-resonance and the Van Hove singularity. Further the DMFT approximation is more justified in three dimensions than in two dimensions.

<sup>16</sup>The GW method approximates the  $k$ -dependent self-energy by a Fock-like self-energy diagram, where the  $k$ -dependent one-particle Green's function  $G$  is contracted with the screened interaction  $W$ . The screened interaction is obtained from a RPA ladder-like construction.

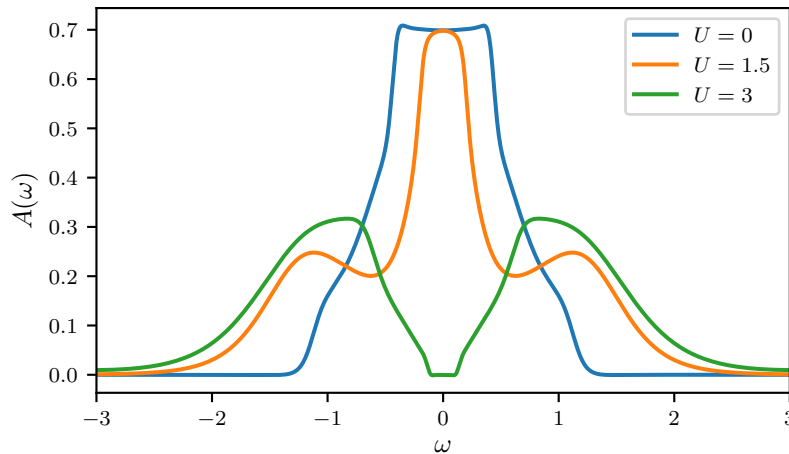


Figure 2.16: Metal-to-insulator transition (MIT) for the half-filled three-dimensional Hubbard model at  $\beta = 100$  and energy-scale  $2\sqrt{6}t = 1$  obtained from DMFT. The critical value of the interaction strength is determined to  $1.5 < U_c < 3$  (*cf.*  $U_c \sim 2.6$  in literature). For  $U < U_c$  a central Kondo-like peak structure develops. For  $U > U_c$  two Hubbard bands separated by  $U$  develop, with no weight at the Fermi energy. The impurity model was solved with iterated perturbation theory and the analytic continuation was performed with Padé approximants.

A body centered cubic (*bcc*) lattice, however, already has eight nearest neighbors and a face-centered cubic (*fcc*) lattice has twelve. The  $1/\sqrt{d}$  rescaling of the kinetic energy is more precisely a  $1/\sqrt{Z}$  scaling, where  $Z$  is the number of neighbors (coordination number). The corresponding derivation was given by Metzner and Vollhardt [Metzner and Vollhardt, 1989] and is also recapitulated by Held [Held, 2007].

A multitude of DMFT calculations for finite-dimensional systems resulted in the following crude observation: for three-dimensional (bulk) lattices, DMFT was able to reproduce various properties obtained by other numerical approaches and measured experimentally. For two-dimensional (surface) lattices, DMFT fails to verify experimental results, especially with regard to long-range orderings on the lattice. While on the one hand, the Mott-Hubbard MIT, Kondo physics and local magnetic moment formation result from *local* electronic correlations, on the other hand, magnetic ordering, *d*-wave superconductivity, etc. are determined by *non-local* electronic correlations.

In order to quantify electronic correlations in low-dimensional systems, the locality assumptions of DMFT need to be relaxed. Two different approaches have proven to be successful. First, the extension of single-site impurities to impurity clusters was proposed. These cluster impurities have to be solved numerically and give insight into medium-range correlations. The two most prominent methods of cluster extensions are the dynamical cluster approximation (DCA) [Hettler et al., 2000] and the cellular dynamical mean field theory (CDMFT) [Lichtenstein and Katsnelson, 2000, Kotliar et al., 2001]. Cluster approaches are capable of describing physics related to correlation lengths up to the cluster size, but fail in describing larger correlation lengths than the cluster size. The cluster

size is usually limited to relatively small clusters ( $N \sim \mathcal{O}(10)$ ) due to the exponential scaling of the Hilbert space. Close to phase transitions, cluster approaches, thus have severe difficulties. The same holds if orbital-realism with more than one-orbital needs to be considered. A recent study compared several thermodynamic quantities of the two-dimensional Hubbard model calculated from various numerical methods including DCA [LeBlanc et al., 2015].

A different route was followed by diagrammatically extending the DMFT equations and lifting the locality of the one-particle irreducible diagrams (self-energy) to the two-particle level. The dynamical vertex approximation (D $\Gamma$ A) [Toschi et al., 2007] and the dual fermion (DF) [Rubtsov et al., 2008] method are the most prominent methods in this field.<sup>17</sup> The approach of diagrammatically extending DMFT is followed in this work. A full review of diagrammatic extensions to DMFT was recently compiled by Rohringer *et al.* [Rohringer et al., 2017].

While DMFT is constructed from one-particle diagrams only (one-particle Green's function and self-energy), D $\Gamma$ A and DF both operate on the two-particle level. A roadmap to two-particle diagrammatics is illustrated in Figure 2.17. An extensive discussion of the local two-particle Green's function and vertex functions is found elsewhere [Rohringer et al., 2012].

### 2.5.1 Dynamical Vertex Approximation

The dynamical vertex approximation (D $\Gamma$ A)<sup>18</sup> extends the local DMFT self-energy by assuming locality on the two-particle level and constructing a non-local self-energy with non-local one-particle propagators and the equation of motion [Toschi et al., 2007, Katanin et al., 2009].

The equation of motion of the one-particle Green's function is the (imaginary) time derivative with respect to either of the creation- or annihilation operator. In case of the latter, the equation of motion yields:

$$(G\Sigma)_\sigma(\vec{k}, i\nu) = \sum_{\substack{\text{BZ} \\ \vec{k}'\vec{q} \\ \nu'\omega}} U G_{\sigma\sigma\sigma'\sigma'}^{\vec{k}\vec{k}'\vec{q},\nu\nu'\omega}, \quad (2.59)$$

where  $\sigma' = -\sigma$ . The above expression connects single-particle propagators on the left hand

<sup>17</sup>Analogous to the extensive list of elementary particles in particle physics, a whole *zoo* of diagrammatic extensions to DMFT emerged during the last decade. Some noteworthy methods include the one-particle irreducible approach (1PI) [Rohringer et al., 2013], DMFT as a starting point to functional renormalization group (DMF2RG) [Taranto et al., 2014], the triply irreducible local expansion (TRILEX) [Ayril and Parcollet, 2015] and the quadruply irreducible local expansion (QUADRILEX) [Ayril and Parcollet, 2016]. All these methods are based on the local two-particle Green's function in one way or another and most can be formulated with diagrammatic ladder approximations or with the Parquet equations.

<sup>18</sup>Historically,  $\Gamma$  referred to the fully irreducible two-particle vertex *and* the irreducible two-particle vertices in a given channel (distinctions were made by subscripts). Today, it is more common to refer to the fully irreducible vertex as  $\Lambda$  and the vertices irreducible in a given channel as  $\Gamma$ . Nevertheless the abbreviation D $\Gamma$ A does specify either a ladder- or Parquet-variant. In case a distinction is necessary, the two are referred to as ladder-D $\Gamma$ A and parquet-D $\Gamma$ A.

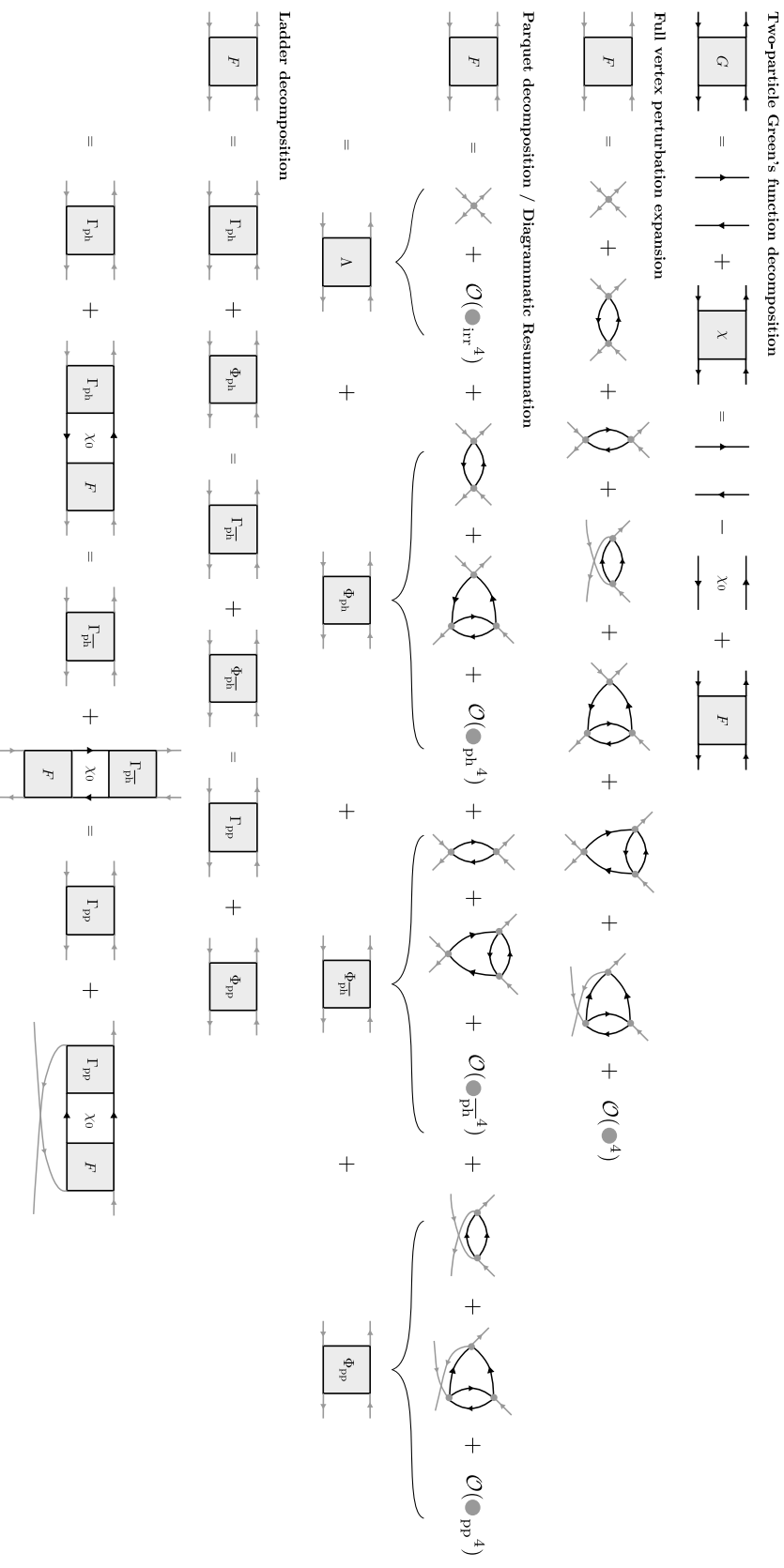


Figure 2.17: Two-particle Feynman diagrams. Black lines represent one-particle propagators. Grey lines represent amputated propagators. First row: two-particle Green's function  $G$  decomposition into disconnected parts and the one-particle irreducible (full) vertex  $F$ , with an alternative decomposition into the susceptibility  $\chi$ . Second row: perturbation series of the full vertex  $F$  up to third order. Third row: Parquet decomposition / diagrammatic resummation in terms of reducibility, starting with two-particle irreducible diagrams  $\Lambda$ , diagrams reducible in the particle-hole channel  $\Phi_{\text{ph}}$ , the particle-hole-transverse channel  $\Phi_{\text{p}\bar{\text{n}}}$  and the particle-particle channel  $\Phi_{\text{pp}}$ . Fourth row: ladder decomposition of the full vertex  $F$  by resumming diagrams irreducible in a given channel  $\Gamma_r$  and diagrams reducible in the same channel  $\Phi_r$  for  $r = \text{ph}, \text{p}\bar{\text{n}}, \text{pp}$ . Relative signs and combinatoric factors, as well as diagrams related by anti-symmetrization are not considered explicitly.

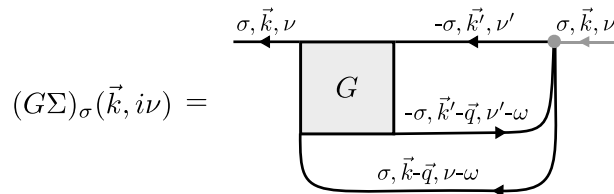


Figure 2.18: Feynman diagrammatic representation of the frequency-momentum dependent self-energy following from the equation of motion.

side with two-particle propagators on the right hand side. Diagrammatically relation (2.59) is illustrated in Figure 2.18. The frequency-momentum dependent two-particle Green's function in the particle-hole notation is defined as

$$G_{\sigma_1 \sigma_2 \sigma_3 \sigma_4}^{\vec{k} \vec{k}' \vec{q}, \nu \nu' \omega} = \int_0^\beta e^{i\nu(\tau_1 - \tau_2)} e^{i\nu'(\tau_3 - \tau_4)} e^{i\omega(\tau_2 - \tau_3)} \times \\ \langle T_\tau \hat{c}_{\sigma_1, \vec{k}}(\tau_1) \hat{c}_{\sigma_2, \vec{k}-\vec{q}}^\dagger(\tau_2) \hat{c}_{\sigma_3, \vec{k}'-\vec{q}}(\tau_3) \hat{c}_{\sigma_4, \vec{k}'}^\dagger(\tau_4) \rangle d\tau_1 d\tau_2 d\tau_3 d\tau_4, \quad (2.60)$$

with the discrete fermionic and bosonic Matsubara frequencies

$$\nu_n^{(\prime)} = (2n^{(\prime)} + 1) \frac{\pi}{\beta} \quad (2.61)$$

$$\omega_n = 2n \frac{\pi}{\beta}, \quad (2.62)$$

and  $n \in \mathbb{Z}$ . Usually the subscript  $n$  is dropped if the equations are exclusively represented in the Matsubara formalism.<sup>19</sup> By assuming time-translational invariance of the two-particle Green's function in relation (2.60), the four (imaginary) time arguments can be rewritten as three (imaginary) time differences. In the (Matsubara) frequency formalism this relates to energy conservation, where the four fermionic frequency arguments (not shown) can be rewritten as two fermionic frequencies and a bosonic transfer frequency. Particular groupings of the imaginary time differences into the Matsubara frequency arguments result in different frequency representations, of which the particle-hole representation was employed. Due to the intrinsic freedom in defining the Fourier transform in relation (2.60) several different frequency conventions exist. Appendix B provides a mapping between the frequency convention employed in this work and frequency conventions in literature.

To obtain the self-energy, the remaining outer leg of the two-particle Green's function needs to be amputated.<sup>20</sup> Further, it is common to write the disconnected part explicitly,

<sup>19</sup>Although it is common to denote the real frequency argument and the bosonic Matsubara frequency argument both with  $\omega$ , the frequency type can be inferred from the context: for generalized two-particle response functions the bosonic Matsubara frequency is employed alongside the fermionic frequency arguments. For physical susceptibilities with a single bosonic frequency, the bosonic Matsubara frequency is recognizable by explicitly prepending the imaginary unit  $i$  or explicitly re-introducing the subscript  $n$ .

<sup>20</sup>The terminology of referring to single-particle propagators in Feynman diagrams as *legs* and the division by the same as *amputations* reveals a short glance onto the dark humor of physicists.

such that

$$\begin{aligned} \Sigma_\sigma(\vec{k}, i\nu) &= U \sum_{\vec{k}'\nu'} G_{\sigma'}(\vec{k}', i\nu') \\ &+ \sum_{\substack{\text{BZ} \\ \vec{k}'\vec{q} \\ \nu'\omega}} U F_{\sigma\sigma'\sigma'}^{\vec{k}\vec{k}'\vec{q},\nu\nu'\omega} G_\sigma(\vec{k}-\vec{q}, i\nu-i\omega) G_{\sigma'}(\vec{k}'-\vec{q}, i\nu'-i\omega) G_{\sigma'}(\vec{k}', i\nu'). \end{aligned} \quad (2.63)$$

The first term of the rewritten EOM evaluates to the Hartree term

$$\Sigma_\sigma^{\text{hartree}} = U \sum_{\vec{k}'\nu'} G_{\sigma'}(\vec{k}', i\nu') \stackrel{n=1}{=} U n_\sigma, \quad (2.64)$$

which at half-filling further yields the expected expression  $U/2$ . It is noted that the Fock term vanishes for a local interaction and a single orbital.

The EOM couples the two-particle frequency-momentum dependent full vertex  $F$  to the local bare interaction  $U$ . Diagrammatically, the Coulomb repulsion  $U$  in itself can be interpreted as a two-particle vertex function. In other words, given a two-particle interaction, knowing the full two-particle vertex  $F$  is sufficient in order to calculate the exact frequency-momentum dependent self-energy or Green's function. On the other hand, extending the approach to the  $n$ -particle level, where  $n > 2$ , the  $n$ -particle vertex is necessary for calculating the exact self-energy. Nevertheless, even for two-particle interactions, obtaining the exact frequency-momentum dependent full vertex  $F$  is a numerically infeasible procedure. Calculating non-local vertex functions becomes considerably difficult due to the fermionic sign problem and the vast amount of degrees of freedom. Thus, the idea of DΓA is to approximate the full vertex  $F$  by assuming a subset of irreducible diagrams to be local in real space.

In the ladder-variant of DΓA, the full vertex  $F$  is rewritten in terms of the local irreducible vertex  $\Gamma$  for a given channel. For the particle-hole channel, the full vertex and the local irreducible vertex follow from ladder constructions of the Bethe-Salpeter equations

$$F_{\sigma_1\sigma_2\sigma_3\sigma_4}^{\vec{k}\vec{k}'\vec{q},\nu\nu'\omega} = \Gamma_{\sigma_1\sigma_2\sigma_3\sigma_4}^{\text{ph},\nu\nu'\omega} + \Phi_{\sigma_1\sigma_2\sigma_3\sigma_4}^{\text{ph},\vec{k}\vec{k}'\vec{q},\nu\nu'\omega} \quad (2.65)$$

$$F_{\sigma_1\sigma_2\sigma_3\sigma_4}^{\vec{k}\vec{k}'\vec{q},\nu\nu'\omega} = \Gamma_{\sigma_1\sigma_2\sigma_3\sigma_4}^{\text{ph},\nu\nu'\omega} - \sum_{\substack{\nu'' \\ \sigma_5\sigma_6}} \Gamma_{\sigma_1\sigma_2\sigma_5\sigma_6}^{\text{ph},\nu\nu''\omega} G_{\sigma_6}(\vec{k}, i\nu'') G_{\sigma_5}(\vec{k}-\vec{q}, i\nu''-i\omega) F_{\sigma_6\sigma_5\sigma_3\sigma_4}^{\vec{k}\vec{k}'\vec{q},\nu''\nu'\omega} \quad (2.66)$$

The local irreducible vertex  $\Gamma_{\text{ph}}$  can be obtained from the local ladder with

$$F_{\sigma_1\sigma_2\sigma_3\sigma_4}^{\nu\nu'\omega} = \Gamma_{\sigma_1\sigma_2\sigma_3\sigma_4}^{\text{ph},\nu\nu'\omega} - \sum_{\substack{\nu'' \\ \sigma_5\sigma_6}} \Gamma_{\sigma_1\sigma_2\sigma_5\sigma_6}^{\text{ph},\nu\nu''\omega} G_{\sigma_6}(i\nu'') G_{\sigma_5}(i\nu''-i\omega) F_{\sigma_6\sigma_5\sigma_3\sigma_4}^{\nu''\nu'\omega}. \quad (2.67)$$

Assuming SU(2)-symmetry, the Bethe-Salpeter equations can be solved for  $\Gamma$  by introducing linear superpositions of different spin combinations. These are commonly referred to as density-, magnetic-, spin- and triplet channels. The Bethe-Salpeter equations decouple in these channels, resulting in inverse Bethe-Salpeter equations similar to the (inverse)



Dyson's equation on the one-particle level. The density- and magnetic two-particle irreducible vertex functions follow as:

$$\Gamma_{d,m}^{\nu\nu'\omega} = \left(\chi_{d,m}^{-1} - \chi_0^{-1}\right)^{\nu\nu'\omega}, \quad (2.68)$$

where the inverses of  $\chi$  and  $\chi_0$  refer to matrix inversions in the discrete fermionic Matsubara frequencies  $\nu$  and  $\nu'$ . The spin superpositions are defined as  $\Gamma_{d/m}^{\nu\nu'\omega} = \Gamma_{\uparrow\uparrow\uparrow}^{\nu\nu'\omega} \pm \Gamma_{\uparrow\uparrow\downarrow}^{\nu\nu'\omega}$  (and equivalently for  $F$ ).

The transverse particle-hole and the particle-particle ladder are constructed in a similar fashion (analogous to the ladders illustrated in Figure 2.17).

In the ladder-variants of D $\Gamma$ A, one is restricted to physical processes linked to the specific channel. While charge- and spin fluctuations are generally encoded in the particle-hole ladders, superconducting fluctuations are encoded in particle-particle ladders. In cases where all three channels compete, they all need to be taken into account on an equal footing. The parquet-variant of D $\Gamma$ A includes all channels by constructing the full vertex  $F$  in terms of the two-particle irreducible local vertex  $\Lambda$  with

$$F_{\sigma_1\sigma_2\sigma_3\sigma_4}^{\vec{k}\vec{k}'\vec{q},\nu\nu'\omega} = \Lambda_{\sigma_1\sigma_2\sigma_3\sigma_4}^{\nu\nu'\omega} + \Phi^{\text{ph},\vec{k}\vec{k}'\vec{q},\nu\nu'\omega} + \Phi^{\overline{\text{ph}},\vec{k}\vec{k}'-\vec{q}\vec{k}-\vec{k}',\nu\nu'-\omega\nu-\nu'} + \Phi^{\text{pp},\vec{k}\vec{k}'\vec{k}+\vec{k}'-\vec{q},\nu\nu'\nu+\nu'-\omega} \quad (2.69)$$

$$F_{\sigma_1\sigma_2\sigma_3\sigma_4}^{\nu\nu'\omega} = \Lambda_{\sigma_1\sigma_2\sigma_3\sigma_4}^{\nu\nu'\omega} + \Phi^{\text{ph},\nu\nu'\omega} + \Phi^{\overline{\text{ph}},\nu\nu'-\omega\nu-\nu'} + \Phi^{\text{pp},\nu\nu'\nu+\nu'-\omega} \quad (2.70)$$

where the local Parquet equation needs to be inverted to obtain the local two-particle irreducible vertex  $\Lambda$  (see i.e. [Valli et al., 2015] or [Li et al., 2016]). Each reducible vertex function  $\Phi^r$  of a given channel  $r$  is calculated from the corresponding Bethe-Salpeter equation, which is evaluated in the natural frequency convention of the respective channel. In order to evaluate the Parquet equations, all reducible vertices must be expressed in the same notation. This results in the frequency transformations of the transverse particle-hole and the particle-particle notation in relations (2.69) and (2.70) into the particle-hole notation.

Extensions of D $\Gamma$ A to the multi-orbital case are in principle straight-forward, although numerically expensive due to the additional orbital prefactor to the (already large) number of local and non-local degrees of freedom of the two-particle vertex functions. A first multi-orbital extension of ladder-D $\Gamma$ A in the context of ab-initio calculations was done by Galler *et al.* [Galler et al., 2017].

## 2.5.2 Dual Fermion Approach

Similar to D $\Gamma$ A, the dual fermion (DF) approach [Rubtsov et al., 2008] quantifies non-local electronic correlations by diagrammatically extending DMFT. The DF approach decouples local and non-local degrees of freedom of the interacting lattice problem through a Hubbard-Stratonovich transformation [Stratonovich, 1957, Hubbard, 1959] of the action, followed by a Taylor expansion of the part linear in the initial and the dual variable. The resulting infinite perturbation series couples single-particle dual propagators to local

$n$ -particle full vertex functions. While the infinite series is an exact representation of the initial problem, in practice, the series is truncated at  $n = 2$  (mostly for practical reasons). As the local  $n$ -particle full vertex becomes the interaction vertex of the dual propagators, the EOM is no longer an exact relation at the two-particle level. Thus, a truncation at the two-particle level approximates the initial problem.

The derivation of the dual fermion approach to the Hubbard model is summarized in Appendix C and is based on the path integral formalism. The action defined in terms of the dual variables follows as [Rubtsov et al., 2008]

$$\tilde{S}[\bar{f}, f] = - \sum_{\nu k \sigma} \tilde{\mathcal{G}}_{k\nu\sigma}^{-1} \bar{f}_{k\nu\sigma} f_{k\nu\sigma} + \sum_i V[\bar{f}, f], \quad (2.71)$$

where  $\bar{f}, f$  are fermionic Grassmann fields of the dual fermions and  $\tilde{\mathcal{G}}_{k\nu\sigma} := \tilde{\mathcal{G}}_{\sigma}(\vec{k}, i\nu)$  is the bare dual Green's function. The dual fermion interactions are encoded in  $V[\bar{f}, f]$ , which follows an infinite Taylor expansion, with

$$V[\bar{f}, f] = \frac{1}{4} \sum_{\substack{\nu_1 \nu_2 \nu_3 \nu_4 \\ \sigma_1 \sigma_2 \sigma_3 \sigma_4}} G_{\nu_1 \sigma_1}^{-1} G_{\nu_2 \sigma_2}^{-1} G_{\nu_3 \sigma_3}^{-1} G_{\nu_4 \sigma_4}^{-1} \bar{f}_{i\nu_1 \sigma_1} f_{i\nu_2 \sigma_2} \bar{f}_{i\nu_3 \sigma_3} f_{i\nu_4 \sigma_4} G_{\sigma_1 \sigma_2 \sigma_3 \sigma_4}^{c, \nu_1 \nu_2 \nu_3 \nu_4} + \dots, \quad (2.72)$$

where  $G_{\nu\sigma} := G_{\sigma}(i\nu)$  is the local one-particle Green's function and  $G^c$  is the connected part of the two-particle Green's function. The term explicitly written in relation (2.72) is a two-particle interaction among the dual fermions. The omitted terms of sixth- and higher order describe three- and higher particle interactions. Truncating the above series at fourth or sixth order implicitly assumes that the dual fermions interact weakly. Having defined the dual action in relation (2.71) proportional to  $Z_{\text{site}}$  (see Appendix C) redefines the functional  $W \sim \ln Z$ . Thus, two-particle propagators extracted from the dual action are *connected* propagators. Additionally, the outer legs of the connected parts are amputated due to the local single-particle Green's functions introduced by the Hubbard-Stratonovich transformation. Effectively, dual fermions couple to connected  $n$ -particle fermion vertices. More intuitively, similar to the bath electrons of DMFT, the dual fermions hybridize onto local impurities, where they interact with a spatially localized (although now dynamical in frequency/time) interaction vertex.

In practice it is most common to truncate the Taylor series at the two-particle level<sup>21</sup> and construct the dual self-energy from ladder equations. For this purpose, the particle-hole dual full vertex function  $\tilde{F}$  is defined by the following Bethe-Salpeter ladder in terms of the dual fermion interaction  $F$  and the dual propagator  $\tilde{G}$ :

$$\tilde{F}_{\sigma_1 \sigma_2 \sigma_3 \sigma_4}^{\vec{k} \vec{k}' \vec{q}, \nu \nu' \omega} = F_{\sigma_1 \sigma_2 \sigma_3 \sigma_4}^{\nu \nu' \omega} - \sum_{\substack{\nu'' \\ \sigma_5 \sigma_6}} F_{\sigma_1 \sigma_2 \sigma_5 \sigma_6}^{\nu \nu'' \omega} \tilde{G}_{\vec{k}, \nu'', \sigma_6} \tilde{G}_{\vec{k}' - \vec{q}, \nu'' - \omega, \sigma_5} \tilde{F}_{\sigma_6 \sigma_5 \sigma_3 \sigma_4}^{\vec{k} \vec{k}' \vec{q}, \nu' \nu' \omega}, \quad (2.73)$$

where the sum is to be taken over all internal degrees of freedom. Diagrammatically, the above relation is illustrated in Figure 2.19. The transverse particle-hole and the particle-particle ladder are constructed in a similar fashion (analogous to the ladders illustrated in Figure 2.17). The non-local dual self-energy is constructed from the dual vertex function

<sup>21</sup>With a notable exception, see Section 4.3.1 for the calculation of dual fermion corrections based on the three-particle vertex.

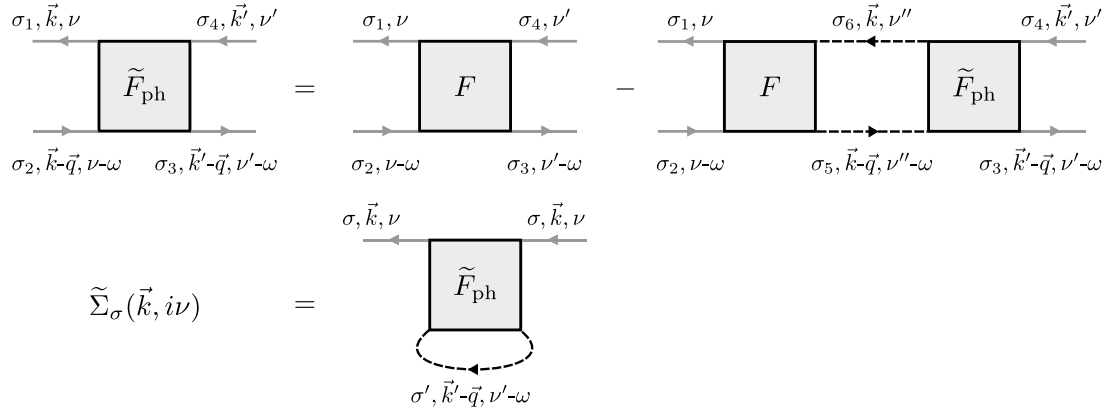


Figure 2.19: Non-local dual (dressed) vertex function  $\tilde{F}$  constructed from the particle-hole ladder. One-particle dual propagators are represented by dashed lines. Dual fermions interact via local two-particle connected vertex functions  $F$ . The dual self-energy is constructed by closing the dual vertex function with a dual propagator.

$\tilde{F}$  by contracting two of its legs with a dual single-particle propagator. The lowest order Hartree-like term vanishes, when demanding the dual propagators to be fully non-local.

Lastly, the mapping of the non-local dual self-energy  $\tilde{\Sigma}$  onto the actual non-local self-energy  $\Sigma$  is defined with

$$\Sigma_{\sigma}(\vec{k}, i\nu) = \frac{\tilde{\Sigma}_{\sigma}(\vec{k}, i\nu)}{1 + G_{\sigma\nu}\tilde{\Sigma}_{\sigma}(\vec{k}, i\nu)} + \Sigma_{\sigma}(i\nu), \quad (2.74)$$

where  $\Sigma_{\sigma}(i\nu)$  is the local self-energy of the DMFT problem.

Extensions of the DF approach to the multi-orbital case are in principle *straight-forward*. The difficulties and numerical complexity of extending ladder-DF approaches are in principle comparable to multi-orbital ladder-DfA. While first proposals of extending the method date back to the original publication [Rubtsov et al., 2008], actual implementations are still under development.

## 2.6 Analytic Continuation

Most of the diagrammatic methods described in the previous sections primarily operate in the Matsubara formalism [Matsubara, 1955]. The imaginary frequencies and imaginary times of the Matsubara formalism follow their real counterpart through a Wick rotation and allow for a treatment of finite-temperature effects in thermal quantum field theories. Intuitively, this can already be observed from the anti-/periodicity of fermionic/bosonic imaginary time many-body Green's functions in the interval  $\tau \in [0, \beta)$  and, equivalently, in the implicit temperature dependence of Matsubara frequencies with  $\sim 1/\beta$ .

Nevertheless, Green's functions can be also formulated (and for many physical questions are required for) in real frequencies or real times. Thus, DMFT in principle does depend on the representation (i.e. real or Matsubara). While some impurity solvers, like perturbation-theory based methods or the analytic Falicov-Kimball impurity equations can be expressed

in real frequencies, this is not true for most of the other impurity solvers. Specifically the continuous-time quantum Monte Carlo methods primarily operate in the Matsubara formalism. It is thus necessary to work out the back-transformation of Matsubara data to real data, which is an analytic continuation of analytic Green's functions from imaginary frequency arguments to real frequencies.

The relation between the fermionic frequency Matsubara Green's function  $G(i\nu)$  and the imaginary part of the real frequency Green's function  $G(\omega)$  is given by

$$G(i\nu) = \frac{1}{\pi} \int_{-\infty}^{\infty} d\omega \frac{1}{\omega - i\nu} \Im(G(\omega)), \quad (2.75)$$

where the real part of the real frequency Green's function can be extracted using the Kramers-Kronig relations

$$\Re(G(\omega)) = \frac{1}{\pi} \mathcal{P} \int_{-\infty}^{\infty} d\omega' \frac{\Im(G(\omega'))}{\omega' - \omega}, \quad (2.76)$$

and  $\mathcal{P}$  denotes the principal value. Alternatively, relation (2.75) can be formulated in the imaginary time domain by evaluating the corresponding Fourier transform, such that

$$G(\tau) = \frac{1}{\pi} \int_{-\infty}^{\infty} d\omega \int_0^{\beta} d\tau' e^{i\nu\tau'} \frac{\Im(G(\omega))}{\omega - i\nu} = \frac{1}{\pi} \int_{-\infty}^{\infty} d\omega \frac{e^{-\tau\omega}}{1 + e^{-\beta\omega}} \Im(G(\omega)). \quad (2.77)$$

More often, one is interested in the spectral function  $A(\omega)$ , which is related to the imaginary part of the (retarded) Green's function as

$$A(\omega) = -\frac{1}{\pi} \Im(G(\omega)). \quad (2.78)$$

Extracting the spectral function (or in that respect the imaginary part of the real frequency Green's function) from relations (2.75) and (2.77) results in evaluating an inverse Laplace transform, which is generally ill-conditioned. To make this more apparent, the two relations are discretized in the continuous variables  $\omega$  and  $\tau$  (where the imaginary frequency  $i\nu$  is already discrete), such that

$$G(i\nu) = \sum_{\omega} K(i\nu, \omega) \bar{A}(\omega) \quad (2.79)$$

$$G(\tau) = \sum_{\omega} K(\tau, \omega) \bar{A}(\omega), \quad (2.80)$$

where  $K(i\nu, \omega)$  and  $K(\tau, \omega)$  are referred to as kernel matrices and  $\bar{A}(\omega)$  is the spectral function including the discretized spectral weight  $\Delta\omega$ . Naively, one can calculate  $\bar{A}(\omega)$  by inverting the kernel matrices. Figure 2.20 illustrates the kernel matrices for an inverse temperature of  $\beta = 50$ . The large variations in the density plot already hint conditioning issues. The magnitude of the actual condition numbers<sup>22</sup> for the above kernel matrices evaluates to orders of  $10^{21}$ . Large condition numbers amplify numerical errors in the floating point representation of otherwise analytic Matsubara Green's functions. This problem becomes much more severe for Green's functions following statistical methods such as Monte Carlo. In the following, different methods to overcome the ill-conditioned nature of the analytic continuation will be discussed.

<sup>22</sup>The condition number of a matrix  $A$  for the 2-norm is calculated as the largest singular value of  $A$  times the largest singular value of  $A^{-1}$ .

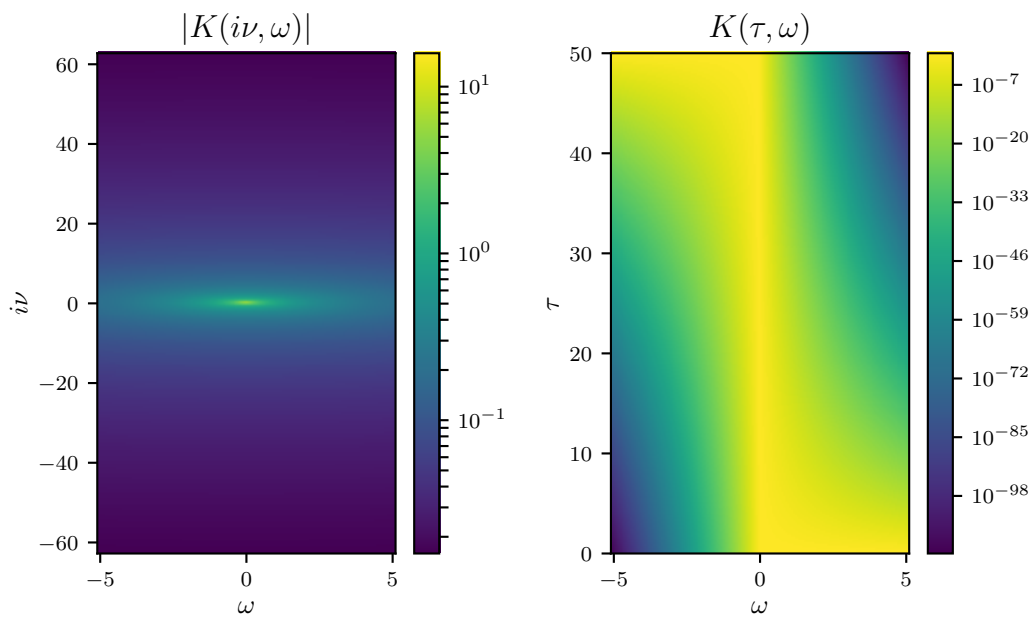


Figure 2.20: Logarithmic density plot of the kernel matrices  $|K(i\nu, \omega)|$  (absolute value) and  $K(\tau, \omega)$  in the Matsubara imaginary frequency and imaginary time representation for an inverse temperature  $\beta = 50$  and a real frequency energy window of  $\omega \in [-5, 5]$ . The condition numbers evaluate to  $9.7 \times 10^{20}$  and  $1.1 \times 10^{21}$  for the  $i\nu$ - and  $\tau$ -kernel respectively.

### 2.6.1 Padé

The Padé approximation is an interpolation of any given function through a low-order rational function. In the context of the analytic continuation of Matsubara data to real frequencies, the Padé approximation was employed long before the development of DMFT and related diagrammatic methods [Vidberg and Serene, 1977]. The underlying idea is to determine an analytic function  $f(z)$ , which evaluates to the given data for a discrete set of points, i.e.  $f(z_i) = f_i$  for the data  $(z_i, f_i)$ . In the context of this work,  $z_i$  is evaluated for the Matsubara frequencies  $z_i = i\nu_i$ , and  $f_i$  are the function values of the Matsubara Green's function  $f_i = G(i\nu_i)$ . Although not required in the general definition of the Padé approximation, one usually encodes  $1/z$  asymptotic behavior of Green's functions. The rational function  $f(z)$  is then defined as

$$f(z) = \frac{p_0 + p_1z + \dots + p_rz^r}{q_0 + q_1z + \dots + q_rz^r + z^{r+1}}, \quad (2.81)$$

where the last term  $z^{r+1}$  in the denominator accounts for the asymptotic behavior. The polynomials  $p(z)$  and  $q(z)$  of order  $r$  follow from the linear system of equations, which can be derived when evaluating relation (2.81) for the  $2r$  data points. A more detailed discussion including some technical details is found elsewhere [Osolin and Žitko, 2013].

It turns out that the coefficient matrix of the linear system of equations is more often not well conditioned. Numerical implementations of Padé approximants should thus be implemented with arbitrary precision libraries.

Particular care needs to be taken when analyzing spectral functions following Padé. In some cases Padé produces results which violate physical intuition, e.g. negative spectral functions. In practice, different rational functions are evaluated by varying the dimension of the input data, thus testing the results of Padé for robustness. Padé has proven to be a valuable tool for “analytic” (i.e. exact within machine precision) methods such as exact diagonalization. Stochastic methods like Monte Carlo, on the other hand, cannot be treated equally well. This is because Padé is not capable of considering the implicit stochastic uncertainties of these methods.

### 2.6.2 Maximum Entropy Method

*This section is based on: B. Hartl. Maximum Entropy Method for Quantum Monte Carlo Simulations. Project Work (2015). Supervised by P.G. and K. Held*

The statistical uncertainties in the input data in combination with the ill-condition nature of the kernels of analytic continuation allow for an infinite set of solutions (i.e. an infinite set of spectral functions) fulfilling the initial data. The idea of the maximum entropy method (MaxEnt) [Gubernatis et al., 1991] is to start with an initial guess for the spectral function, usually referred to as model function  $m(\omega)$ . The Matsubara Green's function  $G$  in imaginary frequencies or imaginary times is calculated according to relation (2.75) or (2.77). In a next step, one can calculate the deviations between the

guessed Green's function  $G$  and the input data  $\overline{G}$  by calculating a weighted least-square value  $\chi^2$  with

$$\chi^2 = \sum_{ij} \frac{(\overline{G}_i - G_i)(\overline{G}_j - G_j)}{C_{ij}}, \quad (2.82)$$

where  $C_{ij}$  is the covariance matrix for the discretized measurements  $i, j$  encoding the stochastic uncertainties. For uncorrelated noise the covariance matrix becomes diagonal with  $C_{ij} = \sigma_i^2 \cdot \delta_{ij}$ . Although in principle some care needs to be taken for Monte Carlo results, empirical investigations of Matsubara imaginary frequency and imaginary time for the CT-HYB algorithm support the assumption of a diagonal covariance matrix.<sup>23</sup>

By straight-forwardly minimizing the  $\chi^2$ -value, one would overfit the initial stochastic data resulting in spectral functions, which show spurious (i.e. unphysical) features. Instead, MaxEnt attempts to introduce physical information as an entropic prior. The entropy may be defined as

$$S = \int d\omega \left( A(\omega) - m(\omega) - A(\omega) \ln \frac{A(\omega)}{m(\omega)} \right), \quad (2.83)$$

where  $m(\omega)$  is the default model and  $A(\omega)$  is the (guessed) spectral function. The above entropy implicitly encodes the normalization and positivity of the spectral function as a physical prior. The last term in the entropy is usually referred to as the relative entropy and is related to the entropy of information theory  $p \ln(p)$ .

The posterior probability  $\Pr[A|\overline{G}]$ , i.e. the probability of calculating  $A$  given  $\overline{G}$ , follows by combining the likelihood function, determined by the least-square value  $\chi^2$ , and the entropy  $S$  as

$$\Pr[A|\overline{G}] = e^{\alpha S - \chi^2/2}, \quad (2.84)$$

where  $\alpha$  is the hyper-parameter determining the relative weight between entropy and least-square fit. A large value of  $\alpha$  favors the entropy term and reproduces (i.e. information fits) the model function as  $S$  becomes maximal for  $A(\omega) = m(\omega)$ . A small value of  $\alpha$ , on the other hand, favors the likelihood term and tends to overfit (i.e. noise fit) statistical fluctuations in the data. In practice the optimal  $\alpha$  may be determined by Bayes statistics [Jarrell and Gubernatis, 1996], or alternatively, simply by visual inspection determining the optimal value between noise fitting and information fitting. When extracting spectral functions from fermionic Matsubara Green's functions, it is common to start from a featureless (i.e. flat) default model.

Further, maximizing the posterior probability in relation (2.84) for a fixed  $\alpha$  can be accomplished through various minimization methods, of which simulated annealing is appealing due to its straight-forward implementation. The minimization can be optimized in terms of numerical efficiency and error robustness by truncating the singular value decomposition of the kernel matrices and conducting a minimization on the reduced subspaces.

---

<sup>23</sup>The covariance matrix of Green's functions in CT-HYB expressed in orthogonal Legendre polynomials is, however, usually much stronger correlated than its Matsubara counterparts (see [Harrer, 2013]).

### 2.6.3 Sparse Modeling

During the last decade the field of machine learning grew significantly in popularity. One of its methods, namely sparse modeling (SpM), was recently adapted to the problem of analytic continuation by Otsuki *et al.* [Otsuki et al., 2017]. In general sparse modeling attempts to reduce the number of variables of noisy initial data to exclude redundant data and hence avoid overfitting. The sparsity constraint is imposed by truncating the singular value decomposition of the coefficient matrix. This approach is closely related to the concept of principal component analysis in statistics, where one attempts to describe a high dimensional set of parameters by their most prominent representatives.

In a next step, the linear system of equations of the reduced subspaces is solved by an  $L_1$ -regularization (similar to the  $\chi^2$  minimization in MaxEnt).<sup>24</sup>

Applying SpM to the problem of analytic continuation, the singular value decomposition of the kernel matrices follows as

$$K = USV^\dagger \quad (2.85)$$

with  $K$  referring to the  $M \times N$ -dimensional kernel matrices introduced in relation (2.79) and  $S$  being the  $M \times N$ -dimensional matrix of singular values, where  $M$  discretizes the number of Matsubara points and  $N$  discretizes the number of real frequency points. Further,  $U$  is an  $M \times M$  matrix and  $V^\dagger$  an  $N \times N$  matrix. Investigating the singular values of the kernel matrices more closely, one observes a strong exponential decay in the singular values, which suggests introducing a threshold for small numbers. Figure 2.21 shows the singular values extracted from the kernel matrices at an inverse temperature of  $\beta = 50$ . Introducing a threshold of  $10^{-14}$  reduces the subspaces dimensionality by an order of magnitude without noticeably changing the numerical representation of the actual kernel matrices. Additionally, the compact dimensionality of the intermediate Matsubara-real frequency notation may be exploited to store Green's functions efficiently (see i.e. [Shinaoka et al., 2017b] or [Shinaoka et al., 2018]).

Finally, the Matsubara Green's function and the spectral function are projected on the (truncated) subspaces with  $\tilde{G} = U^\dagger G$  and  $\tilde{A} = V^\dagger A$ . One now attempts to minimize the expression

$$\frac{1}{2} \|\tilde{G} - S\tilde{A}\|_2^2 + \lambda \|\tilde{A}\|_1, \quad (2.86)$$

which is similar to the minimization problem of MaxEnt in relation (2.84).

Although SpM is a relatively new method in the field of analytic continuation, it benefits from its straight-forward implementation independent of the Kernel matrix under consideration. An extension to bosonic kernel matrices in the context of susceptibility continuations only requires little adaption to the diverging nature of the kernel matrix itself at  $i\omega = \omega = 0$ . MaxEnt, on the other hand, introduces physical intuition through the entropic prior, which in case of off-diagonal Green's functions or bosonic Green's functions needs to be adapted in terms of normalization and positivity. Both methods are formulated as minimization problems, where a Matsubara Green's function is calculated

---

<sup>24</sup>The minimization with respect to an  $L_1$ -regularization is often referred to as least absolute shrinkage and selection operator (Lasso).



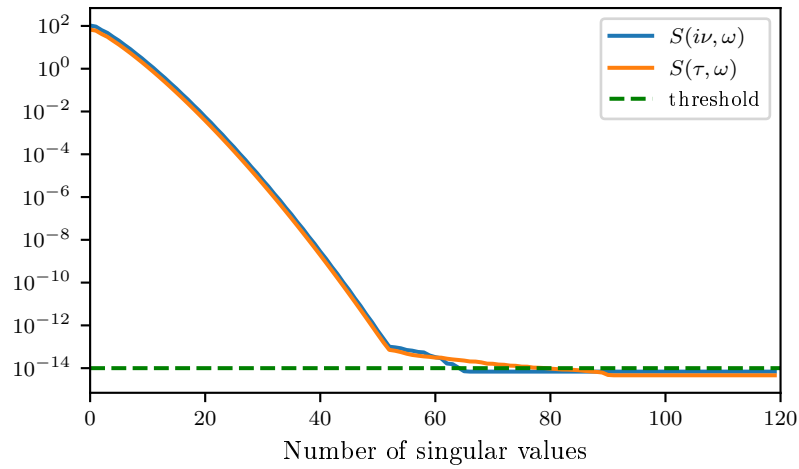


Figure 2.21: Singular values for the Matsubara imaginary time and imaginary frequency kernel matrices for an inverse temperature  $\beta = 50$  and a real frequency energy window of  $\omega \in [-5, 5]$ . The Matsubara- and real frequency grid was discretized to  $M = N = 1000$  points. The resulting singular value matrix includes  $N$  diagonal entries. By imposing a threshold of  $10^{-14}$  the 1000 singular values are truncated to 64 values in case of the imaginary frequency kernel matrix and 79 values in case of the imaginary time kernel matrix.

for a guessed spectral function and deviations relative to the data are evaluated. Future applications will demonstrate which of the two methods is superior.



# Chapter 3

## Continuous-time Quantum Monte Carlo

In the previous chapter the Hubbard Hamiltonian was introduced as a model for strong electronic correlations on a lattice. Due to the fermionic nature of the Hubbard model a straight-forward solution is mostly out of reach. Instead, various limits were discussed, which allow for an intuitive understanding of the physics involved by greatly simplifying the complexity of the original model. For infinite lattice dimension, the mapping of the Hubbard model onto an auxiliary Anderson impurity model is possible exactly, known as the DMFT. Similarly, D $\Gamma$ A and DF and other diagrammatic extensions are based on local diagrams generated from impurity models. As opposed to the underlying lattice models, the impurity models are in principle solvable, although in general only numerically. This is because of two different reasons: without any simplifications to the structure of the bath, the AIM is characterized by infinite Feynman diagrammatic series and secondly, the DMFT mapping procedure of the lattice problem onto an impurity requires a self-consistent dynamic solution.<sup>1</sup>

Generally, the various impurity solvers can be classified into two groups: diagrammatic solvers and solvers based on the diagonalization of the impurity Hamiltonian. Diagrammatic solvers generate a certain set of Feynman diagrams in one way or another. Quantum Monte Carlo methods stochastically sample the infinite series expansion of the partition function. In this process diagrams are sampled according to their weight contributing to the partition function. The Metropolis-Hasting construction assures a numerical convergence within the otherwise infinite sampling space. As no further assumptions are made to the diagrammatic series, these methods are in principle numerically exact, although providing only stochastic results.<sup>2</sup>

---

<sup>1</sup>Similar to the Hubbard model in one dimension, the AIM itself can be solved analytically by the Bethe Ansatz. By assuming a momentum-independent hybridization amplitude  $V$  and the parameters  $U, \mu_d, V^2$  being small relative to the Fermi energy  $\varepsilon_F$  the problem becomes effectively one-dimensional [Wiegmann, 1980]. However, the Bethe Ansatz only yields static quantities.

<sup>2</sup>It is no coincidence that the popularity of the Monte Carlo algorithm coincides with the development of modern computer clusters. The trivial parallelization schemes of Monte Carlo allow for straight-forward implementations with little network communication. The Metropolis Hasting algorithm was elected one of the ten most influential computer algorithms since the breakthrough of supercomputing [Sullivan and Dongarra, 2000].

The traditional approach to deal with Feynman diagrams by partially resumming diagrams, similarly assumes a series expansion of the partition function. By restricting the sum over diagrams to a specific subset of diagrams, such partial resummations allow for analytic expressions for the self-energy. By truncating the diagrammatic expansion of the self-energy at a certain order, these perturbation theory approaches also provide straight-forward expressions of the self-energy. Nevertheless, resummation- and finite perturbation theory approaches do not provide an exact-, nor a numerically exact solution, as certain diagrams are systematically excluded.

A different approach is followed by renormalization group solvers and exact diagonalization. In either case, results are extracted from a finite-dimensional Hamiltonian with a discrete bath, where for the renormalization group approaches the dimension of the Hamiltonian is step-wise adjusted. Approaches based on diagonalizing the Hamiltonian give an exact solution for the discrete bath problem, but only an approximate solution for the continuous bath problem. The accuracy of the method is greatly determined by how well the finite bath approximates the continuous bath. In this respect the numerical renormalization group (NRG) step-wise adjustment is particularly constructed, so as to obtain a logarithmically-good energy resolution around the Fermi energy.

A detailed list of impurity solvers with the corresponding references is given in Tables 3.1 and 3.2. While most of the impurity solvers are capable of providing numerical results for single-site impurities as well as multi-site impurities (i.e. clusters), in the context of this work, only single-site impurity solvers are considered. Nowadays, quantum Monte Carlo methods are the primary choice, due to their numerical exactness and ability to treat continuous baths. Although the (inverse) temperature directly affects the scaling of the sampling and measurement in imaginary time or Matsubara frequencies, QMC algorithms are more suited for low temperatures than exact diagonalization (ED), because the latter discretizes the hybridization function. Nevertheless, zero-temperature results are not obtainable by the QMC methods provided in Table 3.1. The Hirsch-Fye QMC algorithm is generally considered to be outdated by today's standards. Instead, the continuous-time QMC methods are state-of-the-art. This work deals with the continuous-time quantum Monte Carlo hybridization expansion (CT-HYB). This method is especially suited for multi-orbital systems and allows for general local interactions, including (retarded) density-density-, Slater-Kanamori SU(2)-symmetric- and full Coulomb interactions. Due to the exponential scaling in the number of orbitals, CT-HYB algorithms are mostly limited to about five orbitals, which covers the  $d$ -shells of ab-initio material calculations.

In the following chapter the basics of the CT-HYB algorithm are reviewed, the calculation of two-particle functions in the multi-orbital model is discussed, alongside technical improvements to the Monte Carlo estimators. Sections 3.1 and 3.2 describe the CT-HYB method prior to this work. Section 3.3 covers worm sampling as an extensions to the conventional CT-HYB algorithm and represents the primary scientific contribution of this work. Section 3.4 concludes the chapter with a critical discussion of one- and two-particle Green's function estimators in CT-HYB and the continuous-time Monte Carlo interaction expansion (CT-INT). This comparison ultimately motivates the derivation of novel "symmetric" improved estimators, beneficial for future implementations.

The numerical results are mostly benchmarked by exact diagonalization (ED), CT-INT or atomic limit calculations.

Table 3.1: Common impurity solvers for the AIM (Part 1): Continuous-time quantum Monte Carlo methods in the hybridization- (CT-HYB), interaction- (CT-INT) and auxiliary-field (CT-AUX) expansion of the partition function; Hirsch-Fye quantum Monte Carlo method as a discrete time expansion of the partition function; iterated perturbation theory (IPT) as a second-order perturbation theory-based solver.

Method	Description	Advantages	Disadvantages
Quantum Monte Carlo	stochastic sampling of partition function	numerically exact for continuous bath	stochastic error, sign problem
CT-HYB [Werner and Millis, 2006]	continuous time expansion in hybridization	favorable scaling with $U$ , multi-orbital with retarded/general interactions (weak sign problem)	exponential scaling with number of orbitals, high-frequency noise for leg amputations, sign problem for multi-site
CT-INT [Rubtsov and Lichtenstein, 2004]	continuous time expansion in interaction	power-law scaling with number of orbitals, high precision in asymptotics of irreducible quantities	sign problem out-of-half-filling and multi-orbital
CT-AUX [Gull et al., 2008]	continuous time expansion in interaction + auxiliary field decomposition	power-law scaling with number of sites, high precision in asymptotics of irreducible quantities	density-density only, sign problem out-of-half-filling and multi-site
Hirsch-Fye [Hirsch and Fye, 1986]	Suzuki-Trotter expansion in interaction	power-law scaling with number of orbitals, high precision in asymptotics of irreducible quantities	discrete time error, sign problem for multi-site, no Hub.-Strat. transformation for spin-flip and pair-hopping
Perturbation Theory IPT [Georges and Kotliar, 1992]	self-consistent second-order self-energy diagrams	exact within perturbation order $\beta^2$ scaling of Fourier transform	higher-order diagrams ignored

Table 3.2: Common impurity solvers for the AIM (Part 2): diagrammatic resummation techniques, including the non-crossing approximation (NCA) and the one-crossing approximation (OCA); renormalization group-based solvers, including numerical renormalization group (NRG) and density matrix renormalization group (DMRG); exact diagonalization impurity solver.

Method	Description	Advantages	Disadvantages
Partial Resummation	dressing propagators by a specific subset of diagrams	real frequency representation zero-temperature	qualitative results only
NCA [Keiter and Kimball, 1971]	self-consistent summation of dressed diagrams with no crossing of hybridization lines	fast, straight-forward diagrammatic interpretation	non-conserving approximation
OCA [Pruschke and Grewe, 1989]	self-consistent summation of dressed diagrams with up to one hybridization line crossing	more accurate than NCA	non-conserving approximation
Renormalization Group [Wilson, 1975]	step-by-step treatment of degrees of freedom for different energy scales	real frequency representation, accessing exponentially-low energy scales	discretization error for competing energy scales
NRG [Bulla et al., 2008]	logarithmic discretization of conduction band + iterative diagonalization	non-perturbative in system parameters, good for ground state properties and low-energy physics	exponential in local problem truncation effects, broadened finite-temperature excitations
DMRG [White, 1992]	states from density matrix iterative diagonalization	large number of sites compared to ED, good for ground-state properties	exponential in local problem, truncation effects, problems for high-energy excitations
Exact Diagonalization [Caffarel and Krauth, 1994]	diagonalizing Hamiltonian with impurity states and discrete bath states	exact for discrete problem, straight-forward implementation	exponential scaling in number of sites, poor discrete bath approximation problematic for low-temperatures

## 3.1 Impurity Observables

*Parts of this section (marked by a vertical sidebar) have been already published in: P. G., M. Wallerberger, T. Ribic, A. Hausoel, G. Sangiovanni and K. Held; Worm-improved estimators in continuous-time quantum Monte Carlo. Phys. Rev. B. 94, 125153 (2016)*

Before discussing the series expansion of the partition function, it is useful to review the relations between the various observables and the partition function itself. For this matter, the path integral formulation of the partition function of the Anderson impurity model is employed

$$Z = \int \mathcal{D}[\bar{d}, d] e^{-S[\bar{d}, d]} \quad (3.1)$$

where  $\bar{d}, d$  are the fermionic Grassmann fields of the impurity electrons.

The action  $S$  of the AIM, where the non-interacting bath fermions have been integrated out, then reads

$$S = -T[\bar{d}, d] + V[\bar{d}, d] = -\bar{d}_a \mathcal{G}_{ab}^{-1} d_b + \frac{1}{2} U_{abcd} \bar{d}_a \bar{d}_b d_d d_c, \quad (3.2)$$

where  $T[\bar{d}, d]$  is the kinetic part and  $V[\bar{d}, d]$  the interaction part of the action;  $\mathcal{G}_{ab}^{-1} = -\partial/\partial\tau_a - \epsilon_{ab} - \Delta_{ab}$  is the non-interacting Green's function. The hybridization function  $\Delta_{ab}$ , the on-site energies  $\epsilon_{ab}$  and the local orbital-dependent interaction  $U_{abcd}$  are, in terms of the combined orbital-spin-time index, defined as

$$\begin{aligned} \Delta_{ab} &:= \Delta_{\alpha\sigma_a\beta\sigma_b}(\tau_a - \tau_b) \\ \epsilon_{ab} &:= \epsilon_{\alpha\sigma_a\beta\sigma_b}\delta(\tau_a - \tau_b) \\ U_{abcd} &:= U_{\alpha\beta\gamma\delta}\delta_{\sigma_a\sigma_c}\delta_{\sigma_b\sigma_d}\delta(\tau_a - \tau_b)\delta(\tau_a - \tau_c)\delta(\tau_a - \tau_d), \end{aligned} \quad (3.3)$$

where  $\alpha, \beta, \dots$  are the orbitals of the combined indices  $a, b, \dots$ <sup>a</sup> We remind the reader that the summation convention over repeated (Latin) indices requires the summation over orbital (Greek) indices, spin indices as well as integration over  $\tau \in [0, \beta]$ .

<sup>a</sup>The spin-convention in the interaction matrix (3.3) has been adapted for consistency with (2.55).

### 3.1.1 Green's Functions

Starting from the partition function (3.2), the generating functional  $W = \ln Z$  is used to derive an important class of observables - the many-body Green's functions. The interacting one- and two-particle Green's function are defined as the partial derivative with respect to the hybridization function

$$G_{ab} = -\frac{\delta \ln Z}{\delta \Delta_{ba}} = -\frac{1}{Z} \int \mathcal{D}[\bar{d}, d] e^{-S[\bar{d}, d]} d_a \bar{d}_b \quad (3.4)$$

$$G_{abcd} = -\frac{\delta \ln Z}{\delta \Delta_{ba} \delta \Delta_{dc}} = \frac{1}{Z} \int \mathcal{D}[\bar{d}, d] e^{-S[\bar{d}, d]} d_a \bar{d}_b d_c \bar{d}_d, \quad (3.5)$$

where higher-particle Green's functions are generated by further derivatives with respect to the hybridization function.

### 3.1.2 Occupation

Further observables include the generalized density  $n_{ab}$  as a derivative with respect to the on-site energy  $\epsilon_{\alpha\sigma_a\beta\sigma_b}$  and the generalized double occupancy  $D_{abcd}$  as a derivative with respect to the interaction matrix  $U_{\alpha\beta\gamma\delta}$

$$n_{ab} = -\frac{\delta \ln Z}{\delta \epsilon_{\alpha\sigma_a\beta\sigma_b}} = \frac{1}{Z} \int \mathcal{D}[\bar{d}, d] e^{-S[\bar{d}, d]} \bar{d}_{\alpha\sigma_a} d_{\beta\sigma_b} \delta(\tau_a - \tau_b) \quad (3.6)$$

$$D_{abcd} = -\frac{\delta \ln Z}{\delta U_{\alpha\beta\gamma\delta}} = \frac{1}{Z} \int \mathcal{D}[\bar{d}, d] e^{-S[\bar{d}, d]} \bar{d}_{\alpha\sigma_a} \bar{d}_{\beta\sigma_b} d_{\delta\sigma_\delta} d_{\gamma\sigma_\gamma} \times \\ \delta_{\sigma_a\sigma_d} \delta_{\sigma_b\sigma_c} \delta(\tau_a - \tau_b) \delta(\tau_a - \tau_c) \delta(\tau_a - \tau_d) \quad (3.7)$$

The above relations are directly extracted from the partition function. A different approach is followed by investigating the equation of motion, which starts from one of the above relations and considers an imaginary time-derivative of a given fermionic Grassmann field (or equivalently a given operator).<sup>3</sup>

In order to derive the improved estimators of the self-energy and the vertex function, we formulate the identity (master equation)

$$\frac{\mathcal{G}_{ae}}{Z} \int \mathcal{D}[\bar{d}, d] \frac{\partial}{\partial \bar{d}_e} e^{-S[\bar{d}, d]} F[\bar{d}, d] = 0, \quad (3.8)$$

where  $F[\bar{d}, d]$  is an arbitrary function in  $\bar{d}$  and  $d$  and  $S[\bar{d}, d]$  is defined by Eq. (3.2). This identity holds true because the integral of the derivative of a Grassmann field vanishes due to the invariance of the path integral under infinitesimal transformations of this field. A more general discussion of path integrals in a similar framework is found elsewhere [Zinn-Justin, 2002]. Computing the derivative, we find the Schwinger-Dyson equation in the path integral formalism as [Veschgini and Salmhofer, 2013]

$$\frac{1}{Z} \int \mathcal{D}[\bar{d}, d] e^{-S[\bar{d}, d]} d_a F[\bar{d}, d] = \frac{\mathcal{G}_{ae}}{Z} \int \mathcal{D}[\bar{d}, d] e^{-S[\bar{d}, d]} \left( \frac{\partial V[\bar{d}, d]}{\partial \bar{d}_e} F[\bar{d}, d] - \frac{\partial F[\bar{d}, d]}{\partial \bar{d}_e} \right). \quad (3.9)$$

The derivative of the interaction part in (3.9) is given by

$$\frac{\partial V[\bar{d}, d]}{\partial \bar{d}_e} = \frac{1}{2} U_{fghi} (\delta_{fe} \bar{d}_g - \bar{d}_f \delta_{ge}) d_i d_h =: U_{[eg]hi} \bar{d}_g d_i d_h, \quad (3.10)$$

<sup>3</sup>The following derivations marked by a vertical sidebar do not distinguish between observables and Monte Carlo estimators to the same extent as done in this work. Sections 3.1.3 and 3.1.4 show the derivations of the observables, which are later on implemented as Monte Carlo estimators in worm sampling.



where the square brackets [...] denotes the anti-symmetrization over the indices (including a factor  $\frac{1}{2}$ ).

By choosing  $F[\bar{d}, d]$  properly we can generate improved estimators up to an arbitrary order of Green's functions. The important cases of the self-energy and two-particle vertex function are discussed in the next two sections.

### 3.1.3 Self-energy

In order to obtain an estimator for the self-energy we set  $F[\bar{d}, d] = \bar{d}_b$  in Eq. (3.9), recovering the one-particle Green's function (3.4) on the left hand side and the following right hand side

$$G_{ab} = \mathcal{G}_{ab} - \frac{\mathcal{G}_{ac}}{Z} \int \mathcal{D}[\bar{d}, d] e^{-S[\bar{d}, d]} U_{[cg]hi} \bar{d}_g d_i d_h \bar{d}_b. \quad (3.11)$$

Comparing this with the Dyson equation<sup>a</sup> we find

$$(\Sigma G)_{cb} = -\frac{1}{Z} \int \mathcal{D}[\bar{d}, d] e^{-S[\bar{d}, d]} U_{[cg]hi} \bar{d}_g d_i d_h \bar{d}_b. \quad (3.12)$$

The diagrammatic representation of this one-particle improved estimator is given in Figure 3.1 (top). Let us now recall the explicit indices from the combined Latin indices and rewrite the path integral in second quantization as a thermal expectation value

$$(\Sigma G)_{\alpha\sigma, \beta\sigma'}(\tau - \tau') = -\langle T_\tau U_{[\alpha\gamma]\delta\epsilon} \hat{d}_{\gamma\sigma'}^\dagger(\tau) \hat{d}_{\epsilon\sigma}(\tau) \hat{d}_{\delta\sigma}(\tau) \hat{d}_{\beta\sigma'}^\dagger(\tau') \rangle, \quad (3.13)$$

where we have introduced the time-ordering symbol  $T_\tau$  and switched from fermionic Grassmann variables  $\bar{d}, d$  to creation and annihilation operators  $\hat{d}^\dagger, \hat{d}$ . In making the imaginary time index explicit<sup>b</sup>, we find that the spontaneous nature of the interaction contracts three operators to a single (imaginary) time. In terms of computational complexity the calculation of the one-particle improved estimator is thus comparable to the one-particle Green's function.

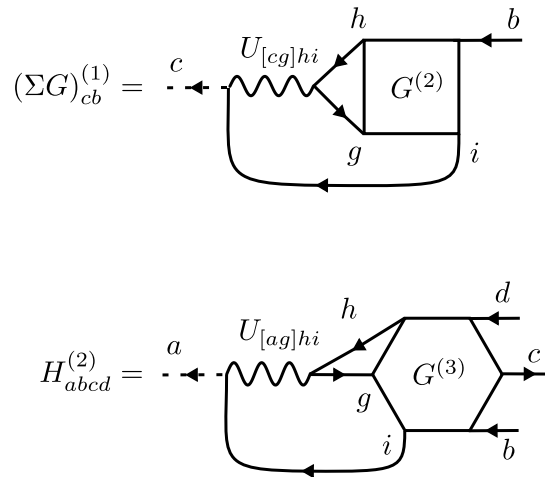


Figure 3.1: Top: diagrammatic representation of the one-particle improved estimator  $(\Sigma G)_{bc}^{(1)}$  [Eq. (3.12)]. Bottom: diagrammatic representation of the two-particle improved estimator  $H_{abcd}^{(2)}$  [Eq. (3.18), the last part of Eq. (3.16)]. The local interaction is represented explicitly by a wiggly line.<sup>c</sup>

### 3.1.4 Vertex Function

In order to obtain an estimator for the vertex-function we set  $F[\bar{d}, d] = -\bar{d}_b d_c \bar{d}_d$  in Eq. (3.9), so that the left hand side becomes the two-particle Green's function (3.5):

$$G_{abcd} = \mathcal{G}_{ab} G_{cd} - \mathcal{G}_{ad} G_{bc} + \frac{\mathcal{G}_{ae}}{Z} \int \mathcal{D}[\bar{d}, d] e^{-S[\bar{d}, d]} U_{[eg]hi} \bar{d}_g d_i d_h \bar{d}_b d_c \bar{d}_d. \quad (3.14)$$

We multiply the above with  $\mathcal{G}_{aj}^{-1}$  from the left and apply the Dyson equation  $\mathcal{G}_{aj}^{-1} = G_{aj}^{-1} + \Sigma_{aj}$

$$(\mathcal{G}_{aj}^{-1} + \Sigma_{aj}) G_{abcd} = \delta_{jb} G_{cd} - \delta_{jd} G_{bc} + \frac{\delta_{je}}{Z} \int \mathcal{D}[\bar{d}, d] e^{-S[\bar{d}, d]} U_{[eg]hi} \bar{d}_g d_i d_h \bar{d}_b d_c \bar{d}_d \quad (3.15)$$

In the following we multiply with  $G_{ja}$  from the left and finally rearrange the terms

$$G_{abcd} - G_{ab} G_{cd} + G_{ad} G_{bc} = -(G\Sigma)_{ae} G_{ebcd} + \frac{G_{ae}}{Z} \int \mathcal{D}[\bar{d}, d] e^{-S[\bar{d}, d]} U_{[eg]hi} \bar{d}_g d_i d_h \bar{d}_b d_c \bar{d}_d. \quad (3.16)$$

We can identify the left-hand side with the connected part  $G^{\text{conn}}$  of the two-particle Green's function. The diagrammatic representation of the two-particle improved estimator is given in Figure 3.1 (bottom). We observe that we are required to obtain the one-particle estimator  $(G\Sigma)$  apart from sampling the two-particle improved estimator. The final result yields

$$G_{abcd}^{\text{conn}} = -(G\Sigma)_{ae} G_{ebcd} + G_{ae} H_{ebcd}. \quad (3.17)$$

For the two-particle improved estimator we recover the explicit indices from the combined Latin indices and rewrite the remaining path integral of Eq. (3.16) as a thermal expectation value in second quantization

$$H_{\alpha\sigma_a, \beta\sigma_b, \gamma\sigma_c, \delta\sigma_d}(\tau_a, \tau_b, \tau_c, \tau_d) = \langle T_\tau U_{[\alpha\epsilon]\zeta\eta} \times \hat{d}_{\epsilon\sigma_e}^\dagger(\tau_a) \hat{d}_{\eta\sigma_e}(\tau_a) \hat{d}_{\zeta\sigma_a}(\tau_a) \hat{d}_{\beta\sigma_b}^\dagger(\tau_b) \hat{d}_{\gamma\sigma_c}(\tau_c) \hat{d}_{\delta\sigma_d}^\dagger(\tau_d) \rangle. \quad (3.18)$$

Again, by making the imaginary time index<sup>b</sup> explicit, we find that three operators are contracted to a single time, whereas the other three operator have each a different time

argument. In terms of computational complexity the two-particle improved estimator is hence comparable to the two-particle Green's function.

<sup>a</sup>The Dyson equation is given by  $G_{ab} = \mathcal{G}_{ab} + \mathcal{G}_{ac}\Sigma_{cd}G_{db}$

<sup>b</sup>According to (3.3) the spin convention in (3.13) has been adapted for consistency with (2.55).

<sup>c</sup>Direction of arrows has been adapted for this work. More commonly, local interactions are illustrated as dots only, whereas wiggly lines are used for non-local interactions.

## 3.2 Hybridization Expansion

### 3.2.1 Partition Function

Having established how different observables can be extracted from the partition function in the path integral formalism, in a next step the partition function is expanded in the Hamiltonian formalism as an infinite perturbation theory, which can then be sampled stochastically. In the context of CT-HYB these derivations were first introduced by Werner and Millis [Werner and Millis, 2006].

The finite-temperature expectation value for an operator  $\hat{\mathcal{O}}(\tau)$  and a Hamiltonian  $\hat{H}$  is given by

$$\langle \hat{\mathcal{O}}(\tau) \rangle = \frac{1}{Z} \text{Tr} \left( T_\tau e^{-\beta \hat{H}} \hat{\mathcal{O}}(\tau) \right), \quad (3.19)$$

where  $\beta$  is the inverse temperature,  $\tau$  is the imaginary time argument and  $T_\tau$  the time-ordering operator. The partition function  $Z$  in the Hamiltonian formalism is defined as

$$Z = \text{Tr} e^{-\beta \hat{H}}. \quad (3.20)$$

In order to write the partition function as an infinite series expansion, the Hamiltonian is split into a non-interacting and an interacting part, with  $\hat{H} = \hat{H}_0 + \hat{H}_I$ .<sup>4</sup> Following perturbation theory, the series expansion of the partition function is given by

$$Z = \text{Tr} e^{-\beta \hat{H}_0} + \sum_{n=1}^{\infty} \frac{(-1)^n}{n!} \int_0^\beta d\tau_n \dots \int_0^\beta d\tau_1 \text{Tr} \left[ T_\tau e^{-\beta \hat{H}_0} \hat{H}_I(\tau_n) \dots \hat{H}_I(\tau_1) \right]. \quad (3.21)$$

The above result is now applied onto the AIM Hamiltonian (2.30), which is repeated in the multi-orbital variant at this point

$$\begin{aligned} \hat{H}_{\text{aim}} = & \overbrace{\sum_{\vec{k}} \sum_{\alpha\sigma} \varepsilon_{\vec{k}\alpha} \hat{c}_{\vec{k}\alpha\sigma}^\dagger \hat{c}_{\vec{k}\alpha\sigma}}^{\hat{H}_{\text{bath}}} + \overbrace{\sum_{\vec{k}} \sum_{\alpha\sigma} \left( V_{\vec{k}\alpha\sigma} \hat{c}_{\vec{k}\alpha\sigma}^\dagger \hat{d}_{\alpha\sigma} + V_{\vec{k}\alpha\sigma}^* \hat{d}_{\alpha\sigma}^\dagger \hat{c}_{\vec{k}\alpha\sigma} \right)}^{\hat{H}_{\text{hyb}}} \\ & - \underbrace{\sum_{\alpha\sigma} \mu_\alpha \hat{d}_{\alpha\sigma}^\dagger \hat{d}_{\alpha\sigma} + \sum_{\alpha\beta\gamma\delta} \sum_{\sigma\sigma'} U_{\alpha\beta\gamma\delta} \hat{d}_{\alpha\sigma}^\dagger \hat{d}_{\beta\sigma'} \hat{d}_{\delta\sigma'}^\dagger \hat{d}_{\gamma\sigma}}_{\hat{H}_{\text{loc}}}. \end{aligned} \quad (3.22)$$

<sup>4</sup>The detailed derivations of the partition function expansion in the given notation follow earlier works by the author [Gunacker, 2015], which may be consulted for a pedagogical introduction. In this work only the main results are summarized.

By choosing  $\hat{H}_I = \hat{H}_{\text{hyb}}$  and  $\hat{H}_0 = \hat{H}_{\text{bath}} + \hat{H}_{\text{loc}}$  the partition function in the hybridization expansion follows as

$$Z = \sum_{k \in 2\mathbb{N}} \int_{\tau_{k-1}}^{\beta} d\tau_k \int_{\tau_{k-2}}^{\beta} d\tau_{k-1} \dots \int_{\tau_1}^{\beta} d\tau_2 \int_0^{\beta} d\tau_1 \sum_{\alpha_k \sigma_k}^{N_b} \dots \sum_{\alpha_1 \sigma_1}^{N_b} \times \text{Tr}_d \left[ e^{-\beta H_{\text{loc}}} d_{\alpha_k \sigma_k}(\tau_k) d_{\alpha_{k-1} \sigma_{k-1}}^\dagger(\tau_{k-1}) \dots d_{\alpha_2 \sigma_2}(\tau_2) d_{\alpha_1 \sigma_1}^\dagger(\tau_1) \right] \times Z_{\text{bath}} \det \mathbf{\Delta}, \quad (3.23)$$

where  $k/2$  is the expansion order of the perturbation series,  $\text{Tr}_d$  is the trace over the impurity states of  $H_{\text{aim}}$ . Only pairs of creation and annihilation operators are inserted in the impurity (and the bath respectively) due to quantum number conservation. Further the imaginary time ordering has been evaluated explicitly. The expansion order, the flavor-summations and the imaginary time integrals represent a configuration space, which can be effectively sampled by Monte Carlo techniques. The  $k/2$ -dimensional hybridization matrix  $\mathbf{\Delta}$  connects all impurity creation operators to all impurity annihilation operators over hybridization events with the non-interacting bath:

$$\mathbf{\Delta} = \begin{pmatrix} \Delta_{\alpha_1 \sigma_1, \alpha_2 \sigma_2}(\tau_1 - \tau_2) & \dots & \Delta_{\alpha_1 \sigma_1, \alpha_k \sigma_k}(\tau_1 - \tau_k) \\ \vdots & \ddots & \vdots \\ \Delta_{\alpha_{k-1} \sigma_{k-1}, \alpha_2 \sigma_2}(\tau_{k-1} - \tau_2) & \dots & \Delta_{\alpha_{k-1} \sigma_{k-1}, \alpha_k \sigma_k}(\tau_{k-1} - \tau_k) \end{pmatrix} \quad (3.24)$$

Due to the non-interacting nature of the bath, the bath trace simplifies to the determinant of the hybridization matrix  $\mathbf{\Delta}$ .

It is common to abbreviate the series expansion (3.23) with

$$Z = \int w_{\text{loc}} w_{\text{bath}}, \quad (3.25)$$

where  $\int$  is the summation/integration over all degrees of freedom,  $w_{\text{loc}}$  is the local weight and  $w_{\text{bath}}$  is the bath weight of the configuration. This work only discusses the Monte Carlo aspects of the weight  $w_{\text{loc}} w_{\text{bath}}$  from a methodological viewpoint, especially focusing on the definition of different Monte Carlo estimators in the following. The numerical evaluation of the weights is not considered in detail. In order to calculate  $w_{\text{bath}}$  one would need to evaluate the determinant of the hybridization matrix. In combination with rank-1 updates of the hybridization matrix for inserting and removing pairs of operators (see i.e. Section 3.3.1) the determinant can be evaluated at numerical cost  $\mathcal{O}((k/2)^2)$  instead of a direct determinant evaluation with  $\mathcal{O}((k/2)^3)$  [Werner et al., 2006]. Generally, the number of operators scales linearly with the inverse temperature  $k/2 \sim \beta$ . The  $\mathcal{O}(\beta^3)$ -scaling common to many QMC algorithms results when including the autocorrelation length scaling with an additional factor of  $\beta$ . The temperature scaling of the local problem, on the other hand, is determined by the number of operators in the local trace and the additional autocorrelation scaling, resulting in an overall scaling of  $\mathcal{O}(\beta^2)$ . For non-density-density interactions, however, the calculation of the local weight accounts to the evaluation of matrix-matrix or matrix-vector products. The dimension of the matrices scales exponentially with the number of orbitals considered. For five orbitals the evaluation of the local trace typically dominates the computational effort. Notable

improvements to the calculation of the time evolution include tree algorithms [Gull, 2008], Krylov implementations [Läuchli and Werner, 2009] or enhanced block-diagonalizations of the local Hamiltonian [Parragh et al., 2012].

### 3.2.2 Hybridization Estimators

*Parts of this section (marked by a vertical sidebar) have been already published in: T. Ribic, P. G., S. Isakov, M. Wallerberger, G. Rohringer, A. Rubtsov, E. Gull and K.Held; Role of three-particle vertex within dual fermion calculations. Phys. Rev. B. 96, 235127 (2017)*

#### Green's Function Estimators

By replacing the functional derivatives introduced in Section 3.1 with partial derivatives and applying them to the partition function in relation (3.23), explicit expressions for the observables in terms of series expansions can be derived. The one-particle Green's function is given by [Werner et al., 2006]

$$G_{ab} = -\frac{1}{Z} \int w_{\text{loc}} Z_{\text{bath}} \frac{\partial \det \Delta}{\partial \Delta_{ba}} = -\frac{1}{Z} \int w_{\text{loc}} Z_{\text{bath}} \det \Delta \sum_{ij}^{k/2} (\Delta^{-1})_{ji} \delta_{ai} \delta_{bj} \quad (3.26)$$

Here, the partial derivative of the determinant with respect to a given matrix element  $\partial \det \Delta / \partial \Delta_{ba}$  follows from Jacobi's formula.<sup>5</sup> Due to numerical reasons,<sup>6</sup> it is often more convenient to relabel the inverse of the hybridization matrix as  $\mathbf{M} = \Delta^{-1}$ , such that the Monte Carlo estimator for the one-particle Green's function follows as

$$G_{ab} = -\frac{1}{\beta} \left\langle \sum_{ij}^{k/2} M_{ji} \delta_{ai} \delta_{bj} \right\rangle_{\text{MC}} \quad (3.28)$$

$$G_{\alpha\sigma\alpha\beta\sigma\beta}(\tau_\alpha, \tau_\beta) = -\frac{1}{\beta} \left\langle \sum_{ij}^{k/2} M_{ji} \delta_{\alpha\alpha_i} \delta_{\sigma\alpha\sigma_{\alpha_i}} \delta_{\beta\alpha_j} \delta_{\sigma\beta\sigma_{\alpha_j}} \delta(\tau_\alpha - \tau_{\alpha_i}) \delta(\tau_\beta - \tau_{\alpha_j}) \right\rangle_{\text{MC}}, \quad (3.29)$$

where in (3.29) the combined indices were resolved into flavor indices and imaginary time arguments. The summation over all elements of the hybridization matrix results in the entire configuration of  $k$  operators in  $w = w_{\text{loc}} w_{\text{bath}}$  to be considered for a single Green's function estimate.

<sup>5</sup> Jacobi's formula in the special case of deriving the determinant  $\det \mathbf{A}$  with respect to its matrix elements follows as

$$\frac{\partial \det \mathbf{A}}{\partial A_{kl}} = \text{adj}(A)_{lk} = \det \mathbf{A} A_{kl}^{-1} \quad (3.27)$$

where the second equality is only true if  $\mathbf{A}$  is invertible, as the adjugate matrix is defined as  $\mathbf{A} \text{adj}^T \mathbf{A} = \det \mathbf{A} \mathbf{1}$ .

<sup>6</sup>It is common for CT-HYB codes to store the inverse of the hybridization matrix and generate updates to the determinant by fast-update matrix algorithms.

In a similar approach to the one-particle Green's function, the two-particle Green's function is given by

$$G_{abcd} = \frac{1}{Z} \sum_{\mathcal{F}} w_{\text{loc}} Z_{\text{bath}} \frac{\partial^2 \det \Delta}{\partial \Delta_{ba} \partial \Delta_{dc}} \quad (3.30)$$

$$= \frac{1}{Z} \sum_{\mathcal{F}} w_{\text{loc}} Z_{\text{bath}} \det \Delta \sum_{ijkl}^{k/2} \left( \Delta_{ji}^{-1} \Delta_{lk}^{-1} - \Delta_{li}^{-1} \Delta_{jk}^{-1} \right) \delta_{ia} \delta_{jb} \delta_{kc} \delta_{ld}, \quad (3.31)$$

where Jacobi's formula was applied twice.<sup>7</sup> The corresponding Monte Carlo estimator follows as

$$G_{abcd} = \frac{1}{\beta^2} \left\langle \sum_{ijkl}^{k/2} \left( M_{ji} M_{lk} - M_{li} M_{jk} \right) \delta_{ia} \delta_{jb} \delta_{kc} \delta_{ld} \right\rangle_{\text{MC}}. \quad (3.33)$$

The estimator for the two-particle Green's function in relation (3.33) displays a special feature, which is usually only observed in non-interacting systems. Considering that the sum over the matrix elements of  $M_{ji}$  in relation (3.28) represents the single-particle bath propagator  $g_{ba}$  for the given configuration,<sup>8</sup> the arrangement of the four sets of matrix elements of  $M$  in (3.33) resembles a Wick decomposition in the non-interacting bath. More precisely, the interacting impurity two-particle Green's function is then build from the non-interacting two-particle bath Green's function (i.e. only disconnected contributions). However, this only holds true within a given configuration, where the Wick decomposition into bath propagators is fulfilled, and not when summed over all configurations. Further, it is important to note that the bath propagators for a given configuration do not share the time-translational invariance of actual propagators. Thus, one cannot reduce the number of time/frequency arguments of the bath propagators. The Monte Carlo estimators for the interacting one-, two- and three-particle Green's function in the hybridization expansion following Wick decompositions into single-particle bath propagators are illustrated in Figure 3.2. A full discussion of this concept and its implications in terms of scaling with respect to Fourier transforms was given by Wallerberger [Wallerberger, 2016].

---

<sup>7</sup>By applying the chain rule the matrix elements of the inverse matrix are derived with respect to the matrix elements of the matrix itself with

$$\frac{\partial A_{ji}^{-1}}{\partial A_{lk}} = -A_{li}^{-1} A_{jk}^{-1} \quad (3.32)$$

<sup>8</sup>Although,  $g_{ba}$  is referred to as "bath propagator" in the context of CT-HYB estimators, formally the bath propagator describes the renormalized propagation of a bath electron due to impurity scatterings (see relation (2.43) in Chapter 2.2). Nevertheless, the CT-HYB estimators resemble the relevant impurity contribution of the bath propagator (c.f. [Haule, 2007]) and are thus referred to as such.

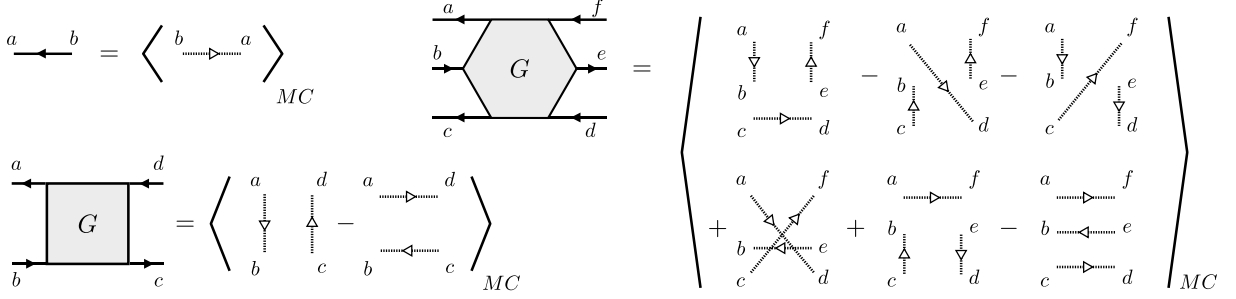


Figure 3.2: Monte Carlo estimators for the one-, two- and three-particle Green's function in the hybridization expansion following the first, second and third derivative of the partition function series with respect to the hybridization matrix. Dashed propagators represent bath propagators. The one-particle Green's function is the Monte Carlo average over the one-particle bath propagator. The two- and three-particle Green's function is the Monte Carlo average over the disconnected two- and three-particle contributions in the bath.

Generalizing Eq. (3.28) to the three-particle Green's function, we find:

$$\begin{aligned}
 G_{ijklmn}(\tau_1, \dots, \tau_6) = & \langle g_{ij}(\tau_1, \tau_2) g_{kl}(\tau_3, \tau_4) g_{mn}(\tau_5, \tau_6) \\
 & - g_{il}(\tau_1, \tau_4) g_{kj}(\tau_3, \tau_2) g_{mn}(\tau_5, \tau_6) \\
 & - g_{in}(\tau_1, \tau_6) g_{kl}(\tau_3, \tau_4) g_{mj}(\tau_5, \tau_2) \\
 & + g_{il}(\tau_1, \tau_4) g_{kn}(\tau_3, \tau_6) g_{mj}(\tau_5, \tau_2) \\
 & + g_{in}(\tau_1, \tau_6) g_{kj}(\tau_3, \tau_2) g_{ml}(\tau_5, \tau_4) \\
 & - g_{ij}(\tau_1, \tau_2) g_{kn}(\tau_3, \tau_6) g_{ml}(\tau_5, \tau_4) \rangle . \tag{3.34}
 \end{aligned}$$

This is nothing but the antisymmetrized sum over all possible removals of three hybridization lines, which reflects the fact that Wick's theorem is valid for the (non-interacting) bath propagator.

It is worth pointing out that Eq. (3.34), and in general any estimator for  $n > 1$  particles constructed in this fashion, is not valid for systems with interactions beyond density-density type and a hybridization function that is (block-)diagonal in  $i$  and  $j$ . In such cases, one would have to resort to worm sampling, which we however gauge as a formidable computational challenge in itself due to the sheer size of the worm configuration space and the size of the measured object itself. Fortunately, this is not an issue here, as we are studying the single-orbital case.

In principle Green's functions up to arbitrary order may be calculated in the above fashion. Numerically, it is worthwhile to Fourier-transform the one-particle bath propagator before assembling it. Because the bath propagator is not time-translation invariant within a given configuration, one needs to consider a two-dimensional Fourier transform even for the one-particle Green's function. In Matsubara frequency space, the resulting bath propagator is assembled accordingly (see i.e. [Gull et al., 2011, Hafermann, 2014a]). The scaling of a direct measurement (i.e. without assembly in Fourier space) and the two-step

measurement (Fourier transform + assembly) follows as:

$$\mathcal{O}\left(N_f^3 \log N_f + M(k/2)^4\right) \quad (\text{direct measurement}) \quad (3.35)$$

$$\mathcal{O}\left(M(N_f^2 \log N_f + (k/2)^2 + N_f^3)\right) \quad (\text{two-step measurement}), \quad (3.36)$$

where  $M$  is the number of measurements,  $N_f$  describes the length of a cubic-frequency box and  $k/2$  is the expansion order. Both measurements assume a nonequispaced fast Fourier transform (NFFT), which is evaluated once in the direct measurement (if memory permits) and  $M$  times in the two-step measurement. For the direct measurement, combinations of four hybridization operators in the stochastic trace have to be considered, while for the two-step measurement only combinations of two operators need to be considered. Assuming that the expansion order  $k/2$  and the number of frequencies  $N_f$  scales linear with the inverse temperature  $\beta$  and  $k/2 \sim N_f$ , the direct measurement scales with  $\mathcal{O}(M(k/2)^4)$ , while the two-step measurement scales with  $\mathcal{O}(MN_f^3) \sim \mathcal{O}(M(k/2)^3)$ . In practice, current post-DMFT methods consider two-particle Green's functions with  $N_f \sim 100$ . Thus, whenever looking at medium- to low-temperature regions, the two-step measurement should be employed. For higher temperatures typically  $k/2 < N_f$ , making the direct measurement more feasible due to the overhead in calling NFFT routines repetitively.

It is noted that the  $n$ -particle Green's function estimators ( $n \geq 1$ ) in the hybridization expansion share a striking similarity to the Green's function estimators of the weak-coupling interaction expansion CT-INT [Rubtsov and Lichtenstein, 2004] and the auxiliary field expansion CT-AUX [Gull et al., 2008]. This is a consequence of the Wick decomposition in terms of bath propagators in the former and non-interacting propagators in the later methods. Nevertheless, the estimators behave differently, mainly because the one-particle estimators are constructed differently. The weak-coupling estimators measure the one-particle Green's function as a correction to the non-interacting Green's function. As the Monte Carlo error is suppressed with  $1/(i\nu)^2$ , the high-frequency behavior is in principle much more precise in weak-coupling algorithms. Historically, this observation motivated the construction of new estimators in the hybridization expansion, which display a  $1/i\nu$  suppression of Monte Carlo errors in the high-frequency region. Such improved estimators are discussed in the next section. Estimators in CT-HYB with the same asymptotic behavior as the estimators in CT-INT and CT-AUX are discussed in Section 3.4.

### Improved Estimators

The improved estimators for the hybridization expansion were introduced by Hafermann *et al.* [Hafermann et al., 2012] for density-density interactions and later on extended in the context of retarded density-density interactions [Hafermann, 2014b].<sup>9</sup>

The improved estimator for the self-energy is based on relation (3.13). The density-density interaction may be parameterized with  $U := U_{\alpha\alpha\alpha\alpha}$  for  $\sigma \neq \sigma'$ ,  $V := U_{\alpha\beta\alpha\beta}$  for  $\sigma = \sigma', \sigma \neq \sigma'$  and  $J := U_{\alpha\beta\beta\alpha}$  for  $\sigma = \sigma'$  as defined in Table 2.1. By excluding spin-flip and pair-hopping terms, two of the three equal time operators in the improved estimator

<sup>9</sup>The two publications are based on the Hamiltonian formalism for deriving the equation of motion and further present the derivation of  $G\Sigma$  instead of  $\Sigma G$ , which is equivalent for flavor-diagonal quantities.



always build a density with a *different* flavor than the remaining annihilator. The improved estimator simplifies to

$$(\Sigma G)_{\alpha\sigma,\beta\sigma'}(\tau - \tau') = -\langle T_\tau \sum_{\gamma,\sigma'' \neq \sigma} U_{[\alpha\gamma]} \hat{n}_{\gamma\sigma''}(\tau) \hat{d}_{\alpha\sigma}(\tau) \hat{d}_{\beta\sigma'}^\dagger(\tau') \rangle, \quad (3.37)$$

where the density-density interaction matrix is reduced to an interaction matrix with two orbital indices only  $U_{\alpha\beta} := U_{\alpha\beta\alpha\beta}$ . The reduced structure can be parameterized with  $U := U_{\alpha\alpha}$  for  $\sigma \neq \sigma'$ ,  $V := U_{\alpha\beta}$  for  $\sigma \neq \sigma'$  and  $V - J := U_{\alpha\beta}$  for  $\sigma = \sigma'$  and  $\alpha \neq \beta$ , where the Hund's coupling picks up a sign due to the exchange of annihilation operators. In this case also the (anti)symmetrization over the indices changes to  $U_{[\alpha\beta]} = \frac{1}{2}(U_{\alpha\beta} + U_{\beta\alpha})$ , which recovers the expressions of Hafermann *et al.*

As the density in proximity (i.e. equal time) of the annihilation operator is of different flavor, it was suggested to calculate the (bath) propagator for a given configuration analogously to (3.29) and read off the corresponding density next to the annihilation operator. This simplification is intrinsic to the density-density interaction and unfolds its true strengths in the segment sampling of CT-HYB. Reformulating (3.37) in terms of a matrix element of the inverse hybridization matrix and an additional density, the Monte Carlo estimator follows as

$$(\Sigma G)_{\alpha\sigma,\beta\sigma'}(\tau - \tau') = -\frac{1}{\beta} \langle \sum_{ij}^{k/2} \sum_{\gamma,\sigma'' \neq \sigma} U_{[\alpha\gamma]} \hat{n}_{\gamma\sigma''}(\tau_{\alpha_i}) \times \\ M_{ji} \delta_{\alpha\alpha_i} \delta_{\sigma\sigma_{\alpha_i}} \delta_{\beta\alpha_j} \delta_{\sigma'\sigma_{\alpha_j}} \delta(\tau - \tau_{\alpha_i}) \delta(\tau' - \tau_{\alpha_j}) \rangle_{MC}. \quad (3.38)$$

The advantages of the improved estimator become apparent in Dyson's equation, where  $G = \mathcal{G} + \mathcal{G}\Sigma G$ . While the errors in the naive measurement (3.29) and the improved estimator (3.38) are constant over the entire time/frequency range, when calculating the Green's function from Dyson's equation and the improved estimator, the errors are rescaled by the  $1/i\nu$  behavior of the non-interacting Green's function,<sup>10</sup> further motivating referring to the estimators as improved estimators. Essentially, the above procedure yields similar advantages as the Green's function estimators of CT-INT, which are however rescaled by a factor  $1/(i\nu)^2$ .

The concept of the improved estimators extracted from the equation of motion may very well be extended to the two-particle level. The situation in this case, however, becomes more involved as the two-particle Green's function includes disconnected contributions. Further, the irreducible two-particle vertex  $F$  is defined with respect to interacting propagator lines  $G$  instead of non-interacting propagators  $\mathcal{G}$  as in the case of Dyson's equation. Following equations (3.17) and (3.18), the same reasoning for the interaction matrix in the density-density case as for the single-particle improved estimator applies, such that the two-particle improved estimator (equal-time three particle contribution)  $H$  simplifies to

$$H_{\alpha\sigma_a,\beta\sigma_b,\gamma\sigma_c,\delta\sigma_d}(\tau_a, \tau_b, \tau_c, \tau_d) = \langle T_\tau \sum_{\epsilon,\sigma_\epsilon \neq \sigma_a} U_{[\alpha\epsilon]} \hat{n}_{\epsilon\sigma_\epsilon}(\tau_a) \hat{d}_{\alpha\sigma_a}(\tau_a) \hat{d}_{\beta\sigma_b}^\dagger(\tau_b) \hat{d}_{\gamma\sigma_c}(\tau_c) \hat{d}_{\delta\sigma_d}^\dagger(\tau_d) \rangle. \quad (3.39)$$

<sup>10</sup>A more formal analysis is found in Section 3.4 and alternatively [Wallerberger, 2016]

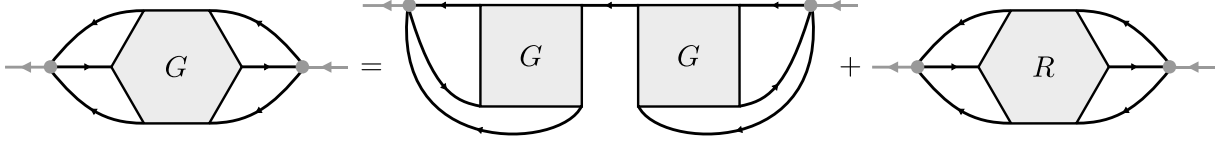


Figure 3.3: Illustration of the three-particle Green’s function contracted by two bare interaction vertices as occurring in the self energy by another application of the equation of motion or by substituting the two-particle improved estimator into the one-particle improved estimator. This “symmetric” improved estimator may be classified into a one-particle reducible contribution  $\Sigma G \Sigma$  and all remaining diagrams  $R$ .

The corresponding Monte Carlo estimator is constructed in analogy to (3.38) by considering the Wick decomposition of the bath propagators introduced in (3.33). For density-density interactions, the equal-time three particle object  $H$  may be calculated by generating a two-particle Green’s function and reading off the densities for the given annihilation operator.

Equation (3.17) sets the two-particle improved estimator  $H$  in relation to the connected contribution  $G^{\text{conn}}$  being proportional to  $G_{ae} H_{abcd}$ . The addition of an external leg generates a correlation function instead of a vertex function, which would be characterized by the absence of outer legs. Thus, a general observation is that the equation of motion amputates one propagator of the target quantity by introducing a bare interaction vertex  $U$  at the time argument of the derivative. Assuming that such implicit amputations improve the high frequency behavior over explicit (post-processing) amputations makes further applications of the equation of motion appealing.

Diagrammatically it seems that ‘improving’ improved estimators may not be beneficial: applying another time derivative to the remaining Grassmann variable  $\bar{d}_b$  in (3.12), or by substituting the two-particle improved estimator into the one-particle improved estimator, generates a three-particle Green’s function contracted with two bare interaction vertices  $U$  as illustrated in Figure 3.3. The three-particle Green’s function, however, includes two two-particle Green’s functions connected by a single-particle Green’s function, which is a one-particle reducible diagram and hence not part of the self-energy. This  $\Sigma G \Sigma$ -type contribution needs to be subtracted from the final estimate. An explicit construction of the diagram  $\Sigma G \Sigma$  diagram from two  $G \Sigma$  estimates requires an amputation of a single-particle propagator  $G$ , not yielding a further enhancement of the self-energy.

However, it is stressed that the above diagrammatic reasoning is somewhat misleading and that a formal derivation of equation of motion hierarchies results in enhanced improved estimators. These estimators are characterized by a high-frequency behavior similar to the estimators of CT-INT. These “symmetric” improved estimators are discussed extensively in Section 3.4.

### Shortcomings of Hybridization Estimators

To this point, the Green's function estimators and the improved estimators for density-density interactions for the hybridization expansion have been presented. However, the above estimators have several issues, which need to be considered:

- Neither the Green's function estimators nor the improved estimators in the hybridization expansion are capable of recovering the atomic limit, as the impurity does not hybridize with the bath, such that  $\Delta = 0$ . It is thus likely that for  $\Delta \rightarrow 0$ , the estimators may break down, even before the atomic limit is fully reached. One can observe this phenomenon for the two-particle Green's function, where the hybridization function of one spin (flavor) is atomic limit like (i.e. vanishes), while the other spin (flavor) is non-vanishing. The above estimator for the two-particle Green's function between these two flavors fails to reproduce correct results (see [Gunacker, 2015]). Similar issues may arise for symmetry-broken systems due to the interaction or the crystal field splitting.
- A very common simplification in CT-HYB is to assume a flavor diagonal hybridization function so that the sign-problem vanishes or becomes weak. In this case, only creation and annihilation operators of the same flavor are connected by hybridization lines to one another. Non-density-density interactions (like the SU(2)-symmetric Slater-Kanamori interaction), however, include further contributions to the two-particle Green's function. A low-order (first and second order) perturbation theory in the one-particle irreducible vertex function  $F$  includes spin-flip and pair-hopping bare interaction vertices, which cannot be measured by sampling the partition function for flavor diagonal hybridization functions. Pairwise flavor diagonal components of the two-particle Green's function, on the other hand, may very well include such spin-flip or pair-hopping terms in a higher perturbation order and thus can be generated by the hybridization estimators. The total number of non-vanishing components of the two-particle Green's function for  $N$  orbitals and the Slater-Kanamori interaction is given by:

$$M = 6N + 36 \binom{N}{2}, \quad (3.40)$$

While for a single orbital, of the possible 16 components, the 6 non-vanishing components are pairwise flavor diagonal (as the Slater-Kanamori interaction reduces to the density-density interaction), for two orbitals of the possible 256 components a total of 48 components are non-vanishing, where only 28 are pairwise flavor diagonal. A analysis of the components shows that for a larger number of orbitals (e.g. already at  $N=5$ ) about half of the components are pairwise flavor diagonal, while the other half is flavor off-diagonal (i.e. with four different flavor indices for the four operators). The origin of relation (3.40) is shown Appendix D.2, where the distinction between pairwise flavor diagonal and flavor off-diagonal components is discussed in detail.

- The improved estimators were introduced in the previous section, where a given fermionic operator in combination with a bare interaction vertex contracting three

further fermionic operators, returns an estimate for  $\Sigma G$ . For density-density interactions, the density can simply be read off due to the flavor diagonal structure of the local Hamiltonian. For non-density-density interactions the density operator preceding the annihilator may no longer be a flavor diagonal operator. While the equal time structure of the three operators in place is formally satisfied, other operators at different time may generate a finite time segment. The density can no longer be read off. As a result, the estimator cannot be generated from the partition function series any more.

### 3.3 Worm Sampling

*Parts of this section (marked by a vertical sidebar) were initially formulated in [Gunacker, 2015] and have been published in: P.G., M. Wallerberger, E. Gull, A. Hausoel, G. Sangiovanni and K. Held; Continuous-time quantum Monte Carlo using worm sampling. Phys. Rev. B. 92, 155102 (2015)*

Conceptually, the shortcomings of the conventional estimators in the hybridization expansion are rooted in the attempt to extract diagrams of a given observable (in most cases Green’s functions) from a diagrammatic series expansion of a different quantity, namely the partition function  $Z$ . While in many cases the diagrammatic series for the partition function and the diagrammatic expansion of the observable are compatible, other cases exist where diagrams of the observable are simply absent in the partition function series and, thus, cannot be generated from it. The above issues may be alleviated by directly sampling the diagrammatic series of the observable in question. In the context of continuous-time quantum Monte Carlo algorithms this was first proposed by Gull [Gull, 2008] for the CT-INT algorithm and extended to the CT-HYB algorithm by Gunacker *et al.* [Gunacker *et al.*, 2015]. The modification of the partition function by inserting additional operators to the diagrammatic series and thereby extending the configuration space is referred to as worm sampling. This method was pioneered for diagrammatic Monte Carlo solvers for bosonic Green’s functions by Prokof’ev *et al.* [Prokof’ev *et al.*, 1998b, Prokof’ev *et al.*, 1998a] and for fermionic Green’s functions by Burovski *et al.* [Burovski *et al.*, 2006].<sup>11</sup>

The following sections discuss the worm algorithm for CT-HYB and represents the core of this work. These sections may be considered the scientific contribution to the former state-of-the-art. The CT-QMC chapter is concluded with a critical discussion of Green’s function estimates in CT-HYB and newly proposed “symmetric” improved estimators. Although this analysis is formally independent of worm sampling, combining the concepts and observations of estimator theory and worm sampling allows for suitable implementations of such estimators in the future.

---

<sup>11</sup>In most worm algorithms (i.e. for determinant Monte Carlo, Ising solvers, etc.), the extended configuration space with the worm operators is considered as an auxiliary configuration space to significantly reduce autocorrelation lengths, while physical measurements are conducted in the partition function space. In CT-QMC algorithms, on the other hand, actual measurements are performed in the worm space.

### 3.3.1 Operator Sampling

In this work, only the worm algorithm for the hybridization expansion will be considered. As already suggested by the terminology of the worm sampling algorithm itself, it is necessary to discuss the details of Monte Carlo sampling prior to defining the estimators and discussing further in-depth implications. Starting from the partition function expressed in terms of local- and bath weights in relation (3.25), for the Metropolis-Hastings algorithm it makes sense to explicitly specify the implicit degrees of freedom for each of the weights with

$$w_{\text{loc}} = w_{\text{loc}}(k; \tau_1, \dots, \tau_k) \quad (3.41)$$

$$w_{\text{bath}} = w_{\text{bath}}(k; \tau_1, \dots, \tau_k) \quad (3.42)$$

The overall weight of a given configuration in the partition function expansion is thus given by:

$$p(k; \tau_1, \dots, \tau_k) = w_{\text{loc}}(k; \tau_1, \dots, \tau_k) w_{\text{bath}}(k; \tau_1, \dots, \tau_k) d\tau_1 \dots d\tau_k, \quad (3.43)$$

where the infinitesimal (imaginary) time arguments  $d\tau_i$  have been explicitly included into the weight.<sup>12</sup> Now, one can define the detailed balance condition for the CT-HYB algorithm for changing the order  $k/2$  of the hybridization expansion with

$$p(k; \tau_1, \dots, \tau_k) t(k \rightarrow k+2) = p(k+2; \tau_1, \dots, \tau_{k+2}) t(k+2 \rightarrow k), \quad (3.44)$$

where  $t(k \rightarrow k+2)$  is the transition probability for adding one pair of creation and annihilation operator at times  $\tau_{k+1}$  and  $\tau_{k+2}$  to the local trace and the corresponding pair to the bath trace. This increases the overall expansion order from  $k/2$  to  $k/2 + 1$ .<sup>13</sup> In order to define the Metropolis-Hastings condition, the transition probability  $t(k \rightarrow k+2)$  is further split into an acceptance probability  $a(k \rightarrow k+2)$  and a proposal probability  $f(k \rightarrow k+2)$ , such that

$$\frac{a(k \rightarrow k+2)}{a(k+2 \rightarrow k)} = \frac{p(k+2; \tau_1, \dots, \tau_{k+2}) f(k+2 \rightarrow k)}{p(k; \tau_1, \dots, \tau_k) f(k \rightarrow k+2)} \quad (3.45)$$

<sup>12</sup>The following discussion assumes that  $p > 0$ , i.e. all weights may be interpreted as probabilities. Due to the fermionic nature of the problem, also probabilities  $p < 0$  are possible, such that the weights need to be reweighed according to their absolute value. Measurements need to be corrected by the average sign, possibly resulting in a vanishingly small denominator. More commonly, this is referred to as “sign problem”. For flavor diagonal hybridization functions and Slater-Kanamori or density-density interactions the sign problem is either weak or completely non-existent. A discussion about the technicalities of calculating the different contributions to the sign in CT-HYB is found elsewhere [Gunacker, 2015].

<sup>13</sup>Attempting to add/remove single operators, i.e. proposing steps  $k \rightarrow k+1$  to the impurity problem fails due to the traces evaluating to zero, which is a consequence of quantum number violations. When dealing with off-diagonal hybridization functions, it is necessary to add/remove four operators during a Monte Carlo step to assure ergodicity with respect to spin-flip and pair-hopping terms contributing to the hybridization expansion of the partition function (see i.e. [Sémon et al., 2014]). Attempting to add/remove even more operators during a single step results in very low acceptance rates, but may be necessary in the case of disconnected histograms for extremely low temperatures.

In order to always move to more probable configurations and only to less probable configurations with a given probability the Metropolis-Hastings condition follows as

$$a(k \rightarrow k+2) = \min \left( 1, \frac{p(k+2; \tau_1, \dots, \tau_{k+2}) f(k+2 \rightarrow k)}{p(k; \tau_1, \dots, \tau_k) f(k \rightarrow k+2)} \right) \quad (3.46)$$

The above relation formally describes the sampling procedure. Calculating the weight  $p$  of a given configuration is, in principle, a straight forward procedure as it boils down to evaluating the local trace explicitly and the determinant for the bath problem. The proposal probabilities encode the Monte Carlo moves, which are required for the sampling process to become ergodic.

The proposal probability for adding a pair of creation and annihilation operators to the series expansion is

$$f(k \rightarrow k+2) = \frac{d\tau^2}{\beta^2}, \quad (3.47)$$

which is motivated by the probability to insert either operator into an infinitesimal time slice  $d\tau$ . The proposal probability for removing a pair, requires one to first select the specific annihilator/creator of all  $(k+2)/2$  annihilators/creators, such that

$$f(k+2 \rightarrow k) = \frac{1}{((k+2)/2)^2}. \quad (3.48)$$

In a similar fashion the proposal probability for shifting a given operator to a given infinitesimal time slice  $d\tau$  is given by

$$f(k \rightarrow k') = \frac{1}{(k/2)} \frac{d\tau}{\beta}, \quad (3.49)$$

where the inverse shift  $f(k' \rightarrow k)$  is defined equivalently, such that the ratio of proposal probabilities drops out of the acceptance ratio.

Having established the Monte Carlo sampling procedure of the infinite series expansion of the partition function  $Z$ , in a next step the sampling procedure of different operator series expansions is considered, which will be referred to as worm sampling. Formally, in the worm algorithm the configuration space of the partition function  $\mathcal{C}_Z$  is extended by the configuration of the worm space  $\mathcal{C}_W$ , such that

$$\mathcal{C} = \mathcal{C}_Z \oplus \mathcal{C}_W. \quad (3.50)$$

While the worm space  $\mathcal{C}_W$  is in principle defined in an abstract fashion, it is pedagogical to introduce worm sampling with respect to the  $n$ -particle Green's function, where  $\mathcal{C}_W \rightarrow \mathcal{C}_{G^{(n)}}$ .

In Figure 3.4 the Monte Carlo moves in  $\mathcal{C}_Z$  and  $\mathcal{C}_{G^{(n)}}$  are illustrated. We included all steps needed to be ergodic and to decrease auto-correlation lengths in both configuration steps. The pair insertion and removal steps in  $\mathcal{C}_Z$  (Figure 3.4 (a),(b)) are typical in the CT-HYB algorithm. We further introduce the operator shift move for  $\mathcal{C}_Z$  (Figure 3.4(c)), which shifts the time of a creation or annihilation operator.

For later discussion, we set up a modified partition function  $Z_{G^{(n)}}$  in configuration space  $\mathcal{C}_{G^{(n)}}$  by integrating over all degrees of freedom of the Green's function  $G^{(n)}$ : [Burovski

et al., 2006]

$$Z_{G^{(n)}} := \int \prod_{\alpha_1, \dots, \alpha_n} G_{\alpha_1, \dots, \alpha_n}^{(n)}(\tau_1, \dots, \tau_n) = \sum_{\alpha_1, \dots, \alpha_n} \int d\tau_1 \dots d\tau_n G_{\alpha_1, \dots, \alpha_n}^{(n)}(\tau_1, \dots, \tau_n). \quad (3.51)$$

This is not a “physical” partition function in the sense that it is connected to a thermodynamic potential, but it simply represents a phase space volume in Green’s function space. We will now discuss all the steps mentioned in Figure 3.4 in full detail.

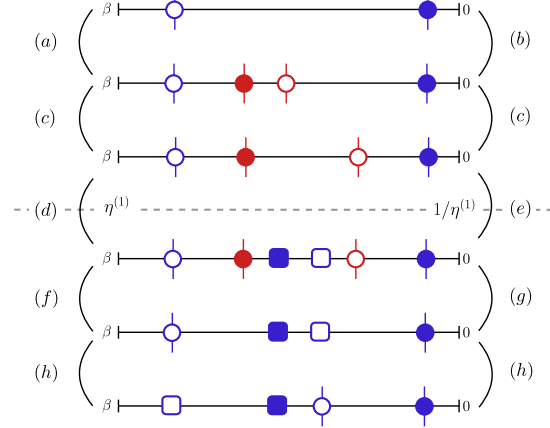


Figure 3.4: Illustration of Monte Carlo moves in the extended configuration space of worm sampling. Circles denote operators connected by hybridization lines (indicated by vertical lines), while rectangles denote worm operators. Moves (a), (b) and (c) correspond to insertion, removal and shift of an hybridization operator pair in the configuration space  $\mathcal{C}_Z$ , respectively. Labels (d) and (e) exemplify worm insertion and removal moves transitioning between the two spaces, where the parameter  $\eta^{(1)}$  rescales the phase space volume of  $\mathcal{C}_{G^{(1)}}$ . Labels (f) and (g) denote removal and insertion of an hybridization operator pair in  $\mathcal{C}_{G^{(1)}}$ ; (h) labels the worm operator replacement move in  $\mathcal{C}_{G^{(1)}}$ .

### 3.3.2 Worm Insertion and Removal Steps

The worm insertion and removal steps are transition steps between the two configuration spaces, depicted in Figure 3.4 (d),(e). In order to sample in  $\mathcal{C}_Z$  and  $\mathcal{C}_{G^{(n)}}$ , jumping between the two spaces is needed. In general, the configuration spaces  $\mathcal{C}_Z$  and  $\mathcal{C}_{G^{(n)}}$  have very different phase space volumes. This difference is balanced out by introducing a weighting factor  $\eta^{(n)}$  so that the total partition function reads

$$W = Z + \eta^{(n)} Z_{G^{(n)}}. \quad (3.52)$$

For now it was not formalized how  $\eta^{(n)}$  scales with the number of orbitals, temperature and interaction strength. It is best to choose  $\eta^{(n)}$  so that the simulation spends an equal amount of steps in  $\mathcal{C}_Z$  and  $\mathcal{C}_{G^{(n)}}$ . We revisit this fact when discussing the normalization of the worm result in the following section.

It is important to mention that the only difference between worm operators and hybridization operators is the missing of hybridization lines. This has some implications

for our Metropolis acceptance rates. The proposal rate of inserting a worm is given by the same expression as the proposal rate of inserting  $n$  hybridization operator pairs, i.e., [Werner and Millis, 2006]

$$f(\mathcal{C}_Z \rightarrow \mathcal{C}_{G^{(n)}}) = \frac{d\tau^{2n}}{\beta^{2n}}. \quad (3.53)$$

Adding worm pairs results in the expansion order  $k/2$  of the local trace being increased by  $n$ , whereas the expansion order in the determinant is kept constant. This adds an ambiguity to the expansion order which needs to be kept in mind. The weight of a configuration in  $\mathcal{C}_{G^{(n)}}$  modified by  $\eta^{(n)}$  is then:

$$p(\mathcal{C}_{G^{(n)}}, \tau_1, \dots, \tau_k; \tau_{i_1}, \dots, \tau_{i_{2n}}) = \eta^{(n)} \cdot w_{\text{loc}}(k + 2n, \tau_1, \dots, \tau_k; \tau_{i_1}, \dots, \tau_{i_{2n}}) w_{\text{bath}}(k, \tau_1, \dots, \tau_k) d\tau_1 \dots d\tau_k. \quad (3.54)$$

We point out that combining the proposal probability and the configuration of the weight, the  $2n$  infinitesimals  $d\tau_{i_1} \dots d\tau_{i_{2n}}$  do not cancel as they would have in partition function sampling. This is due to the extra local degrees of freedom introduced by the worm and is integrated over in the computation of  $Z_{G^{(n)}}(3.51)$ . The proposal probability for removing the worm is simply:

$$f(\mathcal{C}_{G^{(n)}} \rightarrow \mathcal{C}_Z) = 1. \quad (3.55)$$

### 3.3.3 Pair Insertion and Removal Steps in Green's Function Space

In order to generate all possible Green's function configurations, we need to introduce additional updates in the Green's function space  $\mathcal{C}_{G^{(n)}}$ . This is a crucial part of worm sampling: without it, the estimator is not ergodic (cf. Figure 3.5).

This explains why we are required to sample the Green's function space  $\mathcal{C}_{G^{(n)}}$  separately with operators having hybridization lines attached. To this effect, we perform insertions and removals of hybridization operator pairs also in Green's function space (Figure 3.4(f),(g)).

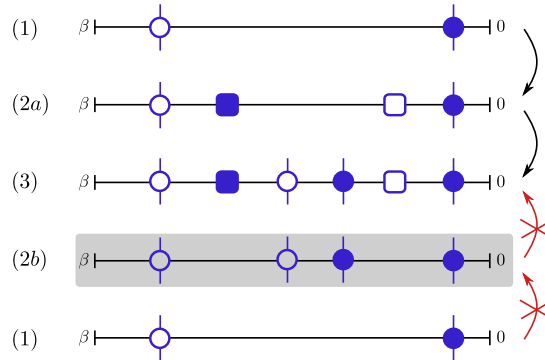




Figure 3.5: An “insertion estimator”, i.e. the mere insertion of local operators into a diagram from  $\mathcal{C}_Z$  without sampling, is not ergodic: it fails to produce diagram (3) because (2b) violates the Pauli principle and is therefore never reached. By first transitioning to  $\mathcal{C}_{G^{(1)}}$  space from (1) and then inserting a hybridization operator pair into (2a), one indeed is able to reach diagram (3).

### 3.3.4 Worm Replacement Step in Green’s Function Space

While insertion and removal moves formally fulfill the condition of ergodicity, worm sampling requires a shift/replacement move in order to allow for acceptable auto-correlation lengths. We elaborate on this requirement here.

Let us assume a local trace filled with hybridization operator pairs. We now attempt to insert a worm pair into this trace. It turns out that inserting a worm pair, where the worm operators are relatively close to one another is probable, while inserting a worm pair where the worm operators are far apart is less probable. This is because of (i) possible quantum number violations since there may be many creation and annihilation operators in between the pair for long time differences, and (ii) the pair insertion might lead to an energetically disadvantageous local configuration which is unfavorable to have for a long time.

Problem (i) is especially severe if we have a large amount of operators in the trace, which occurs at small interaction or low temperatures. Additionally, more restrictive interaction types, such as the density-density interaction, produce more rejects due to quantum number violations of attempted worm inserts. This is why we do not observe this auto-correlation problem at high temperatures, high interaction parameters and more general interactions such as Slater-Kanamori interactions (which may change the quantum number in the local trace).

At this point it is important to stress that this problem is not intrinsic to worm sampling itself, but is present in a similar fashion in the conventional sampling of CT-HYB. For low temperatures or high interaction values, pairs of creation and annihilation operators are inserted over short imaginary time differences, while large time differences become exponentially suppressed. This behavior is illustrated in Figure 3.6, where the imaginary time dependent acceptance rate for hybridization pairs and worm pairs with time difference  $\bar{\tau}$ <sup>14</sup> is shown for two different temperatures.<sup>15</sup> This exponential suppression does not impact the measurement of Green’s functions in conventional sampling, as the Green’s function estimators in partition function space consider all contractions over operator pairs simultaneously (see Section 3.2.2). For worm sampling, on the other hand, the sampling procedure of the operator series expansion directly influences the measurement, as a worm of a given length represents the imaginary time bin of the measurement.

<sup>14</sup>We note that  $\bar{\tau} = |\tau_1 - \tau_2|$ , where  $\tau_1$  is the time argument of the creation operator and  $\tau_2$  the time argument of the annihilation operator. As a result the time dependent acceptance rate is symmetric, such that only the domain  $\bar{\tau} \in [0, \beta/2)$  is of interest.

<sup>15</sup>This observation further triggered the development of window sampling techniques, where operator pairs are proposed only within a short window as opposed to proposing them over the entire trace. The method is extensively discussed by Shinaoka *et al.* [Shinaoka et al., 2014].

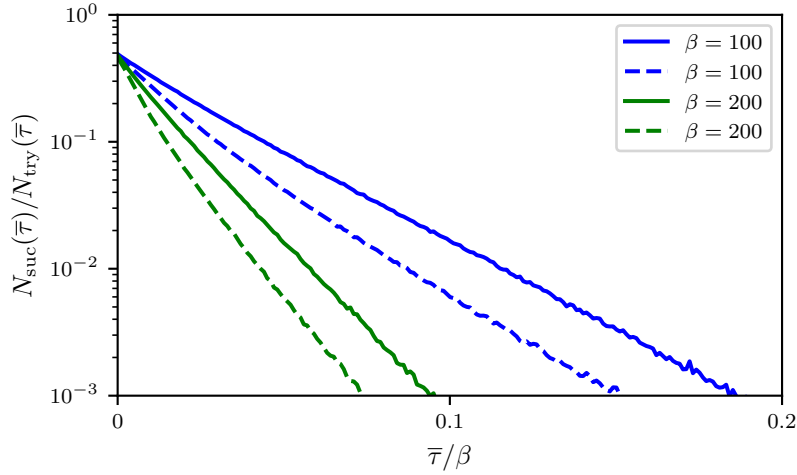


Figure 3.6: Imaginary time dependent acceptance rate for hybridization operator pair inserts (dashed line) and worm operator pair inserts (solid line) with time difference  $\bar{\tau}$  in the Bethe lattice. The parameters are chosen to agree with Figure 3.7. Both the hybridization operator pairs and the worm operator pairs are predominantly inserted for short times and display an exponential suppression with  $\bar{\tau}$ . The exponential decay is faster for lower temperature, such that operator pairs are inserted more locally. Hybridization operator pairs are inserted more locally than worm operator pairs due to additional constraints in the hybridization part, which is absent in worm sampling.

The solution to this problem is found in shift/replacement moves. We consider, instead of a general worm shift move, a replacement move which exchanges one of the worm operators with an operator of the hybridization expansion, i.e., we replace it with one of the same flavor connected by a hybridization line as illustrated in Figure 3.4(h).

This way we do not have to recalculate the local trace, as two locally indistinguishable operators switch position. Instead, we need to recalculate the determinant of the hybridization matrix since the replacement corresponds to a shift of the worm operator and a shift of the hybridization operator. Further we do not encounter any rejects of proposed moves due to local quantum number violations.

It turns out that worm replacement moves (or in the same way worm shift moves) are equally important for traces with very few operators because of problem (ii). This problem typically occurs if the weight  $e^{-U\tau}$  of the worm becomes prohibitively small, i.e., in particular for a large interaction strength and a long  $\tau$  difference such as  $\frac{\beta}{2}$ . We are then effectively restricted to inserting operator pairs into the trace, which are very close to each other in imaginary time. These pairs have similar properties as density operators and can in principle be inserted for very high insulating cases. By inserting hybridization pairs at short distances  $\tau_i - \tau_j$  and then replacing one worm operator with one hybridization operator we are able to pass this restrictions of the time evolution. As we will show in the following, the replacement move only depends on the ratio of the determinant of the hybridization matrix.

The proposal probability of a worm replacement step is given by:

$$f'(\mathcal{C}_{G^{(n)}}, k + 2n \rightarrow k + 2n) = \frac{1}{2n(k/2)}. \quad (3.56)$$

This corresponds to selecting one creation/annihilation operator of the  $2n$  worm operators at random and selecting one creation/annihilation of the same spin-orbit flavor with a hybridization line. In practice, we choose an operator from the  $k/2$  operators of the same type (annihilator/creator) and then discard flavors, which are not equivalent to the worm flavor. The proposal probability of switching the operators back to their original position is hence also given by Eq. (3.56).

We observe that the proposal probabilities for the replacement move cancel out and the acceptance ratio is fully determined by the ratio of weights. Further, the local weights cancel, since a worm operator and the corresponding hybridization operator are indistinguishable within the local trace.

Figure 3.7 shows how worm replacement moves alleviate the ergodicity problem of the worm algorithm for the situation where many operators are found in the local trace.

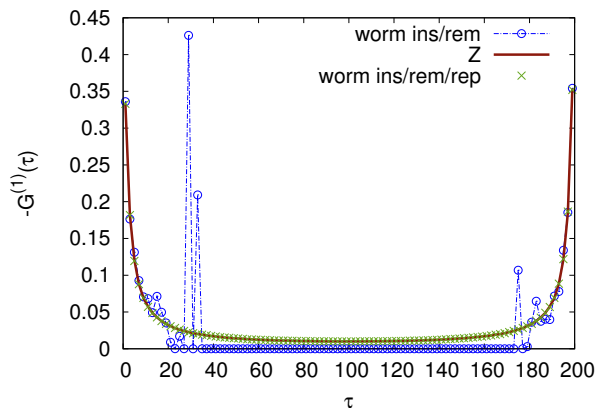


Figure 3.7: One-particle Green's function  $G^{(1)}(\tau)$  in imaginary time  $\tau$ , illustrating the ergodicity problem of the worm algorithm for an average expansion order of  $k/2 \sim 40$ . Parameters: inverse temperature  $\beta = 200/D$ , Coulomb repulsion  $U = 0.5D$  and  $\mu = 0.3D$  (out of half-filling) for the single-orbital AIM with semi-elliptic conduction electron density of states with half-bandwidth  $D = 1$  and  $V = 0.5D$ . The balancing parameter  $\eta^{(1)}$  was chosen in the interval  $[0.15, 0.22]$ . We observe the ergodicity problem between  $\tau = 25/D$  and  $\tau = 175/D$  (blue curve). When adding replacement moves, we are able to insert worm operators for such  $\tau$ 's around  $\beta/2$  (green triangles) and hence obtain much better results. We have additionally supplied  $G^{(1)}(\tau)$  for the measurement in partition function space (red curve).

### 3.3.5 $\delta$ -Estimators

In the previous section worm sampling was proposed as a method to overcome various issues intrinsic to the conventional CT-HYB algorithm. Formally, the Monte Carlo configuration space is extended from the configuration space of diagrams contained in the expansion

series of the partition function to include the configuration space of diagrams contained in the expansion series of the observable. In the following the worm estimators for the Green's function, the improved estimators and further equal time observables will be discussed. As opposed to the conventional estimators of the hybridization expansion, the estimators in worm space may be formulated in a trivial way, which in this work is related to as “ $\delta$ -estimators”.

The  $\delta$ -estimators of worm sampling were first introduced by Gull [Gull, 2008] in the context of CT-INT. The idea is to just consider the contributions to the observable generated by the worm operators themselves, i.e. a single  $\delta$ -like imaginary time bin (or the equivalent Fourier transform) at each measurement step. In the following, the estimators for the one- and two-particle Green's function, the one- and two-particle improved estimator and the asymptotic (i.e. two-particle equal-time) estimators are discussed.

### Green's Function Estimators

*The following paragraph was already published in: P.G., M. Wallerberger, E. Gull, A. Hausoel, G. Sangiovanni and K. Held; Continuous-time quantum Monte Carlo using worm sampling. Phys. Rev. B. 92, 155102 (2015)*

We now show how the measurement of Green's function looks in  $\mathcal{C}_{G^{(n)}}$ . It turns out that the measurement itself is trivial and we only need to find the correct normalization of the Green's functions measured and the correct sign. For the one-particle Green's function  $G^{(1)}$  a worm is defined by the operators  $d(\tau_i)$  and  $d^\dagger(\tau_j)$ . The correct weight is intrinsically given as we sample in the Green's function space  $\mathcal{C}_{G^{(n)}}$ . Thus, the estimator of the Green's function simply follows as:

$$G_{\mathcal{C}_G}^{(1)}(\tau) = \langle \text{sgn} \cdot \delta(\tau, \tau_i - \tau_j) \rangle_{\text{MC}}. \quad (3.57)$$

The Green's function in Matsubara frequencies can be calculated by substituting the  $\delta$ -function by the Fourier transform:

$$G_{\mathcal{C}_G}^{(1)}(i\nu) = \langle \text{sgn} \cdot e^{i\nu(\tau_i - \tau_j)} \rangle_{\text{MC}}. \quad (3.58)$$

The measurement of the two-particle Green's function in Matsubara frequencies in the particle-hole channel<sup>a</sup> is given by:

$$G_{\mathcal{C}_G}^{(2)}(i\nu, i\nu', i\omega) = \langle \text{sgn} \cdot e^{i\nu(\tau_i - \tau_j)} e^{i\nu'(\tau_k - \tau_l)} e^{i\omega(\tau_j - \tau_k)} \rangle_{\text{MC}}. \quad (3.59)$$

While we both employ (3.57) and (3.58) for the one-particle Green's function measurement, the measurement of the two-particle Green's function in Matsubara frequencies, (3.59), is far more convenient than a binned measurement in imaginary time. It is especially difficult to resolve jumps in the imaginary-time measurement due to fermionic sign changes in the time ordering of operators. Measuring the two-particle Green's function in imaginary time using a binning procedure and then applying the Fourier transform

gives wrong high frequency asymptotics, while the direct measurement in Matsubara frequencies is free of errors resulting from binning.

As with conventional sampling, we do not observe any sign-problem for worm sampling in the case of a flavor-diagonal hybridization function. However, unlike in the  $G_{\mathcal{C}_Z}^{(n)}$  estimator, the flavor indices and the imaginary time bins in the worm estimator  $G_{\mathcal{C}_G}^{(n)}$  are outer indices, such that the mean sign in principle also becomes flavor and  $\tau$  dependent.

Eq. (3.57) and Eq. (3.58) are normalized to  $Z_{G^{(1)}}$ , Eq. (3.59) to  $Z_{G^{(2)}}$  as defined in (3.51), as opposed to the physically correct normalization to  $Z$ .

---

<sup>a</sup>The convention for the bosonic Matsubara frequency has been adapted for consistency with other Monte Carlo estimators mentioned in publications referenced in this work.

## Improved Estimators

*The following paragraph was already published in: P. G., M. Wallerberger, T. Ribic, A. Hausoel, G. Sangiovanni and K. Held; Worm-improved estimators in continuous-time quantum Monte Carlo. Phys. Rev. B. 94, 125153 (2016)*

The measurement of observables in worm spaces is trivially determined by recording imaginary time bins during the Monte Carlo sampling ( $\langle \dots \rangle_{\text{MC}}$ ) for a given spin-orbital component and only needs to be corrected in its normalization and sign (sgn), see [Gunnacker et al., 2015] for further technical details:

$$(G\Sigma)_{\mathcal{C}_{(G\Sigma)}}^{(1)}(\tau - \tau') = -\langle \text{sgn}(Uw_{\text{loc}}) \delta(\tau - \tau') \rangle_{\text{MC}}. \quad (3.60)$$

or equivalently in Matsubara frequencies:

$$(G\Sigma)_{\mathcal{C}_{(G\Sigma)}}^{(1)}(i\nu) = \langle \text{sgn}(Uw_{\text{loc}}) e^{i\nu(\tau - \tau')} \rangle_{\text{MC}}. \quad (3.61)$$

Similarly, the two-particle improved estimator in the particle-hole convention is measured as

$$H_{\mathcal{C}_H}^{(2)}(i\nu, i\nu', i\omega) = \langle \text{sgn}(Uw_{\text{loc}}) e^{i\nu(\tau_1 - \tau_2)} e^{i\nu'(\tau_3 - \tau_4)} e^{i\omega(\tau_2 - \tau_3)} \rangle_{\text{MC}}. \quad (3.62)$$

It is important to note that the sign of the configuration now includes an additional sign from the interaction term  $U_{\alpha\beta\gamma\delta}$ , which was introduced to the Metropolis acceptance earlier. We point out that the sign problem of the worm algorithm is identical to the sign problem of the hybridization expansion itself. That is, the average sign in the denominator of the estimators originates from the normalization with respect to the partition function, i.e. being a consequence of the average sign of partition function space.

While Eq. (3.60) may be binned in imaginary time  $\tau$ , and afterwards Fourier transformed to Matsubara frequencies  $i\nu$ , the unbinned Fourier transform in Eq. (3.61) is possible as well. In case of the two-particle quantities a binning procedure becomes much more involved as one needs to generate a grid which further resolves the sign changes due to anti-commuting operators. Thus, employing a nonequispaced fast Fourier transform algorithm [Keiner et al., 2009] in Eq. (3.62) is preferable.

## Asymptotic Estimators

The following paragraph was already published in: J. Kaufmann, P.G and K. Held; Continuous-time quantum Monte Carlo calculation of multi-orbital vertex asymptotics. Phys. Rev. B. 96, 035114 (2017)

In the following the Monte Carlo estimators for the high-frequency asymptotics of the two-particle vertex function  $F$  are defined. The actual construction of the vertex function  $F$  from these observables is discussed in Chapter 5.2.

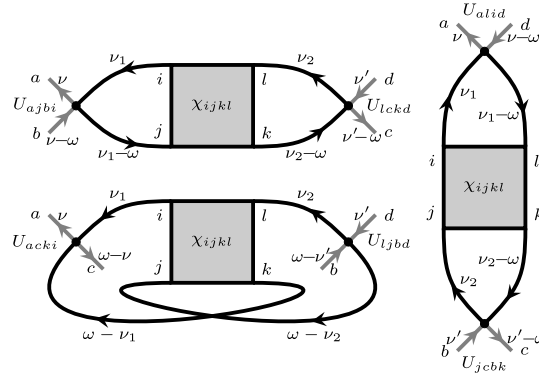


Figure 3.8: Vertex diagrams that depend on only one bosonic frequency, in  $ph$ -channel (top left),  $\overline{ph}$ -channel (right) and  $pp$ -channel (bottom left). Frequencies are given in the channel-specific notation.

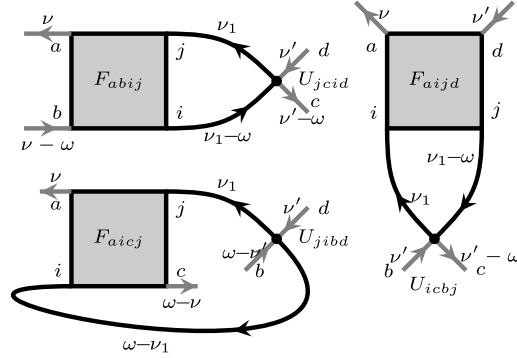


Figure 3.9: Vertex diagrams that depend on one bosonic and one fermionic frequency.

Considering the full Green's function  $G_{ijkl}(\tau_1, \tau_2, \tau_3, \tau_4)$ , we need to form two equal-time pairs for the diagrams of Figure 3.8 to arrive at a function of two time arguments or

one frequency-difference. There are three distinct ways to achieve this:

$$\tau_1 = \tau_2 \equiv \tau, \quad \tau_3 = \tau_4 \equiv \tau' \quad (3.63)$$

$$\tau_1 = \tau_3 \equiv \tau, \quad \tau_2 = \tau_4 \equiv \tau' \quad (3.64)$$

$$\tau_1 = \tau_4 \equiv \tau, \quad \tau_2 = \tau_3 \equiv \tau' \quad (3.65)$$

which relate to the  $ph$ ,  $pp$  and  $\overline{ph}$  channel. The “two-legged” two-particle Green’s function for the  $ph$ -channel is

$$G_{ijkl}^{ph, \nu_1 - \nu_2} = \int d\tau d\tau' e^{i(\nu_1 - \nu_2)(\tau - \tau')} \langle T_\tau d_i(\tau) d_j^\dagger(\tau) d_k(\tau') d_l^\dagger(\tau') \rangle, \quad (3.66)$$

and for the  $pp$ -channel, we get

$$G_{ijkl}^{pp, \nu_1 + \nu_3} = \int d\tau d\tau' e^{i(\nu_1 + \nu_3)(\tau - \tau')} \langle T_\tau d_i(\tau) d_j^\dagger(\tau') d_k(\tau) d_l^\dagger(\tau') \rangle. \quad (3.67)$$

While the above functions have to be measured separately, the third, related to the  $\overline{ph}$ -channel, can be obtained from the first by the crossing relation (see [Galler et al., 2017] for an illustration)

$$G_{ijkl}^{\overline{ph}} = -G_{ilkj}^{ph} \quad (3.68)$$

and depends on the frequency difference  $\nu_1 - \nu_4$ .

From the six ways to form one equal-time pair as needed for the diagrams Figure 3.8, it is sufficient to consider only the following three, with the others related by time-reversal symmetry:

$$\tau_1 \equiv \tau, \quad \tau_2 \equiv \tau', \quad \tau_3 = \tau_4 \equiv \tau'', \quad (3.69)$$

$$\tau_1 \equiv \tau, \quad \tau_3 \equiv \tau', \quad \tau_2 = \tau_4 \equiv \tau'', \quad (3.70)$$

$$\tau_1 \equiv \tau, \quad \tau_4 \equiv \tau', \quad \tau_2 = \tau_3 \equiv \tau''. \quad (3.71)$$

Here, Eqs. (3.69)-(3.71) are related, as before, to the  $ph$ ,  $pp$  and  $\overline{ph}$  channel. The “three-legged” two-particle Green’s function in the  $ph$ -channel corresponding to Eq. (3.69) follows as

$$G_{ijkl}^{ph, \nu_1, \nu_1 - \nu_2} = \int d\tau d\tau' d\tau'' e^{i(\nu_1(\tau - \tau') + (\nu_1 - \nu_2)(\tau' - \tau''))} \times \langle T_\tau d_i(\tau) d_j^\dagger(\tau') d_k(\tau'') d_l^\dagger(\tau'') \rangle, \quad (3.72)$$

and in the  $pp$ -channel (Eq. (3.70)) it is

$$G_{ijkl}^{pp, \nu_1, \nu_1 + \nu_3} = \int d\tau d\tau' d\tau'' e^{i(\nu_1(\tau - \tau') + (\nu_1 + \nu_3)(\tau' - \tau''))} \times \langle T_\tau d_i(\tau) d_j^\dagger(\tau'') d_k(\tau') d_l^\dagger(\tau'') \rangle. \quad (3.73)$$

Again, the Green’s function in the  $\overline{ph}$ -channel can be obtained by the crossing relation, the frequency arguments are then  $\nu_1$  and  $\nu_1 - \nu_4$ . Please note that  $\nu_1 - \nu_2$ ,  $\nu_1 + \nu_3$  and  $\nu_1 - \nu_4$  are referred to as the channel-specific bosonic Matsubara frequencies  $\omega_{ph}$ ,  $\omega_{pp}$  and  $\omega_{\overline{ph}}$ , respectively.

We redefine the single-frequency expectation values in Eqs. (3.66)-(3.67) in terms of worm estimators:

$$G_{\mathcal{C}_{1,\ell}}^{\ell,\omega} = \langle \text{sgn} \times e^{i\omega(\tau-\tau')} \rangle_{MC}, \quad (3.74)$$

where  $\mathcal{C}_{1,\ell}$  are the configuration spaces of the particle-hole and particle-particle single-frequency estimator and ‘sgn’ denotes the sign of the configuration. Further, the two-frequency expectation values in Eqs. (3.72)-(3.73) follow as:

$$G_{\mathcal{C}_{2,\ell}}^{\ell,\nu\omega} = \langle \text{sgn} \times e^{i(\nu(\tau-\tau')+\omega(\tau'-\tau''))} \rangle_{MC}, \quad (3.75)$$

where  $\mathcal{C}_{2,\ell}$  are the configuration spaces of the particle-hole and particle-particle two-frequency estimator. We emphasize that the measured quantities still need to be normalized with respect to the partition function.

### 3.3.6 Full Estimators

The full estimators were introduced by Shinaoka *et al.* [Shinaoka et al., 2017a] for worm sampling in combination with off-diagonal or complex hybridization functions. While  $\delta$ -estimators in worm sampling just consider the explicit worm operators themselves and thus a single imaginary time bin for a given observable (see e.g. Eq. (3.57)), the conventional hybridization estimators consider all operators present in the trace by generating determinant ratios for all elements in the hybridization matrix of the perturbation expansion (see e.g. Eq. (3.29)). This behavior can be mimicked by worm estimators and is here related to as “full estimators”. By evaluating the contributions of several operator pairs for a given configuration, parameter regions become accessible where the expansion order of the algorithm becomes large (i.e. low temperature or weak interactions). This concept is further described in the following.

As discussed in Section 3.3.4, a given worm configuration may be re-casted into another worm configuration with replacement steps, that is, by detaching all hybridization lines of a creation (annihilation) operator of the perturbation expansion and attaching them to a creation (annihilation) worm operator. While the local trace of the problem remains the same, the determinant of the hybridization matrix (i.e. the bath trace) needs to be re-evaluated. The idea of the full-estimators is to include all locally identical traces with different hybridization matrices in a single measurement step, effectively reconstructing the conventional hybridization estimator. Essentially, this amounts to initiating virtual replacement steps (i.e. Monte Carlo steps manipulating the configuration during the measurement, which are reverted to obtain the configuration prior to the measurement) to generate the different weights. The procedure is illustrated in Figure 3.10.

Having motivated the full estimators, the remaining step is to formally define them as Monte Carlo estimators. For the one-particle Green’s function, the worm creation operator can be exchanged with the remaining  $k/2$  creation operators connected to hybridization lines. Additionally, the worm annihilation operator can be exchanged with the remaining  $k/2$  annihilation operators connected to hybridization lines.<sup>16</sup> Thus, the full estimator

<sup>16</sup>For diagonal hybridization functions, the worm creation/annihilation operator is only exchanged with the creation/annihilation operators with hybridization lines of the same flavor.



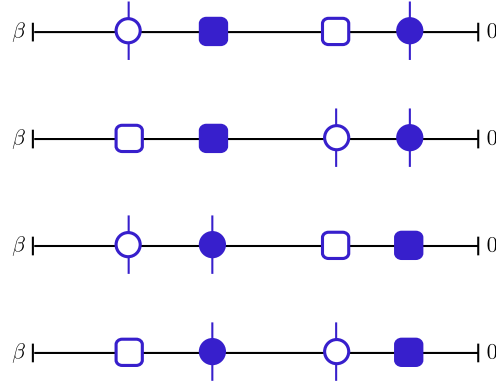


Figure 3.10: Illustration of four different random configurations including a pair of worm operators (rectangles) and a pair of hybridization operators (circles with vertical lines), i.e. operators with hybridization lines attached. In terms of the local trace, all four configurations are equivalent. In terms of the hybridization matrix all four configurations are different. By exchanging hybridization lines (i.e. using virtual replacement steps) each configuration can be casted into all of the other configurations. This scheme is referred to as “full estimators”.

for the one-particle Green’s function scales with  $(k/2)^2$ , identical to the scaling of the hybridization estimator.

Formally, the expectation value of the observable  $A$  expressed as a weighted average over  $N$  configurations follows as

$$\langle A \rangle = \left\langle \frac{\sum_{\kappa}^N w_{\kappa} A_{\kappa}}{\sum_{\kappa}^N w_{\kappa}} \right\rangle_{\text{MC}}, \quad (3.76)$$

where  $w_{\kappa}$  is the weight of the configuration  $\kappa \in \{1, \dots, N\}$  and  $A_{\kappa}$  is the observable evaluated for configuration  $\kappa$ . In order to apply the weighted average to worm sampling, it is necessary to define the weights as they appear in worm sampling

$$w^{ij} = w_{\text{loc}}^{ij} w_{\text{bath}}^{ij}, \quad (3.77)$$

where  $i, j \in \{0, \dots, k/2\}$  is the index denoting the position of the worm creation/annihilation operator and  $k/2$  is the number of creation and annihilation operators with hybridization lines. Further  $w^{00}$  is the initial worm configuration, from which the measurement procedure is initiated. As all further weights need to be considered with respect to this initial weight, the formal weight  $w_{\kappa}$  introduced in Eq. (3.76) is actually a ratio of weights  $w^{ij}/w^{00}$ . The worm sign including sorting the worm to the front of the configuration and the conventional operator sorting, is given by  $\text{sgn}^{00}$  for the base configuration and  $\text{sgn}^{ij}$  for the altered configurations. With this, the weighted average of the one-particle Green’s function in worm sampling becomes:

$$G_{ab} = \left\langle \frac{\sum_{ij}^{k/2} \text{sgn}^{ij} \text{sgn}^{00} (w_{\text{bath}}^{ij}/w_{\text{bath}}^{00}) \delta_{ai} \delta_{bj}}{\sum_{ij}^{k/2} |w_{\text{bath}}^{ij}| / |w_{\text{bath}}^{00}|} \right\rangle_{\text{MC}}. \quad (3.78)$$

The ratio of weights reduces to the ratio of bath weights, as the local weight is not altered by the virtual worm replacement steps. By further expressing the ratio of bath weights as the ratio of determinants of the hybridization matrix, the similarities to the Green's function estimator defined in Eq. (3.29) become apparent.

This observation further suggests a conceptually different interpretation of the full estimators: instead of considering virtual replacement steps for generating various worm contributions, one may choose to connect the worm operators to all remaining operators in the trace using hybridization lines. Essentially, this generates a hybridization matrix of dimension  $(k/2 + 1)$  for the one-particle Green's function and  $(k/2 + 2)$  for the two-particle Green's function. This extended hybridization matrix is constructed only for the measurement procedure, but becomes irrelevant during the sampling procedure. Further, the extended hybridization matrix may be interpreted as a worm bath, which extends the physical bath of the AIM. By inheriting the properties of the worm operators, such as the off-diagonal structure of the two-particle worm, the worm bath has a different structure than the physical bath.

Similar to the one-particle Green's function estimator of traditional CT-HYB, one can generate determinant ratios by reading off the elements of the extended inverse hybridization matrix  $M_{ji}$ . For the two-particle Green's function estimator, one generate determinant ratios by calculating the determinant of two-by-two sub-matrices of  $M_{ji}$ . Computationally, generating an extended inverse matrix  $M_{ji}$  and reformulating the full estimators in terms of the traditional estimators of CT-HYB is more feasible than calculating virtual replacement steps individually. The technicalities of this interpretation are equivalent to the original formulation by Shinaoka *et al.* [Shinaoka et al., 2017a].

Nevertheless, it is important to stress the differences between the full estimator of worm sampling and the conventional hybridization estimators, which follow from the fact that the base configuration of the hybridization estimator is a configuration of the partition function space, as opposed to the base configuration of the worm full estimator being a configuration of worm space.

- While the measurement in partition function space is conducted simply by reading off the values of  $M_{ji}$ , in worm space one either first needs to construct the extended hybridization matrix with the worm operators connected to all other operators, which is then inverted to generate similar matrix elements or, generate all possible worm configurations by applying virtual replacement moves consecutively.
- Although the hybridization estimator and the full estimator of worm sampling consider configurations in a similar manner, the full estimator still profits from the advantages of worm sampling itself. That is, diagrams belonging to the observable series expansion, however, not being part of the partition function series expansion can be measured. These include (but are not limited to) the equal-time diagrams of the improved estimators and the spin-flip and pair-hopping diagrams of the two-particle Green's function for non-density-density interactions. A special case are measurements close to or in the atomic limit, where no hybridization operators are present. While the conventional hybridization estimators fail under these circumstances, any full-estimator simplifies to its  $\delta$ -estimator, i.e. only the imaginary time bin or Matsubara equivalent of the worm operators is recorded.

In principle, any full estimator may be defined for all of the  $\delta$ -estimators of worm sampling, that is for the Green's function estimators, the improved estimators and the asymptotic estimators. The full estimators depend on the number of possible imaginary time bins  $N_\tau$  obtainable through virtual replacements or obtainable from the extended hybridization matrix. Each operator that can be replaced with operators of the perturbation series generates  $(k/2 + 1)$  imaginary time bins (the factor 1 is the initial worm contribution). For flavor diagonal hybridization,  $(k/2)$  reduces to the number of operators with the same flavor  $k_{\text{flav}}/2$ . Further, the equal time two- and three-tuples present in improved- and asymptotic estimators cannot be considered in the extended hybridization matrix or by virtual replacement steps. This is because the probability for such equal time tuples to exist in the series expansion of the partition function is essentially zero. Thus, one cannot exchange the equal time worm operators with hybridization operators. This effectively reduces the complexity of the full estimator corresponding to the improved and asymptotic estimators. Of all observables discussed in this work, the full estimator for the two-particle Green's function has the highest number of possible exchanges with  $(k/2 + 1)^4$ .<sup>17</sup> On the other hand, the full estimator of the asymptotic two-particle Green's function with two equal time pairs, simplifies to a  $\delta$ -estimator, as no exchanges are possible without breaking the equal time condition. A detailed list of all estimators and the corresponding scaling in imaginary time and Matsubara frequencies is given in Table 3.3.

Conceptually the full estimators and the  $\delta$ -estimators result in comparable estimates, when considering the measurement- and sampling procedure together. However, empirically, the full estimators outperform the  $\delta$ -estimators in terms of efficiency. The full estimator offsets the computational burden of the sampling procedure to the measurement. While computationally the latter can be treated more efficiently, the autocorrelation length of the full estimator increases with respect to the  $\delta$ -estimator (see Section 3.3.9).

### 3.3.7 Normalization

Although the  $\delta$ - and full estimators scale differently depending on the expansion order of the series expansion, all worm estimators are normalized to their integrated partition function (3.51), while they are to be normalized with respect to the actual partition function  $Z$ .

In principle we are ergodic in  $\mathcal{C}_{G^{(n)}}$ , when assuming worm replacement or worm shift moves. It turns out however that we need to sample both in  $\mathcal{C}_{G^{(n)}}$  and  $\mathcal{C}_Z$  with about the same number of steps to fix the normalization  $\frac{1}{Z}$  of the thermal expectation value.

When measuring the Green's functions in  $\mathcal{C}_{G^{(n)}}$  we implicitly normalize with the number of steps taken in  $\mathcal{C}_{G^{(n)}}$ . We correct for this factor by explicitly counting how many steps  $N_G$  were taken in  $\mathcal{C}_{G^{(n)}}$ . We further count how many steps  $N_Z$  were taken in  $\mathcal{C}_Z$ . This

---

<sup>17</sup>By formulating the full estimator in terms of an extended hybridization matrix, the two-particle measurement can be written similar to the two-particle measurement of traditional CT-HYB. For low-temperatures it is useful to Fourier transform the matrix-elements  $M_{ji}$  with the corresponding  $\delta$ -functions encoding the time differences and then assemble the resulting "bath propagators" in Matsubara space. This reduces the effective scaling of the estimator from  $\mathcal{O}((k/2)^4)$  to  $\mathcal{O}((k/2)^3)$ . For more details see Section 3.2.2.

Observable / Worm estimator	Imaginary time scaling $\mathcal{O}(N_\tau)$ ( $\delta$ , full)	Matsubara scaling $\mathcal{O}(N_f^d \log(N_f) + N_\tau)$ ( $\delta$ , full)
one-particle Green's function	$N_\tau = 1$ $N_\tau = (k/2 + 1)^2$	$N_\tau = 1, d = 1$ $N_\tau = (k/2 + 1)^2, d = 1$
one-particle improved estimator	$N_\tau = 1$ $N_\tau = (k/2 + 1)$	$N_\tau = 1, d = 1$ $N_\tau = (k/2 + 1), d = 1$
two-particle improved estimator	$N_\tau = 1$ $N_\tau = (k/2 + 1)^3$	$N_\tau = 1, d = 3$ $N_\tau = (k/2 + 1)^3, d = 3$
two-legged two-particle Green's function (asympt.)	$N_\tau = 1$ $N_\tau = 1$	$N_\tau = 1, d = 1$ $N_\tau = 1, d = 1$
three-legged two-particle Green's function (asympt.)	$N_\tau = 1$ $N_\tau = (k/2 + 1)^2$	$N_\tau = 1, d = 2$ $N_\tau = (k/2 + 1)^2, d = 2$
two-particle Green's function	$N_\tau = 1$ $N_\tau = (k/2 + 1)^4$	$N_\tau = 1, d = 3$ $N_\tau = (k/2 + 1)^4, d = 3$

Table 3.3: Formal scaling of various worm estimators represented as  $\delta$ -estimators and full estimators in imaginary time and Matsubara representation. The latter is assumed to follow a NFFT, with the formal scaling  $\mathcal{O}(N_f^d \log(N_f) + N_\tau)$ , where  $N_\tau$  is the number of imaginary time bins and  $N_f$  the number of frequencies in each direction (omitting an additional prefactor  $\log(1/\epsilon)$  to the number of imaginary time bins, where  $\epsilon$  is the desired accuracy). For multi-dimensional NFFT calls, a hyper-cubic box is assumed (i.e. in case of the two-particle Green's function, the number of fermionic and bosonic frequencies agrees). A detailed discussion of NFFT in the context of CT-HYB is found elsewhere [Kaufmann, 2015].

estimates the size of the configuration space  $\mathcal{C}_Z$ , which then gives the correct normalization. The normalization for  $G^{(n)}$  is then given by Gull *et al.* [Gull et al., 2010]

$$G^{(n)} = \frac{1}{\eta^{(n)}} \frac{N_G}{N_Z} G_{\mathcal{C}_G}^{(n)}, \quad (3.79)$$

where  $G_{\mathcal{C}_G}^{(n)}$  is measured in  $\mathcal{C}_{G^{(n)}}$  and the factor  $1/\eta^{(n)}$  is a result of rescaling  $Z_{G^{(n)}}$  in Eq. (3.52).

Let us note that Eq. (3.79) is only one way of normalizing the worm measurement. In a different approach, we could do the entire sampling in worm space, without removing the worm operators at all. We are then required to generate worm configurations by shift moves and replacement moves. In this case, we could normalize the result by assuming some physical knowledge of the Green's function. One possibility is to extract the normalization by assuming the correct behavior of the large-frequency asymptotics of  $G^{(1)}(i\nu)$  or  $G^{(2)}(i\nu, i\nu', i\omega)$ .

In order to calculate the Monte Carlo expectation value Eq. (3.58), we still need to divide by the number of measurements  $N$  taken. It is important to note the difference between the number of measurements  $N$  and the number of steps  $N_G$  and  $N_Z$  taken since it is common to skip steps during two consecutive measurements to assure uncorrelated measurements. This directly relates to the auto-correlation length of the QMC sampling.

### 3.3.8 Component Sampling

The relative phase space volume of the worm space  $\mathcal{C}_W$  and the partition function space  $\mathcal{C}_Z$  is controlled by the balancing factor  $\eta$  (see (3.52)). For observables with a series expansion that is comparable to the partition function series expansion, the balancing factor is approximately one. For series expansions with little overlap, the balancing factor deviates from unity.<sup>18</sup> Up to this point, the actual type of worm space has been determined only in terms of number and imaginary time structure of the worm operators being inserted, while the flavor dependence has been ignored. As a result, the balancing factor  $\eta$  was also considered to be flavor independent.<sup>19</sup> This may turn out to be a severe issue, when considering systems with flavor-dependent hybridization functions, flavor-dependent interaction matrices or crystal field splittings. A straight-forward solution to this problem is to consider the balancing factor to be flavor dependent in a similar manner. This can be achieved in two ways. First, by indexing  $\eta$ , generating a flavor-dependent tensor. In this scenario, the random proposal of worm-operator-inserts determines which element of the  $\eta$ -tensor is accessed. Secondly, the flavor dependence of the observable may be considered as a set of external degrees of freedom. Then, the entire worm sampling procedure may be carried out by only proposing worm-operator-inserts for a given flavor at once. This

<sup>18</sup>An example are observables with large time differences at strong coupling. Such observables do not typically emerge in the partition function expansion in strong coupling.

<sup>19</sup>In principle the balancing factor  $\eta$  has additional dependencies on system properties, such as the inverse temperature or the number of orbitals. However, these dependencies are implicitly accounted for by determining an optimal  $\eta$  at the beginning of the sampling process (either by root finding or Wang Landau sampling), such that the number of steps in worm space are comparable to the number of steps in partition function space.

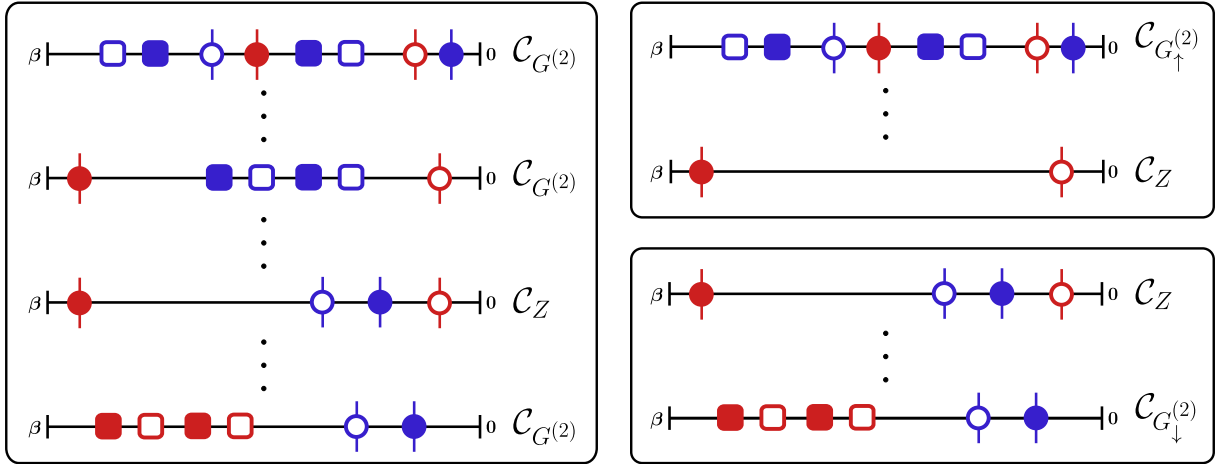


Figure 3.11: Component sampling of the two-particle Green's function of the Anderson impurity model. Left: selected random configurations of worm- and partition function configuration space for the two-particle Green's function. Two different components are sampled simultaneously. Right: selected random configurations of flavor-dependent worm- and partition function configuration space for the two-particle Green's function. The two components are sampled separately. Filled/empty squares (circles) illustrate worm (hybridization) creation/annihilation operators for spin-up (blue) and spin-down (red).

approach will be referred to as component sampling. The procedure for the Anderson impurity model is illustrated in Figure 3.11

In the following, the behavior of the balancing factor in the Falicov-Kimball model with respect to temperature is discussed. The Falicov-Kimball model breaks the  $SU(2)$ -symmetry by assuming one spin of electrons to be itinerant, while the other spin is fixed (i.e. atomic limit-like). Although the Falicov-Kimball model shows no explicit temperature dependence in the Matsubara frequency self-energy and Green's functions, for relatively low temperatures the balancing factor  $\eta$  becomes strongly flavor dependent. The  $fc$ -components (i.e. mixed components) of the two-particle Green's function have a smaller phase space volume than the fixed  $ff$ -components (see Figure 3.12 right). The  $cc$ -components (i.e. the itinerant component) becomes prohibitively small. For moderate to high temperatures the flavor dependency of  $\eta$  vanishes (see Figure 3.12 left). With respect to the partition function, the observable series expansion shares a large overlap with the series expansion in  $Z$  in case of the fixed electrons, but very little overlap in case of the itinerant spins. Assuming a flavor-independent balancing factor  $\eta$ , worm operators are predominantly inserted for fixed spins, but with a much lower probability for itinerant spins. This is because the acceptance rate for inserts of  $f$ -operators into an otherwise empty (sub-) trace is relatively high, while the acceptance rate for inserts of  $c$ -operators is significantly suppressed by a number of additional  $c$ -operators resulting from the perturbation expansion itself. In severe cases, a flavor-independent balancing factor may practically, although not formally, violate ergodicity.

The implications of component sampling are directly visible in the measured compo-

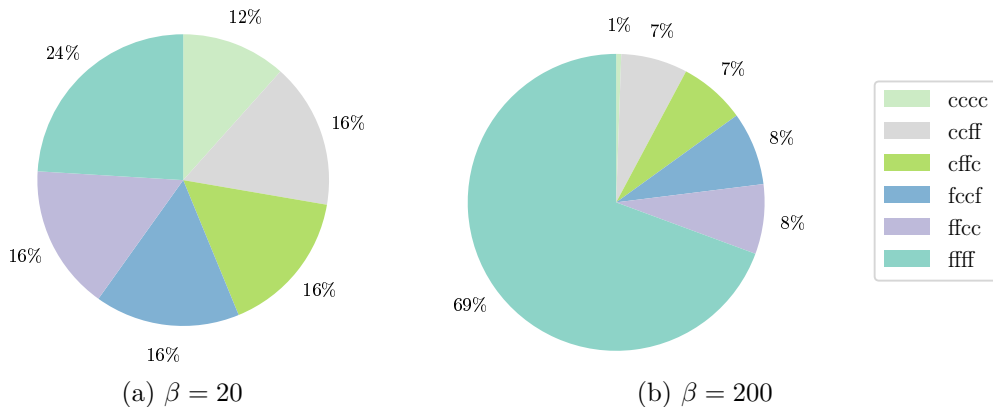


Figure 3.12: Relative phase space volumes (extracted as the inverse of  $\eta$  after balancing) of component-resolved worm spaces of the two-particle Green’s function for the two-dimensional Falicov-Kimball model in the resonant level model ( $D \equiv 1, U = 1$ ) at temperatures (a)  $\beta = 20$  and (b)  $\beta = 200$  and an  $f$ -electron occupation of  $p = 0.25$ . To fix the occupation, for  $\beta = 20$  this results in an  $f$ -electron energy level of  $\epsilon_f = -0.038114$  and for  $\beta = 200$  an energy level of  $\epsilon_f = -0.086125$  in accordance to Falicov-Kimball calculations in [Gunacker et al., 2016]. The spin-up electrons are associated with the itinerant  $c$ -electrons and the spin-down electrons with the fixed  $f$ -electrons.

nents of the two-particle Green’s function. For the Falicov-Kimball model at  $\beta = 200$  this is illustrated in Figure 3.13, where a flavor-independent balancing factor was set such that total number of steps in all worm spaces combined is similar to the total number of steps in partition function space. The phase space volume of the  $cc$ -component is smaller than the phase space volume of the partition function space. The unbalanced algorithm spends about a factor five more steps in partition function space than in worm space (not shown). One can observe in Figure 3.13 (left) the balancing factor in principle reproduces the correct shape relative to the component-wise balancing factor, however, the normalization is off. For all different  $fc$ -components related by crossing symmetry, the algorithm spends approximately four times as much time/steps in the corresponding worm spaces (not shown). Only slight differences in Figure 3.13 (middle) are visible. The phase space volume of the  $ff$ -component is larger than the phase space volume of the partition function space. The algorithm spends almost all of its time in worm space (not shown). In Figure 3.13 (right) one can observe larger error fluctuations relative to a balanced measurement.

While one may consider the Falicov-Kimball model of academic use only, the balancing issues discussed above also occur in systems with higher symmetry. More specifically, the balancing factor may inherit additional constraints from the imaginary time structure of the estimator. The balancing factor of individual components of the equal-time estimators of the two-particle Green’s function (improved estimators and asymptotic estimators) may look very different. While for some components of these estimators the equal-time pairs form actual density pairs, for other components of the same estimator, the equal-time pairs form finite-time “segments” with additional operators in the trace. Intuitively this

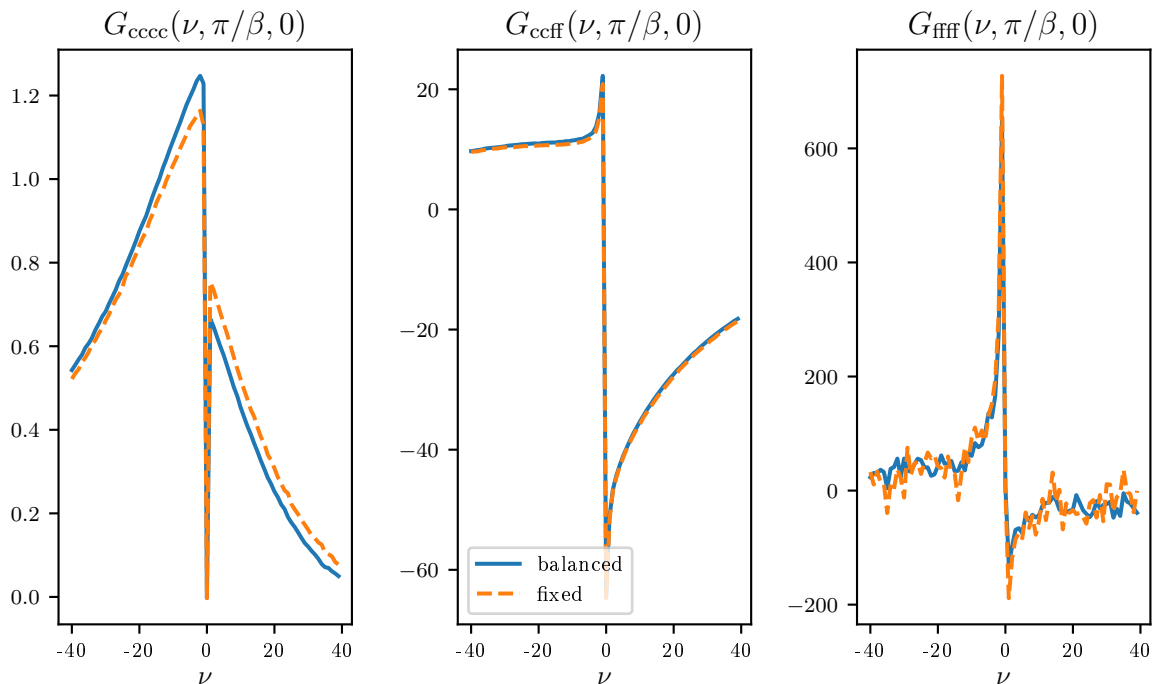


Figure 3.13: Two-particle Green's function of the Falicov-Kimball model with parameters chosen according to Figure 3.12, at  $\beta = 200$  for frequency slices  $(\nu, \pi/\beta, 0)$ . Blue lines relate to component-wise balancing of worm spaces with the partition function space. Orange lines relate to an flavor-independent balancing, where the total number in all worm spaces is similar to the total number of steps in partition function space. The number of measurements was kept constant for the two runs with different balancing factor  $\eta$ . However, measurements are triggered independent of the current configuration space (i.e. worm or partition). If the algorithm spends most of its time in partition function/worm space, most measurements are conducted for partition function/worm estimators and less for worm/partition function estimators.



leads to large variations in the component-wise balancing factor.

Besides the advantages of a more balanced sampling procedure with respect to all components, component sampling is further appealing for computational reasons:

- A component-wise sampling procedure allows one to selectively sample components of an observable, which are of interest. The remaining components may simply be ignored. This results in a more efficient (i.e. faster and more storage efficient) sampling process.
- The flavor dependence of observables is not part of the Monte Carlo procedure itself. Thus, arrays storing the estimators have reduced dimensionality (i.e. more memory efficiency). According to relation (3.40) the two-particle Green's function in the e.g. five-orbital case already has 390 non-vanishing components. This prefactor to the three-dimensional Matsubara arrays results in severe memory restrictions without component sampling.

### 3.3.9 Autocorrelation

*The results of this section (marked by a vertical sidebar) have been obtained in the project work of: P. Heistracher. Autocorrelation measurements in continuous time quantum Monte Carlo simulations (2016), supervised by P.G. and K. Held*

Due to the high dimensionality of the configuration space of the diagrammatic series expansion of the partition function or, in the case of worm sampling, a given observable, the Metropolis Hastings algorithm for Monte Carlo is employed. The underlying method of importance sampling significantly reduces the variance of the Monte Carlo estimate by generating configurations along a Markov chain. Consequently, two random configurations  $i$  and  $j$  of the Markov chain are no longer uncorrelated but rather correlated, where the strength of correlation depends on the number of Monte Carlo steps in between the two configurations. The standard error of the Monte Carlo expectation value for the observable  $A$  then becomes<sup>20</sup>

$$\sigma_A = \sqrt{\frac{\text{Var}(A)}{N}(1 + 2\tau_A)}, \quad (3.80)$$

where  $\tau_A$  is the autocorrelation length defined as

$$\tau_A = \frac{\sum_{t=1}^{\infty} \left( \langle A_1 A_{1+t} \rangle - \langle A \rangle^2 \right)}{\text{Var}(A)}. \quad (3.81)$$

The usual  $1/\sqrt{N}$  scaling of the error is modified by a factor  $\sqrt{(1 + 2\tau_A)}$ . This result is derived in Appendix E.1. In practice one attempts to estimate or calculate  $\tau_A$  beforehand and introduce  $\tau_A$  Monte Carlo steps in between two measurements of the observable to

<sup>20</sup>For a pedagogical introduction to autocorrelation lengths in Monte Carlo see e.g. [Ambegaokar and Troyer, 2010].

assure uncorrelated measurements.<sup>21</sup> By first determining  $\tau_A$ , the number of uncorrelated measurements conducted during the entire sampling procedure is maximized for the given computational resources.

### Numerical considerations

An individual term in relation (3.81) for any given configuration  $A_i$  is often referred to as the autocorrelation function

$$C_A(t) = \frac{\left(\langle A_i A_{i+t} \rangle - \langle A_i \rangle^2\right)}{\langle A_i^2 \rangle - \langle A_i \rangle^2}. \quad (3.82)$$

Equivalently, in the continuous case, where  $\Delta t \rightarrow dt$ , the integral of the autocorrelation function over the infinitesimal length  $dt$  returns the autocorrelation length. The continuous autocorrelation function formally consists of a linear combination of exponentially decaying functions, while generally a single contribution dominates.<sup>22</sup>

In practice, the autocorrelation length is extracted by either integrating the discrete autocorrelation function or by fitting an exponential function. Deviations between the two methods originate from the assumption of the autocorrelation function being constructed of a single exponential function in the latter case, or from not considering the autocorrelation function on a large enough grid, i.e. integrating an autocorrelation function not decaying sufficiently. For a more detailed discussion about autocorrelation and fast algorithms the reader is referred to [Sandvik, 2014].

### Green's functions estimators

In principle it is necessary to determine the autocorrelation length for all degrees of freedom for a given observable. In the following the autocorrelation length of the one-particle Green's function is investigated to analyze the differences between partition function estimators and worm estimators. Figure 3.14 shows the autocorrelation length for the one-particle Green's function estimators for the Bethe lattice averaged over all imaginary time bins. The  $\delta$ -estimator of worm sampling behaves opposite to the partition function estimator: for low interaction values, the  $\delta$ -estimator displays small autocorrelation lengths, whereas the partition function estimator displays larger lengths. Inversely, for large interaction values the  $\delta$ -estimator displays larger autocorrelation lengths, whereas the partition function estimator displays smaller lengths. This is a direct consequence of the  $\delta$ -estimator representing a given imaginary time bin by a single configuration, which is modified upon replacement or reinsertion of a given worm, while the partition function estimator depends on all hybridization operators in the trace, thus displaying larger autocorrelation lengths for higher expansion orders (i.e. small values of interaction  $U$  or low temperatures  $1/\beta$ ). In the strong coupling limit (but not the atomic limit in itself), the

<sup>21</sup>Sometimes the estimated number of steps for two configurations to be uncorrelated is referred to as "sweep". This terminology originated from the Ising model, where the autocorrelation length is estimated by the number of lattice sites  $N$ , such that  $N$  Monte Carlo steps on average "sweep" the entire lattice.

<sup>22</sup>The exponential decay allows for truncating the infinite sum  $t \in [1, \infty)$  to finite order.

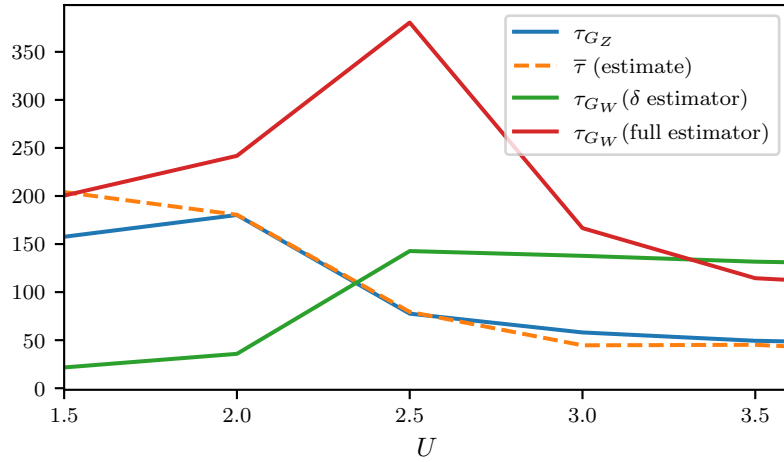


Figure 3.14: Autocorrelation length of the one-particle Green’s function estimator in worm sampling for the Bethe lattice at  $\beta = 40$  and half-bandwidth  $D = 1$  for different values of interaction  $U$ .  $\tau_{G_Z}$  refers to the auto-correlation length in the partition function space  $Z$  in the presence of an additional worm space. Here,  $\bar{\tau}$  refers to the autocorrelation estimate introduced in relation (3.83), normalized to the auto-correlation length  $\tau_{G_Z}$  at  $U = 2$  to account for any additional multiplicative factors. In worm space,  $\tau_{G_W}$  is measured for  $\delta$ -estimators and full estimators. Around  $U = 2.5$ , within the coexistence region of the Mott metal-to-insulator transition the autocorrelation length changes its behavior for all estimators.

partition function estimator outperforms the  $\delta$ -estimator in terms of the autocorrelation length. The full estimator of worm sampling, on the other hand, behaves similar to the partition function estimator, as it takes all operators into account in a similar fashion. Only in the coexistence region of the Mott metal-to-insulator transition, the behavior of the correlation length of the full estimator deviates from the partition function estimator. This results from stable worm configurations, where the autocorrelation length increases due to actual replacement steps compensating virtual replacement steps of the estimator.

Although quantitative differences in the autocorrelation lengths of  $\delta$ -estimators and full estimators in worm sampling formally compensate different scalings of the estimators with the interaction strength  $U$  and the inverse temperature  $\beta$ , empirically it has been observed that the full estimators outperform the  $\delta$ -estimators for high expansion orders. The fact that the full estimator of worm sampling and partition function (Green’s function-like) estimators take all operators into account, adds to the efficiency of these estimators by shifting the computational burden from the sampling towards the measurement procedure.

Due to the similarity between full estimators and partition function estimators, in the following section certain approximations of the autocorrelation length of partition function estimators with respect to the interaction strength  $U$  and the inverse temperature  $\beta$  are examined in more detail.

### Estimates for the Autocorrelation Length

Intuitively, the autocorrelation length refers to the number of Monte Carlo steps necessary to separate two configurations, making them uncorrelated (i.e. independent) from one another. This can be interpreted as a global property of the Markov chain, independent of the type of measurement conducted for individual random configurations. Nevertheless, the autocorrelation length in Eq.(3.81) is defined with respect to the observable  $A$ . While in worm sampling, the Markov chain implicitly follows the structure of the observable expansion, this is not the case in partition function sampling. A priori, there is no reason for the series expansion of the partition function to have any similarity to the series expansion of the observable.

Historically, approximations to the autocorrelation length in partition function sampling were thus independent of the observable under consideration. By investigating the scaling behavior of the expansion order with the inverse temperature  $\beta$  and the interaction  $U$  in CT-HYB, the autocorrelation length may be estimated by a trace renewal rate [Gull et al., 2007]

$$\bar{\tau} = \frac{\langle k/2 \rangle}{r_{\text{rem},Z}}, \quad (3.83)$$

where  $\langle k/2 \rangle$  is the average expansion order (i.e. the number of operator pairs connected with hybridization lines in the local trace) and  $r_{\text{rem},Z}$  is the acceptance rate for removing a pair of operators in partition function space. Thus, the above ratio estimates the number of Monte Carlo steps necessary in order to exchange on average all operator pairs of a given configuration.<sup>23</sup> Figure 3.14 shows the autocorrelation estimate  $\bar{\tau}$  in comparison to the autocorrelation length  $\tau_{G_Z}$ . By normalizing the estimate  $\bar{\tau}$  to the actual autocorrelation length in order to account for multiplicative factors, one can observe a good qualitative agreement of the estimate with the calculated result for different values of interaction  $U$ .

---

<sup>23</sup>The above estimate needs to be further modified by the inverse frequency for removal steps to occur, that is assuming  $N$  removal steps are necessary to remove all operators of a given configuration, the autocorrelation length estimate relates to the number of removal steps times the inverse frequency of removal steps occurring during sampling. Further, one assumes  $r_{\text{rem},Z} \sim r_{\text{ins},Z}$ , i.e. the acceptance rate for removing an operator pair is similar to the acceptance rate of inserting an operator pair, such that the new uncorrelated configuration has a comparable number of operators to the number of operators of the original configuration. In practice, any multiplicative factors to the to the acceptance rates (and hence the autocorrelation length estimate) can be discarded by normalizing the autocorrelation estimate to the calculated autocorrelation length for a given set of parameters.

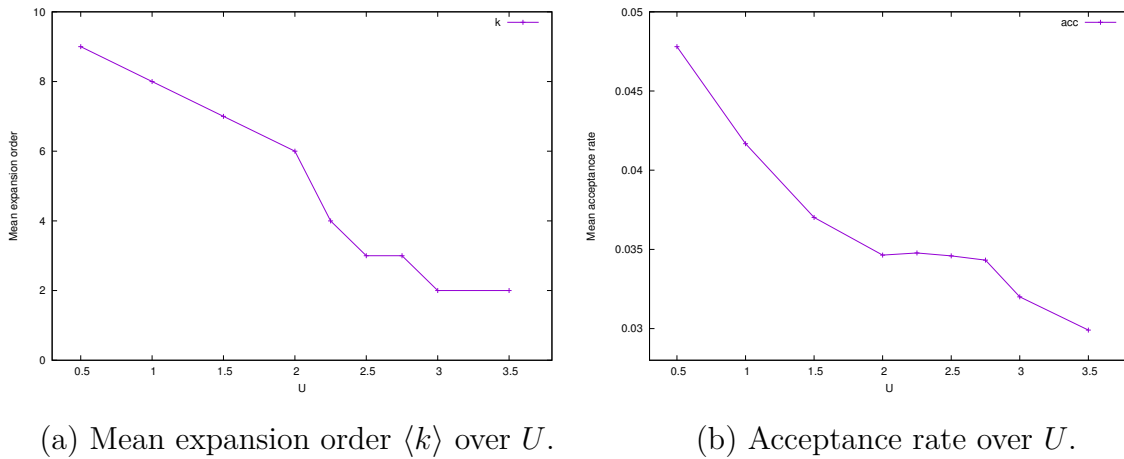


Figure 3.15: A declining behavior of the mean expansion order  $\langle k \rangle$  (a) and the mean acceptance rate (b) with non-linearity at the phase transition can be observed.

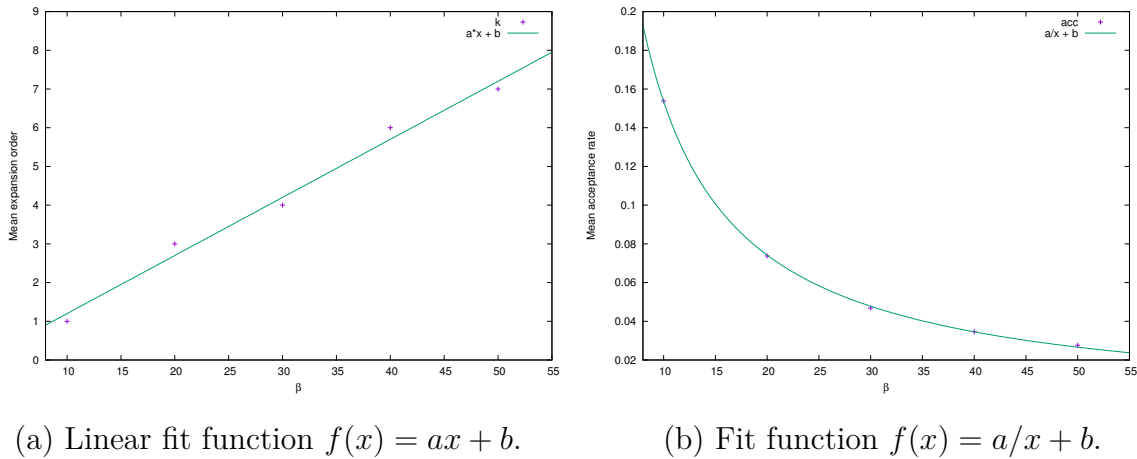


Figure 3.16: Mean expansion order  $\langle k \rangle$  (a) and acceptance rate (b) as a function of  $\beta$ . The green line represents a non-linear least-squares fit for the given fit-functions.

Figures 3.15 and 3.16 show the behavior of the mean expansion order  $\langle k \rangle$  and the acceptance rate for different values of the interaction  $U$  (at  $\beta = 40$ ) and different values of the inverse temperature  $\beta$  (at  $U = 2$ ) for the Bethe lattice with half-bandwidth  $D = 1$ .<sup>24</sup>

The expansion order scales linearly with  $\beta$ , which results from the “length” of the trace being proportional to  $\beta$ , i.e. the longer the trace the more operators may be placed inside the trace. The acceptance rate scales with  $1/\beta$ . According to the autocorrelation estimate the actual autocorrelation length thus scales as  $\beta^2$ .

The scaling of the mean expansion order  $\langle k \rangle$  and the acceptance rate over  $U$  displays comparable trends. The scaling of the mean expansion order of CT-HYB is a direct conse-

<sup>24</sup>Estimating the autocorrelation length according to relation (3.83) for the plotted data gives different results to Figure 3.14. This has two reasons: the mean expansion order in Figure 3.15 and Figure 3.16 needs to be shifted by  $-1$  due to different definitions of the expansion order. Further, the proposal rates for pair insertion and removal rates have changed due to additional off-diagonal flavor pair moves in more recent versions of the algorithm. By normalizing the two estimates to one another at a fixed value of  $U$  the results are in good agreement.

quence of the strong-coupling formulation. A peculiar feature of both the expansion order and the acceptance rate is their behavior in proximity of the Mott metal-to-insulator transition. The first order-phase transition results in plateaus in either quantity. Nevertheless, the autocorrelation estimate is capable of reproducing the behavior of the autocorrelation length in these regions.

## 3.4 Symmetric Improved Estimators

In the previous section worm sampling was introduced as an extension to conventional CT-HYB. The extended algorithm becomes central when considering observables which are not part of the infinite partition function series expansion. For example, the improved estimators in Section 3.1, following the equation of motion for the one- and two-particle Green's function, result in three fermionic operators forming an equal-time object and a fourth operator separated by an (imaginary) time offset. As the specific operator structure is not contained in the series expansion of  $Z$  and can thus not be measured by a removal of hybridization lines, the worm algorithm is required for an ergodic sampling of the observable for non-density-density interactions. For density-density interactions on the other hand, the improved estimators follow by inserting density operators into the local trace. This is equivalent to the insertion of local operators in worm sampling, but ergodicity is fulfilled even without an additional sampling of hybridization operators within this configuration space. In general, the improved- and asymptotic estimators, i.e. estimators with equal-time structure, enhance the high-frequency structure of one- and two-particle Green's functions.

While the improved estimators have been formally introduced in the previous sections, the Monte Carlo error propagation has not been discussed extensively. In order to do so, it is beneficial to compare Monte Carlo estimators of CT-HYB with estimators of CT-INT. Within the CT-QMC community it is generally known that the high-frequency structure of self-energies and irreducible vertex functions calculated in CT-INT is considerably less noisy than when calculated in CT-HYB [Gull et al., 2007]. This even holds true when considering one- and two-particle improved estimators in CT-HYB and has triggered a series of developments for smoothing high-frequency noise in CT-HYB, including expansions of Green's function in Legendre polynomials, effectively filtering high-frequency noise [Boehnke et al., 2011], or measuring moments of the self-energy [Potthoff et al., 1997, Wang et al., 2011] or the vertex functions [Kaufmann et al., 2017] explicitly.

### 3.4.1 One-Particle Symmetric Improved Estimator

Overall, the characteristic noise levels in the high-frequency regions of irreducible one- or two-particle vertices in CT-HYB and CT-INT follow from the Monte Carlo error being suppressed differently. More specifically, the one-particle Green's function estimator in CT-INT is given by [Rubtsov and Lichtenstein, 2004]:

$$G(i\nu) = \mathcal{G}(i\nu) - \frac{1}{\beta} \left\langle \mathcal{G}(i\nu) \left[ \sum_{ij}^k M_{ij} e^{i\nu(\tau_i - \tau_j)} \right] \mathcal{G}(i\nu) \right\rangle_{\text{MC}}, \quad (3.84)$$

where  $M_{ij}$  is now the inverse of the Green's function matrix  $D_{ij} = \mathcal{G}(\tau_i - \tau_j)$  and  $\mathcal{G}(i\nu)$  is the non-interacting Green's function. The sum is evaluated over all  $k$  (bare) interaction vertices in the trace. Although both CT-INT and traditional CT-HYB define Green's function estimators with respect to the matrix  $M_{ij}$ , in the latter case this matrix is constructed as the inverse of the hybridization matrix. If one assumes that the error in relation (3.84) is essentially constant in the Monte Carlo expectation value, the high-frequency error of the one-particle Green's function in CT-INT is suppressed with  $1/(i\nu)^2$ . This results from the corresponding  $1/i\nu$  behavior of the non-interacting Green's functions.

The Green's function estimator of CT-HYB, on the other hand, is given by relation (3.28), which is reformulated in Matsubara frequencies as:

$$G(i\nu) = -\frac{1}{\beta} \left\langle \sum_{ij}^{k/2} M_{ji} e^{i\nu(\tau_i - \tau_j)} \right\rangle_{\text{MC}}, \quad (3.85)$$

where the matrix elements of  $M_{ji}$  follow from the inverse hybridization matrix in CT-HYB. If one assumes a constant error in the Monte Carlo estimator, the one-particle Green's function is no further suppressed by non-interacting Green's functions.<sup>25</sup>

The improved estimator  $\Sigma G(i\nu)$  of CT-HYB is given by relation (3.38). The one-particle Green's function follows from the improved estimator as:

$$G_{\sigma}(i\nu) = \mathcal{G}_{\sigma}(i\nu) - \mathcal{G}_{\sigma}(i\nu) \frac{1}{\beta} \left\langle U \sum_{ij}^{k/2} \hat{n}_{-\sigma} M_{ji}^{\sigma} e^{i\nu(\tau_i - \tau_j)} \right\rangle_{\text{MC}}, \quad (3.86)$$

where the explicit spin index  $\sigma$  distinguishes the flavor of the density from the flavor of the remaining two operators in the expectation value. Furthermore, the density is directly attached to the position of the annihilation operator. If one assumes that the Monte Carlo error is essentially constant for the improved estimator, the high-frequency error of the one-particle Green's function is suppressed with  $1/i\nu$ , resulting from the multiplication with a single non-interacting propagator. This explains the somewhat worse high-frequency behavior of self-energies calculated from improved estimators in CT-HYB as opposed to self-energies calculated in CT-INT.

It is however possible to obtain the same high-frequency behavior of Green's functions and self-energies in CT-HYB as in CT-INT by applying the equation of motion on the one-particle Green's function twice.<sup>26</sup> In the following this procedure is demonstrated for the single-orbital AIM in the Hamiltonian formalism (cf. [Hafermann et al., 2012]), as opposed to the path integral formalism of Section 3.1.3. The equation of motion for the

<sup>25</sup>The direct equivalent of relation (3.84) for CT-HYB corresponds to the measurement of the lattice (i.e. bath) Green's function of the AIM (see relation (2.43) in Chapter 2.2). A more detailed derivation in the context of CT-HYB is found elsewhere [Haule, 2007].

<sup>26</sup>In a different context, the procedure of applying the equation of motion to both the creation and annihilation operator of the one-particle Green's function was used to approximate spectral functions [Górski and Mizia, 2013]. During the finalization of this work, the author was made aware of a recent derivation of the one-particle symmetric improved estimator in the diagMC context [Moutenet et al., 2018], where the self-energy is calculated recursively similar to the diagrammatic representation introduced towards the end of Section 3.2.2.

impurity Green's function is defined as:

$$\begin{aligned}\partial_{\tau_1} G_{\sigma}(\tau_1, \tau_2) &= -\partial_{\tau_1} \langle T_{\tau} \hat{d}_{\sigma}(\tau_1) \hat{d}_{\sigma}^{\dagger}(\tau_2) \rangle \\ &= -\delta(\tau_1 - \tau_2) \langle \{ \hat{d}_{\sigma}, \hat{d}_{\sigma}^{\dagger} \}(\tau_1) \rangle - \langle T_{\tau} \partial_{\tau_1} \hat{d}_{\sigma}(\tau_1) \hat{d}_{\sigma}^{\dagger}(\tau_2) \rangle \\ &= -\delta(\tau_1 - \tau_2) - \langle T_{\tau} [ \hat{d}_{\sigma}, \hat{H}_{\text{aim}} ](\tau_1) \hat{d}_{\sigma}^{\dagger}(\tau_2) \rangle,\end{aligned}\quad (3.87)$$

where the first term results from the time derivative of the time-ordering symbol  $T_{\tau}$  and the anti-commutator of the creation and annihilation operator and the second term is the commutator between the annihilation operator and the AIM Hamiltonian defined in (2.30). The commutator of  $\hat{d}_{\sigma}$  with  $\hat{H}_{\text{aim}}$  evaluates to:

$$[ \hat{d}_{\sigma}, \hat{H}_{\text{aim}} ] = U \hat{n}_{-\sigma} \hat{d}_{\sigma} - \mu \hat{d}_{\sigma} - \sum_{\vec{k}}^{\text{BZ}} V_{\vec{k}\sigma}^* \hat{c}_{\sigma}, \quad (3.88)$$

where the last term with the single bath annihilation operator generates a mixed impurity-bath Green's function when evaluated in relation (3.87). The mixed impurity-bath Green's function can be evaluated by considering the equation of motion for the bath operator:

$$\begin{aligned}\partial_{\tau_1} \langle T_{\tau} \hat{c}_{\sigma}(\tau_1) \hat{d}_{\sigma}^{\dagger}(\tau_2) \rangle &= \langle T_{\tau} [ \hat{c}_{\sigma}, \hat{H}_{\text{aim}} ](\tau_1) \hat{d}_{\sigma}^{\dagger}(\tau_2) \rangle \\ &= \sum_{\vec{k}}^{\text{BZ}} \varepsilon_{\vec{k}} \langle T_{\tau} \hat{c}_{\sigma}(\tau_1) \hat{d}_{\sigma}^{\dagger}(\tau_2) \rangle - \sum_{\vec{k}}^{\text{BZ}} V_{\vec{k}\sigma} \langle T_{\tau} \hat{d}_{\sigma}(\tau_1) \hat{d}_{\sigma}^{\dagger}(\tau_2) \rangle,\end{aligned}\quad (3.89)$$

With the hybridization function in imaginary time defined as

$$\Delta_{\sigma}(\tau_1) = \sum_{\vec{k}} \frac{V_{\vec{k}\sigma}^* V_{\vec{k}\sigma}}{\partial_{\tau_1} - \varepsilon_{\vec{k}}}, \quad (3.90)$$

the one-particle Green's function follows from relation (3.87) with:

$$G_{\sigma}(\tau_1, \tau_2) = -\frac{1}{\partial_{\tau_1} + \mu - \Delta_{\sigma}(\tau_1)} \left( \delta(\tau_1 - \tau_2) + U \langle T_{\tau} \hat{n}_{-\sigma}(\tau_1) \hat{d}_{\sigma}(\tau_1) \hat{d}_{\sigma}^{\dagger}(\tau_2) \rangle \right). \quad (3.91)$$

The above equation recovers the well-known result of the equation of motion, which sets  $G\Sigma$  into relation with a two-particle Green's function with three operators contracted by an interaction vertex.

In the following, the equation of motion is applied yet another time to the remaining creation operator at time  $\tau_2$ , such that:

$$\begin{aligned}\partial_{\tau_2} \langle T_{\tau} \hat{n}_{-\sigma}(\tau_1) \hat{d}_{\sigma}(\tau_1) \hat{d}_{\sigma}^{\dagger}(\tau_2) \rangle &= \\ &= -\delta(\tau_1 - \tau_2) \langle T_{\tau} \{ \hat{n}_{-\sigma} \hat{d}_{\sigma}, \hat{d}_{\sigma}^{\dagger} \}(\tau_1) \rangle + \langle T_{\tau} \hat{n}_{-\sigma}(\tau_1) \hat{d}_{\sigma}(\tau_1) [ \hat{d}_{\sigma}^{\dagger}, \hat{H}_{\text{aim}} ](\tau_2) \rangle\end{aligned}\quad (3.92)$$

In order to evaluate the above expression, the following (anti-) commutators are provided:

$$\{ \hat{n}_{-\sigma} \hat{d}_{\sigma}, \hat{d}_{\sigma}^{\dagger} \} = \hat{n}_{-\sigma} \quad (3.93)$$

$$[ \hat{d}_{\sigma}^{\dagger}, \hat{H}_{\text{aim}} ] = -U \hat{n}_{-\sigma} \hat{d}_{\sigma}^{\dagger} + \mu \hat{d}_{\sigma}^{\dagger} + \sum_{\vec{k}}^{\text{BZ}} V_{\vec{k}\sigma} \hat{c}_{\sigma}^{\dagger}, \quad (3.94)$$



where the resulting mixed impurity-bath Green's function in relation (3.92) can be calculated again through the equation of motion for the bath operators, analogous to relation (3.89). Thus, relation (3.92) can be expressed as:

$$\langle T_\tau \hat{n}_{-\sigma}(\tau_1) \hat{d}_\sigma(\tau_1) \hat{d}_\sigma^\dagger(\tau_2) \rangle = \frac{1}{-\partial_{\tau_2} + \mu - \Delta_\sigma(\tau_2)} \left( \delta(\tau_1 - \tau_2) n_{-\sigma} + U \langle T_\tau \hat{n}_{-\sigma}(\tau_1) \hat{d}_\sigma(\tau_1) \hat{n}_{-\sigma}(\tau_2) \hat{d}_\sigma^\dagger(\tau_2) \rangle \right), \quad (3.95)$$

with the density  $n_{-\sigma} = \langle \hat{n}_{-\sigma} \rangle$ . The last expectation value in the above equation is a three-particle Green's function, where six external legs were contracted by two interaction vertices into two 3-tuples. The Monte Carlo evaluation of this expectation value will be referred to as symmetric improved estimator.

In order to quantify the error scaling of the resulting expression, the Fourier transform is defined as:

$$G_\sigma(i\nu) = \int_0^\beta e^{i\nu(\tau_1 - \tau_2)} G_\sigma(\tau_1, \tau_2) d\tau_1 d\tau_2. \quad (3.96)$$

The resulting expression for the one-particle Green's function in Matsubara frequencies follows as:

$$G_\sigma(i\nu) = \mathcal{G}_\sigma(i\nu) + U \mathcal{G}_\sigma^2(i\nu) \left( n_{-\sigma} + U \langle T_\tau \hat{n}_{-\sigma}(\tau_1) \hat{d}_\sigma(\tau_1) \hat{n}_{-\sigma}(\tau_2) \hat{d}_\sigma^\dagger(\tau_2) \rangle \right). \quad (3.97)$$

Assuming a constant error in the symmetric improved estimator and the density measurement, one observes a  $1/(i\nu)^2$  error suppression in the high-frequency region, just as for the Green's function estimator of CT-INT.

In Figure 3.17, the one-particle Green's function in the atomic limit was calculated by stochastically sampling the local trace for the different estimators discussed above. The number of measurement steps for all three estimators was kept constant. The high-frequency tail of the Green's function following the improved- and symmetric improved estimator is considerably better than of the naive estimator. Figure 3.18 shows the one-particle self-energy corresponding to the Green's functions calculated in Figure 3.17. One can observe that the error scaling of the Green's function directly affects the self-energy. The error in the self-energy scales quadratically for the naive estimator and linear for the improved estimator. For the symmetric estimator a constant scaling in the self-energy is to be expected. The absolute error is illustrated in Figure 3.19. The superior scaling properties of the stochastic error in the high-frequency region of the symmetric improved estimator are clearly visible. The lowest frequencies resulting of the symmetric improved estimator, on the other hand, converge more slowly towards the exact value.

Analytically, the error scaling in the high-frequency regions of the self-energy can be further derived by a formal propagation of errors [Wallerberger, 2016]:

$$\text{Var} [\Sigma(i\nu)] \approx \left| \frac{\partial \Sigma}{\partial G} \right|^2 \text{Var} [G(i\nu)] = |G(i\nu)|^{-4} \text{Var} [G(i\nu)], \quad (3.98)$$

which essentially amounts to calculating the highest-order contribution to the variance after Taylor expanding  $\Sigma(\mathcal{G}, G)$  (i.e. Dyson's equation) in terms of  $\mathcal{G}$  and  $G$  and neglecting any uncertainties in  $\mathcal{G}$ . Now,  $\text{Var} [\Sigma(i\nu)]$  can be calculated from  $\text{Var} [G(i\nu)]$  for

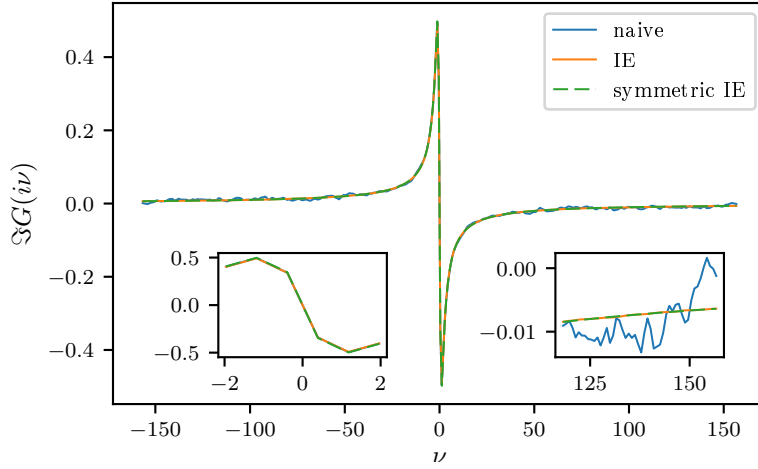


Figure 3.17: Imaginary part of the one-particle Green's function in the atomic limit with  $\beta = 8.0$ ,  $U = 2.0$  and  $\mu = 1.0$ . The Green's function was calculated by stochastically sampling the naive estimator (blue), improved estimator (orange) and symmetric improved estimator (green dashed) with the same number of measurements. Left inset: low-frequency behavior. Right inset: high-frequency behavior.

relations (3.85), (3.86) and (3.97):

$$\lim_{i\nu \rightarrow \infty} \text{Var} [\Sigma_{\text{naive}}(i\nu)] = \mathcal{O}(i\nu^4)\mathcal{O}(1) \quad (3.99)$$

$$\lim_{i\nu \rightarrow \infty} \text{Var} [\Sigma_{\text{imp.}}(i\nu)] = \mathcal{O}(i\nu^4)\mathcal{O}(i\nu^{-2}) \quad (3.100)$$

$$\lim_{i\nu \rightarrow \infty} \text{Var} [\Sigma_{\text{sym.}}(i\nu)] = \mathcal{O}(i\nu^4)\mathcal{O}(i\nu^{-4}), \quad (3.101)$$

where the second  $\mathcal{O}$ -term encodes the variance of each Green's function expression. The error (i.e. standard deviation) in the high-frequency region of the self-energy thus scales quadratically following the naive estimator, linear following the improved estimator and constant following the symmetric improved estimator.

### 3.4.2 Two-Particle Symmetric Improved Estimator

The two-particle symmetric improved estimator can be derived similar to the one-particle symmetric improved estimator by applying time-derivatives to all four operators of the expectation value. Before doing so, it is however useful to reconsider the two-particle estimator of CT-INT [Gull et al., 2008]:

$$G_{1234} = \left\langle \begin{vmatrix} \mathcal{G}_{12} - \mathcal{G}_{1k}M_{kl}\mathcal{G}_{l2} & \mathcal{G}_{14} - \mathcal{G}_{1k}M_{kl}\mathcal{G}_{l4} \\ \mathcal{G}_{32} - \mathcal{G}_{3k}M_{kl}\mathcal{G}_{l2} & \mathcal{G}_{34} - \mathcal{G}_{3k}M_{kl}\mathcal{G}_{l4} \end{vmatrix} \right\rangle_{\text{MC}}, \quad (3.102)$$

where in this simplified notation, the numbered subscripts denote a combined flavor-imaginary-time index and Einstein sum convention is assumed. The matrix  $M_{kl}$  is the inverse of the Green's function matrix  $D_{kl} = \mathcal{G}(\tau_k - \tau_l)$  (see also Section 3.4.1). For CT-INT,

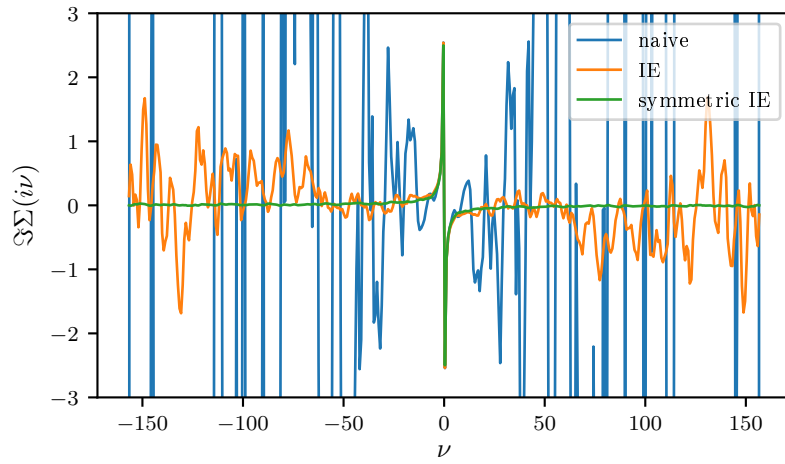


Figure 3.18: Imaginary part of the one-particle self-energy in the atomic limit with  $\beta = 8.0$ ,  $U = 2.0$  and  $\mu = 1.0$ . The self-energy was calculated for the naive estimator (blue), improved estimator (orange) and symmetric improved estimator (green).

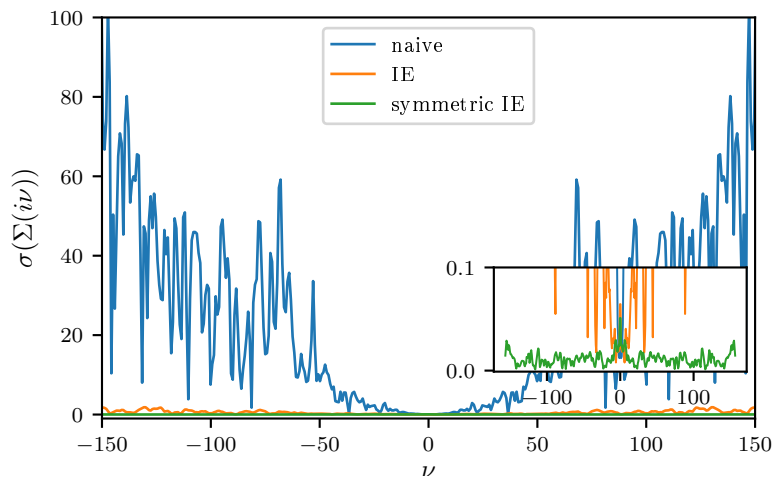


Figure 3.19: Absolute error of self-energy of Figure 3.18 in the atomic limit with  $\beta = 8.0$ ,  $U = 2.0$  and  $\mu = 1.0$ . The error displays a quadratic high-frequency behavior following the naive estimator (blue), linear behavior following the improved estimator (orange) and a constant behavior following the symmetric improved estimator (green). Inset: Error of the symmetric improved estimator showing larger deviations for the lowest frequencies and a constant behavior for all remaining frequencies.

Wick's theorem applies, allowing one to write the two-particle Green's function as a two-by-two determinant of one-particle Green's functions. By explicitly evaluating the determinant and calculating the Fourier transform, it becomes obvious that in the lowest order a constant Monte Carlo error in the sum of matrix-elements  $M_{ij}$  is suppressed by  $1/(i\nu)^3$  of three non-interacting Green's functions. In contrast, the two-particle measurement in CT-HYB has no suppression of Monte Carlo errors in the naive estimator (see relation (3.33)), while the constant error of the two-particle improved estimator is being suppressed by  $1/(i\nu)$  (see relation (3.14)).

When calculating irreducible two-particle vertex functions (e.g.  $F$ ,  $\Gamma$  or  $\Lambda$ ), the disconnected parts of the two-particle Green's function need to be subtracted, while the four outer legs of the remaining connected part need to be amputated. The CT-INT error scaling of the products of one-particle Green's functions in the disconnected part and the two-particle Green's function is relatively stable against these amputations. In CT-HYB, on the other hand, the constant error in the two-particle Green's function results in significant high-frequency noise.

In order to derive the two-particle symmetric improved estimator of the two-particle Green's, a hierarchy of equations of motions needs to be applied to all operators appearing in the expectation value. This derivation is discussed in Appendix F. The two-particle Green's function is given by:

$$G_{\sigma_1, \sigma_2, \sigma_3, \sigma_4}^{\tau_1, \tau_2, \tau_3, \tau_4} = \frac{1}{\partial_{\tau_1} + \mu - \Delta_{\sigma_1}(\tau_1)} \left( R_1 + \frac{U}{-\partial_{\tau_2} + \mu - \Delta_{\sigma_2}(\tau_2)} \times \right. \\ \left. \left( -R_2 + \frac{U}{\partial_{\tau_3} + \mu - \Delta_{\sigma_3}(\tau_3)} \left( R_3 + \frac{U}{-\partial_{\tau_4} + \mu - \Delta_{\sigma_4}(\tau_4)} \times \right. \right. \right. \\ \left. \left. \left. \left( -R_4 + U \langle T_{\tau} \hat{q}_{\sigma_1}(\tau_1) \hat{q}_{\sigma_2}^{\dagger}(\tau_2) \hat{q}_{\sigma_3}(\tau_3) \hat{q}_{\sigma_4}^{\dagger}(\tau_4) \rangle \right) \right) \right) \right), \quad (3.103)$$

where  $R_i$  represents expectation values with an equal-time structure resulting from the time-derivative of the time ordering symbol  $T_{\tau}$  and the 3-tuple operators are abbreviated by  $\hat{q}_{\sigma} := \hat{n}_{-\sigma} \hat{d}_{\sigma}$ . The remaining expectation value of four  $q$ -operators is actually a six-particle Green's function, where twelve external legs were contracted by four interaction vertices into four 3-tuples. The Monte Carlo evaluation of this expectation value will be referred to as two-particle symmetric improved estimator.<sup>27</sup> A constant Monte Carlo error for the two-particle symmetric improved estimator is suppressed by four non-interacting Green's functions. The  $R_i$  terms, however, lift the error suppression to  $1/(i\nu)^3$ , equivalent to the scaling in CT-INT. This can be illustrated by looking at  $R_1$  explicitly:

$$R_1 = \delta(\tau_1 - \tau_2) \delta_{\sigma_1 \sigma_2} \langle T_{\tau} \hat{d}_{\sigma_3}(\tau_3) \hat{d}_{\sigma_4}^{\dagger}(\tau_4) \rangle - \delta(\tau_1 - \tau_4) \delta_{\sigma_1 \sigma_4} \langle T_{\tau} \hat{d}_{\sigma_3}(\tau_3) \hat{d}_{\sigma_2}^{\dagger}(\tau_2) \rangle, \quad (3.104)$$

where each of the two terms above is constructed of a one-particle impurity Green's function. Assuming the naive one-particle estimator, the error in the two-particle Green's function is rescaled to a  $1/(i\nu)$  behavior due to the first non-interacting Green's function in relation (3.103). Only when assuming the one-particle symmetric improved estimator

<sup>27</sup>The symmetric improved estimator of a generalized  $n$ -particle Green's function is hence a  $3n$ -particle Green's function with equal-time structure.

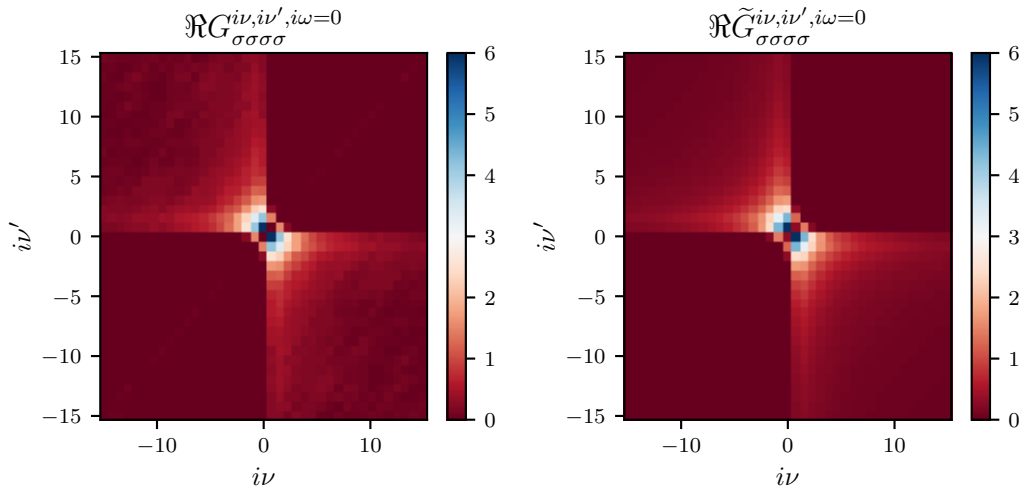


Figure 3.20: Real part of the two-particle Green’s function in the atomic limit with  $\beta = 8.0$ ,  $U = 2.0$  and  $\mu = 1.0$ . The two-particle Green’s function was calculated by stochastically sampling the naive estimator  $G$  (left) and the symmetric improved estimator  $\tilde{G}$  (right) with the same number of measurements.

discussed in Section 3.4.1, the error in the two-particle Green’s function is rescaled with  $1/(i\nu)^3$ . It is thus important to further apply the equation of motion hierarchy to all “free” operators appearing in the  $R_i$  terms.

The remaining  $R_i$  terms are constructed of various anti-commutators with  $q$ -operators and evaluate to different expressions depending on the spins  $\sigma_i$  under consideration. An explicit calculation for the  $G_{\sigma\sigma\sigma\sigma}^{\nu\nu'\omega}$  component of the two-particle Green’s function in the particle-hole Matsubara representation and definitions of  $R_2, R_3$  and  $R_4$  are given in Appendix F.

Figure 3.20 shows the real part of the two-particle Green’s function in the atomic limit with  $\beta = 8.0$ ,  $U = 2.0$  and  $\mu = 1.0$ , calculated with the naive two-particle estimator 3.33 and the two-particle symmetric improved estimator 3.103. The number of measurement steps was kept constant. Deviations between the two estimates are minimal. When calculating the irreducible two-particle vertex function  $F$ , however, differences become more apparent, as illustrated in Figure 3.21. The constant error of the naive two-particle estimator is amplified by the amputation of four outer legs. The irreducible vertex function extracted from the two-particle symmetric improved estimator, on the other hand, displays very little noise in the high-frequency regions. Instead, the typical features of the irreducible vertex function, i.e. a “plus” structure and a “cross” structure are observable over the entire frequency range. It is further instructive to consider the absolute error of the naive and the symmetric improved estimator in Figure 3.22. While the lowest frequencies of the naive estimator converge fast against the analytic expression, the high-frequency region is characterized by the typical noise pattern. The symmetric improved estimator, on the other hand, does a significantly better job in approximating the high-frequency regions. Nevertheless, the lowest frequencies converge slower towards the exact value.

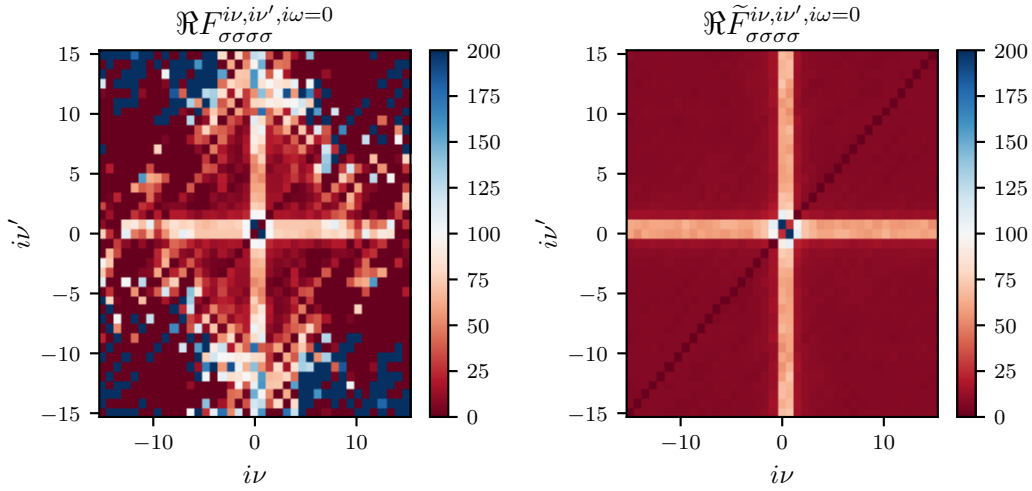


Figure 3.21: Real part of the irreducible two-particle vertex functions corresponding to Figure 3.20. The vertex function  $F$  was calculated from the naive estimator  $G$  (left), while the vertex function  $\tilde{F}$  was calculated from the symmetric improved estimator  $\tilde{G}$  (right). In both cases, the one-particle Green's functions for the outer leg amputations and for the construction of disconnected parts were calculated from the one-particle symmetric improved estimator.

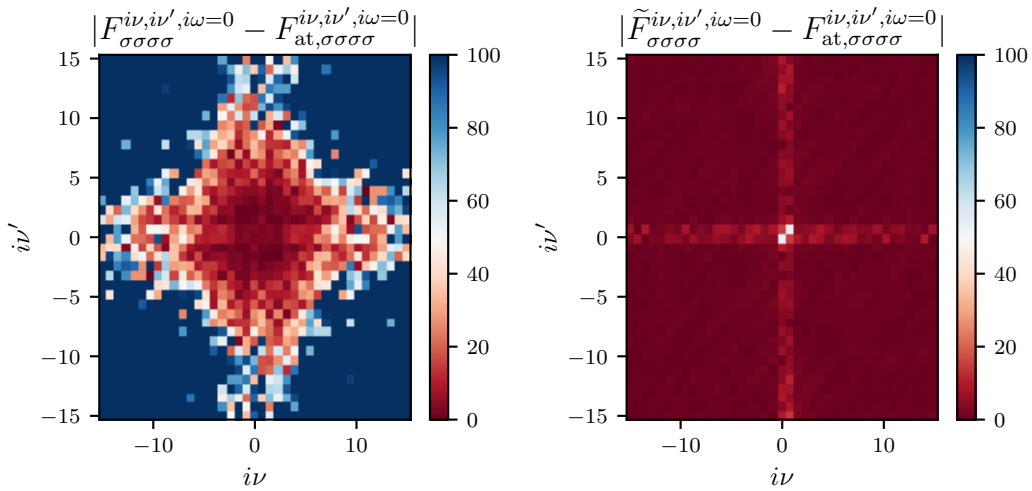


Figure 3.22: Absolute error of the irreducible vertex functions of Figure 3.21 (left: naive estimator; right: symmetric improved estimator; calculated in comparison to the exact atomic limit result  $F_{at}$ ). The high-frequency values of the symmetric improved estimator show a better convergence than high-frequency values of the naive estimator. The low-frequency values of the naive estimator  $F$ , on the other hand, show a better convergence than low-frequency values of the symmetric improved estimator  $\tilde{F}$ .

### 3.4.3 Generalizations and Feasibility

For density-density interactions, symmetric improved estimator can be measured at essentially no computational overhead with respect to the one- or two-particle Green's function (similar to traditional improved estimators). When considering non-density-density interactions, however, worm sampling is necessary to evaluate improved- and symmetric improved estimators (both on the one- and two-particle level). Nevertheless, the “free” operator of traditional improved estimators can still be exchanged with the remaining hybridization operators in the local trace through replacement steps and/or full estimators (see Sections 3.3.4 and 3.3.6). The symmetric improved estimators, on the other hand, only consist of equal-time operator tuples constructed of three individual operators. Thus, the auto-correlation length can no longer be compensated by replacement steps or the full estimator and the burden is offset to the sampling procedure entirely.

The discussion of the symmetric improved estimators is concluded with a word of caution. On the one-particle level, the impurity Green's function is measured as a correction to the non-interacting Green's function. Hence, the high-frequency behavior is given by the exactly known non-interacting Green's function and is not subject to numerical noise. For  $U = 0$ , the impurity Green's function identically evaluates to the non-interacting Green's function. On the two-particle level, the two-particle Green's function is also measured as a correction to the non-interacting disconnected contributions. That is for  $U = 0$ , the two-particle Green's function following the symmetric improved estimator identically evaluates to the two disconnected products of non-interacting one-particle Green's functions. This yields again a better convergence for large Matsubara frequencies. However, as observed in the previous sections, typically the lowest frequencies of Green's functions constructed from symmetric improved estimators converge somewhat slower than when measuring the Green's function naively.<sup>28</sup> This behavior is known to exist for the Green's function estimators of CT-INT [Rubtsov and Lichtenstein, 2004] and is equally present for the improved- and symmetric improved estimator. The low-frequency behavior of the Matsubara Green's function, or equivalently the Matsubara self-energy, largely determines the physics of the system. For example, the low-frequency divergence of the imaginary part of the self-energy characterizes Mott insulators. Ultimately, it is necessary to investigate the rate of convergence in different frequency regions for the naive and the symmetric improved estimator. A numerical solution to this problem would be to measure both the naive and the symmetric improved estimators in Matsubara frequencies, patching together a combined solution depending on the amplitude of the Monte Carlo error. In general this approach would require an additional factor two in memory to store the measurement of the naive- and the symmetric improved estimator, determining the optimal estimate for each frequency in a post-processing step. As the estimators can

---

<sup>28</sup>In the above numerical analysis, the atomic limit was considered, where the diverging behavior of  $\mathcal{G}$  amplifies errors in the lowest frequencies of improved- and symmetric improved estimators. For  $\beta \rightarrow \infty$ , that is  $\Im\mathcal{G}(0_+) \rightarrow -\infty$ , any error in the improved (and more so the symmetric improved) estimators will completely dominate the low-energy behavior of the impurity Green's function. It is to be expected that the low-frequency behavior of the impurity Green's function is more well-behaved in metallic systems where  $\mathcal{G}$  does not diverge.

be measured simultaneously for density-density interactions, this becomes the method of choice. Moreover, symmetric improved estimators seem to render the smoothing abilities of low-pass Legendre filters unnecessary. Instead of potentially filtering-out physical information, orthogonal polynomial representations may be only exploited in order to enhance computational efficiency. Actual implementations of symmetric improved estimators for CT-HYB codes have not been explored in this work (only the atomic limit has been considered) and are left for future investigation.

On a different note, a diagrammatic interpretation of all terms contributing to the final Green's function expressions is still absent. While it is clear that equal-time corrections to the symmetric improved estimator essentially avoid over-counting of diagrams, it seems worthy to explore the connection of these diagrams with asymptotics of self-energy and vertex functions. On the two-particle level, however, the presence of non-interacting Green's function in the equation of motion hierarchy prohibits a straight-forward interpretation in the diagrammatic two-particle description, which otherwise lacks non-interacting propagators.



# Chapter 4

## Single-Orbital Applications

### 4.1 Mass-imbalanced Hubbard Model

*Parts of this section (marked by a vertical sidebar) have been already published in: M. Philipp, M. Wallerberger, P.G. and K. Held; Mott-Hubbard transition in the mass-imbalanced Hubbard model. Eur. Phys. J. B 90,114 (2017)*

In Chapter 2 the Hubbard model was introduced and, in order to provide a deeper understanding of the underlying physics, different limiting cases were discussed in the following. The most fascinating physics of the Hubbard model evolve when assuming the potential energy term to be of the same magnitude as the kinetic energy term by tuning the ratio of the Coulomb repulsion  $U$  over the hopping  $t$ . In the strong coupling limit, where  $U/t \gg 1$ , the Hubbard model at half-filling closely follows the behavior of the Heisenberg model. Electrons tend to stay localized at their initial site and spin-exchange is only possible through second order processes. In combination with the Pauli exclusion principle, this results in the antiferromagnetic ordering of the lattice.

In terms of dynamics, one may consider the mass-imbalanced Hubbard model, where the hopping amplitudes for the two spin species differs, effectively breaking the  $SU(2)$  symmetry of the system. By setting the hopping amplitude of one electron spin to zero, the Falicov-Kimball model is obtained. The Falicov-Kimball model in the limit of the mass-imbalanced Hubbard model orders antiferromagnetically. However, while the order parameter of the Hubbard model and the Heisenberg model obeys  $O(3)$  symmetry, the order parameter of the Falicov-Kimball model obeys  $\mathbb{Z}_2$  symmetry. The Falicov-Kimball model is further capable of describing metal-to-insulator transitions by varying the non-vanishing hopping amplitude accordingly.

A smooth transition between the Hubbard model and the Falicov-Kimball model is obtained by tuning the hopping amplitude of one spin, while the hopping amplitude of the other spin remains unchanged. This is described by the mass-imbalanced Hubbard model, which contains both the Hubbard model and the Falicov-Kimball model as limiting cases. Experimentalists “simulated” the mass-imbalanced Hubbard model by generating an ultra-cold fermionic quantum gas of two different atomic species [Taglieber et al., 2008]. Theoreticians, on the other hand, simulated the model employing DMFT, investigating the

antiferromagnetic ordering [Sotnikov et al., 2012]. The metal-to-insulator transition of the mass-imbalanced Hubbard model in DMFT was discussed at zero temperature [Dao et al., 2012]. What remained to be investigated was the metal-to-insulator transition at finite temperatures. Further, the effects of Kondo physics on the metal-to-insulator transition present in the Hubbard model and absent in the Falicov-Kimball model is discussed in the following.

In the following, we consider a Bethe lattice, i.e., a semi-elliptic densities of states  $D_x(\omega) = \frac{2}{\pi D_x} \sqrt{1 - (\omega/D_x)^2}$  with half bandwidth  $D_x \sim t_x$  for the two fermionic species  $x = c, f$ . In the following, we set  $D_c \equiv 2$  as our unit of energy and vary the mass balance<sup>a</sup>  $D_f/D_c = t_f/t_c$  between 0 and 1.

The two limits of mass imbalance are evident: In the case  $D_f/D_c = 0$ , the  $f$  fermions are truly frozen and we arrive at the FKM. On the other hand, if  $D_f/D_c = 1$ , we can identify  $c$  and  $f$  with spin-up and spin-down, respectively, and obtain the mass-balanced HM.

<sup>a</sup> Let us note here that in the literature sometimes a mass *imbalance* factor  $\zeta \equiv (t_c - t_f)/(t_c + t_f)$  is used instead of our  $t_f/t_c$ .

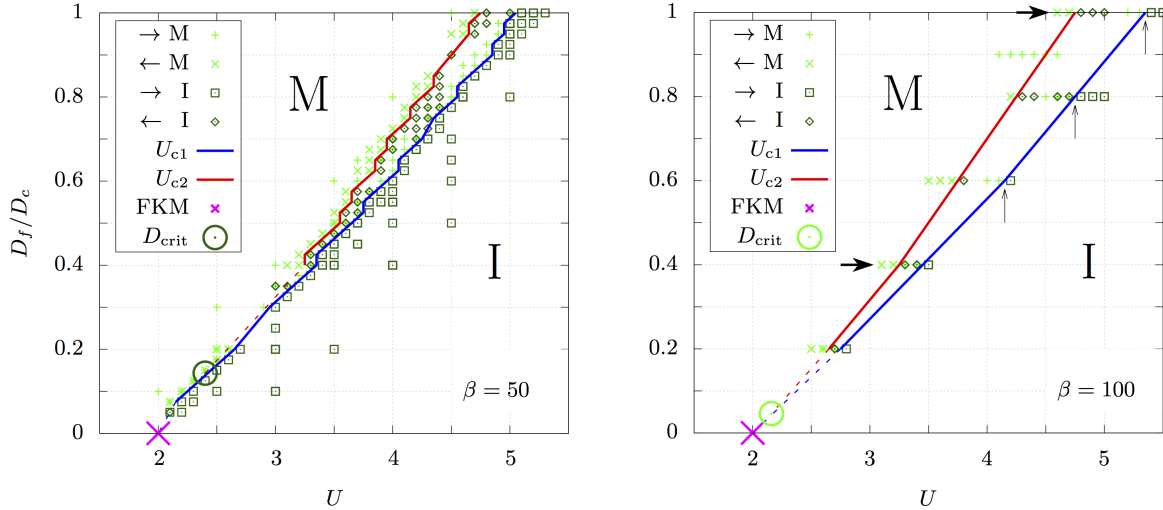


Figure 4.1: Phase diagram of the mass-imbalanced Hubbard model as a function of interaction strength  $U$  and mass imbalance  $D_f/D_c$  at  $\beta = 50$  (left panel) and  $\beta = 100$  (right panel);  $D_c \equiv 2$  sets our unit of energy. The critical interaction strengths  $U_{c1}$  (blue line) has been obtained by increasing  $U$  ( $\rightarrow$ ) and identifying up to which  $U$  value the metallic solution (M, green plus) is still stable and from which  $U$  value on we get an insulating solution (I, green boxes). For decreasing  $U$  ( $\leftarrow$ ),  $U_{c2}$  (red line) marks the point where the insulating solution (green diamonds) turns metallic (green crosses). The critical point where the first order transition with coexistence region ends is extrapolated by hands and indicated here by a green circle. The pink cross denotes the analytical continuous phase transition for the FKM.

Fig. 4.1 shows the phase diagram  $D_f/D_c$  vs.  $U$  of the mass-imbalanced HM in between these two known limits at two inverse temperatures  $\beta = 50$  and  $100$ . The first order coexistence region has been determined in the same way as described above for the HM: The four green symbols in Fig. 4.1 mark up to which point a metallic (M) or insulating (I) solution is found upon increasing or decreasing  $U$ . We observe a coexistence region and hence a first order transition in a wide range of mass imbalances. The coexistence region is increasing upon decreasing temperature to  $\beta = 100$ , and the critical point where the first order transition ends (green circle,  $D_{\text{crit}}$ ) is moving towards the FKM limit  $D_f/D_c = 0$ . To obtain the phase diagram, we discriminate between metallic and insulating solution by means of the imaginary part of the self-energy  $\Sigma(i\omega_n)$ .

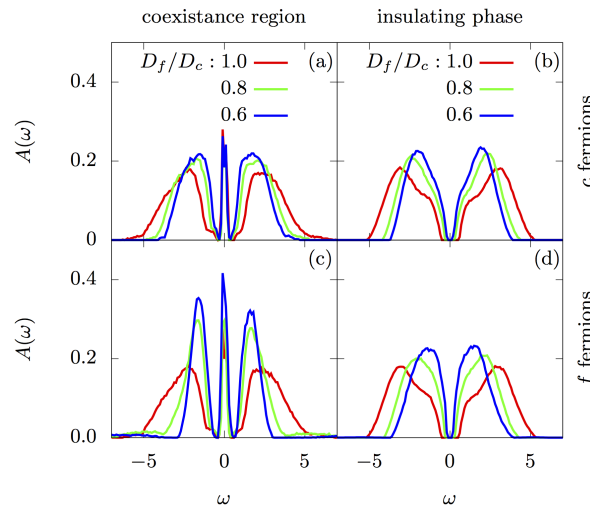


Figure 4.2: Spectral function  $A(\omega)$  near the critical interaction strength  $U_{c1}$  for different mass imbalances  $D_f/D_c$  at  $\beta = 100$ . The upper and lower two panels show the more and less mobile  $c$  and  $f$  fermions, respectively. The left (right) panels show a metallic (insulating) solution just below (above)  $U_{c1}$ , indicated by the three vertical arrows in Fig. 4.1. Specifically the  $D_f, U$  values for the left panels (a) and (c) are:  $D_f = 2.0, U = 5.2$  (red);  $D_f = 1.6, U = 4.1$  (green);  $D_f = 1.2, U = 3.4$  (blue); and for the right panels (b) and (d):  $D_f = 2.0, U = 5.5$  (red);  $D_f = 1.6, U = 4.2$  (green),  $D_f = 1.2, U = 3.5$  (blue).

Fig. 4.2 shows the corresponding spectral function comparing the HM ( $D_f/D_c = 1$ ) and the mass imbalanced HM ( $D_f/D_c = 0.8$  and  $0.6$ ), immediately before (a,c) and after (b,d) the transition  $U_{c1}$  where the metallic solution ceases to exist. We see that the spectral functions are actually quite similar with a three-peak structure on the metallic side, consisting of a lower and upper Hubbard band and a central quasi-particle peak in between. Immediately after the transition  $U_{c1}$  there is a gap in the insulating phase. This is very different from the FKM in Fig. 2.12<sup>a</sup> where we have two peaks which do not overlap any more for  $U$  below the transition, as opposed by the overlap for  $U$  above the transition. There is also no indication of a smooth crossover in Fig. 4.2 from the HM behavior to that of the FKM. The major difference is that with reducing  $D_f/D_c$  in Fig.

4.2, the position of the upper (lower) Hubbard band shift to higher (lower) energies, which is in agreement with the reduced  $U_{c1}$  value at which the transition occurs.

<sup>a</sup>Figure reference adapted for an equivalent figure previously discussed in this work.

We have analyzed the Mott-insulator transition of the mass-imbalanced Hubbard model within the paramagnetic phase. Our phase diagram, Fig. 4.1, shows a first order phase transition in a wide range of mass imbalances  $D_f/D_c$ . With decreasing temperature the region of first order coexistence expands; and our results suggest that the mass-imbalanced Hubbard model always displays a first order metal-insulator transition at zero temperature as soon as a small, but finite, hopping of the less mobile  $f$  fermions is switched on ( $D_f > 0$ ).

For the FKM ( $D_f = 0$ ), we have two bands along with a gap opening with increasing  $U$  as soon as these two bands do not overlap any longer. If we switch on  $f$  fermion hopping however ( $D_f > 0$ ), a central resonance in this gap develops due to the Kondo effect. This stabilizes the metallic phase and shifts the metal-insulator transition in the phase diagram Fig. 4.1 towards larger  $U$  values. This resonance and a three-peak structure can be seen in the spectral function, Fig. 4.2. We find that the width of the central resonance is the same for the  $c$  and  $f$  fermions. This can be understood from the fact that the spin-flip (here  $c$ - $f$ ) scattering is crucial for the Kondo effect. Hence we have a joint Kondo temperature and width of the Kondo resonance for  $c$  and  $f$  fermions.

This is affirmed by an analysis of the quasi-particle renormalization factor  $Z_x^a$ , which shows  $Z_c D_c \rightarrow Z_f D_f$  when approaching the metal-insulator transition, i.e. when we are in the Kondo regime accompanied by a narrow central resonance. It further shows that the metal-insulator transition occurs simultaneously for both,  $c$  and  $f$ , fermions in the mass-imbalanced Hubbard model. The Falicov-Kimball physics, where the  $f$  fermions are insulating for any  $U$  and the  $c$  fermions for  $U > D_c$ , is a singular point of the phase diagram at zero temperature.

Altogether our results show that the physics of the mass-imbalanced Hubbard model in the paramagnetic phase resembles that of the Hubbard model. This is because of the equalizing power of the joint Kondo effect of the two fermionic species. Regarding the antiferromagnetic phase we nonetheless expect a qualitatively different behavior: the mass imbalance breaks the  $c$ - $f$   $O(3)$  rotational symmetry of the order parameter; and Monte-Carlo simulations [Liu and Wang, 2015] indeed indicate an Ising-type ordering. Hence we expect Ising-type critical exponents similar to what has recently been reported for the FKM, [Antipov et al., 2014] whereas we have a Heisenberg-type of ordering and associated critical exponents [Rohringer et al., 2011] for the Hubbard model.

<sup>a</sup>For results see [Philipp et al., 2017].

## Technical Considerations

The transition between the Hubbard model and the Falicov-Kimball model is not only interesting from a physical viewpoint. In the context of this work it is instructive to discuss the technical implications of this transitions within CT-HYB. The ratio between the hybridization function of the fully-mobile spin and the hybridization function of the less-mobile spin in the mass-imbalanced Hubbard model becomes considerably large towards the Falicov-Kimball limit, ultimately diverging for a vanishing hybridization function of

the immobile spin. The hybridization expansion of CT-QMC constructs a perturbation series, where the hybridization function essentially acts as the expansion parameter. While the CT-HYB expansion order of the fully-mobile spin may remain reasonably large, the expansion order of the less-mobile may become considerably small. Thus, the transition between the Hubbard model and the Falicov-Kimball model can be re-interpreted as a transition between the conventional sampling methods of CT-HYB and worm sampling. While in the former case, the two-particle estimators following directly from the partition function series fail to measure the mixed  $fc$ -components in the Falicov-Kimball model,<sup>1</sup> the estimators of worm sampling are specifically constructed around this limit. When considering CT-HYB for further investigations of the mass-imbalanced Hubbard model at finite temperatures (especially with regards to two-particle response functions) worm sampling should be employed.

## 4.2 Vertex Divergences in the AIM

*Parts of this section (marked by a vertical sidebar) have been already published in: P. Chalupa, P.G., T. Schäfer, K. Held and A. Toschi; Divergences of the irreducible vertex functions in correlated metallic systems: Insights from the Anderson Impurity Model. arXiv:1712.04171 (2017)*

In the previous section, the Mott-Hubbard metal-to-insulator phase transition of the mass-imbalanced Hubbard model was investigated. While the Mott transition is best visible on the one-particle level in the Matsubara self-energies or the spectral function, magnetic phase transitions follow from two-particle response functions. For example, the antiferromagnetic ordering of the two-dimensional Hubbard model is linked to the divergence of the momentum-resolved spin-susceptibility at  $\vec{q} = (\pi, \pi)$ . Typically, the magnetic ordering and the transition temperature are probed by analyzing the temperature behavior of different  $q$ -points of the static spin-susceptibility in the paramagnetic phase. In parameter regions away from physical phase transitions, the two-particle response functions seemingly behave normal, i.e. showing no divergences.

It was thus somewhat surprising that certain two-particle diagrams diverge in the absence of physical phase transitions. More precisely, Schäfer *et al.* discovered divergences in the two-particle irreducible diagram subsets  $\Gamma$  of the two-particle vertex function  $F$ , when inverting the respective Bethe-Salpeter equations [Schäfer et al., 2013a]. The divergences of the irreducible vertex functions were observed in various types of impurity models, including the Falicov-Kimball model, the auxiliary AIM (mapping to the Hubbard model in DMFT) and the atomic limit [Schäfer et al., 2016a]. In order to verify that these divergences are not just artifacts of a local treatment, irreducible non-local two-particle vertices were also studied in the dynamical cluster approximation, which shows similar divergences [Gunnarsson et al., 2016].

---

<sup>1</sup>For a vanishing hybridization function, the estimators of partition function sampling may be extended by insertions of local operators. For non-vanishing hybridization functions additional sampling in the perturbation part needs to be considered, resulting in worm sampling

In a different matter, certain peculiarities of the Luttinger-Ward functional [Luttinger and Ward, 1960] were uncovered.<sup>2</sup> More precisely, the (bold) perturbation expansion of the self-energy results in two converged branches, where only one of them has physical relevance. The branching of the self-energy relates to a breakdown of bold perturbation expansions. Gunnarsson *et al.* were able to link the multivaluedness of the Luttinger-Ward functional to the irreducible vertex divergences [Gunnarsson et al., 2017].

While the Luttinger-Ward functional and the Bethe-Salpeter equations describe certain two-particle processes on a diagrammatic level, a proper physical interpretation of the multivaluedness and the divergence lines was still missing. In the Hubbard model in DMFT, the vertex divergences occur in the metallic parameter region prior to the Mott transition. It seemed plausible to interpret these divergences as a breakdown of perturbation theory, shielding the non-perturbative metal-to-insulator transition [Schäfer et al., 2013a]. In order to verify this observation, vertex divergences are investigated in the following in the “plain” AIM, without the self-consistent feedback. As discussed in Chapter 2, the Kondo physics implicit to the AIM prohibits a metal-to-insulator transition. There is always Kondo resonance at the Fermi level.

In the specific AIM chosen for this work the DOS of the bath electrons is  $\rho(\epsilon) = (1/2D)\Theta(D - |\epsilon|)$ , with the half-bandwidth  $D = 10$  being the largest energy scale of the system. The hybridization is assumed to be  $\mathbf{k}$ -independent and set to 2 ( $V_{\mathbf{k}} = V = 2$ ) and the chemical potential is set to  $\mu = U/2$  (half-filled/particle-hole symmetric case). The choice of a box-shaped DOS and a  $\mathbf{k}$ -independent hybridization ensures that no particular features of  $\rho(\epsilon)$  or  $V$  will affect the study of irreducible vertex divergences, and the selected parameter set should guarantee, that the Kondo temperature of our AIM remains sizable with respect to the other energy scales, for the half-filled case considered.

We recall, that, in the case of SU(2)-symmetry, the Bethe-Salpeter equation can be diagonalized in the spin sector defining the usual charge/spin channels. For this work, the *charge* channel [ $\chi_c^{\nu_n\nu_n'\Omega_n} = \chi_{ph,\uparrow\uparrow}^{\nu_n\nu_n'\Omega_n} + \chi_{ph,\uparrow\downarrow}^{\nu_n\nu_n'\Omega_n}$ ] is of particular interest.

Note that  $\Omega_n$  will be set to zero throughout this work, and is therefore omitted hereinafter. This is done to perform comparisons of the results presented here to results of the recent literature [Schäfer et al., 2013b, Schäfer et al., 2016b], but also because the irreducible vertex divergences appear, systematically, at lower interaction values for  $\Omega_n = 0$ , compared to cases for  $\Omega_n \neq 0$ .

The Bethe-Salpeter equation in the charge channel reads:

$$\chi_c^{\nu_n\nu_n'} = \chi_{ph,0}^{\nu_n\nu_n'} - \frac{1}{\beta^2} \sum_{\nu_{n_1}\nu_{n_2}} \chi_{ph,0}^{\nu_n\nu_{n_1}} \Gamma_c^{\nu_{n_1}\nu_{n_2}} \chi_c^{\nu_{n_2}\nu_n'} \quad (4.1)$$

Here  $\Gamma_c^{\nu_n\nu_n'}$  is the irreducible vertex function in the charge channel, the bare susceptibility is given by  $\chi_{ph,0}^{\nu_n\nu_n'\Omega_n} = -\beta G(\nu_n)G(\Omega_n + \nu_n)\delta_{\nu_n\nu_n'}$ .

Inverting Eq. (4.1) and considering  $\Gamma_c$ ,  $\chi_{ph,0}$  and  $\chi_c$  as matrices of the fermionic Matsubara frequencies  $(\nu_n, \nu_n')$  leads to

<sup>2</sup>The Luttinger-Ward functional  $\Phi$  sums all closed two-particle irreducible diagrams. The self-energy  $\Sigma$  and the two-particle irreducible vertex  $\Gamma$  follow from functional derivatives of  $\Phi$  with respect to the one-particle Green’s function propagator  $G$ .

$$\Gamma_c = \beta^2 \left( [\chi_c]^{-1} - [\chi_{ph,0}]^{-1} \right). \quad (4.2)$$

It is obvious, hence, that all divergences of  $\Gamma_c$  must correspond to a singular  $\chi_c$ -matrix [Schäfer et al., 2016b] (typically no divergence is expected in  $[\chi_{ph,0}]^{-1}$ ). In fact, analyzing the matrix in its spectral representation, i.e., the basis of its eigenvectors,

$$[\chi_c]_{\nu_n \nu_{n'}}^{-1} = \sum_i V_i^c(i\nu_{n'})^* (\lambda_i)^{-1} V_i^c(i\nu_n) \quad , \quad (4.3)$$

leads to the one-to-one correspondence of an irreducible vertex divergence to a vanishing eigenvalue ( $\lambda_{i=\alpha} \rightarrow 0$ ) of the matrix  $\chi_c$  in the fermionic frequencies  $\nu_n, \nu_{n'}$ .

It is essential to recall [Schäfer et al., 2016b] that the way the divergence affects the frequency structure of  $\Gamma_c$  is determined by the non-zero components of the eigenvector  $V_\alpha^c(i\nu_n)$  associated to the vanishing eigenvalue  $\lambda_\alpha$ . This leads to a distinction of two classes of irreducible vertex divergences, a *global* one with an eigenvector  $V_\alpha^c(i\nu_n) \neq 0 \forall \nu_n$  and a *local* one, where only for a finite subset of frequencies  $V_\alpha^c(i\nu_n) \neq 0$  holds.

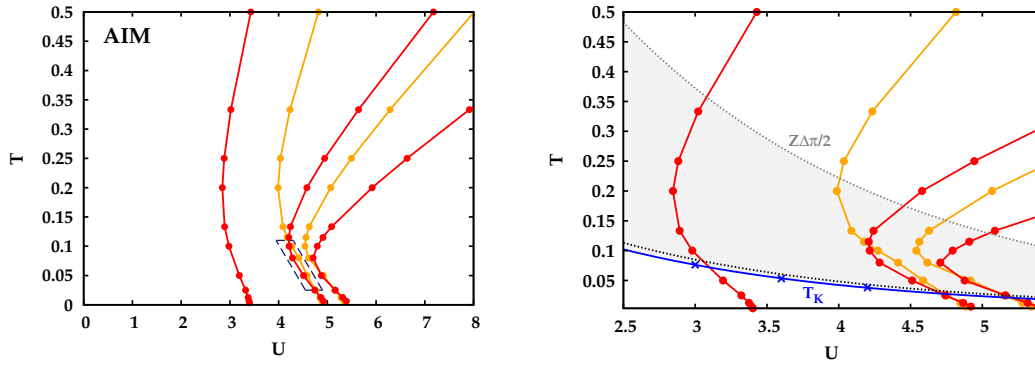


Figure 4.3: Left panel:  $T - U$  diagram of the AIM at half-filling, showing the first divergence lines along which the irreducible vertex functions diverge. For red lines this divergence takes place in the charge channel,  $\Gamma_c^{\nu_n \nu_{n'}}(\Omega_n=0)$ , along the orange lines simultaneous divergences in the charge and the particle-particle up-down channel,  $\Gamma_c^{\nu_n \nu_{n'}}(\Omega_n=0)$  and  $\Gamma_{pp,\uparrow\downarrow}^{\nu_n \nu_{n'}}(\Omega_n=0)$ , are observed. The dashed blue box marks the parameter region where the “atomic” ordering of divergence lines is violated. Right panel: A zoom of the  $T-U$  diagram of the AIM at half-filling is shown. The blue-solid line marks the Kondo temperature ( $T_K$ ), estimated from the rescaling of our numerical data for the magnetic susceptibility to the universal function given in [Krishna-murthy et al., 1980]. The black-dotted line represents an estimate for  $T_K$  obtained from an analytic expression [Hewson, 1993] valid in the limit  $D \gg U, T$ . An additional scale related to the Kondo screening, the half-bandwidth of the  $T \rightarrow 0$  Kondo peak ( $\frac{\pi}{2} Z \Delta$ ) [Hewson, 1993] is marked with a gray-dotted line, and is roughly 5-times larger than  $T_K$ . The light-gray shaded area can be regarded, thus, as the parameter region where the effects of the Kondo screening become visible.

We start to illustrate our numerical results by reporting in the  $T-U$  diagram of the AIM (Fig. 4.3 left panel)<sup>a</sup> the first (five) lines along which the two-particle irreducible

vertex diverges. These correspond to the interaction values  $\tilde{U}$  at given temperatures  $T$ , where an eigenvalue of the generalized susceptibility (charge or particle-particle up-down channel) vanishes, see Eq.(4.2) and Eq.(4.3). Specifically, the red lines mark irreducible vertex divergences taking place in the charge channel only, while orange lines represent divergences taking place in the charge and the particle-particle up-down channel simultaneously.

<sup>a</sup>Right panel of Fig. 4.3 replaced by zoom as opposed to original publication showing the divergence lines of the HM.

Finally, as for the theoretical understanding of the low- $T$  regime of the AIM, it is important to estimate the Kondo scale  $T_K$  and its possible connection to the properties of the irreducible vertex divergences. In Fig. 4.3 (right panel) a zoom of the  $T$ - $U$  diagram of the AIM is presented together with several estimates for the Kondo temperature  $T_K$ . In particular, the black dotted line represents an analytic estimate valid in the  $D \gg U, T$  parameter regime [Hewson, 1993] ( $T_K = 0.4107U(\frac{\Delta}{2U})^{1/2}e^{-\pi U/8\Delta + \pi\Delta/2U}$ , where in our AIM:  $\Delta = \pi\rho_0V^2 = \pi/5$ ), while the blue line is determined through the universal scaling of the numerical susceptibility data [Krishna-murthy et al., 1980]. We note that the two procedures yield extremely close estimates of  $T_K$ . The Kondo temperature marks however not a phase transition but a smooth crossover. Indeed, the screening processes associated with it become active already at temperatures larger than  $T_K$ . For instance, we see that the temperature below which the effects of the Kondo resonance become visible in the spectrum is  $T \lesssim Z\Delta\frac{\pi}{2}$ , the half-bandwidth of the central peak [Hewson, 1993]. We choose this scale to define the upper border of the corresponding crossover regime (shaded gray area in the  $T$ - $U$  diagram of Fig. 4.3 (right panel)). It is quite visible, how the bending of the divergence lines is essentially occurring in this parameter region.

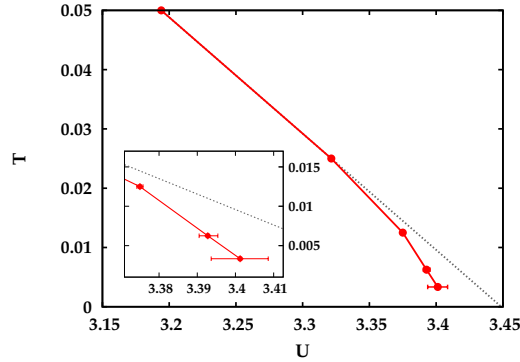


Figure 4.4: Zoom on the first red divergence line showing the low- $T$  behavior (for  $T \ll T_K$ ) which shows, that within the error bars obtained by a Jackknife analysis the line bends towards the  $U$  axis for  $T \rightarrow 0$ . Inset: Further zoom on the lowest temperatures, emphasizing the growth of the error bar with decreasing temperature.

Before proceeding with the interpretation of our results and their implications, we conclude this section with a detailed analysis of our data in the regime of the lowest temperatures accessible to our algorithm.



We start, thus, assessing the numerical accuracy of our results for the first red divergence line in the low- $T$  range ( $0.003\bar{3} < T < 0.05 < T_K \sim 0.07$ ). Our results are shown in Fig. 4.4, together with the corresponding error bars. The latter were obtained from a Jackknife error analysis [Efron and Stein, 1981]. From the error bars in the main plot and the inset of Fig. 4.4 it can be inferred, that the combined scaling ( $\beta^3$  of the CT-QMC sampling and  $\beta^2$  of the Matsubara frequency box of the vertex function for  $\Omega_n = 0$ ) prohibits us to access temperatures lower than  $T = 0.003\bar{3}$ , therefore not yielding any further informative results about the vertex divergences. However, the numerical precision for  $T > 0.003\bar{3}$  was sufficient to accurately define the low- $T$  behavior. In fact, we can compare our data with the dotted gray line, showing a linear extrapolation of the divergence line to  $T \rightarrow 0$  using the (higher) temperatures  $T = 0.05$  and  $T = 0.025$ . Even considering the growing error bars, the first divergence line shows a progressive leftwards deviation from the linear extrapolation when reducing the temperature. This is evidently completely inconsistent with an infinite value of  $\tilde{U}$  of the divergence line endpoint for  $T \rightarrow 0$ .

Indeed, our study could clarify a set of relevant questions about the interpretation and the consequences of the divergences of the two-particle irreducible vertex functions. In particular, our results rule out that the Mott-Hubbard transition plays a crucial role as the origin of the multiple divergence lines. This limits the previously proposed interpretation [Schäfer et al., 2013b] of the vertex divergences as “precursors” of the MIT in the sense of a necessary condition for vertex divergences to occur, consistently with the physical interpretation presented in [Gunnarsson et al., 2016, Gunnarsson et al., 2017]. By a thorough analysis of the low-temperature sector, we could ascribe, at the same time, important characteristics of the vertex divergences, such as their structure in Matsubara frequency space and the re-entrance of the divergences line, to the screening processes of the local impurity moment occurring when approaching  $T_K$ . Moreover, our data for  $T \ll T_K$  has unveiled a perfect scaling of the singular eigenvectors,<sup>a</sup> allowing us to extrapolate the  $T = 0$  behavior of the vertex divergences on the real-frequency axis.

<sup>a</sup>For results see [Chalupa et al., 2017].

## Technical Considerations

From a technical viewpoint the calculation of divergences of the generalized susceptibility is somewhat similar to the procedure followed by diagrammatic extensions to DMFT. Both approaches rely on local one- and two-particle Green’s functions of the AIM as an input, generating eigenvalues in the former case and non-local diagrams in the latter. Usually the extraction of two-particle functions from the impurity problem is numerically the most expensive operation. Thus, computationally, methods building on top of the impurity result may be considered “post-processing”.

Utilizing CT-QMC algorithms as impurity solvers, however, only returns stochastic local Green’s functions including statistical uncertainties. Thus, in principle, a proper error propagation in the aforementioned post-processing methods needs to be considered.<sup>3</sup>

<sup>3</sup>In a similar fashion, analytic continuation methods may be considered as post-processing steps to obtaining results from the AIM, requiring a proper error-propagation. However, MaxEnt implicitly considers stochastic error bars in the weighted least-square value  $\chi^2$ .

Most of the time, however, the treatment of statistical uncertainties is ignored due the complexity of the methods.

Instead of conducting the actual error propagation for any of these “post-DMFT” methods, it is more feasible to generate a set of binned data for the input quantity. The data bins are in principle all identical, but include different stochastic noise. The post-DMFT methods are then calculated individually for each bin and an averaging procedure is applied to the output quantity in order to generate error estimates. For these estimates to be statistically representative, the number of bins should be on the order of  $N \gtrsim 30$ . As Monte Carlo bins may display some autocorrelation effects (see Chapter 3.3.9), it is more suitable to employ re-sampling methods instead of naive error estimates. Two re-sampling methods are noteworthy: Bootstrap [Efron, 1979] and Jackknife [Quenouille, 1956]. Bootstrap attempts to sample the distribution for the output quantity by evaluating the function (i.e. the post-DMFT method) a large number of times (typically  $M \sim 1000$ ) for pre-averaged bins generated from selecting with replacement  $N$  bins of the set of bins. Obviously, bootstrap is not feasible for post-DMFT methods due to the high computational costs of a single function call. The  $(n-1)$  Jackknife procedure, on the other hand, evaluates the function exactly  $M = N + 1$  times, by considering pre-averaged bins generated by always omitting one of the  $N$  bins at a time (another function evaluation is required for calculating the naively averaged bin).

From the Jackknife analysis of the results featured in the above work, the following empirical observation can be made: Jackknife estimates for high-temperature results following from binned two-particle functions behave similar to naive error estimates - when applying post-DMFT methods to low temperatures, however, a proper Jackknife analysis is necessary.

## 4.3 Dual Fermion for the Hubbard Model

### 4.3.1 Three-particle Corrections

*Parts of this section (marked by a vertical sidebar) have been already published in: T. Ribic, P. G., S. Isakov, M. Wallerberger, G. Rohringer, A. Rubtsov, E. Gull and K.Held; Role of three-particle vertex within dual fermion calculations. Phys. Rev. B. 96, 235127 (2017)*

The previous two sections discussed various single-orbital models based on insight obtained from the local one- and two-particle Green’s functions. While the Mott transition in the Hubbard model can be observed from the one-particle Green’s function, determining the magnetic ordering follows the two-particle Green’s function. When considering diagrammatic extensions to DMFT, which build upon irreducible subsets of the local vertex, such as DFA, some care needs to be taken with respect to vertex divergences. DF on the other hand, constructs diagrams from the full vertex function  $F$  and does not suffer from divergences in the irreducible subsets. However, the local full vertex function  $F$  becomes the interaction vertex of the dual fermions. In this case, the equation of motion couples local  $n$ -particle vertex functions to the dual fermions. A priori there is no justification for

truncating the Taylor expansion of the dual action (see Chapter 2.5.2) at the two-particle level.

In the weak-coupling limit, three-particle corrections to DF may be negligible due to the three-particle vertex scaling with  $U^3$ . In the strong coupling limit, however, higher-order vertex functions become dominant and may contribute to the DF corrections.<sup>4</sup> Historically, the importance of three-particle contributions was debated and some arguments became popular in order to neglect these contributions. Actual calculations were mostly avoided due to the computational complexity of three-particle vertex functions. Hafermann *et al.* only found weak effects of three-particle diagrams on the leading eigenvalue of the Bethe-Salpeter equations [Hafermann *et al.*, 2009].

This debate was renewed, when Ribic *et al.* investigated the effects of three-particle corrections to the self-energy in DF for the Falicov-Kimball model [Ribic *et al.*, 2017b].<sup>5</sup> What remained an open question is to what extent three-particle corrections in DF need to be considered in the Hubbard model. In the following the dominant three-particle corrections to the two-dimensional single-orbital Hubbard model within DF are investigated.

Let us start by formally defining the local three-particle Green's function

$$G_{\nu_1\nu\nu'\omega}^{(3)\sigma_1\sigma_2\sigma_3} = \langle c_{\sigma_1}^\dagger(\nu_1)c_{\sigma_1}(\nu_1)c_{\sigma_2}^\dagger(\nu - \omega)c_{\sigma_2}(\nu)c_{\sigma_3}^\dagger(\nu')c_{\sigma_3}(\nu' - \omega) \rangle, \quad (4.4)$$

with three fermionic Matsubara frequencies  $\nu_1, \nu, \nu'$  and one bosonic (transfer) frequency  $\omega$ .

To obtain the fully connected  $n$ -particle vertex functions  $F^{(n)}$  from  $G^{(n)}$ , first any disconnected contribution to the propagators needs to be removed. Subsequently we need to amputate the outer legs of the remaining, fully connected three-particle Green's function  $G_C^{(n)}$ . On the two-particle level, there are only two disconnected contributions to the Green's function  $G^{(2)}$ , both consisting of a product of two one-particle Green's functions:  $G^{(1)}G^{(1)}$ . On the three-particle level, there is much more variety among the disconnected terms. A three-particle Green's function  $G^{(3)}$  contains terms disconnected into three one-particle propagators,  $G^{(1)}G^{(1)}G^{(1)}$  (for example  $\delta_{\omega,0} G_{\nu_1}^{(1)\sigma_1}G_{\nu}^{(1)\sigma_2}G_{\nu_3}^{(1)\sigma_3}$ ), as well as other terms disconnected into a one-particle and a connected two-particle Green's function,  $G^{(1)}G_C^{(2)}$  (for example  $G_{\nu_1}^{(1)\sigma_1}G_C^{(2)\sigma_2\sigma_3}$ ), as well as a fully connected term.

Starting from the dual action (see Chapter 2.5.2), a generalized Schwinger-Dyson equation of motion can be defined, which couples local vertices of arbitrary order to dual vertices:

$$\tilde{\Sigma}_k = - \sum_{n=2}^{\infty} \sum_{k_2, k_3, k_4, \dots} \frac{(-1)^n}{n!(n-1)!} F^{(n)}(k_2, k, k_4, k_3, \dots) \tilde{\mathcal{G}}^{(n)}(k, k_2, k_3, k_4, \dots) / \tilde{\mathcal{G}}_k \quad (4.5)$$

Diagrammatically, the interpretation of the above equation is straightforward: any dual

<sup>4</sup>In the atomic limit, DF corrections vanish as the vertices are suppressed by the vanishing non-local dual fermion single-particle propagators.

<sup>5</sup>The local vertex functions of the Falicov-Kimball model can be calculated analytically up to arbitrary order. At half-filling, odd-ordered vertex functions vanish, which is why the study was conducted out-of-half-filling.

self-energy diagram has to start with an interaction vertex. Since there are infinitely many types of interaction vertices, an infinite sum of contributions to the self-energy exists. Note that the dual Green's functions  $\tilde{\mathcal{G}}^{(n)}$  describe all possible diagrams which can be built from the original local vertices  $F^{(n)}$ . The remaining external leg  $\tilde{\mathcal{G}}_k$  of the dual Green's function has to be amputated to generate a self-energy diagram.

In Eq. (4.5) full dual  $n$ -particle Green's functions appear (not connected ones). However, any disconnected contribution to the Green's function where a dual one-particle Green's function closes a loop locally does not influence the dual self-energy if the one-particle dual Green's functions are required to be completely non-local, i.e.  $\sum_{\mathbf{k}} \tilde{\mathcal{G}}_{\mathbf{k}\nu\sigma} = 0$ . For this reason, e.g. no Hartree or Fock term appears for the dual fermions when truncating on the two-particle vertex level.

In this paper, we consider local interaction terms up to the three-particle vertex.

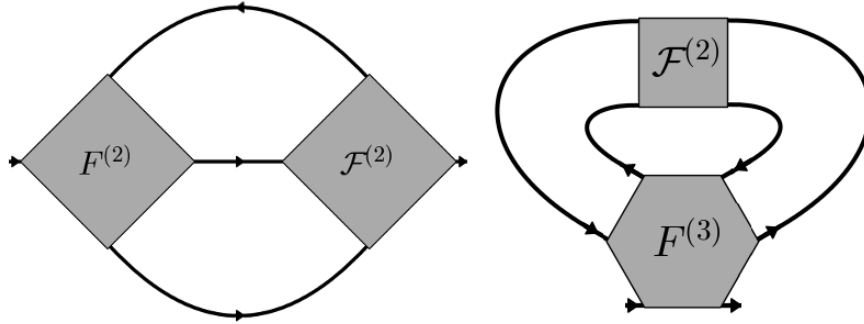


Figure 4.5: Left: Feynman-diagrammatic representation of the dual self-energy in terms of the local two-particle vertex  $F^{(2)}$ , the dual propagator  $\tilde{\mathcal{G}}$  (line) and the full DF vertex  $\mathcal{F}^{(2)}$  (obtained, e.g., through a ladder series). Right: Feynman-diagrammatic representation of an additional contribution to the dual self-energy that includes the local three-particle vertex of the real fermions  $F^{(3)}$ .

Thus, within our approximation, and taking into account all combinatorial prefactors our dual self-energy from the two- and three-particle vertex reads

$$\begin{aligned} \tilde{\Sigma}_k \approx & - \sum_{k_2, k_3, k_4} \frac{1}{2} F^{(2)}(k_2, k, k_4, k_3) \tilde{\mathcal{G}}_{0, k_2} \tilde{\mathcal{G}}_{0, k_3} \tilde{\mathcal{G}}_{0, k_4} \mathcal{F}^{(2)}(k, k_2, k_3, k_4) \\ & + \sum_{k_1, k_2, k_3, k_4} \frac{1}{4} F^{(3)}(k, k, k_2, k_1, k_4, k_3) \tilde{\mathcal{G}}_{0, k_1} \tilde{\mathcal{G}}_{0, k_2} \tilde{\mathcal{G}}_{0, k_3} \tilde{\mathcal{G}}_{0, k_4} \mathcal{F}^{(2)}(k_1, k_2, k_3, k_4). \end{aligned} \quad (4.6)$$

The diagrammatic representation of the first line is given in Fig.4.5 (left panel); it corresponds to standard DF and  $n = 2$  in Eq. (4.5). The new contribution in the second line stems from  $n = 3$  and is illustrated in Fig. 4.5 (right panel).

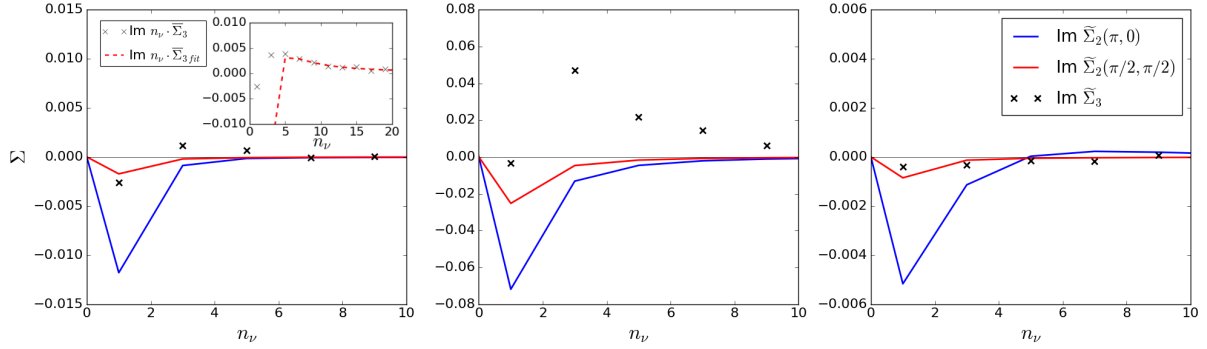


Figure 4.6: Imaginary part of the dual self-energy correction of the standard DF theory  $\tilde{\Sigma}_{\mathbf{k}\nu}$  for two  $\mathbf{k}$ -points and the correction  $\tilde{\Sigma}_3$  based on the three particle vertex and diagram Fig. 4.5. From left to right, we present data for  $U = 1, \beta = 8, n = 1$ ;  $U = 2, \beta = 8, n = 1$  and  $U = 1, \beta = 15, n = 0.8$ . Inset in the first figure shows fitting function used to estimate high-frequency behavior.

Let us now present the numerical results for one-shot DF calculations based on converged DMFT baths for the two-dimensional Hubbard model. For every discussed point, Fig. 4.6 shows the (Matsubara) frequency dependence of the DF self-energy correction.<sup>a</sup>

This self-energy needs to be added to the DMFT self-energy to obtain the physical self-energy of the Hubbard model. We compare in Fig. 4.6 the standard DF self-energy  $\tilde{\Sigma}_{2\mathbf{k}\nu}$  [first line of Eq. (4.5)] at the nodal  $(\pi/2, \pi/2)$  and antinodal  $(\pi, 0)$   $\mathbf{k}$ -point of the Fermi surface with the selected additional contribution based on the three-particle vertex [second line of Eq. (4.5)]. This specific three-particle correction couples the two-particle ladder diagrams with the three particle vertex, see Fig. 4.5, and is  $\mathbf{k}$ -independent.

<sup>a</sup>The presented DF results are without self-consistency. However, for the parameters considered, imposing an inner self-energy self-consistency (not shown) leads only to minor modifications for  $U = 1$  and reduces both two- and three-particle corrections to about half their values for  $U = 2$ . A closer investigation should also include an outer self-consistency with an update of the vertex and local problem, but is beyond the scope of the present paper.

Let us now discuss and interpret these results. At high temperatures [ $(U = 1, \beta = 8, n = 1)$  and  $(U = 2, \beta = 8, n = 1)$ ] and for the doped system [ $(U = 1, \beta = 15, n = 0.8)$ ], the standard dual Fermion self-energy  $\tilde{\Sigma}_2$  is only a relatively small correction to the DMFT self-energy [ $\text{Im}\Sigma_{n\nu=1}^{\text{loc}} = -0.14, -0.96$  and  $-0.075$ , respectively]. For  $U = 1$ , the DF corrections based on the three-particle vertex  $\tilde{\Sigma}_3$  are again considerably smaller than  $\tilde{\Sigma}_2$ . Note that this does not hold for all  $\mathbf{k}$ -points. For example, the scattering rate due to  $\text{Im}\tilde{\Sigma}_3$  is larger than for  $\text{Im}\tilde{\Sigma}_2$  for  $\mathbf{k} = (\pi/2, \pi/2)$ . But  $\tilde{\Sigma}_2$  is much larger for  $\mathbf{k} = (\pi, 0)$ , and also in general the variation of  $\tilde{\Sigma}_2$  with  $\mathbf{k}$  is much larger than  $\tilde{\Sigma}_3$ . While the three-particle vertex corrections appear small in the lowest Matsubara frequency,<sup>a</sup> Fig. 4.6 reveals that  $\tilde{\Sigma}_3$  is actually comparable in magnitude to  $\tilde{\Sigma}_2$  when taking the second (not the first) Matsubara frequency into account. This is particularly true for  $(U = 2, \beta = 8, n = 1)$  which happens to have a particularly small  $\tilde{\Sigma}_3$  at the lowest Matsubara frequency.

<sup>a</sup>For results see [Ribic et al., 2017a].

For different points in the parameter space of the Hubbard model, we find sizable corrections to the DF self-energy when including specific three-particle diagrams. For high enough temperatures and for the doped model, these three-particle vertex corrections are considerably smaller than the standard DF self-energy. In particular they are smaller than the two-particle DF corrections for the nodal point  $(\pi/2, \pi/2)$ . In this parameter regime, our calculations indicate a proper convergence of the DF theory when going to higher orders in the expansions (from the  $n = 2$ - to the  $n = 3$ -vertex).

For higher interaction values, this picture changes. Spin fluctuations are the dominant driving force influencing the self-energy on the two-particle level. The same kind of strong two-particle ladder contributions (the same kind of spin fluctuations) couple additionally via the three-particle vertex to an additional self-energy correction. This correction term yields an additional  $\mathbf{k}$ -independent contribution to the imaginary part of the self-energy, which can be interpreted as additional scattering at spin fluctuations. The considered three-particle vertex correction term also gives a  $1/\nu$  asymptotic behavior which is absent in standard DF and calls for a closer investigation.

### Technical Considerations

When analyzing the asymptotic behavior of self-energy corrections in DF (or DFA) or when attempting to evaluate self-energy corrections at low temperatures, it is essential to calculate local two- and three-particle vertex functions with a reasonable high-frequency behavior.

When comparing local two/three-particle Green's functions extracted from weak-coupling based CT-QMC algorithms, such as CT-INT or CT-AUX to two/three-particle Green's functions extracted from strong-coupling based CT-QMC algorithms (i.e. CT-HYB), at first glance no major differences are visible in the high-frequency region. This is because the (implicitly attached) outer legs of the two/three-particle Green's function essentially suppress all asymptotical structure. However, once subtracting disconnected parts and amputating outer legs, i.e. calculating vertex functions, the asymptotical structure becomes crucial. In this case, vertices extracted from weak-coupling algorithms display a significantly better high-frequency behavior than their strong-coupling counterpart,<sup>6</sup> as illustrated in Figure 4.7 for the two-particle vertex. This can be traced back to the differences in the Monte Carlo estimators. While the weak-coupling estimators construct  $n$ -particle Green's functions from one-particle Green's functions with an error suppression of  $1/i\nu^2$ , the strong-coupling estimators construct them from single-particle Green's functions with a constant Monte Carlo error. The superiority of weak-coupling vertices in one-band models over strong-coupling vertices calculated from naive estimators was already pointed out by Gull *et al.* [Gull et al., 2011]. In strong-coupling solvers this issue was partially alleviated by the introduction of improved estimators. A more detailed discussion is found in Chapter 3.2.2. CT-HYB estimators (i.e. symmetric improved estimators) with the same error behavior as the CT-INT estimators are discussed in Chapter 3.4. For the analysis of dual fermion corrections the high-frequency regions of the vertex functions are mostly irrelevant due to dual propagators decaying with  $1/i\nu^2$ .

<sup>6</sup>This was also found for two-particle vertices calculated from Hirsch-Fye data.

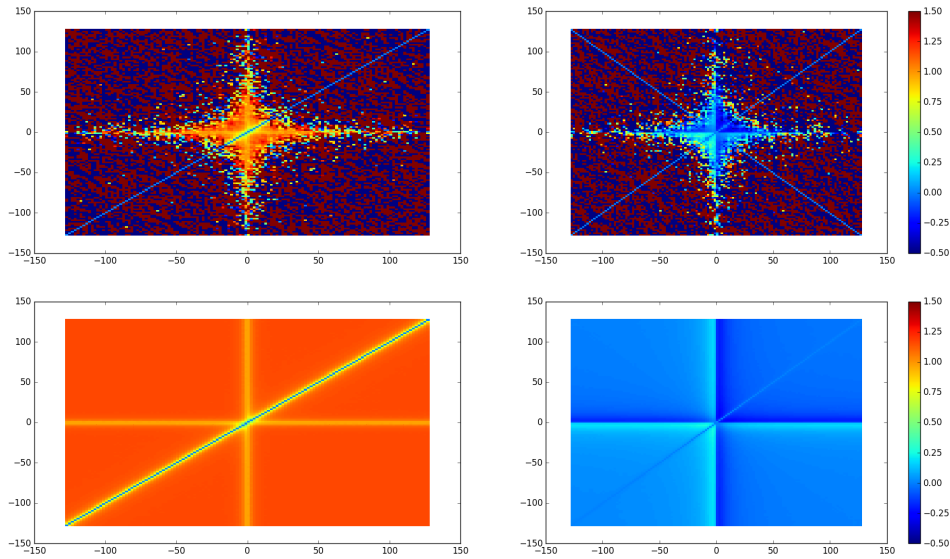


Figure 4.7: Two-particle vertex function  $\Re F_{\uparrow\uparrow}^{\nu,\nu',0}$  (left) and  $\Re F_{\uparrow\downarrow}^{\nu,\nu',0}$  (right) for  $U = 1$ ,  $\beta = 15$ ,  $n = 0.8$ . Data extracted from CT-HYB (upper row) shows significantly more noise in the high-frequency region than data extracted from CT-AUX (lower row).

### 4.3.2 Dual Fermion Self-consistency

In Chapter 2.5 several diagrammatic extensions to DMFT were introduced in an attempt to model non-local correlation effects for a given lattice. Most of these extensions assume a certain subset of two-particle diagrams to be local. By connecting these two-particle vertices with non-local one-particle propagators, non-local momentum dependent self-energies can be calculated. This self-energy, however, again indicates an updated one-particle Green’s function, which may differ from the initial propagator. This already suggests that the equations intrinsic to the diagrammatic extensions (mostly Bethe-Salpeter or Parquet equations and the Schwinger-Dyson equation) need to be calculated in a self-consistent fashion, updating the one-particle propagators. This self-consistency cycle on the one-particle level is referred to as “inner” self-consistency.<sup>7</sup> When considering the two-particle vertex functions fixed, converged DMFT simulations may be a reasonable starting point. This and the fact that the local DMFT corrections are included is why non-local diagrammatic methods are often referred to as diagrammatic extensions to DMFT. Nevertheless, in principle, also an update of the vertex function itself is necessary in order to assure consistency on the one- and two-particle level. This second self-consistency cycle on the two-particle level is referred to as “outer” self-consistency.

Most of the present-day results calculated with DF or DFA are based on “single-shot” calculations, that is, making use of vertex functions following a converged DMFT

<sup>7</sup>Typically, inner self-consistency schemes are considered in parquet-DFA and some DF implementations. Ladder-DFA, on the other hand, uses Moriyasque  $\lambda$ -corrections instead.

calculation (i.e. omitting the outer self-consistency) and calculating the non-local equations for the non-local self-energy once (i.e. omitting the inner self-consistency).

This work attempts to explore the effects of inner- and outer self-consistency within DF for the single-orbital Hubbard model at half-filling. Figure 4.8 illustrates the self-consistency cycle of a full DF calculation. Starting from one- and two-particle propagators extracted from DMFT, first the inner self-consistency loop of DF is converged. In a next step an updated hybridization function for the local reference problem is calculated with

$$\Delta(i\nu) = \Delta_{\text{old}}(i\nu) + G_{\text{loc}}^{-1}(i\nu) - \left[ \frac{1}{N_k} \sum_{\vec{k}}^{\text{BZ}} G(\vec{k}, i\nu) \right]^{-1}, \quad (4.7)$$

where  $\Delta_{\text{old}}(i\nu)$  and  $G_{\text{loc}}(i\nu)$  follow from the previous AIM and  $G(\vec{k}, i\nu)$  is the momentum-dependent one-particle Green's function including DF corrections:

$$G(\vec{k}, i\nu) = \left[ i\nu - \varepsilon_{\vec{k}} - \Sigma_{\text{loc}}(i\nu) - \tilde{\Sigma}(\vec{k}, i\nu) \right]^{-1}. \quad (4.8)$$

The new hybridization function  $\Delta(i\nu)$  is used to determine the local one- and two-particle propagators from the AIM. The inner- and outer self-consistency loops are repeated until convergence (i.e.  $\Delta(i\nu) = \Delta_{\text{old}}(i\nu)$ ).<sup>8</sup> Relation (4.7) constructs the physical bath for the impurity problem corresponding to the lattice problem described by DF in analogy to the DMFT equations.

Figure 4.9 shows which parameters were considered in the phase diagram of the two-dimensional Hubbard model. The antiferromagnetic ordering temperature  $T_N$  of DMFT calculated with Hirsch-Fye QMC is supplied for reference [Kuneš, 2011].

Whenever DF corrections are negligible with respect to DMFT, the inner and outer self-consistency loops converge well. This holds true for high-temperatures above the antiferromagnetic ordering temperature  $T_N$  of DMFT, where correlation effects are generally small.

Approaching the DMFT magnetic ordering temperature  $T_N$  from the paramagnetic side, DF corrections to the DMFT self-energy become larger. The feedback to the outer self-consistency loop weakens correlation effects. This is illustrated in Figure 4.10 (top row), where the local self-energies following converged outer self-consistency DF calculations are generally smaller in magnitude than the converged DMFT self-energies. While local correlations become less pronounced, also the strength of the hybridization function needs to be taken into account. Considering the local Green's functions in Figure 4.10 (bottom row), the interpretation needs to be adapted. At weak interactions ( $U = 1$ ), the local Green's function becomes smaller in magnitude, just as the self-energy, which can be attributed to a larger hybridization function (not shown). At intermediate- ( $U = 2$ ) and strong interaction ( $U = 3$ ), the hybridization no longer compensates the changes in the local self-energy. Instead, the Green's functions become larger in magnitude for the converged DF calculations. Looking at Figure 4.11, the interacting density of states for

<sup>8</sup>In the original DF work, Rubtsov *et al.* suggest a different outer self-consistency condition [Rubtsov *et al.*, 2008], by requiring non-locality of the dual propagator at each step. In this scheme, out of half-filling the chemical potential needs to be recalculated to assure the correct filling. To this point no conclusive statement about the validity of one or the other scheme can be made.



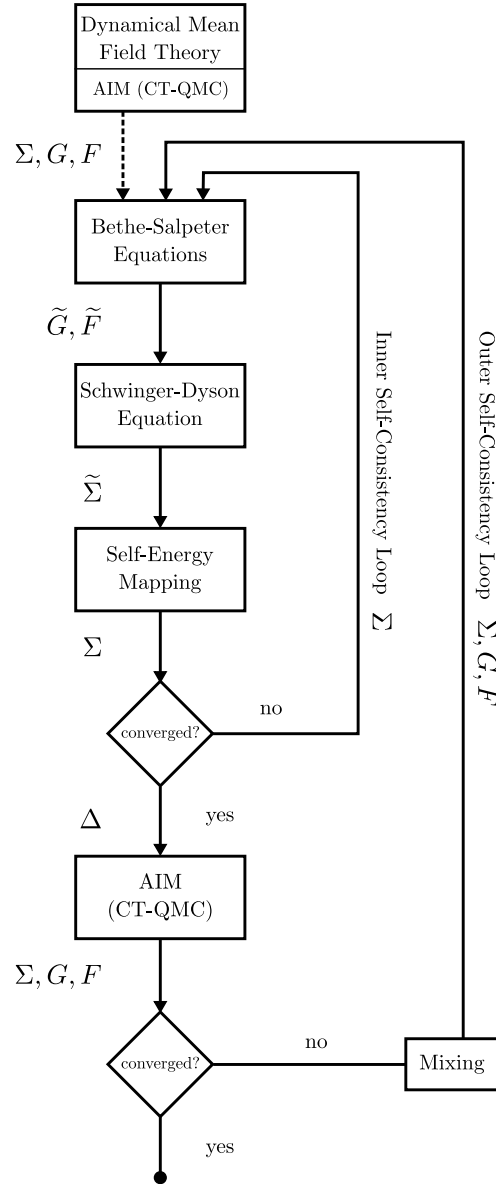


Figure 4.8: Illustration of a full DF cycle with DMFT as a possible starting point. The Bethe-Salpeter equations, the Schwinger-Dyson equation and the self-energy mapping are part of the inner self-consistency cycle of DF. Here, only the one-particle propagators are updated successively with the resulting momentum dependent self-energies. Upon convergence, the outer self-consistency is obtained by solving an AIM for an updated hybridization function yielding new two-particle vertices. The actual self-energy mapping and the actual hybridization function update are not specified.

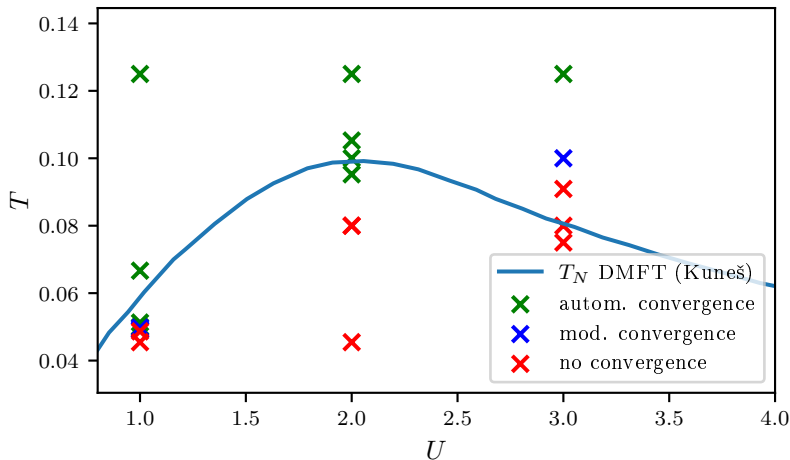


Figure 4.9: Analysis of the DF self-consistency for the two-dimensional Hubbard model at different parameters in units of  $4t = 1$ . The antiferromagnetic ordering temperature  $T_N$  for DMFT [Kuneš, 2011] is given for reference. Parameter sets converged using inner- and outer self-consistency are shown in green crosses. Parameter sets where manual modifications to the self-consistency loops were necessary are shown in blue crosses. Parameter sets which did not converge are shown in red crosses.

intermediate- and strong coupling display a larger weight at the Fermi energy. Conclusive statements about the changes in the effects of the self-energy and the hybridization functions onto the local physics are yet to be made.

What remains to be discussed, is the numerical stability of the inner- and outer self-consistency equations. Generally, the Mermin-Wagner theorem states the absence of any long-range magnetic ordering in the two-dimensional Hubbard model. It seems reasonable to associate this absence with the divergence of the spin-susceptibility being shifted to zero temperature, i.e.  $T_N \rightarrow 0$ . Nevertheless, the inner self-consistency loop for single-shot (in terms of outer self-consistency) DF calculations based on DMFT below the antiferromagnetic ordering temperature of DMFT does not seem to converge well. This can be attributed to physical divergences in the full vertex function  $F$ , which are intrinsic to DMFT. In this case, the DF self-energy corrections can become significantly large and the self-consistency loops start to oscillate wildly after a few iterations. Intuitively, it is problematic to use DMFT as a starting point for non-local extensions, whenever local susceptibilities diverge due to the finite  $T_N$  in DMFT. Instead, it may be beneficial to consider impurity clusters and DCA in combination with DF [Iskakov et al., 2017].<sup>9</sup>

### Technical considerations

The outer self-consistency loop requires numerical solutions to multiple impurity models. Unlike the impurity problem of DMFT, in this case the AIM needs to be solved for

<sup>9</sup>The cluster must be chosen sufficiently large and with a reasonable shape to avoid unphysical effects, which then would propagate into the DF equations.

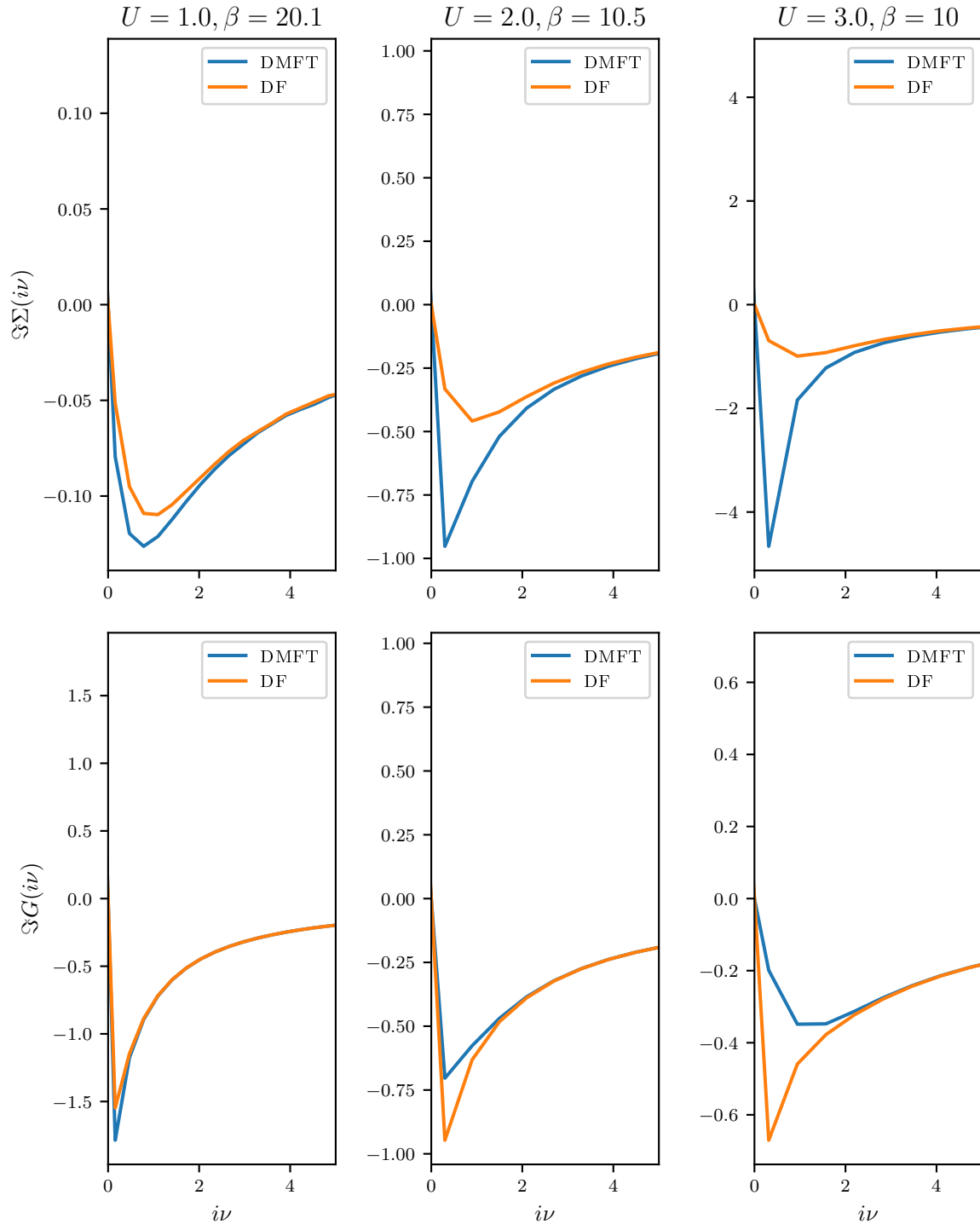


Figure 4.10: Impurity self-energies (top row) and impurity Green's functions (bottom row) for selected parameter sets of Figure 4.9. Blue lines represent self-energies for converged DMFT calculations, while orange lines represent self-energies for converged DF calculations with outer self-consistency. The data points considered at interaction values  $U = 1$  (left column),  $U = 2$  (middle column) and  $U = 3$  (right column) each represent the lowest temperature result with converged outer DF self-consistency available.

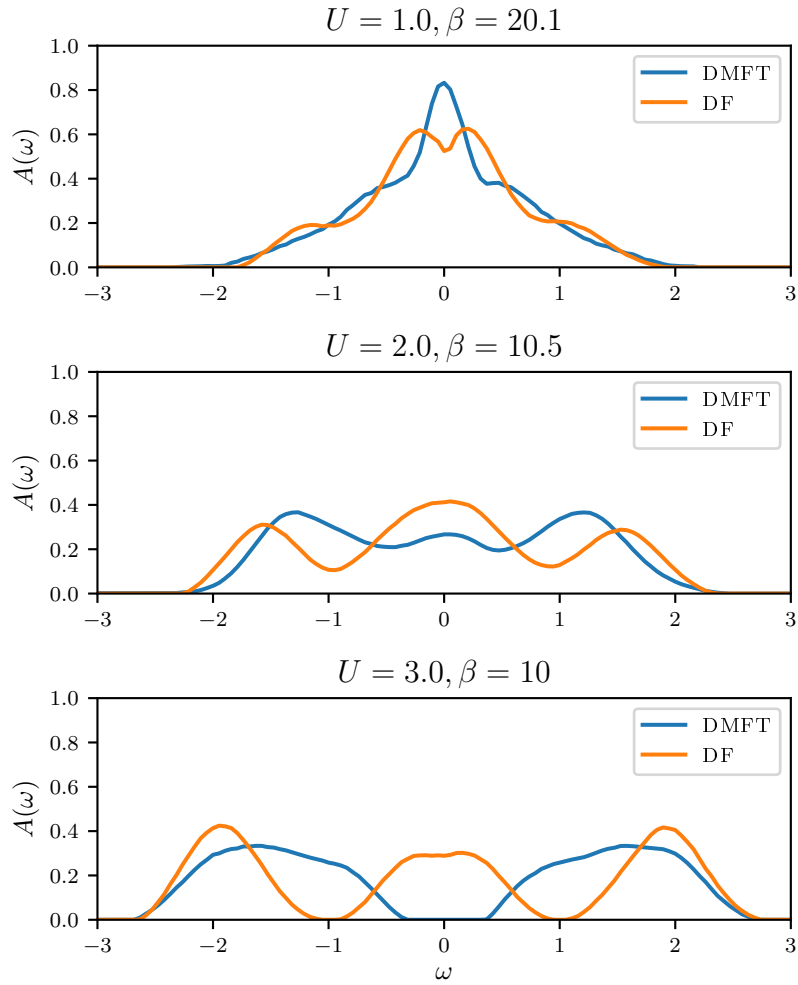


Figure 4.11: Spectral function  $A(\omega)$  for the impurity Green's functions of Figure 4.10 calculated with MaxEnt. When outer self-consistency is obtained, the local spectral function of the impurity problem is equivalent to the momentum-integrated spectral function including the DF corrections, i.e.  $A(\omega) = (1/N_k) \sum_k A(\vec{k}, \omega)$ .

one- and two-particle Green's functions. As discussed in the previous section, the vertex functions extracted from CT-HYB data display a poor asymptotical structure, which is however suppressed by the strong decay of the non-local dual propagators. In order to assess the inner- and outer self-consistency of DF, the CT-HYB algorithm is employed.

While diagrammatic extensions like DF or D $\Gamma$ A operate in the Matsubara formalism, CT-QMC algorithms operate in the imaginary time formalism. The implicit Fourier transform to Matsubara frequencies during the Monte Carlo sampling is straight-forward. On the other hand, some care needs to be taken during the back-transform of Matsubara hybridization functions to the imaginary time domain, which is necessary for the outer self-consistency in DF. Like Green's functions, hybridization functions display a jump in imaginary time at  $\tau = 0$  and respectively a  $1/i\nu$  decay in Matsubara frequencies. This relatively slow decay in Matsubara frequencies needs to be subtracted prior to the Fourier transform in order to avoid unphysical oscillations more generally known as the Gibbs phenomenon. In the imaginary time domain a constant offset is added. The procedure of considering suitable models for Fourier transforms is standard in DMFT and is mentioned here for reasons of completeness.



# Chapter 5

## Multi-orbital Applications

### 5.1 Spin-susceptibilities in the AIM

*Parts of this section (marked by a vertical sidebar) have been already published in: P.G., M. Wallerberger, E. Gull, A. Hausoel, G. Sangiovanni and K. Held; Continuous-time quantum Monte Carlo using worm sampling. Phys. Rev. B. 92, 155102 (2015)*

In the previous chapter the single-orbital Hubbard model was investigated with respect to local- and non-local correlation effects. While the Mott-Hubbard metal-to-insulator transition is described sufficiently by local correlation effects, magnetic ordering is mostly determined by non-local correlation effects. The variety of different phases follows a relatively simple model Hamiltonian, which is determined by a scalar hopping amplitude  $t$  and a Coulomb repulsion  $U$  in the  $SU(2)$ -symmetric case. More so, in the single-orbital case, the  $SU(2)$ -symmetric Slater-Kanamori interaction reduces to the density-density interaction. In the multi-orbital case, on the other hand, the Slater-Kanamori interaction features additional spin-flip and pair-hopping terms, which are not present in the multi-orbital density-density interaction.<sup>1</sup> A detailed discussion is found in Chapter 2.3 and Appendix D. Calculating two-particle Green's functions for the multi-orbital Hubbard model with a diagonal hybridization function by conventional CT-HYB algorithms results in serious limitations. These are extensively discussed in Chapter 3. More precisely, contributions to the two-particle Green's function with an outer leg structure resembling the spin-flip and pair-hopping terms cannot be sampled.

However, for non-density-density interactions, such terms are indeed present in the two-particle Green's function  $G^{(2)}$ . One can immediately see this for the  $SO(n) \otimes SU(2)$ -conserving Slater-Kanamori interaction: here, the spin susceptibility is invariant under spatial rotations, such that, e. g.,  $\langle S_z(\tau)S_z(0) \rangle = \langle S_x(\tau)S_x(0) \rangle$ . The spin susceptibility in

---

<sup>1</sup>The density-density interaction becomes  $SU(2)$ -symmetric in the multi-orbital case when assuming  $J = 0$ . In this case, only intra-orbital couplings  $U$  and inter-orbital couplings  $V$  remain. The Hund's coupling, effectively decreasing the inter-orbital coupling, also vanishes.

$z$ -direction relates to flavor-diagonal terms of  $G^{(2)}$ :

$$\begin{aligned} \langle S_z^i(\tau) S_z^j(0) \rangle &= \frac{1}{4} \langle (n_{\uparrow}^i(\tau) - n_{\downarrow}^i(\tau))(n_{\uparrow}^j(0) - n_{\downarrow}^j(0)) \rangle \\ &= \frac{1}{4} \langle c_{i\uparrow}^\dagger(\tau) c_{i\uparrow}(\tau) c_{j\uparrow}^\dagger(0) c_{j\uparrow}(0) - c_{i\uparrow}^\dagger(\tau) c_{i\uparrow}(\tau) c_{j\downarrow}^\dagger(0) c_{j\downarrow}(0) - \\ &\quad c_{i\downarrow}^\dagger(\tau) c_{i\downarrow}(\tau) c_{j\uparrow}^\dagger(0) c_{j\uparrow}(0) + c_{i\downarrow}^\dagger(\tau) c_{i\downarrow}(\tau) c_{j\downarrow}^\dagger(0) c_{j\downarrow}(0) \rangle. \end{aligned} \quad (5.1)$$

All terms can be obtained in conventional CT-HYB by removing one hybridization line for orbital  $i$  and one for orbital  $j$ . The spin susceptibility in  $x$ -direction on the other hand manifests itself as spin flip terms in  $G^{(2)}$ , which are off-diagonal:

$$\begin{aligned} \langle S_x^i(\tau) S_x^j(0) \rangle &= \frac{1}{4} \langle (S_+^i(\tau) + S_-^i(\tau))(S_+^j(0) + S_-^j(0)) \rangle \\ &= \frac{1}{4} \langle c_{i\uparrow}^\dagger(\tau) c_{i\downarrow}(\tau) c_{j\uparrow}^\dagger(0) c_{j\downarrow}(0) + c_{i\uparrow}^\dagger(\tau) c_{i\downarrow}(\tau) c_{j\downarrow}^\dagger(0) c_{j\uparrow}(0) + \\ &\quad c_{i\downarrow}^\dagger(\tau) c_{i\uparrow}(\tau) c_{j\uparrow}^\dagger(0) c_{j\downarrow}(0) + c_{i\downarrow}^\dagger(\tau) c_{i\uparrow}(\tau) c_{j\downarrow}^\dagger(0) c_{j\uparrow}(0) \rangle. \end{aligned} \quad (5.2)$$

Analyzing Eq. (5.2) more closely, one finds that the first and the last term vanish. The spin in both orbitals  $i$  and  $j$  changes in the same direction violating total spin conservation in  $z$  direction. The remaining second and third term of Eq. (5.2) are actual spin-flip components.

The rotational invariance of the SU(2)-symmetric interaction allows one to calculate such off-diagonal two-particle correlation functions exploiting symmetry relations for the subset of correlation functions accessible to conventional CT-HYB (see i.e. [Hoshino and Werner, 2016]). Whenever the rotational invariance is broken (e.g. through crystal field splittings), such symmetry relations fail and worm sampling becomes relevant.

We choose the two-orbital AIM with semi-elliptic conduction electron density of states and Slater-Kanamori interaction [Kanamori, 1963, Parragh et al., 2012]. This local interaction includes an intra-orbital repulsion  $U$ , SU(2)-symmetric Hund's exchange and pair hopping terms  $J$ , and inter-orbital interaction  $U' = U - 2J$ .

Using partition function sampling, we can calculate the spin susceptibility in  $z$ -direction in a straight-forward manner. Note that we can express  $S_z(\tau) = n_{\uparrow}^i(\tau) - n_{\downarrow}^i(\tau)$  in terms of density operators so that  $\langle S_z(\tau) S_z(0) \rangle$  can eventually be sampled by removing diagonal hybridization functions in partition function sampling.

This is not possible for  $\langle S_x(\tau) S_x(0) \rangle$  which is expressed in terms of spin flip two-particle Green's functions. While this cannot be calculated in conventional partition function sampling, we can do so by using worm sampling. Instead of looking at the imaginary-time resolved spin susceptibility, we verify the SU(2)-symmetry for the local spin susceptibility in terms of its Fourier transform to Matsubara frequencies  $\chi_{\text{loc}}(i\omega) = \int_0^\beta d\tau e^{-i\omega\tau} \langle S_{z(x)}(\tau) S_{z(x)}(0) \rangle$ .

Fig. 5.1 shows the spin-susceptibilities for the two-orbital AIM on a Bethe lattice. The worm sampling estimate for the  $S_x S_x$  susceptibility in  $x$ -direction agrees with the  $S_z S_z$  susceptibility in  $z$ -direction, which can be calculated both by worm and partition function



sampling. This further demonstrates the power of worm sampling to calculate general Green's functions and susceptibilities.

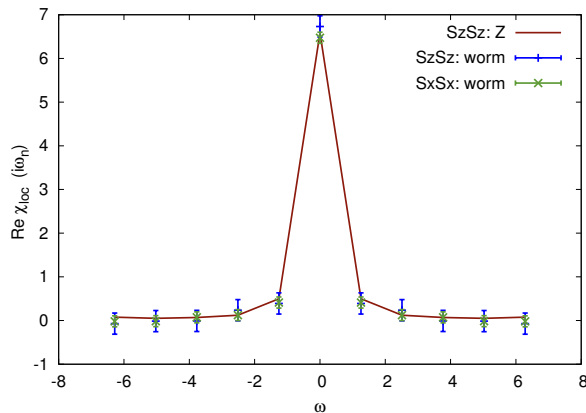


Figure 5.1: Local spin susceptibility  $\text{Re}\chi_{loc}(i\omega)$  of the two-orbital AIM as a function of the bosonic Matsubara frequency  $i\omega$ . Parameters: identical semi-elliptic bands of half-bandwidth  $D$ ,  $\beta = 5/D$ ,  $U = 1.0D$ ,  $J = 0.4D$ ,  $U' = 0.2D$ , and  $\mu = 0.5D$  (half-filling). The balancing parameter was set to  $\eta^{(2)} = 0.08$ . The  $SU(2)$ -symmetry is conserved, as the  $S_x S_x$  susceptibility of the worm algorithm (green error bars) agrees well with the  $S_z S_z$  susceptibility of partition function sampling (red line) and worm algorithm (blue error bars).

## 5.2 Vertex Asymptotics

*Parts of this section (marked by a vertical sidebar) have been already published in: J. Kaufmann, P.G and K. Held; Continuous-time quantum Monte Carlo calculation of multi-orbital vertex asymptotics. Phys. Rev. B. 96, 035114 (2017)*

Presumably, calculating  $SU(2)$ -symmetric multi-orbital  $n$ -particle Green's functions is computationally and conceptually one of the most challenging tasks in CT-HYB.<sup>2</sup> Local two-particle response functions are, however, important for two reasons: first, they provide valuable insight into physical ordering processes on the lattice and allow for a good comparison with experiments, and secondly, two-particle vertices are the essential building blocks of non-local diagrammatic extensions. Therefore, improving upon the numerical quality of two-particle functions and the efficiency during calculation is crucial.

On the one-particle level it is very common to improve the asymptotic behavior of multi-orbital self-energies by calculating densities and double occupancies explicitly (see i.e. [Wang et al., 2011]). Intuitively, the one- and two-particle densities follow from equal-time Green's functions in imaginary time. In a similar fashion, the asymptotics of the two-particle vertex function  $F$  have been derived for the single-orbital case [Wentzell et al., 2016, Li et al., 2016]. One can parameterize the non-vanishing asymptotical structure of the two-particle vertex in terms of Feynman diagrams. The asymptotical structure of the

<sup>2</sup>In terms of complexity, this procedure becomes even more involved when considering arbitrary hybridization functions and retarded interactions, which are not part of this work.

three-frequency function  $F$  consists of two-frequency functions, referred to as “Kernel-2” diagrams, and single-frequency functions, referred to as “Kernel-1” diagrams. In the imaginary time domain, these kernel functions relate to vertices, where one pair- or two pairs of amputated outer legs are contracted. Numerically, the asymptotical structure can be extracted by scanning the high-frequency regions of  $F$  calculated by impurity solvers, such as exact diagonalization methods or weak-coupling CT-QMC solvers. The high-frequency noise of vertex functions intrinsic to CT-HYB, on the other hand, prohibits this approach.

Following a different route, Kuneš demonstrated how to extract the asymptotical behavior for the multi-orbital two-particle irreducible vertex  $\Gamma$  [Kuneš, 2011], although only limiting the analysis to the static (i.e.  $\omega = 0$ ) vertex functions. Due to the two-particle irreducibility of  $\Gamma$  in a given channel, the asymptotical structure is determined by the Kernel functions of the remaining channels. Further, the Kernel-2 diagrams are suppressed for large frequencies, not contributing to the asymptotical structure of  $\Gamma$ .<sup>3</sup>

What remained an open problem is to determine expressions for the kernel functions in the multi-orbital case and derive the connection between equal-time two-particle Green’s functions (including disconnected parts and outer legs) and kernel (i.e. vertex) functions. The technicalities of sampling equal-time two-particle Green’s functions with one- or two pairs of outer legs contracted are found in Chapter 3.3.5, where also the Green’s function and notation are explicitly defined.

We recover the physical single-frequency susceptibility in the particle-hole channel by subtracting the constant “straight term”,

$$\chi_{ijkl}^{ph,\omega} = G_{ijkl}^{ph,\omega} - (1 - n_i)(1 - n_k)\delta_{\omega 0}\delta_{ij}\delta_{kl}, \quad (5.3)$$

whereas the particle-particle susceptibility is already given by

$$\chi_{ijkl}^{pp,\omega} = G_{ijkl}^{pp,\omega}. \quad (5.4)$$

We will now turn to the three-legged Green’s functions, where we are again interested only in the connected part. For the particle-hole channel we find

$$\chi_{ijkl}^{c,ph,\nu\omega} = G_{ijkl}^{ph,\nu\omega} - G_i^\nu \left[ (n_k - 1)\delta_{ij}\delta_{kl}\delta_{\omega 0} - G_k^{\nu-\omega}\delta_{il}\delta_{jk} \right] \quad (5.5)$$

and for the particle-particle channel

$$\chi_{ijkl}^{c,pp,\nu\omega} = G_{ijkl}^{pp,\nu\omega} - (\delta_{ij}\delta_{kl} - \delta_{il}\delta_{jk}) G_i^\nu G_k^{\omega-\nu}. \quad (5.6)$$

As usual, the corresponding expressions for the transverse particle-hole channel can be obtained by applying the crossing relation.

After the subtraction of the disconnected parts from the two-particle Green functions, the next step is to contract the equal-time legs with interaction vertices. The two-legged

---

<sup>3</sup>During the finalization of this work an in-depth comparison of the high-frequency asymptotics of  $\Gamma$  based on Kernel-1 approximations and based on Kernel-1 and Kernel-2 approximations for arbitrary  $\omega$  was published [Tagliavini et al., 2018], albeit only for the single-orbital case.

objects have two pairs of equal times and therefore need two distinct bare vertices to contract their legs and obtain the Kernel-1 functions  $K^{(1),\ell}$ :

$$K_{abcd}^{(1),ph,\omega} = - \sum_{ijkl} U_{ajbi} \chi_{ijkl}^{ph,\omega} U_{lckd} \quad (5.7)$$

$$K_{abcd}^{(1),\bar{ph},\omega} = - \sum_{ijkl} U_{alid} \chi_{ijkl}^{\bar{ph},\omega} U_{jcbk} \quad (5.8)$$

$$K_{abcd}^{(1),pp,\omega} = - \sum_{ijkl} \frac{U_{acki}}{2} \chi_{ijkl}^{pp,\omega} \frac{U_{ljb d}}{2} \quad (5.9)$$

For the Kernel-2 approximations, the procedure is a bit more involved. After the bare vertex contraction, we need to amputate the remaining legs. Thus, the Kernel-2 functions  $K^{(2),\ell}$  in all three channels are

$$K_{abcd}^{(2),ph,\nu\omega} = \sum_{ij} \frac{-\chi_{abji}^{c,ph,\nu\omega}}{G_a^\nu G_b^{\nu-\omega}} U_{icjd} - K_{abcd}^{(1),ph,\omega} \quad (5.10)$$

$$K_{abcd}^{(2),\bar{ph},\nu\omega} = \sum_{ij} \frac{-\chi_{aijd}^{c,\bar{ph},\nu\omega}}{G_a^\nu G_d^{\nu-\omega}} U_{icbj} - K_{abcd}^{(1),\bar{ph},\omega} \quad (5.11)$$

$$K_{abcd}^{(2),pp,\nu\omega} = \sum_{ij} \frac{-\chi_{aicj}^{c,pp,\nu\omega}}{G_a^\nu G_c^{\nu-\omega}} \frac{U_{jib d}}{2} - K_{abcd}^{(1),pp,\omega}, \quad (5.12)$$

where we had to subtract the Kernel-1 functions in order to avoid double-counting of diagrams.

Now we have six functions going to zero for high frequencies  $\nu$  or  $\omega$ , from which we can compile the asymptotic vertex.

According to the (local) parquet equation, the full vertex  $F_{abcd}$  can be decomposed into a fully irreducible and several reducible parts:

$$F_{abcd}^{\nu\nu'\omega} = \Lambda_{abcd}^{\nu\nu'\omega} + \Phi_{abcd}^{ph,\nu\nu'\omega} + \Phi_{abcd}^{\bar{ph},\nu\nu'\omega} + \Phi_{abcd}^{pp,\nu\nu'\omega}. \quad (5.13)$$

We are now able to construct the asymptotic form of the reducible vertices  $\Phi$  using [Wentzell et al., 2016]:

$$\Phi_{abcd}^{\text{asympt},\ell,\nu\nu'\omega} = K_{abcd}^{(1),\ell,\omega} + K_{abcd}^{(2),\ell,\nu\omega} + \bar{K}_{abcd}^{(2),\ell,\nu'\omega}, \quad (5.14)$$

where the functions  $\bar{K}^{(2),\ell}$  are found to be equal to  $K^{(2),\ell}$  due to time-reversal symmetry. Therefore summing up all  $K^{(i),\ell}$ , we get the asymptotic form of the full vertex:

$$\begin{aligned} F_{abcd}^{\text{asympt}}(\nu_\ell, \nu'_\ell, \omega_\ell) - U_{abcd} = & \\ & K_{abcd}^{(1),ph,\omega_{ph}} + K_{abcd}^{(2),ph,\nu_{ph}\omega_{ph}} + K_{abcd}^{(2),ph,\nu'_{ph}\omega_{ph}} + \\ & K_{abcd}^{(1),\bar{ph},\omega_{\bar{ph}}} + K_{abcd}^{(2),\bar{ph},\nu_{\bar{ph}}\omega_{\bar{ph}}} + K_{abcd}^{(2),\bar{ph},\nu'_{\bar{ph}}\omega_{\bar{ph}}} + \\ & K_{abcd}^{(1),pp,\omega_{pp}} + K_{abcd}^{(2),pp,\nu_{pp}\omega_{pp}} + K_{abcd}^{(2),pp,\nu'_{pp}\omega_{pp}} \end{aligned} \quad (5.15)$$

In this way we are now able to build arbitrarily large vertices in any frequency notation, which leads to significant improvements of further calculations.

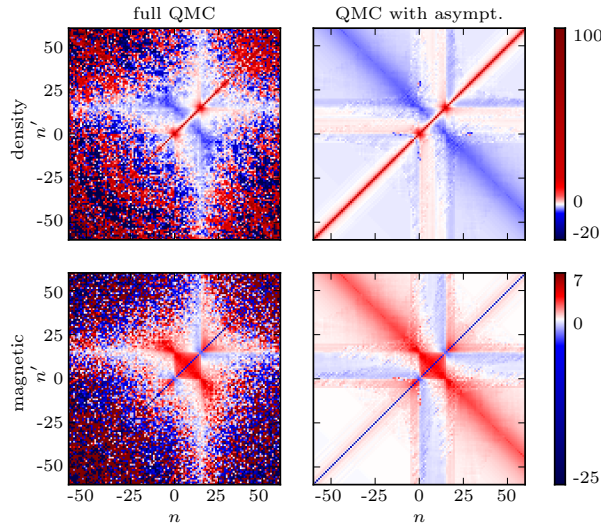


Figure 5.2: (Color online) Matrix element of the full vertex  $F_{d,1111}^{\nu\nu'\omega_{15}}$  (upper row) and  $F_{m,1111}^{\nu\nu'\omega_{15}}$  (lower row) for four times at the same  $t_{2g}$  orbital. Left column:  $F$  extracted from an improved-estimator CT-QMC measurement with full frequency dependence. Right column:  $F$ , combined with asymptotics according to Eq. (5.16) with  $l = 15$ . To remove the constant background,  $F_d$  was shifted by  $U_d = U$  and  $F_m$  by  $U_m = -U$ .

Since the derivations in the previous sections were done without restriction to one-band models or density-density interaction, it is possible to apply the procedure described above to a more general case. As a suitable material, we chose  $\text{SrVO}_3$ , which has a long tradition for benchmarking realistic material calculations using DMFT [Sekiyama et al., 2004, Ishida et al., 2006, Lee et al., 2012, Taranto et al., 2013, Sakuma et al., 2013]. Its band structure can be calculated by WIEN2K [Schwarz and Blaha, 2003], using the generalized gradient approximation. Subsequently,  $t_{2g}$  bands, which cross the Fermi level, are projected onto maximally localized Wannier functions by WIEN2WANNIER [Kuneš et al., 2010]. For these strongly correlated  $t_{2g}$  bands we consider a  $\text{SU}(2)$ -symmetric Slater-Kanamori interaction that is parameterized by an intra-orbital Hubbard  $U$ , an inter-orbital  $U'$  and Hund's coupling  $J$ . Calculations in constrained local density approximation yield values of  $U = 5\text{eV}$ ,  $J = 0.75\text{eV}$  and  $U' = U - 2J = 3.5\text{eV}$  [Sekiyama et al., 2004, Nekrasov et al., 2006]. The following DMFT calculation, as well as the calculation of the one-, two- and three-frequency two-particle Green's functions, was done by W2DYNAMICS at an inverse temperature of  $\beta = 10\text{eV}^{-1}$ .

Since we treat  $\text{SrVO}_3$  as a three-orbital system, the two-particle objects have in general have  $(2 \cdot 3)^4 = 1296$  spin-orbital components, of which due to the structure of the interaction, however, only 126 are non-vanishing. If we use instead of all spin-components the density and magnetic channels, which is possible for  $\text{SU}(2)$ -symmetry, the number of non-vanishing components is reduced to 21 per channel. Furthermore the local vertex functions exhibit orbital symmetry that reduces the number of distinct components to 4

per channel in our case of degenerate orbitals.

In Fig. 5.2 a slice of the vertex with four equal band indices is shown in the density and magnetic channel:  $F_{d/m,1111}^{\nu\nu'\omega_{15}}$ .

The first column shows vertices calculated by the improved-estimator method with worm sampling in about 150000<sup>a</sup> CPU hours. In the second column, the data in the asymptotic regions, defined by

$$\nu_1\nu_2\nu_3\nu_4\frac{\beta^4}{\pi^4} > l^4 |\delta_{\nu_1\nu_2} + \delta_{\nu_1\nu_4} - \delta_{\nu_1\nu_2}\delta_{\nu_1\nu_4}|^4, \quad (5.16)$$

were replaced according to the method proposed in this article, with a replacement parameter of  $l = 15^a$ . For comparison, we show ED results in the third column. The replacement procedure Eq. (5.16) is motivated by atomic limit calculations.

<sup>a</sup>CPU hours and replacement adapted for SrVO<sub>3</sub> study.

## 5.3 AbinitioDΓA

*Parts of this section (marked by a vertical sidebar) have been already published in: A. Galler, J. Kaufmann, P.G., M. Pickem, P. Thunström, J. Tomczak and K. Held; Towards ab initio Calculations with the Dynamical Vertex Approximation. Journal of the Physical Society of Japan 87(4), 041004 (2018)*

In the previous section the asymptotical structure of the multi-orbital two-particle vertex function was derived and calculated for SrVO<sub>3</sub>. The true potential of the asymptotical structure, however, unveils in combination with non-local diagrammatic extensions. The AbinitioDΓA method discussed in the following is the first actual multi-orbital<sup>4</sup> implementation in the entire category of multi-orbital diagrammatic extensions to DMFT [Galler et al., 2017]. First theoretical proposals of fully self-consistent ab initio (i.e. material) diagrammatic extensions date were made by Rubtsov *et al.* for (ladder) DF in their original publication [Rubtsov et al., 2008] and by Toschi *et al.* for (parquet) DΓA [Toschi et al., 2011]. The basic concepts of ladder DΓA have been introduced in Chapter 2.5. In the following, a first AbinitioDΓA (i.e. DFT+DMFT+DΓA) study of non-local correlation effects in SrVO<sub>3</sub> is presented.

In AbinitioDΓA the  $ph$ -irreducible vertex is then approximated by this local  $\Gamma^{\omega\nu\nu'}$  supplemented with the non-local Coulomb interaction  $\mathbf{V}^{\mathbf{q}\mathbf{k}\mathbf{k}'}$ .<sup>a</sup> This can be written in the form

<sup>4</sup>In this work “multi-orbital” refers to a single impurity with multiple orbitals, whereas other works similarly consider multiple impurities with a single-orbital as “multi-orbital”, even though only a single-orbital single-site vertex is calculated for several atoms (see e.g. [Hirschmeier et al., 2017]). While the implementation of diagrammatic extension shares some similarities in the Bethe-Salpeter equations for both cases, a “true” multi-orbital implementation generally includes a more complicated representation of the equation of motion due to the multi-orbital interaction matrix.

of a crossing-symmetric vertex:

$$\Gamma_{\sigma\sigma',lmm'l'}^{\mathbf{qkk}'} \equiv \Gamma_{\sigma\sigma',lmm'l'}^{\omega\nu\nu'} + \mathbf{V}_{\sigma\sigma',lmm'l'}^{\mathbf{qkk}'}, \quad (5.17)$$

where

$$\mathbf{V}_{\sigma\sigma',lmm'l'}^{\mathbf{qkk}'} \equiv \beta^{-2}(V_{lm'm'l'}^{\mathbf{q}} - \delta_{\sigma\sigma'}V_{mm'll'}^{\mathbf{k}'-\mathbf{k}}). \quad (5.18)$$

Approximating the exact vertex by Eq. (5.17) is the essential approximation of AbinitioDΓA. Since  $\Gamma^{\omega\nu\nu'}$  already contains the local Coulomb interaction  $U$  as its lowest-order contribution, Eq. (5.17) represents a natural extension of the local  $\Gamma^{\omega\nu\nu'}$  to non-local interactions. That is, the AbinitioDΓA vertex  $\Gamma^{\mathbf{qkk}'}$  is made up from the local and non-local Coulomb interaction ( $U$  and  $V^{\mathbf{q}}$ ) as well as all local vertex corrections.

The  $ph$ -irreducible vertex  $\Gamma^{\mathbf{qkk}'}$  defined in Eq. (5.17) is then used to calculate the full vertex function  $F^{\mathbf{qkk}'}$  through the BSE.

<sup>a</sup>For a schematic representation of the AbinitioDΓA equations see [Galler et al., 2018].

The latter can be considerably simplified if  $\Gamma^{\mathbf{qkk}'}$  does not depend on the momenta  $\mathbf{k}$  and  $\mathbf{k}'$ . Indeed, this dependence arises only from the second (crossed)  $V^{\mathbf{k}'-\mathbf{k}}$  term in Eq. (5.18) which is, e.g., neglected in the  $GW$  approximation [Hedin, 1965]. If we follow the philosophy of  $GW$  and neglect this term, Eq. (5.17) (now already in the two spin channels  $r \in \{d, m\}$ ) reads

$$\Gamma_{r,lmm'l'}^{\mathbf{q}\nu\nu'} = \Gamma_{r,lmm'l'}^{\omega\nu\nu'} + 2\beta^{-2}V_{lm'm'l'}^{\mathbf{q}}\delta_{r,d}. \quad (5.19)$$

With this simplification, the non-local BSE eventually becomes independent of  $\mathbf{k}$  and  $\mathbf{k}'$  and reads

$$F_{r,lmm'l'}^{\mathbf{q}\nu\nu'} = \Gamma_{r,lmm'l'}^{\mathbf{q}\nu\nu'} + \phi_{r,lmm'l'}^{\mathbf{q}\nu\nu'} \quad (5.20)$$

$$\phi_{r,lmm'l'}^{\mathbf{q}\nu\nu'} = \sum_{\substack{nm'hh' \\ \nu''}} \Gamma_{r,lmm'l'}^{\mathbf{q}\nu\nu''} \chi_{0,nhh'n'}^{\mathbf{q}\nu''\nu''} F_{r,n'h'm'l'}^{\mathbf{q}\nu''\nu'}, \quad (5.21)$$

with

$$\chi_{0,lmm'l'}^{\mathbf{q}\nu\nu} = \sum_{\mathbf{k}} \chi_{0,lmm'l'}^{\mathbf{qkk}} = -\beta \sum_{\mathbf{k}} G_{ll'}^{\mathbf{k}} G_{m'm}^{\mathbf{k}-\mathbf{q}}. \quad (5.22)$$

The full vertex function  $F^{\mathbf{q}\nu\nu'}$  constructed in this way contains non-local diagrams only in the  $ph$ -channel. However, in DΓA we consider also the corresponding non-local diagrams in the  $\overline{ph}$ -channel. The latter do not need to be constructed explicitly, but can be obtained through symmetry considerations, namely by the crossing symmetries. Adding the  $ph$  and  $\overline{ph}$ -channel and subtracting any double counted term yields—after some algebra as discussed in Ref. Galler et al., 2017—the full AbinitioDΓA vertex:

$$\begin{aligned} \mathbf{F}_{d,lmm'l'}^{\mathbf{qkk}'} &= F_{d,lmm'l'}^{\omega\nu\nu'} + F_{d,lmm'l'}^{nl,\mathbf{q}\nu\nu'} - \frac{1}{2}F_{d,m'mll'}^{nl,(k'-k)(\nu'-\omega)\nu'} \\ &\quad - \frac{3}{2}F_{m,m'mll'}^{nl,(k'-k)(\nu'-\omega)\nu'}. \end{aligned} \quad (5.23)$$

Here, the non-local vertex  $F^{nl}$  is defined as

$$F_{r,lm'm'l'}^{nl,q\nu\nu'} \equiv F_{r,lm'm'l'}^{q\nu\nu'} - F_{r,lm'm'l'}^{\omega\nu\nu'} \quad (5.24)$$

with  $F^{q\nu\nu'}$  calculated from  $\Gamma^{q\nu\nu'}$  through the BSE (5.20)-(5.21).

The next step is to use the full vertex  $\mathbf{F}$  of Eq. (5.23) in the Schwinger-Dyson equation of motion to obtain the AbinitioDGA self-energy. Since in the BSE (5.20)-(5.21) we included  $V^{\mathbf{q}}$  through  $\Gamma^{q\nu\nu'}$  but not  $V^{\mathbf{k}'-\mathbf{k}}$ , it is consistent to also neglect corresponding terms for the self-energy in the Schwinger-Dyson equation. We can also explicitly identify the contribution  $\Sigma_{\text{DMFT}}^{\nu}$  that corresponds to the DMFT solution. After some algebra (see Ref. [Galler et al., 2017] for details), the final expression for the non-local AbinitioDGA self-energy reads

$$\begin{aligned} \Sigma^{\text{DGA}} &= \Sigma_{\text{DMFT}}^{\nu} - \beta^{-1} \sum_{q\nu'} U \chi_0^{nl,q\nu'\nu'} F_d^{\omega\nu'\nu} G^{\mathbf{k}-\mathbf{q}} \\ &\quad - \beta^{-1} \sum_{q\nu'} V^{\mathbf{q}} \chi_0^{q\nu'\nu'} F_d^{\omega\nu'\nu} G^{\mathbf{k}-\mathbf{q}} \\ &\quad - \beta^{-1} \sum_{q\nu'} \left( U + V^{\mathbf{q}} \right) \chi_0^{q\nu'\nu'} F_d^{nl,q\nu'\nu} G^{\mathbf{k}-\mathbf{q}} \\ &\quad + \beta^{-1} \sum_{q\nu'} \tilde{U} \chi_0^{q\nu'\nu'} \left( \frac{1}{2} F_d^{nl,q\nu'\nu} + \frac{3}{2} F_m^{nl,q\nu'\nu} \right) G^{\mathbf{k}-\mathbf{q}}. \end{aligned} \quad (5.25)$$

Here  $\tilde{U}_{lm'l'm} = U_{lm'l'm}$ ;  $\chi_0^{nl,q\nu\nu'} \equiv \chi_0^{q\nu\nu'} - \chi_0^{\omega\nu\nu'}$ ; and orbital indices have been suppressed for clarity.

This self-energy contains all DMFT and  $GW$  contributions as well as non-local correlations beyond (e.g., spin fluctuations). It is constructed from the underlying AbinitioDGA approximation of considering only local vertex corrections. From the self-energy, we can also calculate the Green's function via the Dyson equation. This in turn allows us to define a new impurity problem in a self-consistent scheme. Let us now turn to the results obtained by AbinitioDGA, so far without self consistency and without  $V^{\mathbf{q}}$ .

The AbinitioDGA calculations were performed using the local vertex functions defined in Section 5.2,<sup>a</sup> computed for an inverse temperature  $\beta = 10/\text{eV}$ , a Hubbard intra-orbital interaction  $U = 5.0\text{eV}$ , and a Hund's exchange  $J = 0.75\text{eV}$ . The AbinitioDGA self-energy, defined in Eq. (5.25), was computed with  $V^{\mathbf{q}} = 0$

<sup>a</sup>Reference adapted for this work.

We now discuss the effects in the AbinitioDGA self-energy—displayed in Fig. 5.3 for three representative  $\mathbf{k}$ -points—that are beyond DMFT. At low energies the imaginary part of the self-energy on the Matsubara axis is—for all orbitals and  $\mathbf{k}$ -points—slightly smaller than in DMFT. As a result the scattering rate  $\gamma = -\Im\Sigma(i\nu \rightarrow 0)$  very slightly decreases with respect to DMFT, while the quasi-particle weight  $Z_{\mathbf{k}}$  increases. Besides this overall effect, the momentum dependence of  $\Im\Sigma$  is small. Indeed  $Z_{\mathbf{k}}$  varies by less than 2% within the Brillouin zone. The real-part of the self-energy shows larger deviations from the DMFT result. Indeed, at low energies the difference between AbinitioDGA and DMFT

reaches 200meV, which amounts to about 7% of the Hartree term. Further, in DMFT the  $d_{xy}$ ,  $d_{xz}$ , and  $d_{yz}$  self-energy components were identical due to their local degeneracy. As a consequence of the lifting of the momentum-independence, the self-energy can now also acquire an orbital dependence. The splitting between non-equivalent components at the  $X$  and  $M$ -point of the Brillouin zone is displayed in the middle and right panel of Fig. 5.3. The orbital splitting at a given  $\mathbf{k}$ -point reaches up to 100meV.

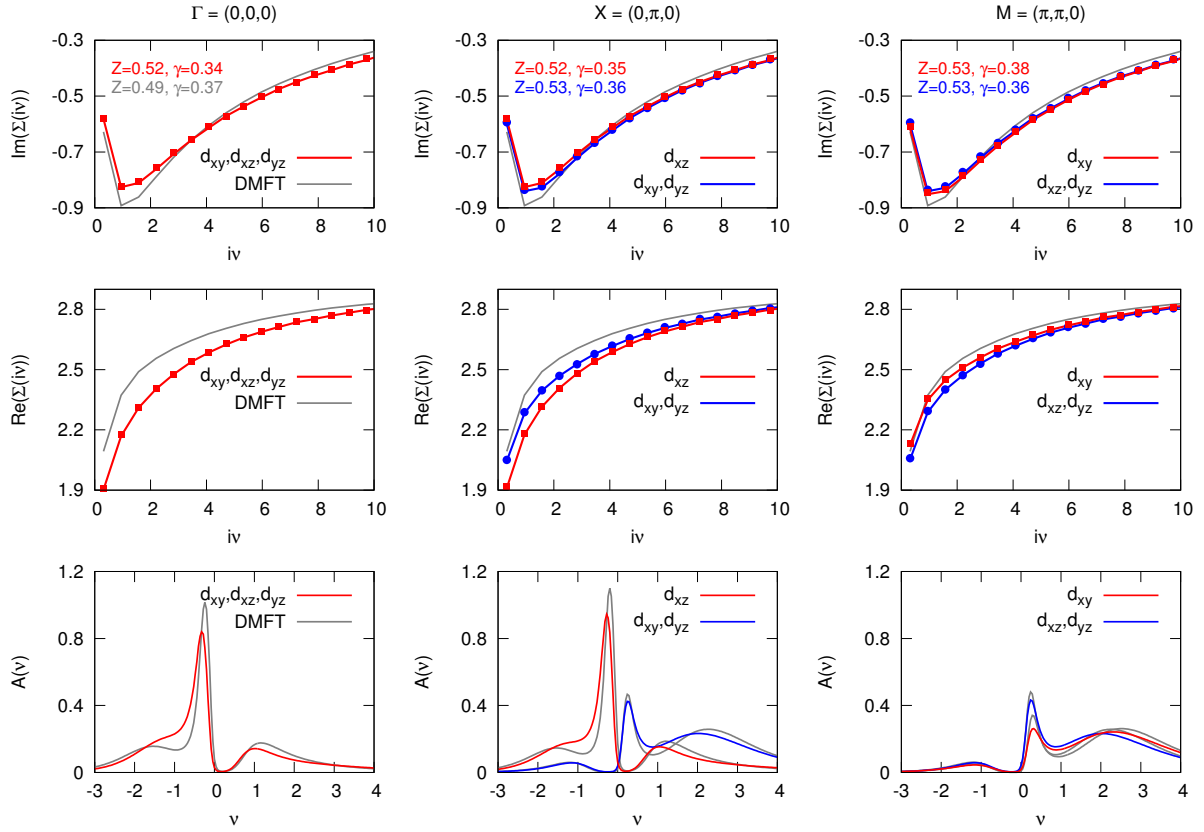


Figure 5.3: AbinitioDFA results for the self-energy (top row: imaginary part, middle row: real part) and real-frequency spectral functions (bottom row) for selected  $\mathbf{k}$ -points in the Brillouin zone ( $\Gamma$ -point: left column,  $X$ -point: middle column,  $M$ -point: right column). In the two top panels, symbols indicate results for a small frequency box ( $N=60$ ) and using no vertex asymptotics, while lines depict results for the largest box ( $N=200$ ) that also makes use of the vertex asymptotics: Both results are on top of each other.



# Chapter 6

## Conclusion

The primary objective of this work was to present a comprehensive description of continuous-time quantum Monte Carlo algorithms, specifically of those formulated in the hybridization expansion. After all, impurity solvers prove to be at the center of various numerical methods attempting to solve the Hubbard model and to describe effects of strong correlations.

Before discussing the technicalities of CT-HYB, this work introduced various limits of the Hubbard model in the first part of Chapter 2. Among others, these include the Anderson impurity model, the Heisenberg model, the tight-binding model and the Falicov-Kimball model. The weak- and strong-coupling limit of the Hubbard model are investigated and several lattice dimensions are considered. Especially the two-dimensional- and the infinite-dimensional Hubbard model are of importance in this work. As for any numerical method, it is necessary to have an understanding of the underlying physics and being able to correctly interpret results. In the following sections, various diagrammatic methods to solve the Hubbard model were discussed, namely DMFT in Chapter 2.4 and the non-local diagrammatic extensions D $\Gamma$ A and DF in Chapter 2.5. These methods are formally expressed in terms of one-particle diagrammatics in the former case and two-particle diagrammatics in the latter. The equations of DMFT and diagrammatic extensions need to be solved self-consistently, making numerical methods necessary. Chapter 2 concluded with a summary of analytic continuation methods. While these methods were only discussed briefly, it turns out that they are a key point for evaluating results obtained by methods based on finite temperature quantum field theories. The analytic continuation defines the transformation of results represented in the Matsubara domain into the (experimentally observable) real frequency/time domain. Hence, any algorithm generating Matsubara results is only as good as the method used for analytic continuation, at least as far as dynamical properties are concerned.

Chapter 3 represents the central chapter of this work. After introducing the most popular impurity solvers, the remaining chapter dealt with CT-HYB exclusively. In this context, the newly introduced worm algorithm was set in contrast to the CT-HYB algorithm prior to its development. Worm sampling attempts to sample the infinite series expansion of different observables directly, avoiding observable estimates from the partition function expansion. Worm sampling becomes necessary for large crystal field splittings, vanishing hybridization functions and for the measurement of certain observables for non-density-density interactions. In this respect, several worm estimators were introduced

which directly link to specific Feynman diagrams. Especially estimators for two-particle diagrams were discussed due to their direct relevance in calculating susceptibilities and their application to non-local diagrammatic extensions. A noteworthy class of estimators discussed throughout the chapter includes the asymptotic two-particle estimators and the improved- and symmetric improved estimators. These estimators enhance the high-frequency behavior of one- and two-particle Green's functions and irreducible vertex functions, effectively circumventing the shortcomings of conventional estimators. Worm estimators can be formulated as  $\delta$ -estimators, where just the positions of the worm operators are recorded. Alternatively, worm estimators may be reformulated in terms of generalized hybridization matrices, allowing the measurement procedure to access the entire configuration at once. On a different note, several technicalities in the worm sampling procedure were analyzed, including the component-wise sampling of observables. While the worm algorithm allows for more flexibility in terms of the estimator structure as opposed to partition function sampling, certain care needs to be taken with respect to balancing and normalization.

Chapters 4 and 5 presented several applications of the CT-HYB algorithm to impurity and lattice models with a specific focus on two-particle response functions. From a technical viewpoint this illustrated the versatility of CT-HYB for different models and parameter set-ups. From a physical viewpoint, phase transitions due to local correlation effects and non-local correlation effects were investigated. Chapter 4 started with an analysis of the Mott-Hubbard metal-to-insulator transition in the mass-imbalanced Hubbard model and its connection to the Falicov-Kimball model. The chapter then proceeded with the discussion of divergences of the irreducible vertex functions of the Anderson impurity model. While on the one hand these divergences need to be accounted for numerically, on the other hand the divergences seem to be connected to the Kondo physics of the AIM. Chapter 4 concluded with a self-consistency study of the two-dimensional Hubbard model in DF. Non-local correlation effects occurring in systems with low lattice-dimension are not adequately described by DMFT. For this purpose, one may consider diagrammatic extensions instead. While the accuracy of methods in quantum chemistry allows for quantitative statements, methods describing the non-local nature of correlations only allow for qualitative interpretations. Applying a single iteration of DF (and similarly DGA) on top of DMFT generally leads to results that are not self-consistent on the one- or two-particle level. A full solution, on the other hand, should be self-consistent on the one- and two-particle level (i.e. inner and outer self-consistency). Chapter 5 discussed an AbinitioDGA study of SrVO<sub>3</sub> with three *d*-orbitals and Slater-Kanamori interaction. As of today, the Hubbard Hamiltonian is mostly analyzed from two directions, namely the “model” approach and the “ab initio” approach. In the former case, one attempts to understand correlation effects by precisely controlling the lattice geometry and the model parameters. In the latter case, strong correlation effects are analyzed in relation to different materials. Calculating the local multi-orbital two-particle Green's function in CT-HYB posed a considerable numerical challenge. The worm algorithm was employed to recover all components of the SU(2)-symmetric two-particle Green's function and vertex asymptotics were used to improve the numerical result. As non-local correlation effects in (bulk) SrVO<sub>3</sub> are minimal at the temperature considered, future investigations will consider materials at lower temperatures (e.g. room temperature) and reduced lattice

dimension. Optimizations for the worm algorithm (and CT-HYB in general) will open a route for understanding how physical properties of such materials are influenced by non-local correlations.

The developments presented in this work may prove to be some of the fundamental building blocks required to advance CT-HYB and are important in generating numerical solutions for the single-orbital and multi-orbital Hubbard model, necessary both for model calculations and *ab initio* calculations. While implementing state-of-the-art CT-QMC algorithms is already a complex task from a developmental point of view, some further details are yet to be worked out. The most complete solutions to the multi-orbital AIM are based upon general hybridization functions (not restricted to diagonality constraints) and retarded interactions. Such solutions to the AIM would, in principle, include Green's functions up to an arbitrary number of particles. Especially with regards to CT-HYB, an accurate treatment of high-frequency regions in the vertex function remains challenging. On an algorithmic level, optimizations to the Monte Carlo measurement and sampling procedures will allow for lower temperatures and more orbitals in the future.

While at some point DMFT may be substituted by (fully) self-consistent non-local diagrammatic methods, solving the AIM remains an intrinsic challenge and a numerical bottleneck of most diagrammatic methods. A thorough algorithmic enhancement of continuous-time impurity solvers may prove to be an essential step in fully uncovering the physics of the Hubbard model.



# Appendices



# Appendix A

## Limits of the Hubbard Model

The following sections provide in-depth derivations of different relations for limiting cases of the Hubbard model.

### A.1 Non-interacting Limit

In order to derive the bubble-term of the non-interacting susceptibility, it is easiest to directly evaluate the corresponding diagram, where the building blocks are non-interacting Green's functions with

$$\mathcal{G}(\vec{k}, i\nu) = \frac{1}{i\nu - \varepsilon_{\vec{k}}}, \quad (\text{A.1})$$

where  $i\nu$  are fermionic Matsubara frequencies. An illustration of the bubble-diagram in Matsubara frequencies is given in Figure A.1. Mathematically, the bubble diagram can be expressed as:

$$\chi_0(\vec{q}, i\omega) = \frac{1}{N} \sum_{\vec{k}}^{\text{BZ}} \frac{1}{\beta} \sum_{i\nu} \mathcal{G}(\vec{k} - \vec{q}, i\nu - i\omega) \mathcal{G}(\vec{k}, i\nu) \quad (\text{A.2})$$

$$= \frac{1}{N} \sum_{\vec{k}}^{\text{BZ}} \frac{1}{\beta} \sum_{i\nu} \frac{1}{i\nu - i\omega - \varepsilon_{\vec{k}-\vec{q}}} \frac{1}{i\nu - \varepsilon_{\vec{k}}} \quad (\text{A.3})$$

The Matsubara sum over the fermionic Matsubara frequency  $i\nu$  can be evaluated, such that

$$\chi_0(\vec{q}, i\omega) = \frac{1}{N} \sum_{\vec{k}}^{\text{BZ}} \frac{f(\varepsilon_{\vec{k}-\vec{q}}) - f(\varepsilon_{\vec{k}})}{i\omega - (\varepsilon_{\vec{k}-\vec{q}} - \varepsilon_{\vec{k}})}, \quad (\text{A.4})$$

where  $f(x) = 1/(1 + e^{\beta x})$  is the Fermi distribution function. While in principle an equivalent substitution  $i\omega \rightarrow \omega + i\delta$  is necessary, the bosonic Matsubara frequency and the real frequency share the same value at zero. This way, one can easily extract the static part of the non-interacting susceptibility.

$$\chi_0(\vec{q}, i\omega) = \text{bubble diagram with } \mathcal{G}(\vec{k}-\vec{q}, i\nu-i\omega) \text{ and } \mathcal{G}(\vec{k}, i\nu)$$

Figure A.1: Bubble diagram of the non-interacting susceptibility  $\chi_0(\vec{q}, i\omega)$  in Matsubara frequencies. Diagrammatically, the susceptibility is obtained by a contraction of two non-interacting Green's functions (dashed lines), where the energy- and momentum transfer is given by the bosonic frequency  $i\omega$  and the transfer momentum  $\vec{q}$  respectively. The fermionic frequency  $i\nu$  and the initial momentum  $\vec{k}$  become internal degrees of freedom, which are then integrated over. The shape of the diagram is reminiscent of a bubble.

## A.2 Atomic Limit

In order to calculate the Green's function and self-energy in the atomic limit, the Lehmann basis is employed. The following discussion is limited to the single orbital atomic limit, although generalizations to multi-orbital systems are straight forward.

One possible basis choice is the (orthonormal) occupation number basis:

$$\left\{ \langle \downarrow |, \langle \uparrow |, \langle \downarrow \downarrow |, \langle \uparrow \downarrow | \right\}, \quad (\text{A.5})$$

with the empty state, two singly-occupied states and a doubly-occupied state. Next, the creation and annihilation operators are expressed in the occupation number basis. A creation operator of spin  $\sigma$  adds to the empty  $\langle \downarrow |$  and the opposite filled state  $\langle -\sigma |$  an electron of spin  $\sigma$ , whereas the annihilation operator removes the electron from the doubly occupied  $\langle \uparrow \downarrow |$  and the equally filled state  $\langle \sigma |$ . Additionally, some care needs to be taken with preceding signs. These signs result from the fermionic anti-commutation rules  $\{\hat{c}_i, \hat{c}_j\} = \{\hat{c}_i^\dagger, \hat{c}_j^\dagger\} = 0$  and  $\{\hat{c}_i^\dagger, \hat{c}_j\} = \delta_{ij}$ . A possible sign convention is to modify the annihilation operator  $\hat{c}_i$  with a sign  $(-1)^N$ , where  $N$  is the number of electrons  $k < i$  being occupied in the many body state. The matrix representation of the operators is given as:

$$c_\uparrow^{mn} = \langle m | \hat{c}_\uparrow | n \rangle = \begin{pmatrix} 0 & 1 & 0 & 0 \\ 0 & 0 & 0 & 0 \\ 0 & 0 & 0 & 1 \\ 0 & 0 & 0 & 0 \end{pmatrix} \quad c_\downarrow^{mn} = \langle m | \hat{c}_\downarrow | n \rangle = \begin{pmatrix} 0 & 0 & 1 & 0 \\ 0 & 0 & 0 & -1 \\ 0 & 0 & 0 & 0 \\ 0 & 0 & 0 & 0 \end{pmatrix} \quad (\text{A.6})$$

$$c_\uparrow^{\dagger, mn} = \langle m | \hat{c}_\uparrow^\dagger | n \rangle = \begin{pmatrix} 0 & 0 & 0 & 0 \\ 1 & 0 & 0 & 0 \\ 0 & 0 & 0 & 0 \\ 0 & 0 & 1 & 0 \end{pmatrix} \quad c_\downarrow^{\dagger, mn} = \langle m | \hat{c}_\downarrow^\dagger | n \rangle = \begin{pmatrix} 0 & 0 & 0 & 0 \\ 0 & 0 & 0 & 0 \\ 1 & 0 & 0 & 0 \\ 0 & -1 & 0 & 0 \end{pmatrix}. \quad (\text{A.7})$$

The Hamiltonian for the atomic is given by:

$$\hat{H}_{\text{at}} = \sum_i^N \left( -\mu(\hat{n}_{i\uparrow} + \hat{n}_{i\downarrow}) + U\hat{n}_{i\uparrow}\hat{n}_{i\downarrow} \right), \quad (\text{A.8})$$



where  $\hat{n}_{i\sigma} = \hat{c}_{i\sigma}^\dagger \hat{c}_{i\sigma}$  is the density operator. The above Hamiltonian can now be expressed in the occupation number basis as:

$$H_{\text{at}}^{mn} = \langle m | \hat{H}_{\text{at}} | n \rangle = \begin{pmatrix} 0 & 0 & 0 & 0 \\ 0 & -\mu & 0 & 0 \\ 0 & 0 & -\mu & 0 \\ 0 & 0 & 0 & U - 2\mu \end{pmatrix}. \quad (\text{A.9})$$

The matrix  $H_{\text{at}}^{mn}$  is already diagonal, such that the basis states form the eigenvectors and the eigenvalues  $\varepsilon_{\text{at}}^n$  can be immediately read off. With the above tools the Green's function can be evaluated explicitly:

$$G_\sigma(\tau) = -\frac{1}{Z} \text{Tr} \left( e^{-\beta \hat{H}_{\text{at}}} \hat{c}_\sigma(\tau) \hat{c}_\sigma^\dagger \right) = -\frac{\sum_n \langle n | e^{-\beta \varepsilon_{\text{at}}^n} \hat{c}_\sigma(\tau) \hat{c}_\sigma^\dagger | n \rangle}{\sum_n \langle n | e^{-\beta \varepsilon_{\text{at}}^n} | n \rangle}, \quad (\text{A.10})$$

where the creation and annihilation operator are given in the interaction picture, with an explicit time-dependence according to  $\hat{c}_\sigma^{(\dagger)}(\tau) = e^{\tau \hat{H}_{\text{at}}} \hat{c}_\sigma^{(\dagger)} e^{-\tau \hat{H}_{\text{at}}}$  and  $\tau \in [0, \beta)$ . Evaluating expression (A.10) yields:

$$G_\sigma(\tau) = -\frac{e^{\tau\mu} + e^{\beta\mu} e^{\tau(\mu-U)}}{1 + 2e^{\beta\mu} + e^{-\beta(U-2\mu)}}. \quad (\text{A.11})$$

For the half-filling case with  $\mu = \frac{U}{2}$  this simplifies to:

$$G_\sigma(\tau) = -\frac{1}{2} \frac{e^{\tau \frac{U}{2}} + e^{(\beta-\tau) \frac{U}{2}}}{1 + e^{\beta \frac{U}{2}}}. \quad (\text{A.12})$$

Sometimes the Hamiltonian  $H_{\text{at}}^{mn}$  is shifted relative to the zero-point energy (the lowest lying eigenvalue  $\min(\varepsilon_{\text{at}}^n)$ ) as  $H_{\text{at}}^{mn} \rightarrow H_{\text{at}}^{mn} - \min(\varepsilon_{\text{at}}^n)$  to avoid the Boltzmann weight  $e^{-\beta \hat{H}}$  to diverge for  $\beta \rightarrow \infty$ . This has no consequences on the expectation value itself, as this is the ratio of the trace over the operator (with a factor  $e^{-\beta \hat{H}}$  relative to the partition function. Any energy shift in the nominator and denominator cancels out.

In order to extract the DOS and self-energy it is convenient to convert the imaginary time result in equation (A.11) into Matsubara frequencies. This is done by evaluating the Fourier transform:

$$G_\sigma(i\nu) = \int_0^\beta e^{i\nu\tau} G_\sigma(\tau) = \frac{1}{1 + 2e^{\beta\mu} + e^{-\beta(U-2\mu)}} \left( \frac{1 + e^{\beta\mu}}{i\nu + \mu} + \frac{e^{\beta\mu} + e^{\beta(2\mu-U)}}{i\nu + \mu - U} \right), \quad (\text{A.13})$$

where the fermionic Matsubara frequency  $i\nu = i \frac{(2n+1)\pi}{\beta}$  was used. For the half-filling case the above simplifies to:

$$G_\sigma(i\nu) = \frac{1}{2} \left( \frac{1}{i\nu - \frac{U}{2}} + \frac{1}{i\nu + \frac{U}{2}} \right). \quad (\text{A.14})$$

From the poles of the Green's function, one can immediately read off the spectral function as:

$$A_\sigma(\omega) = \frac{1}{2} \left( \delta\left(\omega - \frac{U}{2}\right) + \delta\left(\omega + \frac{U}{2}\right) \right). \quad (\text{A.15})$$

The  $\delta$ -peak at  $\omega = -\frac{U}{2}$  corresponds to the filled singly-occupied orbitals  $\langle \uparrow |$  and  $\langle \downarrow |$ , while the  $\delta$ -peak at  $\omega = +\frac{U}{2}$  corresponds to the empty and doubly occupied state  $\langle \quad |$  and  $\langle \uparrow \downarrow |$ . The self-energy at half-filling can now simply be extracted from Dyson's equation with

$$\Sigma_\sigma(i\nu) = \mathcal{G}(i\nu)^{-1} - G_\sigma(i\nu)^{-1}, \quad (\text{A.16})$$

with the non-interacting Green's function  $\mathcal{G}(i\nu) = \frac{1}{i\nu + \mu}$ .

### A.3 Heisenberg Limit

In the limit of  $U \gg t$  the Hubbard Hamiltonian simplifies to the  $tJ$ -Hamiltonian, further reducing to the Heisenberg model for half-filling. The limit  $U \gg t$  (but not  $t = 0$ ) suggests formulating a perturbation theory based on the atomic limit to derive the Heisenberg model. A very similar derivation is found elsewhere [Cleveland and Medina, 1976]. Starting from the Hubbard model the potential energy term is set to the unperturbed Hamiltonian  $\hat{H}_0$  and the kinetic energy term as the perturbation  $\hat{H}_1$ .

$$\hat{H}_0 = \sum_i^N U \hat{n}_{i\uparrow} \hat{n}_{i\downarrow} \quad (\text{A.17})$$

$$\hat{H}_1 = \frac{1}{2} \sum_{\langle ij \rangle, \sigma}^N t_{ij} (\hat{c}_{i\sigma}^\dagger \hat{c}_{j\sigma} + \hat{c}_{j\sigma}^\dagger \hat{c}_{i\sigma}) \quad (\text{A.18})$$

In order to derive the energy-corrections in perturbation theory it is necessary to define a basis set for the ground state. In the half-filled case, where each site is either spin-up or spin-down occupied this basis scales with  $2^N$ , where  $N$  is the number of sites. For nearest-neighbor hopping, the ground state is given by  $|\sigma_i, \sigma_j\rangle$ , where  $\sigma_i$  is the spin of the electron on site  $i$ . The energy of the unperturbed system follows as  $E^{(0)} = -N\mu$ . The energy correction in first order perturbation theory follows as:

$$E^{(1)} = \frac{1}{2} \sum_{\langle ij \rangle, \sigma}^N \langle \sigma_i, \sigma_j | H_1 | \sigma_i, \sigma_j \rangle = 0 \quad (\text{A.19})$$

The first-order correction vanishes as every site is singly occupied and any hopping from a given site would result in a neighboring site being doubly occupied. Doubly occupied states are, however, forbidden in the ground state of the unperturbed system. By alleviating the restriction of half-filling, the first order energy correction recovers the dynamics of the more general  $tJ$ -model.

In second order perturbation theory the energy correction is given by

$$E^{(2)} = -\frac{1}{2} \sum_{\langle ij \rangle}^N \sum_{\sigma\sigma'} \sum_I \frac{\langle \sigma_i, \sigma_j | H_1 | \Phi_I \rangle \langle \Phi_I | H_1' | \sigma'_i, \sigma'_j \rangle}{E_I - E_{ij}}, \quad (\text{A.20})$$

where  $|\Phi_I\rangle$  are the intermediate excited states  $|0, \uparrow \downarrow\rangle$  and  $|\uparrow \downarrow, 0\rangle$  with energy  $E_I = U - 2\mu$ . The ground-state of two neighboring sites has energy  $E_{ij} = -2\mu$ . Expanding the factors

of the above expression results in:

$$E^{(2)} = \frac{1}{2} \sum_{\langle ij \rangle}^N \sum_{\sigma\sigma'} \frac{t_{ij}^2}{U} \langle \sigma_i, \sigma_j | \left( \hat{c}_{i\sigma}^\dagger \hat{c}_{i\sigma'} \hat{c}_{j\sigma'}^\dagger \hat{c}_{j\sigma} + \hat{c}_{i\sigma'}^\dagger \hat{c}_{i\sigma} \hat{c}_{j\sigma}^\dagger \hat{c}_{j\sigma'} \right) | \sigma'_i, \sigma'_j \rangle. \quad (\text{A.21})$$

The expression inside the parentheses can be simplified to  $(4\hat{S}_i \hat{S}_j - \hat{n}_i \hat{n}_j)$ , where  $\hat{n}_i = \hat{n}_{i\uparrow} + \hat{n}_{i\downarrow}$  and

$$\hat{S}_i = \frac{1}{2} \begin{pmatrix} \hat{c}_{i\uparrow}^\dagger & \hat{c}_{i\downarrow}^\dagger \end{pmatrix} \vec{\sigma} \begin{pmatrix} \hat{c}_{i\uparrow} \\ \hat{c}_{i\downarrow} \end{pmatrix}. \quad (\text{A.22})$$

Further,  $\vec{\sigma} = (\sigma_x, \sigma_y, \sigma_z)^T$  is the vector of Pauli-matrices. One can now extract a corrected Hamiltonian (with  $\hat{n}_i = 0$  at half-filling)

$$\hat{H}_{\text{heisenberg}} = \frac{1}{2} \sum_{\langle ij \rangle}^N J_{ij} \vec{S}_i \cdot \vec{S}_j, \quad (\text{A.23})$$

where  $J_{ij} = 4t_{ij}^2/U$ . This is exactly the spin- $\frac{1}{2}$  Heisenberg Hamiltonian for an antiferromagnetically ordering lattice.

## A.4 Falicov-Kimball Limit

The (itinerant)  $c$ -electron Green's function for the Falicov-Kimball impurity can be calculated analytically. This is achieved by applying the equation of motion (EOM), i.e. the (imaginary) time derivative of either the itinerant creation or annihilation operator, on the impurity- and on the bath-level successively. While in a fully interacting system the equation of motion results in a hierarchy of Green's functions (i.e. the EOM for the one-particle Green's function generates a two-particle Green's function), the localized electrons of the Falicov-Kimball model truncate this series. The following derivations are based on [Brandt and Mielsch, 1989] and [Ribic, 2015]. One starts by defining the EOM for the itinerant  $c$ -electron impurity Green's function

$$\partial_\tau G^c(\tau) = -\partial_\tau \langle T_\tau \hat{c}_0(\tau) \hat{c}_0^\dagger(0) \rangle \quad (\text{A.24})$$

$$= -\langle T_\tau \partial_\tau \hat{c}_0(\tau) \hat{c}_0^\dagger(0) \rangle - \delta(\tau), \quad (\text{A.25})$$

where  $c_0^{(\dagger)}(\tau)$  is the annihilation (creation) operator for the impurity site  $i = 0$  at imaginary time  $\tau$ . Evaluating the time derivative generates a  $\delta(\tau)$  contribution following from the jump of the fermionic Green's function at equal times. The time derivative applied onto an operator follows as  $\partial_\tau \hat{c}_0(\tau) = [\hat{H}_{\text{fk}}, \hat{c}_0](\tau)$ , where square-brackets denote the commutator (i.e. Heisenberg's equation of motion). At this point, the Falicov-Kimball Hamiltonian (2.49) in the resonant level model is restated:

$$\hat{H}_{\text{fk}} = - \sum_{l>1}^N \left( t_{0l} \hat{c}_0^\dagger \hat{c}_l + t_{l0}^* \hat{c}_l^\dagger \hat{c}_0 + \mu_c \hat{c}_l^\dagger \hat{c}_l \right) + U \hat{f}^\dagger \hat{f} \hat{c}_0^\dagger \hat{c}_0 - \mu_f \hat{f}^\dagger \hat{f} - \mu_c \hat{c}_0^\dagger \hat{c}_0. \quad (\text{A.26})$$

With the Falicov-Kimball Hamiltonian, Heisenberg's equation of motion evaluates to:

$$\partial_\tau \hat{c}_0(\tau) = [\hat{H}_{\text{fk}}, \hat{c}_0](\tau) \quad (\text{A.27})$$

$$= - \sum_{l>1}^N \left( t_{0l} [\hat{c}_0^\dagger \hat{c}_l, \hat{c}_0] + t_{l0}^* [\hat{c}_l^\dagger \hat{c}_0, \hat{c}_0] + \mu_c [\hat{c}_l^\dagger \hat{c}_l, \hat{c}_0] \right) + \quad (\text{A.28})$$

$$+ U [\hat{f}^\dagger \hat{f} \hat{c}_0^\dagger \hat{c}_0, \hat{c}_0] - \mu_f [\hat{f}^\dagger \hat{f}, \hat{c}_0] - \mu_c [\hat{c}_0^\dagger \hat{c}_0, \hat{c}_0] \quad (\text{A.29})$$

The next step is to expand the above commutators and apply the fermionic anti-commutation rules  $\{c_i, c_j\} = \{c_i^\dagger, c_j^\dagger\} = 0$ ,  $\{c_i^\dagger, c_j\} = \delta_{ij}$ . The anti-commutator between  $f$ - (or multiples of  $f$ ) and  $c$ -operators vanishes for all combinations of creation and annihilation operators, such that:

$$\partial_\tau \hat{c}_0(\tau) = \sum_{l>1}^N t_{0l} \hat{c}_l(\tau) - U \hat{f}^\dagger(\tau) \hat{f}(\tau) \hat{c}_0(\tau) + \mu_c \hat{c}_0(\tau) \quad (\text{A.30})$$

The (imaginary) time derivative of the  $c$ -electron impurity Green's function follows as:

$$\partial_\tau G^c(\tau) = -\langle T_\tau \sum_{l>1}^N t_{0l} \hat{c}_l(\tau) \hat{c}_0^\dagger(0) \rangle + U \langle T_\tau \hat{f}^\dagger(\tau) \hat{f}(\tau) \hat{c}_0(\tau) \hat{c}_0^\dagger(0) \rangle - \mu_c \langle T_\tau \hat{c}_0(\tau) \hat{c}_0^\dagger(0) \rangle - \delta(\tau), \quad (\text{A.31})$$

The mixed two-particle Green's function between  $f$ -electrons and  $c$ -electrons can be further simplified by realizing that the impurity is either unoccupied or occupied by a localized  $f$  electron with  $N_f = \{0, 1\}$  (where a capital  $N_f$  was used to denote a classical (binary) occupation), such that:

$$\partial_\tau G^c(\tau) = -\langle T_\tau \sum_{l>1}^N t_{0l} \hat{c}_l(\tau) \hat{c}_0^\dagger(0) \rangle - U N_f G^c(\tau) + \mu_c G^c(\tau) - \delta(\tau). \quad (\text{A.32})$$

The mixed one-particle Green's function between  $c$ -electrons in the bath and the impurity is evaluated by applying Heisenberg's equation of motion for the bath operators  $\hat{c}_l$  another time:

$$-\partial_\tau \langle T_\tau \sum_{l>1}^N t_{0l} \hat{c}_l(\tau) \hat{c}_0^\dagger(0) \rangle = \sum_{l>1}^N t_{0l} t_{l0}^* \langle T_\tau \hat{c}_0(\tau) \hat{c}_0^\dagger(0) \rangle + \mu_c \langle T_\tau \hat{c}_l(\tau) \hat{c}_0^\dagger(0) \rangle \quad (\text{A.33})$$

$$-\langle T_\tau \sum_{l>1}^N t_{0l} \hat{c}_l(\tau) \hat{c}_0^\dagger(0) \rangle = - \sum_{l>1}^N \frac{t_{0l} t_{l0}^*}{\partial_\tau + \mu_c} G^c(\tau) \quad (\text{A.34})$$

where for the mixed bath-impurity Green's function the equal-time anti-commutator vanishes and, as such, the  $\delta(\tau)$  contribution vanished.

In a last step, a Fourier-transform of relation (A.32) into fermionic Matsubara frequencies yields:

$$G^c(i\nu) = \frac{1}{i\nu + \mu_c - \Delta(i\nu) - U N_f}, \quad (\text{A.35})$$

with the hybridization function defined as  $\Delta(i\nu) = \sum_{l>1}^N \frac{t_{0l} t_{l0}^*}{i\nu + \mu_c}$ .

# Appendix B

## Two-particle Frequency Conventions

In the following the frequency convention of this work is mapped onto the frequency convention of [Rohringer et al., 2017]. The particle-hole frequency convention employed in this work follows as:

$$G_{\sigma_1\sigma_2\sigma_3\sigma_4}^{\vec{k}\vec{k}'\vec{q},\nu\nu'\omega} = \int_0^\beta e^{i\nu(\tau_1-\tau_2)} e^{i\nu'(\tau_3-\tau_4)} e^{i\omega(\tau_2-\tau_3)} \times \\ \langle T_\tau \hat{c}_{\sigma_1,\vec{k}}(\tau_1) \hat{c}_{\sigma_2,\vec{k}-\vec{q}}^\dagger(\tau_2) \hat{c}_{\sigma_3,\vec{k}'-\vec{q}}(\tau_3) \hat{c}_{\sigma_4,\vec{k}'}^\dagger(\tau_4) \rangle d\tau_1 d\tau_2 d\tau_3 d\tau_4. \quad (\text{B.1})$$

The particle-hole convention employed by Rohringer *et al.* follows as:

$$G_{\sigma_1\sigma_2\sigma_3\sigma_4}^{\vec{k}\vec{k}'\vec{q},\nu\nu'\omega} = \int_0^\beta e^{i\nu(\tau_1-\tau_2)} e^{i\nu'(\tau_3-\tau_4)} e^{i\omega(\tau_3-\tau_2)} \times \\ \langle T_\tau \hat{c}_{\sigma_1,\vec{k}}(\tau_1) \hat{c}_{\sigma_2,\vec{k}-\vec{q}}^\dagger(\tau_2) \hat{c}_{\sigma_3,\vec{k}'-\vec{q}}(\tau_3) \hat{c}_{\sigma_4,\vec{k}'}^\dagger(\tau_4) \rangle d\tau_1 d\tau_2 d\tau_3 d\tau_4. \quad (\text{B.2})$$

The mapping between the two convention is given by  $\omega \rightarrow -\omega$ . These conventions equivalently apply for two-particle correlation functions  $\chi$ ,  $\chi^{\text{con}}$  and disconnected correlation functions, as well as for two-particle vertex functions  $F, \Gamma, \Phi$  and  $\Lambda$  in the particle-hole frequency notation. Furthermore, the convention extends identically to momentum space with  $\nu \rightarrow \vec{k}$ ,  $\nu' \rightarrow \vec{k}'$  and  $w \rightarrow \vec{q}$ . For multi-orbital systems the spin-indices are replaced by generalized indices, i.e.  $\sigma_i \rightarrow a_i$ .

This work further sketches two-particle diagrams differently than the two-particle diagrams of Rohringer *et al.*. While the former labels operators counter-clockwise starting from the upper left, the latter labels operators clockwise, starting from the lower left. The two conventions are illustrated in Figure B.1. Although these diagrams are topologically equivalent, some care needs to be taken when constructing equations of motions etc.

Further popular works in literature with different (although very similar) conventions are [Rohringer et al., 2012] (with a different operator order in the two-particle Green's function) and [Boehnke et al., 2011] (with the bosonic frequency attached to the first annihilation- and second creation operator).

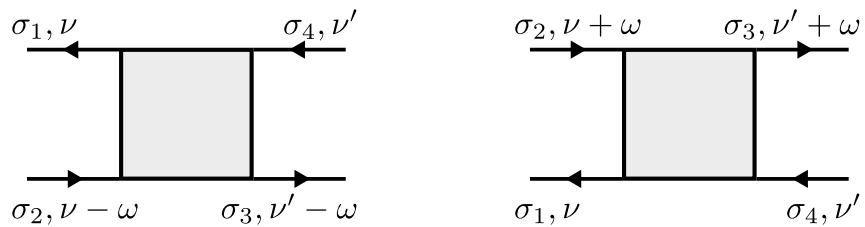


Figure B.1: Particle-hole frequency convention for two-particle quantities. Left: Frequency convention employed in this work. Right: Frequency convention employed by Rohringer *et al.* [Rohringer et al., 2017]. The frequency conventions apply for two-particle Green's functions, correlation functions and vertex functions equivalently. Extensions to for momentum-dependent- or multi-orbital two-particle functions follow by replacing the frequency- and spin indices respectively.

# Appendix C

## Functional Derivation of the Dual Fermion Approach

The following derivation of the dual action of the Hubbard model is based on the original work of [Rubtsov et al., 2008]. The derivation is based on the action (path integral) formalism, where the partition function of the Hubbard model follows as

$$Z_{\text{hubbard}} = \int \mathcal{D}[\bar{c}, c] e^{S_{\text{hubbard}}[\bar{c}, c]}. \quad (\text{C.1})$$

Here  $\bar{c}, c$  are fermionic Grassmann fields of the electrons and  $\mathcal{D}$  represents the integration over all paths. In the following the subscript label ‘‘hubbard’’ is dropped. More explicitly the action of the Hubbard model follows as

$$S[\bar{c}, c] = -\bar{c}_{k\nu\sigma} \mathcal{G}_{k\nu\sigma}^{-1} c_{k\nu\sigma} + U \sum_i \int_0^\beta d\tau \bar{c}_{i\uparrow}(\tau) c_{i\uparrow}(\tau) \bar{c}_{i\downarrow}(\tau) c_{i\downarrow}(\tau), \quad (\text{C.2})$$

where the non-interacting lattice propagator is defined as

$$\mathcal{G}_{k\nu\sigma}^{-1} = i\nu + \mu - \varepsilon_{\vec{k}}. \quad (\text{C.3})$$

The non-local and local physics are formally separated by introducing the impurity action to the above expression (which accounts to adding and subtracting a hybridization function), such that

$$S[\bar{c}, c] = \sum_i S_{\text{imp}}[\bar{c}, c] - \sum_{k\nu\sigma} \left( \Delta(i\nu) - \varepsilon_{\vec{k}} \right) \bar{c}_{k\nu\sigma} c_{k\nu\sigma}, \quad (\text{C.4})$$

with the impurity action

$$S_{\text{imp}}[\bar{c}, c] = -\bar{c}_{\nu\sigma} \mathcal{G}_{\nu\sigma}^{-1} c_{\nu\sigma} + U \int_0^\beta \bar{c}_\uparrow(\tau) c_\uparrow(\tau) \bar{c}_\downarrow(\tau) c_\downarrow(\tau) \quad (\text{C.5})$$

and the impurity propagator

$$\mathcal{G}_{\nu\sigma}^{-1} = i\nu + \mu - \Delta(i\nu). \quad (\text{C.6})$$

In order to decouple impurity and lattice physics, a Hubbard-Stratonovich transformation is applied to relation (C.4), resulting in the new action<sup>1</sup>

$$S[\bar{c}, c; \bar{f}, f] = \sum_i S_{\text{imp}}[\bar{c}, c] + \sum_{k\nu\sigma} \left[ G_{\nu\sigma}^{-1} (\bar{f}_{k\nu\sigma} c_{k\nu\sigma} + \bar{c}_{k\nu\sigma} f_{k\nu\sigma}) + G_{\nu\sigma}^{-2} (\Delta(i\nu) - \varepsilon_{\vec{k}})^{-1} \bar{f}_{k\nu\sigma} f_{k\nu\sigma} \right], \quad (\text{C.7})$$

where  $\bar{f}, f$  are fermionic Grassmann fields of the dual fermions. Further the partition function follows as

$$Z[\bar{c}, c; \bar{f}, f] = Z_f \int \mathcal{D}[\bar{c}, c; \bar{f}, f] e^{-S[\bar{c}, c; \bar{f}, f]}, \quad (\text{C.8})$$

with an additional factor  $Z_f = G_{\nu\sigma} (\Delta(i\nu) - \varepsilon_{\vec{k}})$  from the Hubbard-Stratonovich transformation. Up to this point the mapping between the initial problem and the dual problem is exact. The functional derivative of the identical partition functions  $Z[\bar{c}, c]$  and  $Z[\bar{c}, c; \bar{f}, f]$  with respect to  $\varepsilon_{\vec{k}}$  connects the lattice Green's function  $G_{k\nu\sigma}$  and the dual Green's function  $\tilde{G}_{k\nu\sigma}$  with

$$G_{k\nu\sigma} = (\Delta(i\nu) - \varepsilon_{\vec{k}})^{-2} G_{\nu\sigma}^{-2} \tilde{G}_{k\nu\sigma} + (\Delta(i\nu) - \varepsilon_{\vec{k}})^{-1}. \quad (\text{C.9})$$

By requiring  $\sum_k \tilde{G}_{k\nu\sigma} = 0$ , i.e. the dual propagator being completely non-local in space, the hybridization function  $\Delta(i\nu)$  is equivalent to the DMFT hybridization function.

In a last step the electrons are effectively integrated out of the action. For that matter the coupling term between the electrons and dual fermions in relation (C.7) is Fourier transformed into real space

$$\begin{aligned} \sum_i S^{\text{coupling}}[\bar{c}, c; \bar{f}, f] &= \sum_{k\nu\sigma} G_{\nu\sigma}^{-1} (\bar{f}_{k\nu\sigma} c_{k\nu\sigma} + \bar{c}_{k\nu\sigma} f_{k\nu\sigma}) \\ &= \sum_{i\nu\sigma} G_{\nu\sigma}^{-1} (\bar{f}_{i\nu\sigma} c_{i\nu\sigma} + \bar{c}_{i\nu\sigma} f_{i\nu\sigma}). \end{aligned} \quad (\text{C.10})$$

Now, the electrons are integrated out by Taylor-expanding the action part including the

---

<sup>1</sup>The Hubbard-Stratonovich transformation is essentially a completion of the square in the Gaussian part of the path integral. It expresses an interacting problem given by a quadratic form in the path integral by a dual quadratic form and a coupling between the two. The dual problem may be chosen to be non-local (as in this case) or, more common, non-interacting when decoupling the bare interaction, overall resulting in a simplified, nevertheless exact, formulation of the initial problem.



electrons at each site  $i$ , such that

$$\begin{aligned}
Z_{\text{site}} &= \int \mathcal{D}[\bar{c}, c] e^{-S_{\text{imp}} - S_{\text{coupling}}} = \int \mathcal{D}[\bar{c}, c] e^{-S_{\text{imp}}} \times \\
&\left[ 1 - \frac{1}{2} \sum_{\substack{\nu_1 \nu_2 \\ \sigma_1 \sigma_2}} G_{\nu_1 \sigma_1}^{-1} G_{\nu_2 \sigma_2}^{-1} \left( \bar{f}_{i\nu_1 \sigma_1} f_{i\nu_2 \sigma_2} c_{i\nu_1 \sigma_1} \bar{c}_{i\nu_2 \sigma_2} + \{ \nu_1 \leftrightarrow \nu_2; \sigma_1 \leftrightarrow \sigma_2 \} \right) + \right. \\
&\quad + \frac{1}{4} \sum_{\substack{\nu_1 \nu_2 \nu_3 \nu_4 \\ \sigma_1 \sigma_2 \sigma_3 \sigma_4}} G_{\nu_1 \sigma_1}^{-1} G_{\nu_2 \sigma_2}^{-1} G_{\nu_3 \sigma_3}^{-1} G_{\nu_4 \sigma_4}^{-1} \left( \bar{f}_{i\nu_1 \sigma_1} f_{i\nu_2 \sigma_2} \bar{f}_{i\nu_3 \sigma_3} f_{i\nu_4 \sigma_4} c_{i\nu_1 \sigma_1} \bar{c}_{i\nu_2 \sigma_2} c_{i\nu_3 \sigma_3} \bar{c}_{i\nu_4 \sigma_4} + \right. \\
&\quad \left. \left. + \{ \nu_1 \leftrightarrow \nu_2, \nu_3 \leftrightarrow \nu_4; \sigma_1 \leftrightarrow \sigma_2, \sigma_3 \leftrightarrow \sigma_4 \} + \dots \right) + \mathcal{O}(N^3) \right] \\
&= Z_{\text{imp}} \left[ 1 - \sum_{\nu\sigma} G_{\nu\sigma}^{-1} \bar{f}_{i\nu\sigma} f_{i\nu\sigma} + \right. \\
&\quad \left. + \frac{1}{4} \sum_{\substack{\nu_1 \nu_2 \nu_3 \nu_4 \\ \sigma_1 \sigma_2 \sigma_3 \sigma_4}} G_{\nu_1 \sigma_1}^{-1} G_{\nu_2 \sigma_2}^{-1} G_{\nu_3 \sigma_3}^{-1} G_{\nu_4 \sigma_4}^{-1} \bar{f}_{i\nu_1 \sigma_1} f_{i\nu_2 \sigma_2} \bar{f}_{i\nu_3 \sigma_3} f_{i\nu_4 \sigma_4} (G_{\sigma_1 \sigma_2 \sigma_3 \sigma_4}^{c, \nu_1 \nu_2 \nu_3 \nu_4} + \dots) + \mathcal{O}(N^3) \right] \\
&= Z_{\text{imp}} \left( 1 - \sum_{\nu\sigma} G_{\nu\sigma}^{-1} \bar{f}_{i\nu\sigma} f_{i\nu\sigma} + V[\bar{f}, f] \right), \tag{C.11}
\end{aligned}$$

where in the Taylor expansion only even orders result in a non-vanishing contribution as creation and annihilation operators in either the electrons and the dual fermions need to appear pairwise. The couplings between dual and real fermions due to the Taylor expansion are now reintroduced to the action (C.7), resulting in the new action being defined in terms of the dual variables only

$$\tilde{S}[\bar{f}, f] = \sum_{k\nu\sigma} [G_{\nu\sigma}^{-2} (\Delta(i\nu) - \varepsilon_{\vec{k}})^{-1} + G_{\nu\sigma}^{-1}] \bar{f}_{k\nu\sigma} f_{k\nu\sigma} + \sum_i V[\bar{f}, f] \tag{C.12}$$

$$= - \sum_{k\nu\sigma} \tilde{\mathcal{G}}_{k\nu\sigma}^{-1} \bar{f}_{k\nu\sigma} f_{k\nu\sigma} + \sum_i V[\bar{f}, f]. \tag{C.13}$$

By Taylor-expanding the action  $S^{\text{coupling}}$  in relation (C.11), one effectively assumes the functional  $W \sim \ln Z$ . Thus, the interaction  $V[\bar{f}, f]$  only includes connected propagators  $G^c$ , excluding any disconnected contributions.



# Appendix D

## Multi-orbital Hubbard Model

### D.1 Half-filling Condition in DMFT

The half-filling conditions for  $N$  orbitals can be extracted from the local part of the Anderson impurity model (see e.g. relation (3.22)). In the single orbital case ( $N = 1$ ), the local part of the Anderson impurity model is given by:

$$H_{\text{at}}^{mn} = \langle m | \hat{H}_{\text{at}} | n \rangle = \begin{pmatrix} 0 & 0 & 0 & 0 \\ 0 & -\mu & 0 & 0 \\ 0 & 0 & -\mu & 0 \\ 0 & 0 & 0 & U - 2\mu \end{pmatrix}. \quad (\text{D.1})$$

Half-filling is obtained by setting the eigen-energy of the doubly occupied state  $U - 2\mu$  to be equal to the eigen-energy of the empty state  $\varepsilon_0 = 0$ , resulting in a filling-symmetric Hamiltonian. The condition for the chemical potential then follows as  $\mu = U/2$ .

A straight-forward extension to the multi-orbital case requires the determination of the eigen-energy of the fully occupied state  $|\uparrow\downarrow, \uparrow\downarrow, \dots\rangle$ . In the multi-orbital case, the SU(2)-symmetric Slater-Kanamori interaction may be parametrized by  $U, V$  and  $J$ . The intra-orbital coupling  $U$  adds an energy cost for anti-parallel spins within a given orbital; the inter-orbital coupling  $V$  adds an energy for having two electrons in different orbitals independent of their spin; the Hund's coupling  $J$  lowers the energy for parallel spins between different orbitals. The total energy for the fully occupied state for  $N$  orbitals may then be read off as presented in Table D.1. It is noted that the spin-flip and pair-hopping term of the SU(2)-symmetric Slater-Kanamori interaction do not contribute to

Table D.1: Number of interaction terms contributing to the eigen-energy of the fully occupied state in the local  $N$ -orbital Hamiltonian.

coupling	number of terms
$U$ (intra-orbital)	$N$
$V$ (inter-orbital)	$2 \sum_{n=1}^N 2(n-1) = 2(N^2 - N)$
$-J$ (Hund)	$2 \sum_{n=1}^N (n-1) = N^2 - N$

the total energy of the fully occupied state due to Pauli's exclusion principle. This can be directly verified by calculating the (vanishing) matrix elements of a fully occupied state for the spin-flip or pair-hopping terms. Thus, the fully occupied state has the same energy independent of the local interaction being SU(2)-symmetric or simply density-density. In addition to the two-particle contributions stemming from the interaction part of the Hamiltonian, the single-particle energy contributes with a factor  $-2N\mu$ , such that the total eigen-energy of the fully occupied state is given by

$$\varepsilon_{\text{full}} = NU + (N^2 - N)(2V - J) - 2N\mu \quad (\text{D.2})$$

Assuming particle-hole symmetry, the chemical potential at half-filling follows by setting  $\varepsilon_0 = \varepsilon_{\text{full}}$ , such that:

$$\mu = \frac{U}{2} + (N - 1)(V - \frac{J}{2}) \quad (\text{D.3})$$

For  $V = J = 0$  only the intra-orbital coupling remains, so that  $\mu = U/2$  is recovered. For the SO(N)  $\times$  SU(2) symmetric Slater-Kanamori interaction, with  $V = U - 2J$ , the chemical potential is given by  $\mu = (N - \frac{1}{2})U - (N - 1)\frac{5}{2}J$ .

## D.2 Lowest-order Contributions to $F$

The number of components present in the vertex function  $F$  (and by extension also in the two-particle Green's function) can be determined by a perturbation expansion in terms of the bare interaction vertex  $U$ . The following analysis is based on the SU(2)-symmetric Slater-Kanamori bare interaction vertex, which is parametrized by  $U, V$  and  $J$  including spin-flip and pair-hopping terms, as an extension to the density-density bare interaction vertex, where the latter are missing.<sup>1</sup>

type	component	lowest order	number of terms
flavor-diagonal	$\hat{c}_{\alpha\sigma}\hat{c}_{\alpha\bar{\sigma}}^\dagger\hat{c}_{\alpha\bar{\sigma}}\hat{c}_{\alpha\sigma}^\dagger$	$U$	$2N$
	$\hat{c}_{\alpha\sigma}\hat{c}_{\alpha\sigma}^\dagger\hat{c}_{\alpha\bar{\sigma}}\hat{c}_{\alpha\bar{\sigma}}^\dagger$	$U$	$2N$
	$\hat{c}_{\alpha\sigma}\hat{c}_{\alpha\sigma}^\dagger\hat{c}_{\alpha\sigma}\hat{c}_{\alpha\sigma}^\dagger$	$U^2, V^2, (V - J)^2$	$2N$
	$\hat{c}_{\alpha\sigma}\hat{c}_{\beta\bar{\sigma}}^\dagger\hat{c}_{\beta\bar{\sigma}}\hat{c}_{\alpha\sigma}^\dagger$	$V$	$4\binom{N}{2}$
	$\hat{c}_{\alpha\sigma}\hat{c}_{\alpha\sigma}^\dagger\hat{c}_{\beta\bar{\sigma}}\hat{c}_{\beta\bar{\sigma}}^\dagger$	$V$	$4\binom{N}{2}$
	$\hat{c}_{\alpha\sigma}\hat{c}_{\beta\sigma}^\dagger\hat{c}_{\beta\sigma}\hat{c}_{\alpha\sigma}^\dagger$	$V - J$	$4\binom{N}{2}$
	$\hat{c}_{\alpha\sigma}\hat{c}_{\alpha\sigma}^\dagger\hat{c}_{\beta\sigma}\hat{c}_{\beta\sigma}^\dagger$	$V - J$	$4\binom{N}{2}$
flavor off-diagonal	$\hat{c}_{\alpha\sigma}\hat{c}_{\alpha\bar{\sigma}}^\dagger\hat{c}_{\beta\bar{\sigma}}\hat{c}_{\beta\sigma}^\dagger$	$J$ (SF)	$4\binom{N}{2}$
	$\hat{c}_{\alpha\sigma}\hat{c}_{\beta\sigma}^\dagger\hat{c}_{\beta\bar{\sigma}}\hat{c}_{\alpha\bar{\sigma}}^\dagger$	$J$ (SF)	$4\binom{N}{2}$
	$\hat{c}_{\alpha\sigma}\hat{c}_{\beta\sigma}^\dagger\hat{c}_{\alpha\bar{\sigma}}\hat{c}_{\beta\bar{\sigma}}^\dagger$	$J$ (PH)	$4\binom{N}{2}$
	$\hat{c}_{\alpha\sigma}\hat{c}_{\beta\bar{\sigma}}^\dagger\hat{c}_{\alpha\bar{\sigma}}\hat{c}_{\beta\sigma}^\dagger$	$J$ (PH)	$4\binom{N}{2}$
	$\hat{c}_{\alpha\sigma}\hat{c}_{\beta\sigma}^\dagger\hat{c}_{\alpha\sigma}\hat{c}_{\beta\sigma}^\dagger$	$J^2$ (SF + PH)	$4\binom{N}{2}$

Table D.2: Perturbation order and number of components of the two-particle Green's function for the SU(2)-symmetric Slater-Kanamori interaction, with  $\alpha \neq \beta$  and  $\sigma \neq \bar{\sigma}$ .

The four operators of the two-particle Green's function allow in principle for a total of  $(2N)^4$  spin-orbital components for the two-particle Green's function. Due to the structure of the Slater-Kanamori interaction, only a subset of components results in a non-vanishing contribution to the two-particle Green's function as analyzed in detail in Table D.2. Contributions with a single orbital index have a spin-multiplicity of 2 and a factor  $N$  for the number of orbitals. Contributions with two orbital indices have a spin-multiplicity of 2,

<sup>1</sup>This discussion is especially relevant for CT-HYB implementations with diagonal hybridization functions, which in the conventional way of "removing hybridization lines" do not sample all two-particle objects, but only a subset of diagrams with pairwise flavor-diagonal outer legs. While for density-density interactions, this is indeed no restriction, for more general interactions a significant amount of components of the two-particle Green's function is ignored.

the binomial coefficient  $\binom{N}{2}$  for selecting 2 out of  $N$  orbitals and an additional factor 2 for exchanging the two orbital indices. The number of pairwise flavor-diagonal components  $M_{\text{diag}}$  (Table D.2 upper category) for the two-particle Green's function follows as:

$$M_{\text{diag}} = 6N + 16\binom{N}{2}. \quad (\text{D.4})$$

The number of flavor-off-diagonal (i.e. four different flavors) components  $M_{\text{offdiag}}$  (Table D.2 lower category) for the two particle Green's function follows as:

$$M_{\text{offdiag}} = 20\binom{N}{2}. \quad (\text{D.5})$$

The total number of components  $M = M_{\text{diag}} + M_{\text{offdiag}}$  for the two particle Green's function, thus follows as

$$M = 6N + 36\binom{N}{2}, \quad (\text{D.6})$$

which evaluates to  $M = \{6, 48, 126, 240, 390\}$  for  $N = \{1, 2, 3, 4, 5\}$ . The ratio of pairwise flavor-diagonal components over the total number of components  $R_N = M_{\text{diag}}/M$  evaluated in the limits of a single orbital is  $R_1 = 1$  and for infinitely many orbitals

$$R_\infty = \lim_{N \rightarrow \infty} \frac{6N + 16\binom{N}{2}}{6N + 36\binom{N}{2}} = \frac{4}{9}, \quad (\text{D.7})$$

which means that approximately 44 percent can be attributed to pairwise flavor-diagonal components. Already at  $N = 5$ , the ratio evaluates to  $R_5 = 0.48$ .

# Appendix E

## Autocorrelation in CT-HYB

### E.1 Error Estimation for Correlated Samples

In order to estimate the autocorrelation length it is necessary to compare the error estimates for uncorrelated and correlated samples. A more detailed discussion of the derivations is found elsewhere [Heistracher, 2016].

#### E.1.1 Standard Error of Uncorrelated Samples

In the following the expectation value of an observable  $A$  is denoted as  $\langle A \rangle$ . The sample mean  $\bar{A}$  for individual samples  $A_i$  for  $i = 1, \dots, N$  is defined as:

$$\bar{A} = \frac{1}{N} \sum_{i=1}^N A_i \quad (\text{E.1})$$

The expectation value of the mean follows as:

$$\langle \bar{A} \rangle = \frac{1}{N} \langle \sum_{i=1}^N A_i \rangle = \frac{N}{N} \langle A \rangle = \langle A \rangle, \quad (\text{E.2})$$

where  $\langle A_i \rangle = \langle A \rangle$ . Thus, the expectation value of the mean is the expectation value of the observable itself, such that the mean is often considered as an approximation to the expectation value  $\bar{A} \approx \langle A \rangle$ . The square of the standard error is defined as:

$$\sigma_A^2 = \langle (\bar{A} - \langle A \rangle)^2 \rangle \quad (\text{E.3})$$

Expanding the mean in the above expression yields:

$$\sigma_A^2 = \langle \bar{A}^2 \rangle - 2\langle \bar{A} \rangle \langle A \rangle + \langle A \rangle^2 = \langle \bar{A}^2 \rangle - \langle A \rangle^2 \quad (\text{E.4})$$

The expectation value of the square of the mean needs to be evaluated explicitly:

$$\langle \bar{A}^2 \rangle = \langle \left( \frac{1}{N} \sum_{i=1}^N A_i \right)^2 \rangle = \langle \frac{1}{N^2} \sum_{i=1}^N A_i^2 \rangle + \langle \frac{1}{N^2} \sum_{i \neq j}^N A_i A_j \rangle = \frac{1}{N} \langle A^2 \rangle + \frac{N-1}{N} \langle A \rangle^2, \quad (\text{E.5})$$

where for uncorrelated samples  $\langle A_i A_j \rangle = \langle A_i \rangle \langle A_j \rangle = \langle A \rangle^2$ . The standard square of the error follows as:

$$\sigma_A^2 = \frac{1}{N} \left( \langle A^2 \rangle - \langle A \rangle^2 \right) = \frac{1}{N} \text{Var}(A) \quad (\text{E.6})$$

The above relation encodes the  $1/\sqrt{N}$  error scaling encountered in Monte Carlo.

### E.1.2 Standard Error of Correlated Samples

For correlated samples  $\langle A_i A_j \rangle \neq \langle A_i \rangle \langle A_j \rangle$ . Thus, equation (E.6) needs to be corrected with:

$$\sigma_A^2 = \frac{1}{N} \text{Var}(A) + \frac{1}{N^2} \sum_{i \neq j}^N \left( \langle A_i A_j \rangle - \langle A \rangle^2 \right). \quad (\text{E.7})$$

This correction term includes the auto-correlation length:

$$\frac{1}{N^2} \sum_{i \neq j}^N \left( \langle A_i A_j \rangle - \langle A \rangle^2 \right) = \frac{2}{N^2} \sum_{i < j}^N \left( \langle A_i A_j \rangle - \langle A \rangle^2 \right) \quad (\text{E.8})$$

$$= \frac{2}{N^2} \sum_{t=1}^{N-1} \sum_{i=1}^{N-t} \left( \langle A_i A_{i+t} \rangle - \langle A \rangle^2 \right) \quad (\text{E.9})$$

$$\approx \frac{2}{N} \sum_{t=1}^{\infty} \left( \langle A_1 A_{1+t} \rangle - \langle A \rangle^2 \right), \quad (\text{E.10})$$

where in the approximation a large samples size of  $N \rightarrow \infty$  is considered, such that one of the two sums can be reduced by considering any one sample as a reference point. With the auto-correlation length defined as

$$\tau_A = \frac{\sum_{t=1}^{\infty} \left( \langle A_1 A_{1+t} \rangle - \langle A \rangle^2 \right)}{\text{Var}(A)} \quad (\text{E.11})$$

the square of the standard error for correlated samples follows as:

$$\sigma_A^2 = \text{Var}(A) \frac{(1 + 2\tau_A)}{N}. \quad (\text{E.12})$$

While in principle, the  $1/\sqrt{N}$  error scaling in Monte Carlo is preserved even for correlated configurations of a Markov chain, the error scaling further obtains a  $\sqrt{1 + 2\tau_A}$  factor, which enlarges the error.



# Appendix F

## Symmetric Improved Estimators

### F.1 Two-particle Symmetric Improved Estimator

In the following derivation of the two-particle symmetric improved estimator, the single-orbital Hubbard model is considered and the following derivations are in analogy to the one-particle symmetric improved estimator in Section 3.4.1. In order to simplify the following equations, the three fermionic operators occurring at equal time are written in a compact form as:

$$\hat{q}_\sigma := \hat{n}_{-\sigma} \hat{d}_\sigma = \hat{d}_{-\sigma}^\dagger \hat{d}_{-\sigma} \hat{d}_\sigma \quad (\text{F.1})$$

$$\hat{q}_\sigma^\dagger := \hat{d}_\sigma^\dagger \hat{n}_{-\sigma} = \hat{d}_\sigma^\dagger \hat{d}_{-\sigma}^\dagger \hat{d}_{-\sigma}. \quad (\text{F.2})$$

Some of the following intermediate steps are not shown explicitly, but are in principle equivalent to the steps in Section 3.4.1. This includes the evaluation of commutators of fermionic operators with the AIM Hamiltonian (i.e. Heisenberg equation of motion), originating of the time-derivative of the specific operator. The resulting expression includes a mixed bath-impurity expectation value, which can be expressed as an impurity expectation value by applying an equation of motion onto the bath operator. Intuitively, the equation of motion procedure sets an impurity expectation value in relation to a lower-order impurity expectation value multiplied by a non-interacting Green's function. Additional terms are generated by the time-derivative of the time ordering symbol  $T_\tau$ .

The hierarchy of equation of motions for the two-particle Green's function is defined as:

$$\begin{aligned} \partial_{\tau_1} \langle T_\tau \hat{d}_{\sigma_1}(\tau_1) \hat{d}_{\sigma_2}^\dagger(\tau_2) \hat{d}_{\sigma_3}(\tau_3) \hat{d}_{\sigma_4}^\dagger(\tau_4) \rangle &= R_1 + \langle T_\tau \partial_{\tau_1} \hat{d}_{\sigma_1}(\tau_1) \hat{d}_{\sigma_2}^\dagger(\tau_2) \hat{d}_{\sigma_3}(\tau_3) \hat{d}_{\sigma_4}^\dagger(\tau_4) \rangle \\ (\partial_{\tau_1} + \mu - \Delta_{\sigma_1}(\tau_1)) \langle T_\tau \hat{d}_{\sigma_1}(\tau_1) \hat{d}_{\sigma_2}^\dagger(\tau_2) \hat{d}_{\sigma_3}(\tau_3) \hat{d}_{\sigma_4}^\dagger(\tau_4) \rangle &= \\ R_1 + U \langle T_\tau \hat{q}_{\sigma_1}(\tau_1) \hat{d}_{\sigma_2}^\dagger(\tau_2) \hat{d}_{\sigma_3}(\tau_3) \hat{d}_{\sigma_4}^\dagger(\tau_4) \rangle & \quad (\text{F.3}) \end{aligned}$$

$$\begin{aligned}
\partial_{\tau_2} \langle T_{\tau} \hat{q}_{\sigma_1}(\tau_1) \hat{d}_{\sigma_2}^{\dagger}(\tau_2) \hat{d}_{\sigma_3}(\tau_3) \hat{d}_{\sigma_4}^{\dagger}(\tau_4) \rangle &= R_2 + \langle T_{\tau} \hat{q}_{\sigma_1}(\tau_1) \partial_{\tau_2} \hat{d}_{\sigma_2}^{\dagger}(\tau_2) \hat{d}_{\sigma_3}(\tau_3) \hat{d}_{\sigma_4}^{\dagger}(\tau_4) \rangle \\
\left( -\partial_{\tau_2} + \mu - \Delta_{\sigma_2}(\tau_2) \right) \langle T_{\tau} \hat{q}_{\sigma_1}(\tau_1) \hat{d}_{\sigma_2}^{\dagger}(\tau_2) \hat{d}_{\sigma_3}(\tau_3) \hat{d}_{\sigma_4}^{\dagger}(\tau_4) \rangle &= \\
& - R_2 + U \langle T_{\tau} \hat{q}_{\sigma_1}(\tau_1) \hat{q}_{\sigma_2}^{\dagger}(\tau_2) \hat{d}_{\sigma_3}(\tau_3) \hat{d}_{\sigma_4}^{\dagger}(\tau_4) \rangle \quad (\text{F.4})
\end{aligned}$$

$$\begin{aligned}
\partial_{\tau_3} \langle T_{\tau} \hat{q}_{\sigma_1}(\tau_1) \hat{q}_{\sigma_2}^{\dagger}(\tau_2) \hat{d}_{\sigma_3}(\tau_3) \hat{d}_{\sigma_4}^{\dagger}(\tau_4) \rangle &= R_3 + \langle T_{\tau} \hat{q}_{\sigma_1}(\tau_1) \hat{q}_{\sigma_2}^{\dagger}(\tau_2) \partial_{\tau_3} \hat{d}_{\sigma_3}(\tau_3) \hat{d}_{\sigma_4}^{\dagger}(\tau_4) \rangle \\
\left( \partial_{\tau_3} + \mu - \Delta_{\sigma_3}(\tau_3) \right) \langle T_{\tau} \hat{q}_{\sigma_1}(\tau_1) \hat{q}_{\sigma_2}^{\dagger}(\tau_2) \hat{d}_{\sigma_3}(\tau_3) \hat{d}_{\sigma_4}^{\dagger}(\tau_4) \rangle &= \\
& R_3 + U \langle T_{\tau} \hat{q}_{\sigma_1}(\tau_1) \hat{q}_{\sigma_2}^{\dagger}(\tau_2) \hat{q}_{\sigma_3}(\tau_3) \hat{d}_{\sigma_4}^{\dagger}(\tau_4) \rangle \quad (\text{F.5})
\end{aligned}$$

$$\begin{aligned}
\partial_{\tau_4} \langle T_{\tau} \hat{q}_{\sigma_1}(\tau_1) \hat{q}_{\sigma_2}^{\dagger}(\tau_2) \hat{q}_{\sigma_3}(\tau_3) \hat{d}_{\sigma_4}^{\dagger}(\tau_4) \rangle &= R_4 + \langle T_{\tau} \hat{q}_{\sigma_1}(\tau_1) \hat{q}_{\sigma_2}^{\dagger}(\tau_2) \hat{q}_{\sigma_3}(\tau_3) \partial_{\tau_4} \hat{d}_{\sigma_4}^{\dagger}(\tau_4) \rangle \\
\left( -\partial_{\tau_4} + \mu - \Delta_{\sigma_4}(\tau_4) \right) \langle T_{\tau} \hat{q}_{\sigma_1}(\tau_1) \hat{q}_{\sigma_2}^{\dagger}(\tau_2) \hat{q}_{\sigma_3}(\tau_3) \hat{d}_{\sigma_4}^{\dagger}(\tau_4) \rangle &= \\
& - R_4 + U \langle T_{\tau} \hat{q}_{\sigma_1}(\tau_1) \hat{q}_{\sigma_2}^{\dagger}(\tau_2) \hat{q}_{\sigma_3}(\tau_3) \hat{q}_{\sigma_4}^{\dagger}(\tau_4) \rangle \quad (\text{F.6})
\end{aligned}$$

The remaining terms  $R_i$  result from the time-derivative of the time-ordering symbol  $T_{\tau}$ , with:

$$R_1 = \delta(\tau_1 - \tau_2) \delta_{\sigma_1 \sigma_2} \langle T_{\tau} \hat{d}_{\sigma_3}(\tau_3) \hat{d}_{\sigma_4}^{\dagger}(\tau_4) \rangle - \delta(\tau_1 - \tau_4) \delta_{\sigma_1 \sigma_4} \langle T_{\tau} \hat{d}_{\sigma_3}(\tau_3) \hat{d}_{\sigma_2}^{\dagger}(\tau_2) \rangle \quad (\text{F.7})$$

$$\begin{aligned}
R_2 = -\delta(\tau_1 - \tau_2) \langle T_{\tau} \{ \hat{q}_{\sigma_1}, \hat{d}_{\sigma_2}^{\dagger} \}(\tau_1) \hat{d}_{\sigma_3}(\tau_3) \hat{d}_{\sigma_4}^{\dagger}(\tau_4) \rangle \\
+ \delta(\tau_2 - \tau_3) \delta_{\sigma_2, \sigma_3} \langle T_{\tau} \hat{q}_{\sigma_1}(\tau_1) \hat{d}_{\sigma_4}^{\dagger}(\tau_4) \rangle \quad (\text{F.8})
\end{aligned}$$

$$\begin{aligned}
R_3 = -\delta(\tau_1 - \tau_3) \langle T_{\tau} \{ \hat{q}_{\sigma_1}, \hat{d}_{\sigma_3} \}(\tau_1) \hat{q}_{\sigma_2}^{\dagger}(\tau_2) \hat{d}_{\sigma_4}^{\dagger}(\tau_4) \rangle - \\
\delta(\tau_2 - \tau_3) \langle T_{\tau} \hat{q}_{\sigma_1}(\tau_1) \{ \hat{q}_{\sigma_2}^{\dagger}, \hat{d}_{\sigma_3} \}(\tau_2) \hat{d}_{\sigma_4}^{\dagger}(\tau_4) \rangle + \delta(\tau_3 - \tau_4) \delta_{\sigma_3, \sigma_4} \langle T_{\tau} \hat{q}_{\sigma_1}(\tau_1) \hat{q}_{\sigma_2}^{\dagger}(\tau_2) \rangle \quad (\text{F.9})
\end{aligned}$$

$$\begin{aligned}
R_4 = -\delta(\tau_1 - \tau_4) \langle T_{\tau} \{ \hat{q}_{\sigma_1}, \hat{d}_{\sigma_4}^{\dagger} \}(\tau_1) \hat{q}_{\sigma_2}^{\dagger}(\tau_2) \hat{q}_{\sigma_3}(\tau_3) \rangle - \\
\delta(\tau_2 - \tau_4) \langle T_{\tau} \hat{q}_{\sigma_1}(\tau_1) \{ \hat{q}_{\sigma_2}^{\dagger}, \hat{d}_{\sigma_4}^{\dagger} \}(\tau_2) \hat{q}_{\sigma_3}(\tau_3) \rangle - \delta(\tau_3 - \tau_4) \langle T_{\tau} \hat{q}_{\sigma_1}(\tau_1) \hat{q}_{\sigma_2}^{\dagger}(\tau_2) \{ \hat{q}_{\sigma_3}, \hat{d}_{\sigma_4}^{\dagger} \}(\tau_3) \rangle \quad (\text{F.10})
\end{aligned}$$

The anti-commutators in the above relations can be evaluated explicitly by setting the spin-indices  $\sigma_i$  to either  $\sigma$  or  $-\sigma$ , i.e. considering specific components of the two-particle

Green's function. Combining the above hierarchy into a single equation, one finds:

$$G_{\sigma_1, \sigma_2, \sigma_3, \sigma_4}^{\tau_1, \tau_2, \tau_3, \tau_4} = \frac{1}{\partial_{\tau_1} + \mu - \Delta_{\sigma_1}(\tau_1)} \left( R_1 + \frac{U}{-\partial_{\tau_2} + \mu - \Delta_{\sigma_2}(\tau_2)} \times \right. \\ \left. \left( -R_2 + \frac{U}{\partial_{\tau_3} + \mu - \Delta_{\sigma_3}(\tau_3)} \left( R_3 + \frac{U}{-\partial_{\tau_4} + \mu - \Delta_{\sigma_4}(\tau_4)} \times \right. \right. \right. \\ \left. \left. \left. \left( -R_4 + U \langle T_\tau \hat{q}_{\sigma_1}(\tau_1) \hat{q}_{\sigma_2}^\dagger(\tau_2) \hat{q}_{\sigma_3}(\tau_3) \hat{q}_{\sigma_4}^\dagger(\tau_4) \rangle \right) \right) \right) \right) \quad (\text{F.11})$$

As each of the  $R_i$  terms represents a Monte Carlo estimator in itself it is better to assemble the two-particle Green's function in Matsubara space. The above expression for the two-particle Green's function in Matsubara frequencies follows as:

$$G_{\sigma_1, \sigma_2, \sigma_3, \sigma_4}^{\nu, \nu', \omega} = \mathcal{G}(\nu) \left( \mathcal{F}(R_1) + U \mathcal{G}(\nu - \omega) \left( -\mathcal{F}(R_2) + U \mathcal{G}(\nu' - \omega) \left( \mathcal{F}(R_3) + \right. \right. \right. \\ \left. \left. \left. U \mathcal{G}(\nu') \left( -\mathcal{F}(R_4) + U \mathcal{F} \left[ \langle T_\tau \hat{q}_{\sigma_1}(\tau_1) \hat{q}_{\sigma_2}^\dagger(\tau_2) \hat{q}_{\sigma_3}(\tau_3) \hat{q}_{\sigma_4}^\dagger(\tau_4) \rangle \right] \right) \right) \right) \right) \quad (\text{F.12})$$

In the Matsubara domain the error scaling of the symmetric improved estimator becomes obvious. If one assumes a constant Monte Carlo error on the symmetric improved estimator and no error on the estimators encoded in the  $R_i$  terms, the high-frequency error of the two-particle Green's function is suppressed by  $\mathcal{O}(i\nu^{-4})$ . In the following the  $R_i$  terms are calculated in particle-hole Matsubara representation for the  $\mathbf{G}_{\sigma\sigma\sigma\sigma}^{\nu\nu'\omega}$  component of the two-particle Green's function:

$$\mathcal{F}(R_1) = \int e^{i\nu(\tau_1 - \tau_2)} e^{i\nu'(\tau_3 - \tau_4)} e^{i\omega(\tau_2 - \tau_3)} \left[ \delta(\tau_1 - \tau_2) \langle T_\tau \hat{d}_\sigma(\tau_3) \hat{d}_\sigma^\dagger(\tau_4) \rangle - \right. \\ \left. \delta(\tau_1 - \tau_4) \langle T_\tau \hat{d}_\sigma(\tau_3) \hat{d}_\sigma^\dagger(\tau_2) \rangle \right] d\tau \\ = \delta_{\omega 0} G_\sigma(\nu') - \delta_{\nu\nu'} G_\sigma(\nu' - \omega) \quad (\text{F.13})$$

$$\mathcal{F}(R_2) = \int e^{i\nu(\tau_1 - \tau_2)} e^{i\nu'(\tau_3 - \tau_4)} e^{i\omega(\tau_2 - \tau_3)} \left[ -\delta(\tau_1 - \tau_2) \langle T_\tau \hat{n}_{-\sigma}(\tau_1) \hat{d}_\sigma(\tau_3) \hat{d}_\sigma^\dagger(\tau_4) \rangle + \right. \\ \left. \delta(\tau_2 - \tau_3) \langle T_\tau \hat{q}_\sigma(\tau_1) \hat{d}_\sigma^\dagger(\tau_4) \rangle \right] d\tau \\ = -\int e^{i\nu'(\tau_3 - \tau_4)} e^{i\omega(\tau_2 - \tau_3)} \langle T_\tau \hat{n}_{-\sigma}(\tau_2) \hat{d}_\sigma(\tau_3) \hat{d}_\sigma^\dagger(\tau_4) \rangle d\tau + \\ \delta_{\nu\nu'} \int e^{i\nu(\tau_1 - \tau_4)} \langle T_\tau \hat{q}_\sigma(\tau_1) \hat{d}_\sigma^\dagger(\tau_4) \rangle d\tau \quad (\text{F.14})$$

$$\begin{aligned}
\mathcal{F}(R_3) &= \int e^{i\nu(\tau_1-\tau_2)} e^{i\nu'(\tau_3-\tau_4)} e^{i\omega(\tau_2-\tau_3)} \left[ -\delta(\tau_2 - \tau_3) \langle T_\tau \hat{q}_\sigma(\tau_1) \hat{n}_{-\sigma}(\tau_2) \hat{d}_\sigma^\dagger(\tau_4) \rangle + \right. \\
&\quad \left. \delta(\tau_3 - \tau_4) \langle T_\tau \hat{q}_\sigma(\tau_1) \hat{q}_\sigma^\dagger(\tau_2) \rangle \right] d\tau \\
&= \int e^{i\nu(\tau_1-\tau_2)} e^{i\nu'(\tau_2-\tau_4)} \langle T_\tau \hat{q}_\sigma(\tau_1) \hat{n}_{-\sigma}(\tau_2) \hat{d}_\sigma^\dagger(\tau_4) \rangle + \\
&\quad \delta_{\omega 0} \int e^{i\nu(\tau_1-\tau_2)} \langle T_\tau \hat{q}_\sigma(\tau_1) \hat{q}_\sigma^\dagger(\tau_2) \rangle d\tau \quad (\text{F.15})
\end{aligned}$$

$$\begin{aligned}
\mathcal{F}(R_4) &= \int e^{i\nu(\tau_1-\tau_2)} e^{i\nu'(\tau_3-\tau_4)} e^{i\omega(\tau_2-\tau_3)} \left[ -\delta(\tau_1 - \tau_4) \langle T_\tau \hat{n}_{-\sigma}(\tau_1) \hat{q}_\sigma^\dagger(\tau_2) \hat{q}_\sigma(\tau_3) \rangle - \right. \\
&\quad \left. \delta(\tau_3 - \tau_4) \langle T_\tau \hat{q}_\sigma(\tau_1) \hat{q}_\sigma^\dagger(\tau_2) \hat{n}_{-\sigma}(\tau_3) \rangle \right] d\tau \quad (\text{F.16})
\end{aligned}$$

In order to fully profit of the superior scaling of the two-particle symmetric improved estimator, another hierarchy of equations of motion needs to be applied onto the  $R_1$ ,  $R_2$  and  $R_3$  to all remaining “free” fermionic operators. That is, for example for  $R_1$ , the one-particle Green’s functions need to be represented as one-particle symmetric improved estimators. Essentially, this procedure advances some parts of  $R_1$ ,  $R_2$  and  $R_3$  to deeper levels of the hierarchy. The error scaling of the final two-particle Green’s function expression is nevertheless determined by the  $R_i$  terms and not the two-particle symmetric improved estimator itself. Assuming the error of the one-particle Green’s function to scale with  $\mathcal{O}(i\nu^{-2})$  in  $R_1$ , the error in the two-particle Green’s function is suppressed by  $\mathcal{O}(i\nu^{-3})$ , due to the additional non-interacting propagator in (F.13).

The expressions of the  $G_{\sigma\sigma-\sigma-\sigma}^{\nu\nu'\omega}$  component, or the crossing symmetric  $G_{\sigma-\sigma-\sigma\sigma}^{\nu\nu'\omega}$  component can be derived in a similar fashion. However, the anti-commutators evaluate differently when combining opposite flavor combinations, generating different overall contributions.

# Bibliography

- [Ambegaokar and Troyer, 2010] Ambegaokar, V. and Troyer, M. (2010). Estimating errors reliably in monte carlo simulations of the ehrenfest model. *American Journal of Physics*, 78(2):150–157.
- [Anderson, 1961] Anderson, P. W. (1961). Localized Magnetic States in Metals. *Physical Review*, 124:41–53.
- [Anisimov et al., 1997] Anisimov, V. I., Poteryaev, A. I., Korotin, M. A., Anokhin, A. O., and Kotliar, G. (1997). First-principles calculations of the electronic structure and spectra of strongly correlated systems: dynamical mean-field theory. *Journal of Physics: Condensed Matter*, 9:7359–7367.
- [Anisimov, V. I. et al., 2002] Anisimov, V. I., Nekrasov, I. A., Kondakov, D. E., Rice, T. M., and Sigrist, M. (2002). Orbital-selective mott-insulator transition in ca<sub>2</sub>-xsr<sub>x</sub>ruo<sub>4</sub>. *Eur. Phys. J. B*, 25(2):191–201.
- [Antipov et al., 2014] Antipov, A. E., Gull, E., and Kirchner, S. (2014). Critical exponents of strongly correlated fermion systems from diagrammatic multiscale methods. *Phys. Rev. Lett.*, 112:226401.
- [Aryasetiawan et al., 2004] Aryasetiawan, F., Biermann, S., and Georges, A. (2004). A first principles scheme for calculating the electronic structure of strongly correlated materials: GW+DMFT. *Proceedings of the conference "Coincidence Studies of Surfaces, Thin Films and Nanostructures", Ringberg castle, Sept. 2003*.
- [Ayral and Parcollet, 2015] Ayral, T. and Parcollet, O. (2015). Mott physics and spin fluctuations: A unified framework. *Phys. Rev. B*, 92:115109.
- [Ayral and Parcollet, 2016] Ayral, T. and Parcollet, O. (2016). Mott physics and collective modes: An atomic approximation of the four-particle irreducible functional. *Phys. Rev. B*, 94:075159.
- [Bassani and Parravicini, 1975] Bassani, G. F. and Parravicini, G. P. (1975). *Electronic states and optical transitions in solids*. Pergamon Press, Oxford.
- [Bethe, 1931] Bethe, H. (1931). Zur Theorie der Metalle. *Zeitschrift für Physik*, 71(3):205–226.

- [Boehnke et al., 2011] Boehnke, L., Hafermann, H., Ferrero, M., Lechermann, F., and Parcollet, O. (2011). Orthogonal polynomial representation of imaginary-time green's functions. *Phys. Rev. B*, 84:075145.
- [Bohm and Pines, 1953] Bohm, D. and Pines, D. (1953). A collective description of electron interactions: III. coulomb interactions in a degenerate electron gas. *Phys. Rev.*, 92:609–625.
- [Brandt and Mielsch, 1989] Brandt, U. and Mielsch, C. (1989). Thermodynamics and correlation functions of the Falicov-Kimball model in large dimensions. *Zeitschrift für Phys. B Condens. Matter*, 75(3):365–370.
- [Bulla et al., 2008] Bulla, R., Costi, T. A., and Pruschke, T. (2008). Numerical renormalization group method for quantum impurity systems. *Rev. Mod. Phys.*, 80:395–450.
- [Burovski et al., 2006] Burovski, E., Prokof'ev, N., Svistunov, B., and Troyer, M. (2006). The fermi-hubbard model at unitarity. *New Journal of Physics*, 8(8):153.
- [Caffarel and Krauth, 1994] Caffarel, M. and Krauth, W. (1994). Exact diagonalization approach to correlated fermions in infinite dimensions: Mott transition and superconductivity. *Phys. Rev. Lett.*, 72:1545–1548.
- [Chalupa et al., 2017] Chalupa, P., Gunacker, P., Schäfer, T., Held, K., and Toschi, A. (2017). Divergences of the irreducible vertex functions in correlated metallic systems: Insights from the anderson impurity model. *arXiv:1712.04171*.
- [Cleveland and Medina, 1976] Cleveland, C. L. and Medina, R. A. (1976). Obtaining a Heisenberg Hamiltonian from the Hubbard model. *American Journal of Physics*, 44(1):44–46.
- [Coleman, 2015] Coleman, P. (2015). *Introduction to Many-Body Physics*. Cambridge University Press.
- [Dao et al., 2012] Dao, T.-L., Ferrero, M., Cornaglia, P. S., and Capone, M. (2012). Mott transition of fermionic mixtures with mass imbalance in optical lattices. *Phys. Rev. A*, 85:013606.
- [Doniach, 1977] Doniach, S. (1977). The Kondo lattice and weak antiferromagnetism. *Physica B+C*, 91:231–234.
- [Efron, 1979] Efron, B. (1979). Bootstrap methods: Another look at the jackknife. *Ann. Statist.*, 7(1):1–26.
- [Efron and Stein, 1981] Efron, B. and Stein, C. (1981). The jackknife estimate of variance. *Ann. Statist.*, 9(3):586–596.
- [Falicov and Kimball, 1969] Falicov, L. M. and Kimball, J. C. (1969). Simple model for semiconductor-metal transitions:  $\text{Smb}_6$  and transition-metal oxides. *Phys. Rev. Lett.*, 22(19):997–999.

- [Galler, 2017] Galler, A. (2017). *Towards an ab initio treatment of materials with local and non-local electronic correlations*. PhD thesis, Vienna University of Technology.
- [Galler et al., 2018] Galler, A., Kaufmann, J., Gunacker, P., Pickem, M., Thunström, P., Tomczak, J., and Held, K. (2018). Towards ab initio calculations with the dynamical vertex approximation. *Journal of the Physical Society of Japan*, 87(4):041004.
- [Galler et al., 2017] Galler, A., Thunström, P., Gunacker, P., Tomczak, J. M., and Held, K. (2017). Ab initio dynamical vertex approximation. *Phys. Rev. B*, 95:115107.
- [Georges and Kotliar, 1992] Georges, A. and Kotliar, G. (1992). Hubbard model in infinite dimensions. *Phys. Rev. B*, 45:6479–6483.
- [Górski and Mizia, 2013] Górski, G. and Mizia, J. (2013). Equation of motion solutions to hubbard model retaining kondo effect. *Physica B: Condensed Matter*, 427:42 – 46.
- [Gubernatis et al., 1991] Gubernatis, J. E., Jarrell, M., Silver, R. N., and Sivia, D. S. (1991). Quantum monte carlo simulations and maximum entropy: Dynamics from imaginary-time data. *Phys. Rev. B*, 44:6011–6029.
- [Gull, 2008] Gull, E. (2008). *Continuous-time quantum Monte Carlo algorithms for fermions*. PhD thesis, ETH Zurich.
- [Gull et al., 2011] Gull, E., Millis, A. J., Lichtenstein, A. I., Rubtsov, A. N., Troyer, M., and Werner, P. (2011). Continuous-time monte carlo methods for quantum impurity models. *Reviews of Modern Physics*, 83(2):349–404.
- [Gull et al., 2010] Gull, E., Reichman, D. R., and Millis, A. J. (2010). Bold-line diagrammatic monte carlo method: General formulation and application to expansion around the noncrossing approximation. *Phys. Rev. B*, 82:075109.
- [Gull et al., 2007] Gull, E., Werner, P., Millis, A., and Troyer, M. (2007). Performance analysis of continuous-time solvers for quantum impurity models. *Phys. Rev. B*, 76:235123.
- [Gull et al., 2008] Gull, E., Werner, P., Parcollet, O., and Troyer, M. (2008). Continuous-time auxiliary-field monte carlo for quantum impurity models. *EPL (Europhysics Letters)*, 82(5):57003.
- [Gunacker, 2015] Gunacker, P. (2015). Diagrammatic quantum monte carlo with worm sampling. Master’s thesis, Vienna University of Technology.
- [Gunacker et al., 2015] Gunacker, P., Wallerberger, M., Gull, E., Hausoel, A., Sangiovanni, G., and Held, K. (2015). Continuous-time quantum monte carlo using worm sampling. *Phys. Rev. B*, 92:155102.
- [Gunacker et al., 2016] Gunacker, P., Wallerberger, M., Ribic, T., Hausoel, A., Sangiovanni, G., and Held, K. (2016). Worm-improved estimators in continuous-time quantum monte carlo. *Phys. Rev. B*, 94:125153.

- [Gunnarsson et al., 2017] Gunnarsson, O., Rohringer, G., Schäfer, T., Sangiovanni, G., and Toschi, A. (2017). Breakdown of traditional many-body theories for correlated electrons. *Phys. Rev. Lett.*, 119:056402.
- [Gunnarsson et al., 2016] Gunnarsson, O., Schäfer, T., LeBlanc, J. P. F., Merino, J., Sangiovanni, G., Rohringer, G., and Toschi, A. (2016). Parquet decomposition calculations of the electronic self-energy. *Phys. Rev. B*, 93:245102.
- [Hafermann, 2014a] Hafermann, H. (2014a). Self-energy and vertex functions from hybridization-expansion continuous-time quantum monte carlo for impurity models with retarded interaction. *Phys. Rev. B*, 89:235128.
- [Hafermann, 2014b] Hafermann, H. (2014b). Self-energy and vertex functions from hybridization-expansion continuous-time quantum monte carlo for impurity models with retarded interaction. *Phys. Rev. B*, 89:235128.
- [Hafermann et al., 2009] Hafermann, H., Li, G., Rubtsov, A. N., Katsnelson, M. I., Lichtenstein, A., and Monien, H. (2009). Efficient perturbation theory for quantum lattice models. *Phys. Rev. Lett.*, 102:206401.
- [Hafermann et al., 2012] Hafermann, H., Patton, K. R., and Werner, P. (2012). Improved estimators for the self-energy and vertex function in hybridization-expansion continuous-time quantum monte carlo simulations. *Phys. Rev. B*, 85:205106.
- [Harrer, 2013] Harrer, G. (2013). Statistical methods for the w2dynamics project. Bachelor thesis, Vienna University of Technology.
- [Hartl, 2015] Hartl, B. (2015). Maximum entropy method for quantum monte carlo simulations. Project work, Vienna University of Technology.
- [Haule, 2007] Haule, K. (2007). Quantum monte carlo impurity solver for cluster dynamical mean-field theory and electronic structure calculations with adjustable cluster base. *Phys. Rev. B*, 75:155113.
- [Hedin, 1965] Hedin, L. (1965). New method for calculating the one-particle green's function with application to the electron-gas problem. *Phys. Rev.*, 139:A796.
- [Heisenberg, 1928] Heisenberg, W. (1928). Zur Theorie des Ferromagnetismus. *Zeitschrift für Physik*, 49(9):619–636.
- [Heistracher, 2016] Heistracher, P. (2016). Autocorrelation measurements in continuous-time quantum monte carlo simulations. Bachelor's thesis, Vienna University of Technology.
- [Held, 2007] Held, K. (2007). Electronic structure calculations using dynamical mean field theory. *Advances in Physics*, 56(6):829–926.
- [Held and Bulla, 2000] Held, K. and Bulla, R. (2000). Mott transition of the f-electron system in the periodic anderson model with nearest neighbor hybridization. *Eur. Phys. J. B*, 17(1):7–10.



- [Held et al., 2000] Held, K., Huscroft, C., Scalettar, R. T., and McMahan, A. K. (2000). Similarities between the hubbard and periodic anderson models at finite temperatures. *Phys. Rev. Lett.*, 85:373–376.
- [Held and Vollhardt, 1998] Held, K. and Vollhardt, D. (1998). Microscopic conditions favoring itinerant ferromagnetism: Hund’s rule coupling and orbital degeneracy. *Eur. Phys. J. B*, 5(3):473–478.
- [Hettler et al., 2000] Hettler, M., Mukherjee, M., Jarrell, M., and Krishnamurthy, H. R. (2000). Dynamical cluster approximation: Nonlocal dynamics of correlated electron systems. *Phys. Rev. B*, 61:12739.
- [Hewson, 1993] Hewson, A. C. (1993). *The Kondo Problem to Heavy Fermions*. Cambridge Studies in Magnetism. Cambridge University Press.
- [Hirsch and Fye, 1986] Hirsch, J. E. and Fye, R. M. (1986). Monte carlo method for magnetic impurities in metals. *Phys. Rev. Lett.*, 56:2521.
- [Hirschmeier et al., 2017] Hirschmeier, D., Hafermann, H., and Lichtenstein, A. I. (2017). Multiband dual fermion approach to quantum criticality in the hubbard honeycomb lattice. *arXiv:1710.08199*.
- [Hoshino and Werner, 2016] Hoshino, S. and Werner, P. (2016). Electronic orders in multiorbital hubbard models with lifted orbital degeneracy. *Phys. Rev. B*, 93:155161.
- [Hoshino and Werner, 2017] Hoshino, S. and Werner, P. (2017). Spontaneous orbital-selective mott transitions and the Jahn-Teller metal of  $A_3C_{60}$ . *Phys. Rev. Lett.*, 118:177002.
- [Hubbard, 1959] Hubbard, J. (1959). Calculation of partition functions. *Phys. Rev. Lett.*, 3:77–78.
- [Hubbard, 1964] Hubbard, J. (1964). Electron correlations in narrow energy bands. III. An improved solution. *Proc R. Soc. London*, 281(1386):401–419.
- [Ishida et al., 2006] Ishida, H., Wortmann, D., and Liebsch, A. (2006). Electronic structure of srvo<sub>3</sub> (001) surfaces: A local-density approximation plus dynamical mean-field theory calculation. *Phys. Rev. B*, 73(24):245421.
- [Iskakov et al., 2017] Iskakov, S., Terletska, H., and Gull, E. (2017). Momentum-space cluster dual fermion method. *arXiv*.
- [Janiš and Augustinský, 2008] Janiš, V. and Augustinský, P. (2008). Kondo behavior in the asymmetric Anderson model: Analytic approach. *Phys. Rev. B*, 77:085106.
- [Jarrell and Gubernatis, 1996] Jarrell, M. and Gubernatis, J. E. (1996). Bayesian inference and the analytic continuation of imaginary-time quantum monte carlo data. *Physics Reports*, 269(3):133 – 195.

- [Källén, 1952] Källén, G. (1952). On the definition of the renormalization constants in quantum electrodynamics. *Helvetica Physica Acta*, 25(4):417–434.
- [Kanamori, 1963] Kanamori, J. (1963). Electron correlation and ferromagnetism of transition metals. *Progress of Theoretical Physics*, 30(3):275–289.
- [Katanin et al., 2009] Katanin, A. A., Toschi, A., and Held, K. (2009). Comparing pertinent effects of antiferromagnetic fluctuations in the two- and three-dimensional hubbard model. *Phys. Rev. B*, 80:075104.
- [Kaufmann, 2015] Kaufmann, J. (2015). Applications of the NFFT3 library to quantum monte carlo solvers. Project work, Vienna University of Technology.
- [Kaufmann et al., 2017] Kaufmann, J., Gunacker, P., and Held, K. (2017). Continuous-time quantum monte carlo calculation of multiorbital vertex asymptotics. *Phys. Rev. B*, 96:035114.
- [Keiner et al., 2009] Keiner, J., Kunis, S., and Potts, D. (2009). Using NFFT 3—a software library for various nonequispaced fast fourier transforms. *ACM Trans. Math. Softw.*, 36(4):19:1–19:30.
- [Keiter and Kimball, 1971] Keiter, H. and Kimball, J. C. (1971). Diagrammatic approach to the anderson model for dilute alloys. *Journal of Applied Physics*, 42(4):1460–1461.
- [Kennedy, 1998] Kennedy, T. (1998). Phase separation in the neutral Falicov–Kimball model. *Journal of Statistical Physics*, 91(5):829–843.
- [Kennedy and Lieb, 1986] Kennedy, T. and Lieb, E. H. (1986). An itinerant electron model with crystalline or magnetic long range order. *Physica A*, 138(1-2):320–358.
- [Kotliar et al., 2001] Kotliar, G., Savrasov, S., Palsson, G., and Biroli, G. (2001). Cellular dynamical mean field approach to strongly correlated systems. *Phys. Rev. Lett.*, 87:186401.
- [Kramers, 1927] Kramers, H. A. (1927). La diffusion de la lumiere par les atomes. *Atti Cong. Intern. Fisici*, 2:545–557.
- [Krishna-murthy et al., 1980] Krishna-murthy, H. R., Wilkins, J. W., and Wilson, K. G. (1980). Renormalization-group approach to the anderson model of dilute magnetic alloys. i. static properties for the symmetric case. *Phys. Rev. B*, 21:1003–1043.
- [Kronig, 1926] Kronig, R. (1926). On the theory of dispersion of x-rays. *J. Opt. Soc. Am.*, 12(6):547–557.
- [Kuneš, 2011] Kuneš, J. (2011). Efficient treatment of two-particle vertices in dynamical mean-field theory. *Phys. Rev. B*, 83:085102.
- [Kuneš et al., 2010] Kuneš, J., Arita, R., Wissgott, P., Toschi, A., Ikeda, H., and Held, K. (2010). Wien2wannier: From linearized augmented plane waves to maximally localized wannier functions. *Computer Physics Communications*, 181(11):1888–1895.

- [Langreth, 1966] Langreth, D. C. (1966). Friedel sum rule for Anderson's model of localized impurity states. *Phys. Rev.*, 150:516–518.
- [Läuchli and Werner, 2009] Läuchli, A. M. and Werner, P. (2009). Krylov implementation of the hybridization expansion impurity solver and application to 5-orbital models. *Phys. Rev. B*, 80:235117.
- [LeBlanc et al., 2015] LeBlanc, J. P. F., Antipov, A. E., Becca, F., Bulik, I. W., Chan, G. K.-L., Chung, C.-M., Deng, Y., Ferrero, M., Henderson, T. M., Jiménez-Hoyos, C. A., Kozik, E., Liu, X.-W., Millis, A. J., Prokof'ev, N. V., Qin, M., Scuseria, G. E., Shi, H., Svistunov, B. V., Tocchio, L. F., Tupitsyn, I. S., White, S. R., Zhang, S., Zheng, B.-X., Zhu, Z., and Gull, E. (2015). Solutions of the two-dimensional hubbard model: Benchmarks and results from a wide range of numerical algorithms. *Phys. Rev. X*, 5:041041.
- [Lee et al., 2012] Lee, H., Foyevtsova, K., Ferber, J., Aichhorn, M., Jeschke, H. O., and Valentí, R. (2012). Dynamical cluster approximation within an augmented plane wave framework: Spectral properties of  $\text{SrVO}_3$ . *Phys. Rev. B*, 85:165103.
- [Lehmann, 1954] Lehmann, H. (1954). Über Eigenschaften von Ausbreitungsfunktionen und Renormierungskonstanten quantisierter Felder. *Il Nuovo Cimento (1943-1954)*, 11(4):342–357.
- [Li et al., 2016] Li, G., Wentzell, N., Pudleiner, P., Thunström, P., and Held, K. (2016). Efficient implementation of the parquet equations: Role of the reducible vertex function and its kernel approximation. *Phys. Rev. B*, 93:165103.
- [Lichtenstein and Katsnelson, 1998] Lichtenstein, A. I. and Katsnelson, M. I. (1998). Ab initio calculations of quasiparticle band structure in correlated systems: Lda++ approach. *Phys. Rev. B*, 57:6884–6895.
- [Lichtenstein and Katsnelson, 2000] Lichtenstein, A. I. and Katsnelson, M. I. (2000). Antiferromagnetism and  $d$ -wave superconductivity in cuprates: A cluster dynamical mean-field theory. *Phys. Rev. B*, 62:R9283–R9286.
- [Lieb et al., 1961] Lieb, E., Schultz, T., and Mattis, D. (1961). Two soluble models of an antiferromagnetic chain. *Annals of Physics*, 16(3):407 – 466.
- [Lieb and Wu, 1968] Lieb, E. H. and Wu, F. Y. (1968). Absence of mott transition in an exact solution of the short-range, one-band model in one dimension. *Phys. Rev. Lett.*, 20:1445–1448.
- [Liu and Wang, 2015] Liu, Y.-H. and Wang, L. (2015). Quantum Monte Carlo study of mass-imbalanced Hubbard models. *Phys. Rev. B*, 92(23):235129.
- [Luttinger and Ward, 1960] Luttinger, J. M. and Ward, J. C. (1960). Ground-state energy of a many-fermion system. ii. *Phys. Rev.*, 118:1417–1427.

- [Mahmoud and Gebhard, 2015] Mahmoud, Z. M. and Gebhard, F. (2015). Non-interacting single-impurity Anderson model: solution without using the equation-of-motion method. *Annalen der Physik*, 527(11-12):794–805.
- [Matsubara, 1955] Matsubara, T. (1955). A new approach to quantum-statistical mechanics. *Prog. Theor. Phys.*, 14:351.
- [Mermin and Wagner, 1966] Mermin, N. and Wagner, H. (1966). Absence of ferromagnetism or antiferromagnetism in one- or two-dimensional isotropic Heisenberg models. *Phys. Rev. Lett.*, 17:1133.
- [Metzner and Vollhardt, 1989] Metzner, W. and Vollhardt, D. (1989). Correlated lattice fermions in  $d=\infty$  dimensions. *Phys. Rev. Lett.*, 62:324–327.
- [Mott, 1968] Mott, N. F. (1968). Metal-insulator transition. *Rev. Mod. Phys.*, 40:677–683.
- [Moutenet et al., 2018] Moutenet, A., Wu, W., and Ferrero, M. (2018). Determinant monte carlo algorithms for dynamical quantities in fermionic systems. *Phys. Rev. B*, 97:085117.
- [Nekrasov et al., 2006] Nekrasov, I. A., Held, K., Keller, G., Kondakov, D. E., Pruschke, T., Kollar, M., Andersen, O. K., Anisimov, V. I., and Vollhardt, D. (2006). Momentum-resolved spectral functions of  $\text{SrVO}_3$  calculated by LDA+DMFT. *Phys. Rev. B*, 73:155112.
- [Nobel Media, 2014] Nobel Media (2014). The Nobel Prize in Physics 1918.
- [Osolin and Žitko, 2013] Osolin, i. c. v. and Žitko, R. (2013). Padé approximant approach for obtaining finite-temperature spectral functions of quantum impurity models using the numerical renormalization group technique. *Phys. Rev. B*, 87:245135.
- [Otsuki et al., 2017] Otsuki, J., Ohzeki, M., Shinaoka, H., and Yoshimi, K. (2017). Sparse modeling approach to analytical continuation of imaginary-time quantum monte carlo data. *Phys. Rev. E*, 95:061302.
- [Parragh et al., 2012] Parragh, N., Toschi, A., Held, K., and Sangiovanni, G. (2012). Conserved quantities of  $su(2)$ -invariant interactions for correlated fermions and the advantages for quantum monte carlo simulations. *Phys. Rev. B*, 86:155158.
- [Philipp et al., 2017] Philipp, M.-T., Wallerberger, M., Gunacker, P., and Held, K. (2017). Mott-hubbard transition in the mass-imbalanced hubbard model. *The European Physical Journal B*, 90(6):114.
- [Potthoff et al., 1997] Potthoff, M., Wegner, T., and Nolting, W. (1997). Interpolating self-energy of the infinite-dimensional hubbard model: Modifying the iterative perturbation theory. *Phys. Rev. B*, 55:16132–16142.
- [Prokof'ev et al., 1998a] Prokof'ev, N. V., Svistunov, B., and Tupitsyn, I. (1998a). “worm” algorithm in quantum monte carlo simulations. *Physics Letters A*, 238(4-5):253–257.

- [Prokof'ev et al., 1998b] Prokof'ev, N. V., Svistunov, B. V., and Tupitsyn, I. S. (1998b). Exact, complete, and universal continuous-time worldline monte carlo approach to the statistics of discrete quantum systems. *Journal of Experimental and Theoretical Physics*, 87(2):310–321.
- [Pruschke and Grewe, 1989] Pruschke, T. and Grewe, N. (1989). The anderson model with finite coulomb repulsion. *Zeitschrift für Physik B Condensed Matter*, 74(4):439–449.
- [Quenouille, 1956] Quenouille, M. H. (1956). Notes on bias in estimation. *Biometrika*, 43(3/4):353–360.
- [Ribic, 2015] Ribic, T. (2015). Vertex extensions of the dynamical mean field theory for the Falicov-Kimball model. Master's thesis, Vienna University of Technology.
- [Ribic, 2018] Ribic, T. (2018). *The Vertexnomicon: Considerations on effective path-integral methods in solid state theory*. PhD thesis, Vienna University of Technology.
- [Ribic et al., 2014] Ribic, T., Assmann, E., Tóth, A., and Held, K. (2014). Cubic interaction parameters for  $t_{2g}$  wannier orbitals. *Phys. Rev. B*, 90:165105.
- [Ribic et al., 2017a] Ribic, T., Gunacker, P., Iskakov, S., Wallerberger, M., Rohringer, G., Rubtsov, A. N., Gull, E., and Held, K. (2017a). Role of three-particle vertex within dual fermion calculations. *Phys. Rev. B*, 96:235127.
- [Ribic et al., 2017b] Ribic, T., Rohringer, G., and Held, K. (2017b). Local correlation functions of arbitrary order for the falicov-kimball model. *Phys. Rev. B*, 95:155130.
- [Rohringer et al., 2017] Rohringer, G., Hafermann, H., Toschi, A., Katanin, A. A., Antipov, A. E., Katsnelson, M. I., Lichtenstein, A. I., Rubtsov, A. N., and Held, K. (2017). Diagrammatic routes to non-local correlations beyond dynamical mean field theory. *ArXiv e-prints*.
- [Rohringer et al., 2013] Rohringer, G., Toschi, A., Hafermann, H., Held, K., Anisimov, V. I., and Katanin, A. A. (2013). One-particle irreducible functional approach: A route to diagrammatic extensions of the dynamical mean-field theory. *Phys. Rev. B*, 88:115112.
- [Rohringer et al., 2011] Rohringer, G., Toschi, A., Katanin, A., and Held, K. (2011). Critical properties of the half-filled hubbard model in three dimensions. *Phys. Rev. Lett.*, 107:256402.
- [Rohringer et al., 2012] Rohringer, G., Valli, A., and Toschi, A. (2012). Local electronic correlation at the two-particle level. *Phys. Rev. B*, 86:125114.
- [Rubtsov and Lichtenstein, 2004] Rubtsov, A. and Lichtenstein, A. (2004). Continuous-time quantum monte carlo method for fermions: Beyond auxiliary field framework. *Journal of Experimental and Theoretical Physics Letters*, 80(1):61–65.

- [Rubtsov et al., 2008] Rubtsov, A. N., Katsnelson, M. I., and Lichtenstein, A. I. (2008). Dual fermion approach to nonlocal correlations in the hubbard model. *Phys. Rev. B*, 77:033101.
- [Sakuma et al., 2013] Sakuma, R., Werner, P., and Aryasetiawan, F. (2013). Electronic structure of srvo<sub>3</sub> within *gw*+dmft. *Phys. Rev. B*, 88:235110.
- [Sandvik, 2014] Sandvik, A. (2014). Monte Carlo simulations in classical statistical physics. <http://physics.bu.edu/~py502/lectures5/mc.pdf>. Last accessed on Dec 19, 2017.
- [Schäfer et al., 2016a] Schäfer, T., Ciuchi, S., Wallerberger, M., P., T., Gunnarsson, O., Sangiovanni, G., Rohringer, G., and Toschi, A. (2016a). Non-perturbative landscape of the mott-hubbard transition: Multiple divergence lines around the critical endpoint. *Phys. Rev. B*, 94:235108.
- [Schäfer et al., 2015] Schäfer, T., Geles, F., Rost, D., Rohringer, G., Arrigoni, E., Held, K., Blümer, N., Aichhorn, M., and Toschi, A. (2015). Fate of the false mott-hubbard transition in two dimensions. *Phys. Rev. B*, 91:125109.
- [Schäfer et al., 2016b] Schäfer, T., Katanin, A., Held, K., and Toschi, A. (2016b). Quantum criticality with a twist - interplay of correlations and kohn anomalies in three dimensions. *preprint arXiv:1605.06355*.
- [Schäfer et al., 2013a] Schäfer, T., Rohringer, G., Gunnarsson, O., Ciuchi, S., Sangiovanni, G., and Toschi, A. (2013a). Divergent precursors of the mott-hubbard transition at the two-particle level. *Phys. Rev. Lett.*, 110:246405.
- [Schäfer et al., 2013b] Schäfer, T., Rohringer, G., Gunnarsson, O., Ciuchi, S., Sangiovanni, G., and Toschi, A. (2013b). Divergent precursors of the mott-hubbard transition at the two-particle level. *Phys. Rev. Lett.*, 110:246405.
- [Schrieffer and Wolff, 1966] Schrieffer, J. R. and Wolff, P. A. (1966). Relation between the Anderson and Kondo hamiltonians. *Phys. Rev.*, 149:491–492.
- [Schwarz and Blaha, 2003] Schwarz, K. and Blaha, P. (2003). Solid state calculations using wien2k. *Computational Materials Science*, 28(2):259–273. Proceedings of the Symposium on Software Development for Process and Materials Design.
- [Sekiyama et al., 2004] Sekiyama, A., Fujiwara, H., Imada, S., Suga, S., Eisaki, H., Uchida, S. I., Takegahara, K., Harima, H., Saitoh, Y., Nekrasov, I. A., Keller, G., Kondakov, D. E., Kozhevnikov, A. V., Pruschke, T., Held, K., Vollhardt, D., and Anisimov, V. I. (2004). Mutual experimental and theoretical validation of bulk photoemission spectra of sr<sub>1-x</sub>ca<sub>x</sub>vo<sub>3</sub>. *Phys. Rev. Lett.*, 93(15):156402.
- [Sémon et al., 2014] Sémon, P., Sordi, G., and Tremblay, A.-M. S. (2014). Ergodicity of the hybridization-expansion monte carlo algorithm for broken-symmetry states. *Phys. Rev. B*, 89:165113.

- [Shimahara and Takada, 1988] Shimahara, H. and Takada, S. (1988). Superconductivity and spin density wave in two dimensional Hubbard model. *Journal of the Physical Society of Japan*, 57(3):1044–1055.
- [Shinaoka et al., 2014] Shinaoka, H., Dolfi, M., Troyer, M., and Werner, P. (2014). Hybridization expansion monte carlo simulation of multi-orbital quantum impurity problems: matrix product formalism and improved sampling. *Journal of Statistical Mechanics: Theory and Experiment*, 2014(6):P06012.
- [Shinaoka et al., 2017a] Shinaoka, H., Gull, E., and Werner, P. (2017a). Continuous-time hybridization expansion quantum impurity solver for multi-orbital systems with complex hybridizations. *Computer Physics Communications*, 215:128–136.
- [Shinaoka et al., 2018] Shinaoka, H., Otsuki, J., Haule, K., Wallerberger, M., Gull, E., Yoshimi, K., and Ohzeki, M. (2018). Overcomplete compact representation of two-particle green’s functions. *preprint arXiv:1803.01916*.
- [Shinaoka et al., 2017b] Shinaoka, H., Otsuki, J., Ohzeki, M., and Yoshimi, K. (2017b). Compressing green’s function using intermediate representation between imaginary-time and real-frequency domains. *Phys. Rev. B*, 96:035147.
- [Slater and Koster, 1954] Slater, J. C. and Koster, G. F. (1954). Simplified LCAO method for the periodic potential problem. *Phys. Rev.*, 94:1498–1524.
- [Sotnikov et al., 2012] Sotnikov, A., Cocks, D., and Hofstetter, W. (2012). Advantages of mass-imbalanced ultracold fermionic mixtures for approaching quantum magnetism in optical lattices. *Phys. Rev. Lett.*, 109:065301.
- [Stratonovich, 1957] Stratonovich, R. L. (1957). On a Method of Calculating Quantum Distribution Functions. *Soviet Physics Doklady*, 2:416.
- [Sullivan and Dongarra, 2000] Sullivan, F. and Dongarra, J. (2000). Guest editors’ introduction: The top 10 algorithms. *Computing in Science and Engineering*, 2:22–23.
- [Tagliavini et al., 2018] Tagliavini, A., Hummel, S., Wentzell, N., Andergassen, S., Toschi, A., and Rohringer, G. (2018). Efficient bethe-salpeter equations’ treatment in dynamical mean-field theory. *arXiv*.
- [Taglieber et al., 2008] Taglieber, M., Voigt, A.-C., Aoki, T., Hänsch, T. W., and Dieckmann, K. (2008). Quantum degenerate two-species fermi-fermi mixture coexisting with a bose-einstein condensate. *Phys. Rev. Lett.*, 100:010401.
- [Taranto et al., 2014] Taranto, C., Andergassen, S., Bauer, J., Held, K., Katanin, A., Metzner, W., Rohringer, G., and Toschi, A. (2014). From infinite to two dimensions through the functional renormalization group. *Phys. Rev. Lett.*, 112:196402.
- [Taranto et al., 2013] Taranto, C., Kaltak, M., Parragh, N., Sangiovanni, G., Kresse, G., Toschi, A., and Held, K. (2013). Comparing quasiparticle  $gw+dmft$  and  $lda+dmft$  for the test bed material  $srvo_3$ . *Phys. Rev. B*, 88:165119.

- [Tokura and Nagaosa, 2000] Tokura, Y. and Nagaosa, N. (2000). Orbital physics in transition-metal oxides. *Science*, 288(5465):462–468.
- [Toschi et al., 2007] Toschi, A., Katanin, A. A., and Held, K. (2007). Dynamical vertex approximation: A step beyond dynamical mean-field theory. *Phys. Rev. B*, 75(4):045118.
- [Toschi et al., 2011] Toschi, A., Rohringer, G., Katanin, A., and Held, K. (2011). Ab initio calculations with the dynamical vertex approximation. *Annalen der Physik*, 523(8-9):698.
- [Valli et al., 2015] Valli, A., Schäfer, T., Thunström, P., Rohringer, G., Andergassen, S., Sangiovanni, G., Held, K., and Toschi, A. (2015). Dynamical vertex approximation in its parquet implementation: Application to hubbard nanorings. *Phys. Rev. B*, 91:115115.
- [Van Hove, 1953] Van Hove, L. (1953). The occurrence of singularities in the elastic frequency distribution of a crystal. *Phys. Rev.*, 89:1189–1193.
- [Veschgini and Salmhofer, 2013] Veschgini, K. and Salmhofer, M. (2013). Schwinger-Dyson renormalization group. *PRB*, 88:155131.
- [Vidberg and Serene, 1977] Vidberg, H. J. and Serene, J. W. (1977). Solving the eliashberg equations by means of n-point padé approximants. *Journal of Low Temperature Physics*, 29(3):179–192.
- [Wallerberger, 2016] Wallerberger, M. (2016). *w2dynamics: continuous time quantum Monte Carlo calculations of one- and two-particle propagators*. PhD thesis, Vienna University of Technology.
- [Wang et al., 2011] Wang, X., Dang, H. T., and Millis, A. J. (2011). High-frequency asymptotic behavior of self-energies in quantum impurity models. *Phys. Rev. B*, 84:073104.
- [Wentzell et al., 2016] Wentzell, N., Li, G., Tagliavini, A., Taranto, C., Rohringer, G., Held, K., Toschi, A., and Andergassen, S. (2016). High-frequency asymptotics of the vertex function: diagrammatic parametrization and algorithmic implementation. *arXiv*.
- [Werner et al., 2006] Werner, P., Comanac, A., de’ Medici, L., Troyer, M., and Millis, A. J. (2006). Continuous-time solver for quantum impurity models. *Phys. Rev. Lett.*, 97:076405.
- [Werner and Millis, 2006] Werner, P. and Millis, A. J. (2006). Hybridization expansion impurity solver: General formulation and application to kondo lattice and two-orbital models. *Phys. Rev. B*, 74:155107.
- [White, 1992] White, S. R. (1992). Density matrix formulation for quantum renormalization groups. *Phys. Rev. Lett.*, 69:2863–2866.
- [Wiegmann, 1980] Wiegmann, P. (1980). Towards an exact solution of the anderson model. *Physics Letters A*, 80(2):163 – 167.



- [Wilson, 1975] Wilson, K. G. (1975). The renormalization group: Critical phenomena and the Kondo problem. *Rev. Mod. Phys.*, 47:773–840.
- [Wolff, 1983] Wolff, U. (1983). Saddle point mean field calculation in the Hubbard model. *Nuclear Physics B*, 225(3):391–408.
- [Zener, 1951] Zener, C. (1951). Interaction between the  $d$  shells in the transition metals. *Phys. Rev.*, 81:440–444.
- [Zinn-Justin, 2002] Zinn-Justin, J. (2002). *Quantum Field Theory and Critical Phenomena*. International series of monographs on physics. Clarendon Press.



# Acknowledgements

A couple of years ago I was deeply convinced that a PhD in computational physics was a lone and long journey, characterized by endless nights of aligning modern-age hieroglyphs on computer screens, driven by an increasingly health-damaging coffee addiction. Today, I know how mistaken I was in this belief. More so, I became conscious of the fact that a significant amount of my work has been completed during daytime, without an excessive intake of caffeine, but most importantly, with the considerable help of various people.

First and foremost, my special thanks goes to my supervisor **Karsten Held**. On numerous occasions during the last several years I was amazed about his ability to seemingly create time in an otherwise so full schedule of any professor and active group leader with more than 15 group members. During our discussions, I got to appreciate his deep physical intuition and great knowledge of the field of condensed matter physics. These attributes were further complemented by his expertise in quantum Monte Carlo methods, which was of great help during my own research. Last but not least, he granted me the chance to visit various international conferences and schools during the last years.

In that respect, I also like to greatly thank **Giorgio Sangiovanni**, who managed to hold together the developments of our *w2dynamics* code for the last eight years. Many times I was astonished how a professor and active group leader is capable of keeping track of a scientific code, as Giorgio did. Also, I would like to thank Giorgio for giving me several opportunities visiting him and **Andreas Hausoel** in Würzburg. I feel honored to be part of such a great developer team.

I would like to thank **Emanuel Gull**, who invited me to Ann Arbor in 2017 for several weeks to work on three-particle estimators. During an extended hike in the Austrian mountains in fall 2013 he suggested to Markus implementing the worm algorithm to CT-HYB. Eventually, this out-of-office discussion determined my research for the next coming years.

Also, I would like to thank **Alessandro Toschi** for spending several hours teaching me condensed matter physics in lecture halls and his own office.

I would like to thank the **VSC Team** for giving me the opportunity to partake in the VSC School, covering the expenses during my PhD, further providing me with a limitless amount of computational resources and organizing several VSC conferences I was able to attend. Special thanks goes to **Claudia Blaas-Schenner**, who coordinated the VSC School and was my always-responsive contact person.

At this point I want to thank all my colleagues at TU Wien for providing such a great research environment. A special thanks goes to **Markus Wallerberger**, who was my unofficial supervisor and colleague during the last years. In many situations, I was able

to learn from his physical intuition and excellent programming style. Not only I sincerely enjoyed working together with him, but I am also happy sharing various non-work related experiences with him.

Another group of people I would like to thank are several students I was able to supervise during the last years: namely **Benedikt Hartl** (project work), **Josef Kaufmann** (project work and diploma thesis), **Paul Heistracher** (project work) and **Patrick Chalupa** (diploma thesis). Working together with these excellent students proved to be a valuable experience and taught me a great bit about physics. I got to enjoy many conversations with Josef on the topic of MaxEnt and analytic continuations and I am curious what he will come up with some day.

Being so tied-up in method development sometimes makes one ignorant of the physical aspects. I would like to thank all of my co-workers with whom I was able to publish papers. I spent several hours with **Anna Galler** constructing and benchmarking local vertices for AbinitioDGA. On a different note, there were times I was most troubled with technicalities, while **Tin Ribic** was solely concerned with the workings of the Falicov-Kimball model. At some point we were obliged to work together, which resulted in a great on-going cooperation.

I would like to use this opportunity to thank **Marie-Therese Philipp** and **Thomas Schäfer**, with whom I was able to organize the journal club. With **Patrik Thunstöm** and **Daniel Springer** I had some of the most interesting “outside-the-box” technical discussions.

Finally, I would like to thank the members of my family, my own parents and my parents-in-law for providing a stable environment during my entire education. Let me further mention my siblings and siblings-in-law for keeping in touch despite my unresponsiveness at times. Last but by no means least, I would like to thank my loving wife **Grace** for keeping up with me during the last years and her always-encouraging attitude. She herself is one of the most disciplined and yet kindhearted persons I know and my all-time example.

# Curriculum Vitae

## Personal Information

**Name:** Patrik Gunacker  
**Date of Birth:** 23 April 1990  
**Place of Birth:** Vienna, Austria

## Education

**2015-present:** Ph.D. in Physics, Vienna University of Technology, Austria  
**2013-2015:** M.Sc. in Technical Physics (with distinction), Vienna University of Technology, Austria  
**2008-2013:** B.Sc. in Technical Physics, Vienna University of Technology, Austria  
**2005-2008:** International Baccalaureate / US High School Diploma, American International School Riyadh, Saudi Arabia

## Academic Employment and Teaching

**02/2015-present:** Vienna Scientific Cluster Project Assistant, Vienna University of Technology, Austria  
**10/2012-06/2015:** Tutor for Computing in Physics (C/C++), Scientific Computing (Fortran), Numerical Methods and Simulations (Fortran), Vienna University of Technology, Austria  
**07/2013-09/2013:** European Research Council Project Assistant, Vienna University of Technology, Austria

## Conferences and Research Visits

**2018:** University of Würzburg - Research Stay, Prof. Giorgio Sangiovanni, 02/2018, Würzburg (Germany)  
**2017:** Austrian High Performance Computing Meeting, 02/2017, Grundlsee (Austria)  
Contributed talk: Diagrammatic Quantum Monte Carlo for Strongly Correlated Electron Systems

University of Michigan - Research Stay, Prof. Emanuel Gull, 01/2017, Ann Arbor (USA)

Seminar talk: Worm Estimators in the Hybridization Expansion Continuous-time Quantum Monte Carlo

Theory Winter School - Modeling of Correlated Electron Materials, 01/2017, Tallahassee (USA)

Poster: Worm Improved Estimators in Continuous-time Quantum Monte Carlo

**2016:** International Summer School on Computational Quantum Materials, 06/2016, Sherbrooke (Canada)

Poster: Worm Improved Estimators in Continuous-time Quantum Monte Carlo

University of Würzburg - Research Stay, Prof. Giorgio Sangiovanni, 04/2016, Würzburg (Germany)

Austrian High Performance Computing Meeting, 02/2016, Grundlsee (Austria)  
Contributed talk: Diagrammatic Quantum Monte Carlo for Strongly Correlated Electron Systems

**2015:** 2nd International Workshop on Dynamical Mean-field Approach for Strongly Correlated Materials, 09/2015, Dresden (Germany)

Poster: Continuous-time Quantum Monte Carlo using Worm Sampling

Second Annual Summer School Simons Collaboration on the Many Electron Problem, 06/2015, Stony Brook (USA)

Contributed talk: Diagrammatic Quantum Monte Carlo with Worm Sampling

Austrian High Performance Computing Meeting, 02/2015, Obergurgl (Austria)

## Thesis Co-Supervisions

**2017:** Irreducible vertex divergences in strongly correlated metallic systems, P. Chalupa, Diploma thesis

Calculation of vertex asymptotics from local correlation functions, J. Kaufmann, Diploma thesis

**2016:** Autocorrelation measurements in continuous-time quantum Monte Carlo simulations, P. Heistracher, Project work

**2015:** Application of the NFFT3 library to quantum Monte Carlo solvers, J. Kaufmann, Project work

Maximum entropy method for quantum Monte Carlo simulations, B. Hartl, Project work

# Publication List

## Peer-reviewed journal publications:

A. Galler, J. Kaufmann, P. Gunacker, M. Pickem, P. Thunström, J. Tomczak and K. Held; Towards ab initio Calculations with the Dynamical Vertex Approximation. Journal of the Physical Society of Japan 87(4), 041004 (2018)

T. Ribic, P. Gunacker, S. Iskakov, M. Wallerberger, G. Rohringer, A. Rubtsov, E. Gull and K.Held; Role of three-particle vertex within dual fermion calculations. Phys. Rev. B. 96, 235127 (2017)

J. Kaufmann, P. Gunacker, and K. Held; Continuous-time quantum Monte Carlo calculation of multi-orbital vertex asymptotics. Phys. Rev. B. 96, 035114 (2017)

M. Philipp, M. Wallerberger, P. Gunacker and K. Held; Mott-Hubbard transition in the mass-imbalanced Hubbard model. Eur. Phys. J. B 90,114 (2017)

A. Galler, P. Thunström, P. Gunacker, J. Tomczak and K. Held; Ab initio dynamical vertex approximation. Phys. Rev. B. 95, 115107 (2017)

P. Gunacker, M. Wallerberger, T. Ribic, A. Hausoel, G. Sangiovanni and K. Held; Worm-improved estimators in continuous-time quantum Monte Carlo. Phys. Rev. B. 94, 125153 (2016)

P. Gunacker, M. Wallerberger, E. Gull, A. Hausoel, G. Sangiovanni and K. Held; Continuous-time quantum Monte Carlo using worm sampling. Phys. Rev. B. 92, 155102 (2015)

E. Gruber, G. Kowarik, F. Ladinig, J. P. Waclawek, D. Schrempf, F. Aumayr, R. J. Berezky, K. Tokesi, P. Gunacker, T. Schweigler, C. Lemell, and J. Burgdörfer; Temperature control of ion guiding through insulating capillaries. Phys. Rev. A. 86, 062901 (2012)

## Preprints:

T. Ribic, P. Gunacker and K. Held; Impact of choosing self-consistent impurity problems in Dual Fermion calculations. In preparation (2018)

A. Hausoel, A. Kowalski, P. Gunacker and G. Sangiovanni; Having Monte Carlo decide which part of the weight to calculate: eigenstate-sampling in CTQMC. In preparation (2018)

M. Wallerberger, A. Hausoel, P. Gunacker, A. Kowalski, N. Parragh, F. Goth, K. Held and G. Sangiovanni; w2dynamics: Local one- and two-particle quantities from dynamical mean field theory. arXiv:1801.10209 (2018)

P. Chalupa, P. Gunacker, T. Schäfer, K. Held and A. Toschi; Divergences of the irreducible vertex functions in correlated metallic systems: Insights from the Anderson Impurity Model. arXiv:1712.04171 (2017)